

UC Berkeley

UC Berkeley Electronic Theses and Dissertations

Title

Neutron-based Measurements in Large Neutrino Detectors and Characterization of Water-based Liquid Scintillator

Permalink

<https://escholarship.org/uc/item/8nh1p1cd>

Author

Callaghan, Edward Joseph

Publication Date

2023

Peer reviewed|Thesis/dissertation

Neutron-based Measurements in Large Neutrino Detectors and Characterization of
Water-based Liquid Scintillator

by

Edward J. Callaghan

A dissertation submitted in partial satisfaction of the

requirements for the degree of

Doctor of Philosophy

in

Physics

in the

Graduate Division

of the

University of California, Berkeley

Committee in charge:

Professor Gabriel Orebi Gann, Chair

Professor Marjorie Shapiro

Professor Jessica Lu

Fall 2023

Neutron-based Measurements in Large Neutrino Detectors and Characterization of
Water-based Liquid Scintillator

Copyright 2023
by
Edward J. Callaghan

Abstract

Neutron-based Measurements in Large Neutrino Detectors and Characterization of Water-based Liquid Scintillator

by

Edward J. Callaghan

Doctor of Philosophy in Physics

University of California, Berkeley

Professor Gabriel Orebi Gann, Chair

This dissertation presents neutron-based measurements made using the water-Cherenkov SNO detector filled with heavy water, and the scintillator-based SNO+ detector filled with liquid scintillator, as well as lab-scale R&D measurements of water-based liquid scintillator (WbLS), a candidate material for achieving hybrid Cherenkov/scintillation technology. The results are of interest for the design of future detectors, from the perspectives of both background prediction and reconstruction capabilities, as well as improving the understanding of the nucleus and its interactions and the nature of dark matter, and the cosmos at large.

Neutrons produced by cosmic-ray muons in the SNO detector are characterized, and their production rate is measured to be, in units of $10^{-4} \text{ cm}/(\text{g} \cdot \mu)$, $7.28 \pm 0.09 \text{ (stat.)}^{+1.59}_{-1.12} \text{ (syst.)}$ and $7.30 \pm 0.07 \text{ (stat.)}^{+1.40}_{-1.02} \text{ (syst.)}$ in pure deuterium and deuterium loaded with NaCl at 0.02% by weight, respectively. A comparison of high-level observables in the accumulated data and a set of GEANT4-based simulations reveals generally accurate modeling of the production and transport physics in heavy water, but may indicate shortcomings in high-energy interactions with sodium and chlorine nuclei, which warrants further investigation.

A preliminary search for extraterrestrial antineutrinos with SNO+, which would manifest as an excess of tens-of-MeV inverse β -decay (IBD) events and be indicative of new astrophysical phenomena, potentially shedding light on the nature of dark matter, has yielded no significant signal. Statistical analysis in a Bayesian framework has produced a 90% credible limit on the flux of astrophysical antineutrinos of approximately $10^3 \text{ cm}^{-2} \text{ s}^{-1} \text{ MeV}^{-1}$, further decreasing as a function energy. Sensitivity projections for an updated analysis on 5 years worth of data indicate that SNO+ would achieve limits comparable to the current world-leading limits, which would be further improved by extensions to reconstruction techniques to adapt to a higher-energy regime.

Also presented is a characterization of the response of both WbLS and LAB+PPO, a con-

ventional scintillator cocktail, to MeV-scale protons via a broad-spectrum neutron beam, and electrons and α particles via radioactive sources. The results of this characterization are relevant for measurements made in a low-energy regime, including antineutrinos from nuclear reactors and solar neutrinos, and demonstrate timing-based Cherenkov/scintillation discrimination in electron interactions at the benchtop scale.

This dissertation is dedicated to Charlotte McGalliard Cone; a brilliant scientist, a sustaining inspiration, and a grandmother, both loving and loved.

Acknowledgments

What a terribly difficult task it is to enumerate the many people who have helped produce this document. One might think it's just a matter of writing a few names, but alas, it is more than a few, and each person is worth more than their name. I am now sure that these sections are subject to a Gödel-like incompleteness theorem, but nonetheless, here is my best attempt, inexhaustive as it may be.

Principal thanks go to my advisor, Gabriel, who gave me the coveted Goldilocks' freedom — an allowance to explore and develop my own ideas, methods, and results, but firm enough support for the path to always lead somewhere productive. When I would inevitably encounter a problem that I deemed insurmountable — they have come technical, practical, political, and personal — she always found a solution, and it was never to leave me behind. Her composure in the difficult times was steady, and her momentum through to the many joyous days exemplified the difference between a project and a research program. I am proud of the work presented in this document, and I could not imagine having produced it under the guidance of anyone else.

I am also remarkably fortunate to have worked with a real “who’s who” of postdocs during my time at Berkeley — in particular, Dr. Javi Caravaca, Dr. Tanner Kaptanoglu, Dr. Morgan Askins, and Dr. Logan Lebanowski. Javi made me appreciate the importance of maintaining knowledge of the larger context of our physics research program, and his sage advice to “just look at the waveforms” almost always bailed me out of troubleshooting that would have taken several times longer using the analytic means that I insisted would be “easier.” I hope I can always remember this trick as I continue in science. Tanner took the same sentiment even further by seeming to *always* have the *maximally complementary* approach to a problem as I did — it may have been frustrating sometimes, but it was this complementarity that produced our near-gapless understanding of the data coming out of that dark box. From Tanner I learned a little about electronics, a little about optics, and a lot about losing bets — with a larger paycheck coming, I may finally pay up. I first met Morgan almost ten years ago, and I remember asking him about isotropy estimators used in SNO — “they’re just Legendre polynomials, nothing more than what you find in E&M” was his response. That was the first of many great, cross-sectional answers he gave to the questions I brought to him. And the important lesson is one step higher level — I have learned much from him about physics, statistics, and computing, but the illustration of what it is to diagonalize a topic is what has let me excel, to any extent that I have. I also *promise* that I will give *Julia* a fair try. Logan provided me with many technical ideas and, frankly, hilarious gossip, but most importantly he constituted the anchor for my analysis of SNO+ data. That project was defined and executed relatively quickly, and I simply can’t imagine that it would stand anywhere near as firmly were it not for his sage grounding and near-encyclopedic knowledge of how to do what what needed to be done.

The Bay Area Neutron Group welcomed me in collaboratively performing the proton light yield measurements contained in this work, and to simply say that “I couldn’t have done it without them” would border on shameless insult. Collaborating across disciplines can

sometimes feel difficult, but I am grateful to have worked with experts who were able to teach me about both engineering and the physics of scintillation — things that have propagated to have impact beyond the lab-scale measurements which we jointly published. In particular, I must name Thibault Laplace, who acted as my *de facto* mentor, having taught me many things which I thought I already knew, from the very first explanations of quenching models through to the quantitative importance of correlated uncertainties. Thibault never judged my naïvete in his field, whether due to silly differences in terminology or my genuinely lacking any clue about the physics, and always stuck with his pedagogy until I was on the same page — even at five o'clock in the morning, in a sleepy cyclotron facility lounge.

Other researchers who taught me something substantial or otherwise caused me to change the way that I approach science, whether they know it or not, include (in no particular order): Josh Klein, Tony LaTorre, Minfang Yeh, Richie Bonventre, Ben Land, Hans Steiger, Andy Mastbaum, Sam Naugle, Jeff Tseng, Lawrence Hall, Bethany Goldblum, Juan Manfredi, Josh Brown, Guang Yang, Stefan Schoppmann, Stephane Zsoldos, Zara Bagdasarian, Alan Poon, and Joe Formaggio.

I acknowledge the Consortium for Monitoring, Technology, and Verification (MTV) for their intellectual and financial support for several of the past few years, as well as numerous trips to Ann Arbor, which somehow proved that work travel can be fun.

Of course I must mention Max Smiley, who suffered through the trials of both neutrino physics and graduate school with me for almost all of my time as a student. He has many times acted as a desperately-needed voice of sanity, ranging from times of unspeakable silliness committed by collaborators new and old to the exhausting stretches of the strike. I have been relieved to always know I could turn to him and ask, “*Are you seeing this?*”

I continue with a nod to the rest of my comrades in the physics department, who are too numerous to name — though I will explicitly realize Kayla, Scott, and Roger, for your company in the Alcatraz house over those years. I survived the dark days of the pandemic not only with you but, really, because of you — it’s a wonder that we didn’t tear each other to pieces, but without each of your friendships during that time I would surely have gone mad.

I’d like to acknowledge a group of educators who I feel somewhat blessed to have intersected with during high school. Joy Nichols, Michael Clancy, and Dennis Andrews each provided me with support and encouragement during a critical time in my development, and as teachers in this country are seldom given the thanks they deserve. In the sense of chaos theory, my life could be very different today had the years they knew me gone only so slightly differently, and I credit these three, among others, with helping me along the direction that ultimately led me to pursuing graduate school.

Finally, I thank my family, whose blanket-support and understanding of my choices in life have become more appreciably clear, and, I hope, clearly appreciated as the years have gone on. Their passion for my passion, and willingness to overlook how it may conflict with their views of the world or choices of where to live have not gone unnoticed.

So, that is the cast — and now, the production!

Contents

Contents	iv
List of Figures	vii
List of Tables	xiii
List of Acronyms	xix
1 Introduction and Context	1
2 Neutrinos in and out of the Standard Model	2
2.1 The structure of the Standard Model	2
2.2 The Solar Neutrino Problem	4
2.3 Massive neutrinos, and open questions	6
2.4 Dark matter	8
3 Optical Neutrino Detectors	10
3.1 Historical radiation detection technology	10
3.1.1 Cherenkov light	10
3.1.2 Organic scintillation	11
3.2 Detectors of the past and present	12
3.3 Hybrid detector technology	14
3.4 Particle astrophysics with neutrino detectors	17
4 Cosmogenic Neutrons in SNO	20
4.1 Introduction	20
4.2 The SNO Detector	21
4.3 Simulating SNO: GEANT4 and SNOMAN	23
4.4 Analysis	25
4.4.1 Muon reconstruction	26
4.4.2 Data set and event selection	26
4.4.3 Tests of model predictions	28
4.4.4 Neutron yield	28

4.4.5	Capture efficiency	29
4.4.6	Observation efficiency	31
4.4.7	Backgrounds	31
4.5	Study of Event Distributions	33
4.5.1	Follower selection	33
4.5.2	Follower multiplicity	35
4.5.3	Capture position	35
4.5.4	Capture clustering	36
4.5.5	Lateral capture distance	37
4.5.6	Time delay	39
4.6	Results for neutron yield	39
4.6.1	Evaluation of the Poisson hypothesis	40
4.6.2	Comparison to other experiments	41
5	Extraterrestrial Antineutrinos in SNO+	43
5.1	Introduction	43
5.2	The SNO+ detector	44
5.3	Simulating SNO+: RAT	45
5.4	Reconstruction	45
5.4.1	Overview	45
5.4.2	Performance at high energy	47
5.5	Data set and event selection	47
5.5.1	Prompt event selection criteria	48
5.5.2	Delayed event selection criteria	48
5.5.3	Detector response matrix and signal efficiency	50
5.6	High-energy backgrounds	50
5.6.1	Cosmic-ray muons	50
5.6.2	Accidental coincidences	52
5.6.3	Atmospheric neutrino interactions	52
5.7	Statistical analysis	55
5.7.1	Systematic uncertainties	55
5.7.2	Limit-setting routine	56
5.8	Results	57
5.9	Interpretation and discussion	57
6	R&D toward Hybrid Detectors	60
6.1	Introduction	60
6.2	Proton light yield	60
6.2.1	Introduction	61
6.2.2	Experimental setup	61
6.2.3	Analysis methods	64
6.2.4	PMT linearity correction	64

6.2.5	Reference charge calibration	64
6.2.6	Auxiliary detector particle identification	66
6.2.7	Time-of-flight calibration	67
6.2.8	Energy reconstruction	69
6.2.9	Proton light yield extraction	74
6.2.10	Modeling ionization quenching	76
6.2.11	Results	77
6.2.12	Proton light yield	77
6.2.13	Model compatibility	81
6.3	Precision scintillator time-profile measurements	83
6.3.1	Introduction	83
6.3.2	Experimental setup and waveform processing	84
6.3.3	Analysis strategy	86
6.3.4	Modeling the trigger profile	87
6.3.5	Trigger PMT Calibration	89
6.3.6	Determining the Occupancy Spectrum	90
6.3.7	Results	92
6.3.8	Cherenkov/Scintillation Separation	94
6.4	Summary of R&D measurements	97
7	Concluding Remarks	99
Bibliography		101
A GENIE systematic uncertainties		121
B Excess IBD interaction posterior distributions		126
C Proton light yield PMT linearity measurement		129
C.1	Overview of methodology	129
C.2	Hardware	130
C.3	Time walk	131
D Supplementary material for proton light yield measurement		133
E LAPPD strip-level reconstruction		153
F Analytic scintillator timing model		156

List of Figures

2.1	Matter fields and their couplings to force carriers in the Standard Model. Each lepton or quark and connected to a boson has a nonzero coupling in the Standard Model. Coupling strengths are not reflected in this diagram.	4
4.1	Feynman diagrams for main reaction channels at SNO: (top left) flavor-inclusive neutral-current elastic scattering, (top right) electron-type-exclusive charged-current elastic scattering, (bottom left) flavor-inclusive neutral-current reaction, (bottom right) electron-type exclusive charged-current reaction.	22
4.2	Final constraints on electron-type and muon-/tau-type solar neutrino fluxes from SNO. The measurement of three different reaction channels with different sensitivities to the electron flavor overconstrained the flux ratios, unambiguously demonstrating flavor transformation. Figure reproduced from [144].	22
4.3	Schematic diagram of the SNO detector. Figure reproduced from [70].	23
4.4	The spectrum of starting energies of muon-induced neutrons at SNO, as generated by GEANT4.	30
4.5	GEANT4-based capture efficiencies for cosmogenic neutrons in Phases I (red) and II (blue). Error bars represent the spread in efficiency due to the neutron energy spectrum.	30
4.6	SNOMAN-based observation efficiency for neutron captures on D in Phase I (red), and ^{35}Cl in Phase II (blue). Error bars are statistical.	31
4.7	Determination of ^{12}B contamination, in Phases I (left) and II (right). The time delay and reconstructed energy (shown here) distributions are fit to a combination of exponentials, corresponding to neutron captures and ^{12}B decays.	32
4.8	Area-normalized impact parameters b^2/R_{PSUP}^2 of all muons (top) and only muons with followers (bottom), in Phase I (left) and II (right). $R_{\text{PSUP}} = 850$ cm is the radius of the PSUP. The AV boundary is at abscissa value ≈ 0.5 . The MC reproduces the data adequately, demonstrating that muons through the center of the detector generically produce more neutrons than those passing near the boundary.	34
4.9	Entrance zenith angles of muons with detected followers, in Phases I (left) and II (right). The MC adequately reproduces the data.	34

4.10 Number of detected neutron followers per muon, in Phases I (left) and II (right). Each entry to the histograms represents one muon. The MC reproduces the data well, save for the far tail of the Phase-II distribution, which may indicate mismodeling of reactions involving sodium and chlorine nuclei.	35
4.11 Volume-normalized capture position r^3/R_{AV}^3 of detected followers, in Phases I (left) and II (right). $R_{\text{AV}} = 600$ cm is the radius of the AV. The MC adequately reproduces the data, demonstrating largely uniform detection of neutrons, save for neutron escape from the fiducial volume, which is suppressed in Phase II.	36
4.12 Per-muon spreads of capture position measured along the track, in Phases I (left) and II (right). The bottom row shows contributions from muons of different multiplicities. The MC reproduces the data well, indicating that the multiplicity of specific neutron-producing reactions is well-modeled.	38
4.13 Lateral capture distances from track, in Phases I (left) and II (right). The MC reproduces the data adequately, save for the tail of the Phase-II distribution, which may indicate mismodeling of of reactions involving sodium and chlorine nuclei.	38
4.14 Follower delay from most recent muon, in Phases I (left) and II (right). The MC reproduces the data well, indicating that the neutron capture cross sections and material densities are implemented correctly.	39
4.15 Low-energy capture efficiencies as calculated by simulating ^{252}Cf neutrons with GEANT4, compared with analytic fits performed to ^{252}Cf calibration data taken during Phases I and II.	40
4.16 Power-law fit for the cosmogenic neutron yield in liquid scintillator, performed by the Daya Bay Collaboration [136], with the SNO Phase I, LSD, Jinping, and Super-Kamiokande+Gd measurements overlaid. The SNO, LSD, Jinping, and Super-Kamiokande measurements are not included in the fit, and the target materials used in SNO and Super-Kamiokande+Gd are not liquid scintillators.	42
5.1 Reconstruction of hit-based position (left) and energy (right) reconstruction for electrons with energy up to 100 MeV. Different colors denote different radial shells in starting position. The energy of central electrons can be accurately reconstructed up to 40 MeV, with performance degrading at higher radii.	48
5.2 Reconstructed energy of simulated neutron captures on hydrogen which reconstruct within a 5.7 m fiducial volume, with the selection cuts used in this analysis demarcated.	49
5.3 Detector response matrix (left) and detection efficiency (right) for positrons distributed within the central 3.3 m detector volume.	50
5.4 Distributions of reconstructed z -position (left), radial position (middle), and energy (right) for ROI electrons (blue) and cosmic-ray muons (red). Muons reconstruct toward the top of the detector and saturate energy reconstruction, and hence lie do not contribute to the ROI.	51

5.5 (Left) Primary cosmic ray energy spectrum used in solar minimum simulations of atmospheric neutrino production, and spread of measured cosmic proton flux values during data-taking. (Right) Sunspot number and integrated cosmic proton flux over the last decade, with data-taking period shaded. Simulated flux values are taken from [185], sunspot number records from [184], and proton flux measurements from [183].	53
5.6 (Left) Correlation between observed sunspot number and integrated cosmic proton flux, with fit of rectified linear model overlaid and data-taking period shaded. (Right) Same, for observed 10.7 cm solar flux data. Uncertainty bands are scaled by a factor of 10 for visualization. Sunspot number and solar flux records are taken from [184], and proton flux measurements from [183].	54
5.7 Nominal atmospheric neutrino fluxes at surface (left) and underground (right). The discontinuity in muon- and tau-neutrino oscillated fluxes originates from the discontinuity in muon-type oscillated fluxes at the transition between Bartol and Battistoni flux tables.	55
5.8 Gross prompt energy spectra, both nominal and after propagating uncertainties on GENIE inputs, of atmospheric neutrino interactions. The colored bands denote the systematic uncertainty due to interaction modeling, and the grey dashed lines demarcate the analysis ROI.	56
5.9 (Left) Observed prompt event energy spectrum, and expected atmospheric neutrino background, over 149.5 days of livetime. The shaded band denotes the systematic uncertainty on the background prediction. (Right) Corresponding model-independent limits on the flux of astrophysical $\bar{\nu}_e$. Existing limits from other detectors are overlaid [114–118], along with sensitivity projections for 5 years of exposure.	57
5.10 Limits on light dark matter thermally-averaged annihilation cross section and sensitivity projections for 5 years of data-taking, with limits derived from existing flux from SNO, KamLAND, Borexino, Super-Kamiokande, and Super-Kamiokande+Gd overlaid [114–118].	58
6.1 Experimental setup for proton light yield measurements. The neutron beam travels along the axis designated with an arrow to the target scintillator cell, shown in green. Eleven auxiliary detectors are positioned at forward scattering angles with respect to the incoming neutron beam. The shortest and longest target-to-auxiliary trajectories are shown, labeled as in the configuration for WbLS data-taking. The upper face and side walls of the target cell, highlighted in green, was wrapped with Teflon tape; the lower face was unwrapped and optically coupled to a PMT. Top and bottom panels show the experimental geometry from lateral and from-above vantage points.	63
6.2 (Left) Sealed target cell containing LAB+PPO before wrapping with PTFE tape. (Right) Both target cells after wrapping in PTFE.	63

6.3	Deviation of output current from linear operation of the PMTs used in this measurement, as biased during runtime operations. The blue and orange curves correspond to the PMTs mounted to the LAB+PPO and WbLS samples, respectively. The abscissa spans the full scale range of the employed digitizer. The uncertainty bands are scaled up by a factor of 20 for visualization.	65
6.4	Best fit charge models compared to LAB+PPO (left) and WbLS (right) calibration data using a ^{137}Cs source. Best-fit model parameters courtesy of T. A. Laplace [211].	66
6.5	(Left) PSD metric vs charge collected in the PMT for beam events in an example auxiliary detector, showing separation between neutrons and γ rays at high charge. (Right) Projection onto the PSD-axis for events with charge above 15000adc, along with a normal-lognormal fit and subsequently optimized discrimination threshold.	67
6.6	Charge collected in target PMT vs uncalibrated time since beam extraction during LAB+PPO data collection. Low energy beam-correlated γ rays appear as an isochronic population at low charge. The selection window is illustrated using the red dashed lines.	68
6.7	Distribution of measured time differences between the cyclotron RF signal and γ -ray events in the measurement sample, with empirical fit overlaid, during LAB+PPO (left) and WbLS (right) data collection.	70
6.8	Distribution of measured time differences between γ -ray events in the measurement sample and a representative auxiliary detector, with empirical fit overlaid, during LAB+PPO (left) and WbLS (right) data collection. The data for each material is shown for channel 2, which is located at nominal scattering angles of 80° and 78° , respectively. Analogous figures for all auxiliary detectors are available in Appendix D.	70
6.9	Uncertainty on neutron energy due to timing (left), cell coordinates (middle), and both sources (right), for LABPPO (top) and WbLS (bottom) data. Differently colored dashed lines refer to outgoing trajectories established using different auxiliary detectors.	72
6.10	Uncertainty on proton energy calculated using the incoming neutron energy due to neutron energy (left), scattering angle (middle), and both sources (right), for LABPPO (top) and WbLS (bottom) data. Differently colored lines refer to trajectories established using different auxiliary detectors.	73
6.11	Uncertainty on proton energy calculated using the post-scatter neutron energy due to neutron energy (left), scattering angle (middle), and both sources (right), for LABPPO (top) and WbLS (bottom) data. Differently colored lines refer to trajectories established using different auxiliary detectors.	73

6.12 Uncertainty on proton energy calculated as the difference between pre- and post-scatter neutron energies due to the pre-scatter energy (left), post-scatter energy (middle), and both sources (right), for LABPPO (top) and WbLS (bottom) data. Differently colored lines refer to trajectories established using different auxiliary detectors.	74
6.13 Charge collected in the target PMT vs incoming time-of-flight for neutron-like events in WbLS, which were tagged in channel 5.	75
6.14 Charge collected in the target PMT vs energy deposited in the scintillator for kinematically-consistent events in LAB+PPO (left) and WbLS (right) data.	75
6.15 Distributions of charge values for kinematically consistent events, with empirical fits overlaid, of individual proton energy bins: 4.0–4.5 MeV events in LAB+PPO (left) and 8.0–9.0 MeV events in WbLS (right). Analogous figures for all energy bins are available in Appendix D.	76
6.16 Proton light yield of LAB + 2 g/L PPO and 5% WbLS, relative to that of a 477 keV electron. A previous measurement of deoxygenated 2 g/L LAB+PPO by von Krosigk et al. [196] is overlaid.	78
6.17 Correlation matrices of proton light yield uncertainties in different energy bins, for LAB+PPO (left) and WbLS (right) data.	78
6.18 Best-fit quenching models compared to the measured PLY for LAB+PPO (left) and WbLS (right), shown with both linear (top) and logarithmic (bottom) axes. The Birks model fails to reproduce the low-energy behavior of both materials, which is better modeled with the inclusion of the Chou bimolecular quenching term.	82
6.19 Experimental setup used in scintillator time profile measurements, exemplifying a sample, β -decay source, and available photodetectors. Figure borrowed from [228].	85
6.20 Example single-PE waveforms from the LAPPD and SPE PMT (left), and multi-PE waveform from the trigger PMT (right), sampled from ^{90}Sr data taken with a LAB + 2 g/L PPO target.	86
6.21 Example trigger profiles (left) and observed time profiles (right) for increasing trigger occupancy levels, for a pure scintillation emission time profile with the following parameters: $t_R = 100$ ps, $\tau_1 = 3$ ns, $\tau_2 = 15$ ns, $A_1 = 0.75$. As the trigger occupancy increases, the trigger profile becomes symmetric, and the rising edge of the observed time profile steepens.	88
6.22 Distributions of trigger PMT charge when flashing an LED, calculated using 18 ns integration window.	90
6.23 Distribution of trigger PMT charge during α data-taking, with best-fit multi-PE charge model overlaid, for 5% WbLS (left), 10% WbLS (middle), and LAB+PPO (right).	92
6.24 Best-fit spectra of trigger PMT occupancies during α data-taking, for 5% WbLS (left), 10% WbLS (middle), and LAB+PPO (right), under different modality-penalization strengths.	92

6.25 Distribution of detected times relative to trigger, with best-fit Cherenkov/scintillation model overlaid, for 1% (top), 5% (middle), and 10% (bottom) WbLS data, in the peak region of the LAPPD (left), full analysis window of the LAPPD (middle), and full analysis window of the timing PMT (right).	93
6.26 Distribution of detected times relative to trigger, with best-fit Cherenkov/scintillation model overlaid, for LAB loaded with PPO at 2.0 g/L (left), 1.1 g/L (middle), and 0.61g/L (right), in response to electrons, in the LAPPD (top) and PMT (bottom) channels.	94
6.27 Distribution of detected times relative to trigger, with best-fit scintillation model overlaid, for 5% WbLS (left), 10% WbLS (middle), and LAB+PPO (right), in response to α radiation, in linear (top) and logarithmic (bottom) scales.	95
6.28 Statistical significance of Cherenkov selection, as a function of the timing cut value, for WbLS and LAB+PPO samples observed with the LAPPD (left) and PMT (right). The dashed lines denote the optimal cut value for each material.	97
A.1 Correlation matrix of bin-wise correlations of systematic uncertainties on atmospheric neutrino event rates.	121
A.2 Distribution of atmospheric neutrino events in various energy bins, under resamplings of GENIE inputs. The grey dashed line denotes the nominal prediction, and the blue dashed line denotes the mean resampled prediction.	125
B.1 Posterior distribution of excess atmospheric neutrino interactions in various energy bins, sampled using MCMC. The dashed line denotes the 90% probability mass upper limit.	128
C.1 Schematic for the LED-driving circuitry. Note that the passive component specifications may differ from those used in the final measurement. Figure courtesy of T. L. Laplace [236].	131
C.2 Diagram visualizing the construction of interweaving pulse trains via multiplexing a common system signal. Reproduced from [237].	132
D.1 Two-dimensional distributions of charge and PSD metric in each scatter cell, in LAB+PPO data, with semi-optimized PID discriminants overlaid.	134
D.2 Two-dimensional distributions of charge and PSD metric in each scatter cell, in WbLS data, with semi-optimized PID discriminants overlaid.	135
D.3 Normal/log-normal fits to charge-selected PSD metrics in each scatter cell, in LAB+PPO data.	136
D.4 Normal/log-normal fits to charge-selected PSD metrics in each scatter cell, in WbLS data.	137
D.5 Gaussian signal and linear background fits to LAB+PPO coincidence data. . . .	137
D.6 Gaussian signal and linear background fits to WbLS coincidence data.	138
D.7 Gaussian signal and double-exponential background fits to LAB+PPO proton charge data.	139

D.8	Gaussian signal and double-exponential background fits to WbLS proton charge data.	140
D.9	Difference in LAB+PPO per-energy-bin relatively PLY as a function of chronological place in data set.	141
D.10	Difference in WbLS per-energy-bin relatively PLY as a function of chronological place in data set.	142
D.11	Predicted and measured coincident pulse amplitudes, as a function of the interpulse delay, for the PMT used in LAB+PPO data-taking, at various supply voltages.	144
D.12	Predicted and measured coincident pulse amplitudes, as a function of the interpulse delay, for the PMT used in WbLS data-taking, at various supply voltages.	147
D.13	Deficit of measured coincident pulse amplitudes, and quadratic fit as a function of interpulse delay, for the PMT used in LAB+PPO data-taking, at various supply voltages. The fit is performed over the 15 central data-points about the maximum pulse amplitude.	149
D.14	Deficit of measured coincident pulse amplitudes, and quadratic fit as a function of interpulse delay, for the PMT used in WbLS data-taking, at various supply voltages. The fit is performed over the 15 central data-points about the maximum pulse amplitude.	152
E.1	Diagram of typical LAPPD layered construction, showing (from top to bottom): glass window and multialkali photocathode, structural spacer, first MCP, structural spacer, second MCP, structural spacer, silver strip-line anode. Figure reproduced from [238].	153
E.2	Single-PE time response of LAPPD # 93, with a Gaussian fit to the prompt region overlaid. Data courtesy of INCOM [233].	155

List of Tables

3.1	Summary of relevant properties of Cherenkov and scintillation light, and corresponding features of detectors and analysis techniques utilizing each.	15
4.1	Approximate cross section ratios for different neutrino flavors at the \sim MeV-scale, for the three reaction channels observed in the SNO detector.	23

4.2	Breakdown of cosmogenic neutron producing processes at SNO, as modeled by GEANT4. All processes labeled “inelastic” refer to inelastic scattering, and “ μ -nuclear” refers to direct muon-nucleus interactions via virtual photon exchange.	25
4.3	The specific size of the data set, i.e. the number of muons included in this analysis and fraction with followers, indicating the scarcity of neutrons. Uncertainties are statistical only.	27
4.4	Relative uncertainties on the yield measurement.	41
6.1	Distances between various experimental apparatus, and nominal scattering angles associated with each auxiliary detector.	62
6.2	Compton charges for both LAB+PPO and WbLS. The first uncertainty corresponds to the statistical uncertainty obtained from parameter fitting. The second uncertainty corresponds to the standard deviation of the Compton charge determined using simultaneous fits of multiple calibration spectra (i.e., all combinations of pairs and triplets). Best-fit model parameters courtesy of T. A. Laplace [211].	67
6.3	Standard deviations of best-fit Gaussian models for TOF distributions of all neutron trajectories, in both the LAB+PPO and WbLS datasets. Uncertainties on all Gaussian parameters are significantly below 1%.	69
6.4	Light yield of proton recoils, relative to that of a 477 keV electron, in LAB + 2 g/L PPO, and associated uncertainties (from left to right): statistical uncertainty, uncertainty on reference charge, and total uncertainty including systematic effects.	79
6.5	Light yield of proton recoils, relative to a 477 keV electron, in 5% WbLS, and associated uncertainties (from left to right): statistical uncertainty, uncertainty on reference charge, and total uncertainty including systematic effects.	80
6.6	Correlation matrix of proton light yield uncertainties in different energy bins, for LAB+PPO data. Bins are ordered as in Table 6.4.	81
6.7	Correlation matrix of proton light yield uncertainties in different energy bins, for WbLS data. Bins are ordered as in Table 6.5.	81
6.8	Best-fit model parameters for the LAB+PPO and WbLS proton light yields, relative to that of a 477 keV electron. Neither material is well modeled using the Birks formalism, but both are adequately described using the Chou model.	82
6.9	Correlation matrices of parameter uncertainties for the Chou quenching model, in units of percent.	83
6.10	Lower bound on charge collected in trigger PMT in electron data, to remove low-energy yttrium and strontium decays from analysis. Lower values are used for 1% and 5% WbLS to recover statistics from the body of the β spectrum and establish reasonably-sized data sets.	89
6.11	Best-fit electron time profile model parameters for WbLS and LAB+PPO samples. Subscripts L and P refer to the LAPPD and PMT channels, respectively; σ refers to the effective system resolution; and f_C refers to fractional contribution of Cherenkov light.	94

6.12	Best-fit α time profile model parameters for WbLS and LAB+PPO samples	95
6.13	Maximal statistical significance of Cherenkov selection, and associated Cherenkov purity, for electron time profiles detected in WbLS and LAB+PPO samples using the LAPPD. The cut time t_c is defined relative to the peak of the Cherenkov time profile.	96
6.14	Maximal statistical significance of Cherenkov selection, and associated Cherenkov purity, for electron time profiles detected in WbLS and LAB+PPO samples using the PMT. The cut time t_c is defined relative to the peak of the Cherenkov time profile.	97
A.1	List of identifiers and descriptions of systematic uncertainties in GENIE modeling. Reproduced as a subset of [187].	123
A.2	Correlation matrix of per-bin systematic uncertainties on atmospheric neutrino events, labeled by the energy of the lower bin edges. The bottom row quotes the uncertainty for each bin.	123

List of Acronyms

Λ CDM Λ plus Cold Dark Matter, a cosmological model for the expansion of a universe containing baryonic matter, sterile dark matter, and dark energy, subject general relativity, from a Big Bang, which is used to parameterize the observed large-scale structure and nuclear content of the universe, among other observables.

ADC Analog-to-Digital Converter, refers to both the device and the units of discretized output

AMS Alpha Magnetic Spectrometer, a modular tracking detector mounted on the International Space Station which measures, among other things, cosmic ray fluxes

ANNIE Accelerator Neutrino-Neutron Interaction Experiment, a ton-scale water-based detector located at FermiLAB

AV Acrylic Vessel, used to refer to the inner container of SNO and SNO+, as well as R&D setups

BANG Bay Area Neutron Group, a group of nuclear engineers located at UC Berkeley and LBNL which measuremes neutron reactions

CC Charged-Current, refers to a weak interactions which at tree level are mediarted by W -exchange

CCQE Charged-Current Quasi-Elastic, i.e. neutrino-necleus interactions for which the final state contains one charged lepton and the original nucleus, potentially in an excited state

CCRES Charged-Current Resonant, i.e. neutrino-nucleus interactions for which the final state contains a one charged lepton and is mediated via a resonant nuclear state

CFD Constant Fraction Discrimination, refers to assigning a detection-time of an electronic signal as the time at which the signal reaches a prescribed fraction of its amplitude

CKM Cabibba-Kobayashi-Maskawa, refers to a weight matrix encoding the relative strength of charged-current weak couplings between different generations of quarks

- CMB** Cosmic Microwave Background, residual electromagnetic radiation which ceased interacting strongly with matter when primordial electrons and protons became combined into hydrogen atoms $\sim 378,000$ years after the Big Bang
- DIS** Deep Inelastic Scattering, refers to interactions with nuclei in which the principal interaction is with internal structure, e.g. individual quarks
- DSNB** Diffuse Supernova Neutrino Background, an accepted but undetected cosmic flux of neutrinos emitted from past supernovae
- ES** Elastic Scattering, usually refers to scattering of a neutrino off an electron, which at low energies does not admit any novel final states
- GEANT4** Geometry And Tracking, a common software library for modeling particle dynamics and interactions with matter
- IBD** Inverse β decay, a reaction in which an electron (anti)neutrino and a nucleus ${}^A_Z X$ interact, with the final state containing a positron (electron) and ${}^{A-1}_{Z-1} X'$ nucleus
- IMB** Irvine-Michigan-Brookhaven, an experiment searching for nucleon decay in a water volume which also observed neutrinos from supernova SN1987A
- LAB** Linear Alkyl-Benzene, an organic mineral oil-like substance which is used as a solvent in liquid scintillator formulations
- LAPPD** Large-Area Picosecond Photodetector, a large-area MCP-based photodetector
- LBNL** Lawrence Berkeley National Laboratory
- LSND** Liquid Scintillator Neutrino Detector, a 100-ton scale scintillator detector which operated at Los Alamos National Laboratory searching for flavor transformation of accelerator neutrinos
- MCMC** Markov Chain Monte Carlo, a sampling-based method for approximating probability distributions, often used to marginalize over high-dimensional likelihoods
- MCP** Micro-channel plate, a photodetector with improved timing precision over PMTs
- MSW** Mikheyev-Smirnov-Wolfenstein, refers to an adjustment to the neutrino oscillation framework in while traversing ordinary matter to account for preferential interaction of electron-type neutrinos with ambient electrons
- NC** Neutral current, referring to weak reactions mediated at tree level by Z -exchange
- NCEL** Neutral-current Elastic, i.e. neutrino-nucleus interactions for which the final state contains a single neutrino and the original nucleus

NCRES Neutral-Current Resonant, i.e. neutrino-nucleus interactions for which the final state contains a single neutrino and is mediated via a resonant nuclear state

NDE Nucleon Decay Experiment, as in the Kamioka Nucleon Decay Experiment (KamiokaNDE) and its successors

NOAA National Oceanic and Atmospheric Administration, an agency within the United States federal government concerned with weather and climate forecasting

OWL Outward Looking PMT, PMTs in SNO and SNO+ which face radially outward from the PSUP

PBH Primordial Black Hole, a black hole formed early in the universe and has evaporated to a relatively small present-day mass, considered a candidate explanation for dark matter

PE Photoelectron, the equivalent of an incident photon after applying the photodetector quantum efficiency

PID Particle Identification

PMNS Pontecorvo-Maki-Nakagawa-Sakata, refers to a (believed to be) unitary matrix relating neutrino states in the flavor and mass bases

PMT Photomultiplier Tube, a device used to detect photons

PPO 2,5-diphenyloxazole, a fluorescent chemical used as a fluor in liquid scintillator formulations

PSD Pulse Shape Discrimination, a PID technique utilizing ratios of integrals of collected light over time

PSUP PMT Support Structure, the mechanical structure which holds the PMTs of SNO and SNO+ in place

PTB Physikalisch–Technische Bundesanstalt, a metrology institute located in Germany

PTFE Polytetrafluoroethylene, a commonly available synthetic polymer often employed in R&D setups for its reflective properties

RAT Reactor Analysis Tool, historically, but current expansion is a subject of intense debate; it is the Monte Carlo and official analysis framework used in SNO+

RAT-PAC RAT Plus Additional Code, an open-source simulation and analysis framework based on RAT

ROI Region of Interest, a subset of observable-space which is selected for statistical analysis

SNO Sudbury Neutrino Observatory, a kt-scale heavy water neutrino detector

SNP Solar Neutrino Problem, a discrepancy between solar neutrino flux predictions and measurements which lasted several decades

SPE Single Photoelectron, usually in reference to a PMT response characteristics

SSM Standard Solar Model, used to predict solar neutrino fluxes

TOF Time Of Flight, usually meaning the time difference between two successive detections of the same particle

WbLS Water-based Liquid Scintillator, a surfactant-stabilized mixture of LAB, PPO, and water

WIMP Weakly Interacting Massive Particle, moniker for a hypothetical particle explanation for dark matter which, typically, has multi-GeV mass and interacts with a cross-section at the scale of the weak interaction

Chapter 1

Introduction and Context

The existence of neutrinos was first hypothesized in 1930 by Wolfgang Pauli, in absentia via a now-infamous conference letter [1], as a possible explanation for the broad and non-trivial energy spectra observed for the electrons produced in nuclear β -decays. Since their first experimental observation in 1956 by Cowan and Reines [2], neutrinos have provided numerous avenues for humankind to learn about fundamental physics and the symmetries of nature, both terrestrial and astrophysical phenomena, and human-driven nuclear activity. That first observation was achieved by coincidentally detecting a positron and a neutron, both of which are emitted when an *antineutrino* undergoes *inverse* β -decay with a nucleus, in a scintillation chamber. As well as the first proof of the existence of neutrinos, this provides the first example of neutron detection in a dedicated neutrino detector. This dissertation presents two more recent examples in similar optical detectors, utilizing both water and liquid scintillator, and developmental work toward so-called “hybrid” Cherenkov/scintillation detectors of the future.

A brief overview of the neutrino’s role in the Standard Model of Particle Physics, a description of unaccounted-for phenomena via nonzero neutrino mass, and active areas of research are presented in Chapter 2. Chapter 3 provides a review of historical optical neutrino detectors, highlighting the common detection media and analysis methods that have conventionally been employed, and a description of the hybrid detector concept. A measurement of the neutron production rate by high-energy cosmic-ray muons in the Sudbury Neutrino Observatory (SNO) is presented in Chapter 4, which provides an opportunity for advancing nuclear interaction models as well as informing background cosmogenic estimates for future experiments. A search for extraterrestrial antineutrinos, an exceptionally clean experimental sign of new astrophysical phenomena, using SNO+, an upgrade to the SNO detector, is presented in Chapter 5. Chapter 6 exhibits lab-scale R&D measurements of samples of both pure and water-based liquid scintillator (WbLS) samples, which constitute part of a campaign to establish hybrid optical neutrino detection technologies. Concluding thoughts and an outlook for the near future are given in Chapter 7.

Chapter 2

Neutrinos in and out of the Standard Model

2.1 The structure of the Standard Model

Like other human endeavors, the field of physics underwent tremendous development in the 20th century — from Einstein’s theory of special relativity¹ and nascent paradoxes in quantum mechanics, to their unification in the language of quantum field theory. Along the way, experimentalists collected a growing taxonomy of “particles” — some apparently fundamental and others composite, breaking down further in collisions or as decay products. The achievement of this pursuit was the development, in the 1970s and 1980s, of a comprehensive quantum field theory known as the Standard Model of Particle Physics (SM). The complete Lagrangian of the SM can be written concisely, if not most explicitly, as the sum of four groups of terms:

$$\begin{aligned} \mathcal{L} = & \sum_{\text{fermions } \chi} \bar{\chi} \not{D} \chi && \text{Matter kinetic} \quad (2.1) \\ & - \frac{1}{4} \sum_{\text{gauge fields } F} F_{\mu\nu} F^{\mu\nu} && \text{Gauge-field kinetic} \\ & + D_\mu h^\dagger D^\mu h - V(h) && \text{Higgs, weak boson mass} \\ & + \sum_{\text{fermions } \chi} y_\chi \bar{\chi}_L h \chi_R + \text{h.c.} && \text{Yukawa couplings.} \end{aligned}$$

The first group contains kinetic energy terms for the fermionic fields, as well as interactions via the bosonic fields; the second group, kinetic terms for the bosonic fields themselves; the third group is the “Higgs sector,” containing interactions of the bosonic fields with the scalar Higgs field, and the famous Higgs potential; the fourth group is comprised of Yukawa

¹The general theory of relativity is, of course, worthy of mention, but its unification with a quantum framework eludes us to this day.

couplings between the Higgs and fermionic fields, which reduce to Dirac mass terms for the fermionic fields after symmetry-breaking. The various physical particles and their couplings are visualized in Figure 2.1.

The general gauge group under which the Lagrangian of Equation 2.1 is invariant is

$$\mathrm{SU}(3)_C \otimes \mathrm{SU}(2)_L \otimes \mathrm{U}(1)_Y \quad (2.2)$$

where $\mathrm{SU}(n)$ and $\mathrm{U}(n)$ denote the special unitary (i.e. unit determinant) and unitary groups of dimension n , respectively, which has dimension $12 = 8 + 3 + 1$. The six quark fields u , d , c , s , t , and b have color charge (hence the C subscript), and are arranged in triplets under the action of $\mathrm{SU}(3)$, wherein 8 gluons mediate the strong force. All fermionic fields are charged under $\mathrm{SU}(2)$, so-called weak isospin (\vec{T}), with the action determined by chirality: the left-chiral projections form $\mathrm{SU}(2)$ -doublets (hence the L subscript), whereas the right-chiral projections exist as $\mathrm{SU}(2)$ -singlets. All fermionic fields are charged under $\mathrm{U}(1)$ with a quantum number termed weak hypercharge (Y). The bosons associated with the $\mathrm{SU}(2)$ and $\mathrm{U}(1)$ symmetry groups, conventionally written \vec{A} and B , are linear combinations of the physical bosons W^\pm , Z and A , which mediate the weak and electromagnetic force respectively, according to

$$W_\pm^\mu = \frac{A_1^\mu \mp i A_2^\mu}{\sqrt{2}} \quad (2.3)$$

$$\begin{pmatrix} Z^\mu \\ A^\mu \end{pmatrix} = \begin{pmatrix} \cos \theta & -\sin \theta \\ \sin \theta & \cos \theta \end{pmatrix} \begin{pmatrix} A_3^\mu \\ B^\mu \end{pmatrix}, \quad (2.4)$$

where μ is the spacetime index, and $\theta \approx 28^\circ$ [3], is the so-called weak mixing angle, which determines the strengths of the neutral-current weak and electromagnetic forces in terms of the coupling constants for \vec{A} and B which appear in the Standard Model Lagrangian [4]. The quantum number associated with A^μ is $Q = T_3 + \frac{1}{2}Y$, in terms of the third-component of the weak isospin and weak hypercharge, and corresponds to electromagnetic charge. Perhaps surprisingly, Q is a conserved quantum number associated with a residual $\mathrm{U}(1)$ symmetry in the wake of electroweak symmetry breaking, as described below.

The Higgs field h is a scalar $\mathrm{SU}(2)$ -doublet, comprised of a charged and neutral component $h = \begin{pmatrix} h^+ \\ h^0 \end{pmatrix}$, and is subject to the potential

$$V(h) = \lambda (h^\dagger h)^2 + \mu^2 h^\dagger h = \lambda \left(h^\dagger h - \frac{v}{2} \right)^2, \quad (2.5)$$

where $v^2 = \mu^2/\lambda$, and the last equality absorbs an unphysical offset [5–7]. If $\mu < 0$ and $\lambda > 0$, then this potential has a minimum at $h^\dagger h = \frac{v}{2}$, and hence the fluctuations of the field are from this “vacuum expectation value,” which are conventionally written as $\langle h \rangle = \begin{pmatrix} 0 \\ v/\sqrt{2} \end{pmatrix}$ so as to lie at the potential minimum and choose a convenient phase for the Higgs components.

When Equation 2.1 is rewritten in terms of fluctuations from the vacuum expectation value, we find terms quadratic in both the bosonic fields and v , which are ultimately interpreted as bosonic mass terms, and terms quadratic in the fermionic fields and linear in v , which are Dirac mass terms for fermions. For example, the electron mass comes about from the relevant Yukawa term as

$$y_e \bar{L}_e h e_R \rightarrow y_e \bar{L}_e \begin{pmatrix} 0 \\ v/\sqrt{2} + \phi \end{pmatrix} e_R = \frac{y_e v}{\sqrt{2}} (\bar{\nu}_{e,L} \quad \bar{e}_L) \begin{pmatrix} 0 \\ 1 \end{pmatrix} e_R + \dots = \frac{y_e v}{\sqrt{2}} \bar{e}_L e_R + \dots, \quad (2.6)$$

where the vacuum expectation value of the Higgs field selects the left-handed electron component, from its SU(2)-doublet, to pair with the right-handed singlet. Unlike the Yukawa couplings to the Higgs doublet, such mass terms are not SU(2)-invariant (the action of SU(2) could map $\bar{e}_L \rightarrow \bar{\nu}_L$, for example), and hence the symmetry of the model is broken, reducing $SU(2)_L \otimes U(1)_Y \rightarrow U(1)_Q$. This is representative of how all fermion mass appears in the Standard Model — such terms are present for all quarks and charged leptons, but not neutrinos, which are only present as the left-chiral projections which participate in weak interactions.

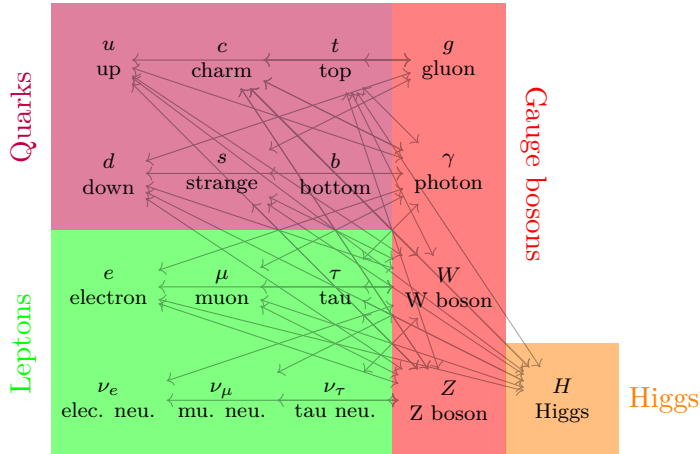


Figure 2.1: Matter fields and their couplings to force carriers in the Standard Model. Each lepton or quark connected to a boson has a nonzero coupling in the Standard Model. Coupling strengths are not reflected in this diagram.

2.2 The Solar Neutrino Problem

The sun, long a fascination of human wonder and scientific investigation, is powered by a set of thermonuclear fusion reactions. The energy released in these reactions provides virtually all of the energy delivered externally to our planet, and provides the opportunity for life as we know it. By the 1960s, astrophysicists had developed sophisticated models of solar reaction chains (so-called Standard Solar Models (SSMs)), with an understanding that

several reactions would yield electron-type neutrinos in the final state [8]. Photons produced deep in the solar core interact aggressively, and only exit to free space some tens of thousands of years later, having lost all memory of their origin. Neutrinos, on the other hand, naturally pass through the solar mass and transit directly to Earth. As such, measurements of so-called solar neutrinos provide a unique opportunity to verify models of solar physics in close to real time.

In the late 1960s, Ray Davis devised the Homestake Experiment, which would measure the flux of solar neutrinos via chemically counting argon atoms which had transmuted from chlorine via charged-current reactions with neutrinos. A deficit from the predicted flux, of roughly a factor of 3, was observed [9], which persisted despite systematic checks and changes to analysis techniques. Later experiments using complementary detector technologies, including the water-Cherenkov KamiokaNDE-II [10] and Gallium-based SAGE [11] and GNO/GALLEX [12, 13] detectors, confirmed the deficit, although at different magnitudes, ultimately attributable to sensitivities to different energy ranges. The longstanding tension between theory and observation became known as the Solar Neutrino Problem (SNP).

Intense theoretical effort was devoted to constructing solutions to the problem — some examples include the possibility of neutrinos decaying in-flight to Earth, and mechanisms for the neutrinos to change chirality and thus become undetectable. The accepted solution, the “large mixing angle” solution augmented by preferential enhancement of the electron-type component via the Mikheyev-Smirnov-Wolfenstein (MSW) effect [14, 15], asserts that flavor states which participate in weak interactions and the mass states which propagate through space are not the same, but are only related by unitary transformation. The “large” qualification draws distinction from the analogous situation in the quark sector, where weak interactions across SU(2)-doublets are highly suppressed.

Historically, Super-Kamiokande observed a deficit in the flux of muon-type neutrinos produced in the atmosphere [16], which spurred interest in flavor-changing mechanisms as SNP solutions. The Sudbury Neutrino Observatory (SNO) unequivocally demonstrated that solar neutrinos change flavor, by simultaneously measuring the solar flux via different reaction channels with different cross-section ratios for different flavors [17]. In doing so, the ratio of electron-type to muon/tau-type fluxes was overconstrained. The results were a confirmed deficit of electron-type neutrinos, but a flavor-inclusive solar flux consistent with the SSM prediction [18]. A few years later, the KamLAND experiment utilized higher spectral resolution to demonstrate that the mechanism for flavor-changing can be described by the interference of quantum flavor states, i.e. “mixing” [19]. This paradigm fundamentally changed the accepted view of leptons, and casts neutrinos in an exciting role in the search for physics beyond the Standard Model, as described below.

2.3 Massive neutrinos, and open questions

Mathematically, neutrino mixing is accommodated by relating neutrino states of definite flavor and mass via

$$\begin{pmatrix} \nu_e \\ \nu_\mu \\ \nu_\tau \end{pmatrix} = U_{\text{PMNS}} \begin{pmatrix} \nu_1 \\ \nu_2 \\ \nu_3 \end{pmatrix}, \quad (2.7)$$

where $\{\nu_\alpha\}$ on the left are flavor states, i.e. the members of SU(2)-doublets which participate in weak interactions, $\{\nu_i\}$ on the right are mass states, which propagate through spacetime, and U_{PMNS} is the Pontecorvo-Maki-Nakagawa-Sakata (PMNS) matrix [20, 21]. Somewhat analogous (though not equivalent, per se) to the Cabibbo-Kobayashi-Maskawa (CKM) matrix in the quark sector, the PMNS matrix encodes the misalignment of flavor and mass states. Assuming unitarity, i.e. that the known neutrinos mix in a “closed system,” the PMNS matrix is conventionally factored in terms of three mixing angles θ_{12} , θ_{23} , and θ_{13} as

$$U_{\text{PMNS}} = \overbrace{\begin{pmatrix} 1 & 0 & 0 \\ 0 & c_{23} & s_{23} \\ 0 & -s_{23} & c_{23} \end{pmatrix}}^{\text{“atmospheric”}} \overbrace{\begin{pmatrix} c_{13} & 0 & s_{13}e^{-i\delta} \\ 0 & 1 & 0 \\ -s_{13}e^{i\delta} & 0 & c_{13} \end{pmatrix}}^{\text{“reactor”}} \overbrace{\begin{pmatrix} c_{12} & s_{12} & 0 \\ -s_{12} & c_{12} & 0 \\ 0 & 0 & 1 \end{pmatrix}}^{\text{“solar”}}, \quad (2.8)$$

where $s_{ij} = \sin \theta_{ij}$ and $c_{ij} = \cos \theta_{ij}$, and δ is an unremovable phase which manifests as a CP-violating term in flavor transformation probabilities. Specifically, the probability for a neutrino produced in a weak interaction with flavor α to be detected via a weak interaction with flavor β is determined by evolving the mass states in time:

$$P(\alpha \rightarrow \beta) = |\langle \nu_\beta | \nu_\alpha \rangle|^2 = \sum_{i,j} U_{\alpha i}^* U_{\beta i} U_{\alpha j} U_{\beta j}^* e^{-i(E_i - E_j)t}. \quad (2.9)$$

Assuming that the neutrino is ultrarelativistic, the energy eigenvalues appearing in the interference factors can be expanded as a series in the neutrino mass, and this expands to lowest order as

$$\begin{aligned} P(\alpha \rightarrow \beta) = & \delta_{\alpha\beta} - 4 \sum_{i>j} \text{Re} (U_{\alpha i}^* U_{\beta i} U_{\alpha j} U_{\beta j}^*) \sin^2 \left(\frac{\Delta m_{ij}^2 L}{4E} \right) \\ & + 2 \sum_{i<j} \text{Im} (U_{\alpha i} U_{\beta i}^* U_{\alpha j}^* U_{\beta j}) \sin^2 \left(\frac{\Delta m_{ij}^2 L}{2E} \right), \end{aligned} \quad (2.10)$$

where E is “the” neutrino energy, neglecting any contribution from mass, $L \sim t$ is the spatial distance separating the production and detection reactions, and $\Delta m_{ij}^2 = m_j^2 - m_i^2$ is the squared-mass-splitting between the respective mass eigenvalues. Two important observations can be made about this expression. First, the latter term, involving the imaginary component of entries of the PMNS matrix, changes sign under the action of $U_{\text{PMNS}} \rightarrow U_{\text{PMNS}}^*$,

which manifests as a CP-violating asymmetry in the transition probabilities of neutrinos and antineutrinos, proportional to $\sin \delta$. Second, in order for the transition probability to be nonzero, the mass splittings must not at all be zero, and hence, based on the various observations of flavor transformation, at least two of the mass eigenvalues must be nonzero. The reality of massive neutrinos constitutes the first definitive departure of observation from the Standard Model.

To accomodate neutrino mass into a quantum field theory requires the introduction of right-chiral neutrinos ν_R , as mass terms must conserve parity to avoid inconsistencies in the theory arising from quantum anomalies [22], but the exact terms which should appear in the Lagrangian are an open question. Yukawa couplings analogous to the existing fermion mass terms, so-called Dirac mass terms $\mathcal{L}_D = -M_D \bar{\nu}_L \nu_R$, may be written, but pose a naturalness problem, in that the associated coupling constants would be many orders of magnitude below the scale of those of the quarks and charged leptons. Being uncharged electromagnetically, unique among Standard Model fermions, new mass terms are allowed for right-chiral neutrinos:

$$\mathcal{L}_M = -M_R \bar{\nu}_L^c \nu_R, \quad (2.11)$$

where ψ^c is the charge-conjugate of the field ψ , which reverses the sign of the Q quantum number [23]. Such Majorana mass terms are qualitatively novel, in that they exist completely parallel to the Higgs mechanism, and can have dramatic consequences. So-called “seesaw” models, for example, balance Dirac and Majorana mass terms such that the masses of left-chiral states are lighter than the scale set by the Higgs mechanism, and of the right-chiral states are above the energy scales probed by modern experimentation [22, 23]. This provides both an explanation for the smallness of the observed neutrino mass, and a first foray into the energy scale of grand unified theories, which attempt to explain the gauge group of Equation 2.2 as the residual of the breaking of a larger symmetry group [24]. Further still, Majorana mass terms are not invariant under phase transformations generated by lepton number, and thus provide a mechanism for lepton-number-violating processes [25].

Strongly CP-violating flavor transitions and lepton-number-violation via Majorana mass each represent tantalizing potential revolutions in our understanding of particle physics. Further still, their union can provide a route for the generation of a matter-antimatter imbalance in the development of an electrically neutral universe, such as is typically assumed in Big Bang cosmology [26]. As such, intense experimental effort is currently focused on addressing the questions of both CP-violating flavor transitions and the nature of neutrino mass. The T2K and NO ν A experiments have each measured significant asymmetries in the transition probabilities for neutrinos and antineutrinos [27, 28]. In a turn of fate at once intriguing and cruel, the data from these two experiments which underlie this qualitative agreement prefer quantitatively inconsistent values of the CP-violating phase δ [29]. To resolve this tension and enter a regime of precision measurements, the Deep Underground Neutrino Experiment (DUNE) [30, 31] and Hyper-Kamiokande [32] experimental programs are currently under construction. Several generations of experiments searching for neutrinoless double- β decay ($0\nu\beta\beta$), the experimental hallmark of Majorana mass [33], have been performed, and the

design and implementation of next-generation ton-of-isotope-scale experiments is underway [34–37].

Other avenues of active research are the determination of the absolute neutrino masses [38, 39] and their ordering, which have implications for the potential rate of neutrinoless double- β decay, such as its suppression below measurable levels [40]; investigation of oscillations of neutrinos into sterile flavor states, a candidate explanation for the so-called Gallium and LSND/MiniBooNE anomalies [41–45]; and the search for nonstandard interactions with matter, which would manifest as a distorted transformation probability for several-MeV solar neutrinos [46, 47].

2.4 Dark matter

While the Standard Model has shown resiliency in the face of terrestrial experiments, it fails to account for the full dynamics of the universe. Indeed, according to the 2018 fit of the Λ -Cold Dark Matter (Λ CDM) cosmological model to cosmic microwave background (CMB) data from the Planck satellite, approximately 86% of the matter content of the universe is non-baryonic [48], and absent from the Standard Model entirely. This striking statement is supported by vast experimental evidence collected over the last century, beginning with early observations of anomalous rotation speeds of galactic clusters in the 1930s [49] and individual galaxies in the 1970s [50], to stunning comparisons of cluster mass estimates from direct-optical and gravitational-lensing inferences [51], to the nature of the large scale structure of the visible matter content of the universe [52]. While the nature of dark matter remains a mystery, a number of models have been posited which to explain its presence and inertness while offering experimental hope for detection with baryonic means [53].

The leading candidate, historically, is the Weakly Interacting Massive Particle (WIMP), which is a hypothetical particle with mass $O(100 \text{ GeV})$, which interacts via couplings on the order of the Standard Model weak interactions. Under such assumptions, a population of WIMPs present in the early universe that self-annihilate, naturally with a weak-scale cross section, would evolve to an asymptotically constant density comparable to that inferred from cosmological observations [54]. Furthermore, certain classes of supersymmetric extensions to the Standard Model naturally predict stable particles with mass at the GeV-scale and above [54]. Unfortunately, searches for direct WIMP-nucleon interactions and the production of WIMP at colliders have not produced any observations to date [55, 56].

Among other theories [53], two alternatives to the conventional WIMP are light particle dark matter and primordial black holes (PBHs). The light dark matter proposition posits the existence of a WIMP-like particle with loosened constraints on its mass and interactions, e.g. a mass at the MeV-scale, to which direct-detection and collider searches are less sensitive. PBHs, as a dark matter candidate, refer to sub-stellar-mass black holes which formed early in the universe. All black holes are believed to emit so-called Hawking radiation, wherein vacuum fluctuations of particle-antiparticle pairs divided by the event horizon result in a net particle flux away from the black hole [57]. This acts, on the theoretical side, to preserve

the information content of the universe [58] and, practically, as a mechanism for the black hole to evaporate over time [59]. Both light particle dark matter and PBHs can be observed indirectly via neutrinos, as discussed further in Section 3.4.

Chapter 3

Optical Neutrino Detectors

3.1 Historical radiation detection technology

The detection of ionizing radiation via electromagnetic signals has a long history spanning many designs and applications, from the early scintillation counters produced during the Manhattan Project [60] to modern radiowave-based detectors searching for ultra-high-energy neutrinos [61]. In particular, the use of light of near-visible wavelengths has proven reliable. Standard means of detecting such photons, both photographic and electronic via the photoelectric effect, have been available since early in the 20th century, and thus the conversion of a charged particle into a collection of detectable photons is now an established science. We briefly review the physics of two dominant sources of near-visible light — Cherenkov and scintillation light — employed in experimental nuclear and particle physics below. Both of these sources mediated central observations in the history of experimental neutrino physics, as detailed further in Section 3.2.

3.1.1 Cherenkov light

The observation of Cherenkov light was first formally reported by a graduate student in the Soviet Union in the early 1930s, when it was observed that uranium salt solutions, as well as the full catalog of other pure liquids available in the local lab, faintly emitted anisotropic blue light when subjected to γ radiation [62]. In only a few years, a relativistic theory of the production of a conical wavefront in dielectric materials by locally-superluminal charged particles was formulated by Ilya Frank and Igor Tamm [63], with the connecting mechanism to Cherenkov's observations being scattering of the incident γ -rays off local electrons in the liquid.

Their theory, an electromagnetic analog to Mach wave theory, predicts the spatial, chromatic, and angular distributions of the emitted light, and, impressively, does so analytically. Spatially, photons are produced immediately and continuously along the trajectory of the charged particle, in response to the relaxation of the local polarization induced by its presence. This continues so long as the particle travels with velocity $v > c/n$, where n is

the refractive index of the material. The spectral distribution is described by the Frank-Tamm formula, which states that the differential spectrum of energy released into photons is weighted by the photon frequency:

$$\frac{dE}{d\omega} \propto \omega \left(1 - \frac{c^2}{v^2 n(\omega)^2}\right) \mu(\omega), \quad (3.1)$$

up to the energy-dependence of the refractive index and magnetic permeability μ . In practice, this manifests as a broad-spectrum distribution which is a decreasing function of wavelength — this is why Cherenkov light is often quoted as appearing blue, such as in the glow of water tanks in nuclear reactors.

As to the angular distribution, Cherenkov photons are emitted exactly at an angle θ with respect to the direction of travel of the charged particle, satisfying $\cos \theta = \frac{c}{nv}$. This is known as the “Cherenkov angle,” and is typically regarded as a constant specific to each material, as the majority of Cherenkov light is emitted in the ultrarelativistic regime, where $\cos \theta \approx \frac{1}{n}$. It is this δ -function angular distribution that makes Cherenkov radiation attractive for detectors which require directional information, as the direction of the originating charged particle can be inferred from the directions of the detected photons. However, the high-velocity requirement translates to a particle-dependent energy threshold for Cherenkov production. In pure water ($n \approx 1.3$), for example, the threshold is $\sim 50\%$ of the particle mass, which translates to a modest 250 keV for electrons, but scales quickly to hundreds of MeV for heavier ions.

3.1.2 Organic scintillation

Scintillating materials have been under study since early observations of phosphorescent salts in the 19th century [64], and operate via more general chemical mechanisms than the electromagnetic mechanism of Frank and Tamm [63]. Generically, charged particles deposit energy, via interactions with both ambient nuclei and electrons, as they traverse in the material [3]. This causes local excitation of molecular states and full ionization of ambient electrons. These excited states and free electrons then convert, by a variety of means, to prepare an excited molecular state which then relaxes via the emission of near-visible photons, potentially through multiple intermediate states [65].

So-called organic scintillators, which have historically been preferred for use in neutrino detectors, are naturally comprised of carbon chains and aromatic compounds, which form the base solvent. A common feature are aromatic rings, the chemical structure of which provides for delocalized π -bond electrons occupying orbitals orthogonal to the ring plane. Scintillation is mediated via the excitation of these π -bond electrons into both singlet and triplet states [65]. Secondary, and even tertiary, compounds are often disbursed in the base solvent, to which energy is transferred non-radiatively; these secondary fluors are usually impractical to deploy at the scale of the base solvent, but have more favorable scintillation characteristics, such as spectral or timing emission profiles.

Because the spectral profile can be adjusted in this way, the relatively narrow emission band can be matched to the sensitive region of the photodetectors at hand in a given application. In contrast to a Cherenkov-based design, this leads to a relatively large amount of light actually detected and available for analysis. The emission time profile is driven by the structure of the available molecular states, and is exponential in form, usually over time scales of several nanoseconds and longer. For radiation at the MeV-scale and below, this is much longer than the picosecond-scale stopping time over which Cherenkov light is emitted. Scintillation light is emitted isotropically, as it is the product of the relaxation of molecular states, perhaps excited indirectly, with little relation to the incident radiation.

Finally, because the relevant energy quanta are molecular excitations, which are below the single-eV scale, radiation detection in scintillators is effectively thresholdless, independent of the nature of the incident radiation. At sufficiently high energy (MeV-scale and above, for electrons), the number of photons produced is approximately proportional to the energy deposited in the scintillator, with the constant of proportionality referred as the “light yield” of the scintillator, and nonlinearities typically arise at lower energies. The latter feature, known as “quenching,” is discussed in more detail in Section 6.2.10 and Section 6.2.13. There is, further, a degeneracy between the amount of light produced by a particle and its the particle’s identity, stemming from the following: Heavier particles are subject to larger stopping material powers, and the relatively rapid deposition of energy translates to relatively dense populations of ionization electrons and different distributions of excited molecular states. The differences in both emission time profile and light yield are also referred to as “quenching,” and it is a generally accepted that there is a connection between low-energy light yield nonlinearity and particle-dependent scintillation, as they each ultimately originate in the distribution of and self-interactions between molecular states, but there is no universal model which reproduces measurements across different materials quantitatively (see, for example, [66]).

3.2 Detectors of the past and present

Mediated only via the weak force, interactions of neutrinos with matter typically have small cross sections, in particular at the MeV-scale and below. To establish reasonable event rates, then, neutrino detectors must maximize their target mass. Subject to constraints of cost, practicality, and cleanliness from backgrounds in low energy scenarios, liquid phase targets have proven an optimal choice, as they are relatively dense, easy to scale/reshape, and can, generically, be purified to remove radioactive contaminants. Given a large liquid target, the preferred detection mechanism is via the detection of photons produced by the interaction of final-state particles with the detector medium¹, in the wake of a neutrino interaction itself.

The first example of such a detector is provided by the very first successful neutrino detector. The detector used in the Poltergeist Experiment of 1956 [2] illustrates many of

¹A notable exception is the Homestake Experiment, which initiated the SNP by measuring the solar neutrino flux by periodically counting cumulative interaction rates via chemical means.

the techniques that would be scaled up and refined in the following decades. It consisted of two tanks of water in which cadmium-chloride was dissolved, which were placed between two tanks filled with liquid scintillator. When antineutrinos from a nearby reactor initiated inverse β decay (IBD) of hydrogen in the water,

$$\bar{\nu}_e + p \rightarrow e^+ + n,$$

the positron would annihilate with an ambient electron and produce two γ rays which would exit the water volume and Compton scatter off electrons in the liquid scintillator; hence, the positron was identified via the light produced by the interaction of the scattered electrons with the scintillator. Some time later, after thermalizing, the final-state neutron would capture radiatively on the dissolved ^{108}Cd , and the emitted γ ray would be detected similarly. The hallmark coincidence signal of IBDs, namely the detection of first a positron, followed by a radiative neutron capture some time later, provides for a powerful background rejection criteria which was critical in establishing the first direct observation of neutrino interactions, and is still in use today.

The 1980s and 1990s saw the operation of large-scale pure water detectors searching for proton decay, with the intermediate photons being produced by Cherenkov radiation from the theorized final-state positrons, with kinetic energy in the hundreds of GeV. It was realized that lower-energy leptons produced in neutrino interactions could also be observed with these detectors, with two famous examples being the (first, and only to do date) detection of neutrinos from a supernova, SN1987A, by the Irvine-Michigan-Brookhaven (IMB) [67] and KamiokaNDE-II [68] detectors, and the initial observation of a deficit atmospheric neutrino flux by KamiokaNDE-II [69]. These observations were made via elastic scattering, IBD reactions, and more general charged-current (CC) reactions involving muon neutrinos.

In the mid 1990s, a 50 kt successor to KamiokaNDE, Super-Kamiokande, was constructed in Japan for enhanced sensitivity to both proton decay and neutrino interactions. The SNO detector began operating soon after with a heavy water, D_2O , target [70]. The mediating photons in both were Cherenkov light, either from a final-state electron, or Compton scattering of a radiative neutron capture γ . Critical to observations of both Super-Kamiokande and SNO was the directional reconstruction afforded by Cherenkov light: because Cherenkov light is emitted conically about the momentum axis of a charged particle, the direction-of-travel of the charged particle can be inferred from the locations of the detected photons. In the context of solar neutrinos, this was used to distinguish elastic scattering events, which are preferentially directed away from the sun, from isotropic radioactive backgrounds intrinsic to the detector.

Early in the 2000s, the KamLAND detector operated with an organic liquid scintillator target [71], principally observing IBD reactions on hydrogen. The use of liquid scintillator offered improved energy resolution over the earlier water detectors, owing to the greater number of photons collected for a given event, which enabled its relatively-precise measurement of the energy-dependence of flavor transformations of antineutrinos produced in nuclear reactors [19]. Other early scintillator detectors, which contributed earlier constraints on oscillation models, include the Liquid Scintillator Neutrino Detector (LSND)

[72], Karlsruhe-Rutherford Medium Energy Neutrino experiment (KARMEN) [73], and the Palo Verde Neutrino Experiment [74], though the latter two implemented segmented detector volumes.

The next generation of large-scale optical detectors included continued operations and upgrades to the Super-Kamiokande and KamLAND detectors, as well the construction of new dedicated detectors. The Daya Bay experiment employed gadolinium-loaded liquid scintillator to improve on measurements of flavor transformation of reactor neutrinos, which the detection efficiency of IBD neutrons enhanced by the larger capture cross section and radiative energy release afforded by ^{157}Gd [75, 76]. The Borexino detector was a 278 t liquid scintillator detector which, after an extensive calibration campaign, made precision measurements of low-energy solar neutrino spectra [77], made possible by both the low threshold and spectral resolution offered by scintillation light. The SNO detector underwent upgrades to the readout electronics and structural support systems in transition to SNO+, which in the late 2010s operated as a light water detector, publishing limits on nucleon decay to neutral final states [78, 79], low-background solar neutrino flux measurements [80], and the first-ever observation of reactor antineutrinos in a Cherenkov detector [81]. During the COVID-19 pandemic, the light water was replaced with a liquid scintillator, and SNO+ now operates as a scintillator detector.

Parallel to both SNO and KamLAND, the MiniBooNE experiment began operating at the turn of the century to constrain transformations of relatively high-energy neutrinos produced using an accelerator [82]. Nominally a Cherenkov detector, a mineral oil target was deployed, with the higher index of refraction translating to an increased production of Cherenkov light. The mineral oil was weakly scintillating, and while the level of scintillation light collected did not offer much improvement to event reconstruction, it proved useful for purposes of particle identification (PID) and background rejection [83]. This constituted a first foray into the dual use of Cherenkov and scintillation light in a single detector, but due to the nature of the mineral oil and relatively high energy regime, the utility of the collected scintillation light was limited.

More recently, liquid scintillator detectors have begun to isolate the relatively weak Cherenkov signal and exploit the encoded directional information. The Borexino collaboration, by considering only the first detected photon in each event, has demonstrated aggregate directional inference of solar neutrinos at the scale of ~ 700 keV [84]. The SNO+ collaboration has since demonstrated eventwise directional reconstruction in scintillator, again using solar neutrinos, at the scale of several MeV [85]. In both cases, the limiting factor is the small amount of high-purity Cherenkov light available, a product of both the time distribution and relative magnitude of the scintillation component.

3.3 Hybrid detector technology

As discussed above, optical neutrino detectors have historically fallen into two broad classes: water-based detectors, which detect radiation via Cherenkov light, and scintillator-based

detectors, which principally detect radiation via scintillation light. A current area of active research is the development of hybrid detectors, which are designed to simultaneously collect both Cherenkov and scintillation photons, with the capability to distinguish the two populations and treat each preferentially in advanced reconstruction techniques, as demonstrated by the results from Borexino and SNO+ described above. The SNO and SNO+ detectors relevant to this thesis exemplify Cherenkov- and scintillation-based technologies operating independently, and highlight some of their core differences, including energy threshold, directionality, and energy resolution. These features, and their consequences on the reconstruction capabilities available from a detector are summarized in Table 3.1, and are discussed in more detail below.

Feature	Cherenkov- / water-based	Scintillation-based
Energy reconstruction	Low light yield	High light yield
Directional reconstruction	Intrinsic via conical emission	Limited by isotropic emission
Vertex reconstruction	Limited by low light yield	Improved by high light yield
Vertex reconstruction	Improved by prompt emission time profile	Limited by long-scale emission time profile
Energy threshold	\gtrsim MeV-scale particle-dependent threshold	Effectively thresholdless
Particle Identification	Limited to high energy; depends on trajectory	Mass-dependent emission timing
Scalability	Inexpensive, optically transparent	Relatively costly, self-absorption
Intrinsic radioactivity	Relatively high as water is universal solvent	Typically lowered via well-established purification techniques

Table 3.1: Summary of relevant properties of Cherenkov and scintillation light, and corresponding features of detectors and analysis techniques utilizing each.

Perhaps the most pronounced difference between Cherenkov and scintillation light, and the origin of much of the current interest in hybridizing, is the angular information encoded in the former, which allows for reconstruction of the direction-of-travel of a charged particle. For many neutrino interactions, most prominently elastic scattering off an electron, this correlates with the direction of the incident neutrino. The detection of a sample of Cherenkov photons thus allows for, at some level, reconstruction of the incident neutrino direction, which is generically useful for classifying events by their source. Modern applications include solar neutrinos which, on the one hand, are under active interrogation as a probe to resolve the solar metallicity problem, related to the discrepancies in existing measurements of the high- Z content of the sun, which influences models of stellar development; on the other hand, solar neutrinos can present as a major background to other physics topics. As an example of the latter, solar neutrinos will constitute the dominant background to an upcoming search for neutrinoless double- β decay of ^{130}Te [86] with SNO+.

Dual to reconstructing directionality of incident neutrinos is the reconstruction of the interaction location and energy deposited in the detector which, for the MeV-scale neutrinos relevant for this work, is equal to the full energy of the interaction. The resolution of the latter is, to first order, determined by Poisson statistics of the collected photons and, hence, is enhanced in scintillator detectors. The resolution of the former, i.e. vertex reconstruction, tends to be greater in scintillator detectors, but ultimately is the result of competing effects: on the one hand, the higher photon collection of scintillator detectors offers more precise reconstruction, but on the other hand the broader emission time profile of scintillation light relative to Cherenkov light degrades performance [87]. The angular emission profiles play a

role as well, as the conical nature of Cherenkov light provides a relatively weak constraint on the vertex position longitudinally along the axis of the cone, in comparison to isotropic scintillation light.

With regard to practicality and scalability, scintillator detectors encounter complications as they are implemented in ever-larger sizes. Water, being an abundant natural resource, can be sourced in arbitrary quantities, and its optical transparency around the visual spectrum translates to robust extrapolation of analysis techniques from smaller to larger detectors. This contrasts with the reality of deploying large-scale scintillator detectors — resourcing and processing large quantities of scintillator requires overcoming relatively challenging financial, environmental, and engineering constraints, and reconstruction techniques must be adapted to acknowledge the self-absorption and potential reemission of the scintillation light internal to the detector volume. Even with improved algorithms, a degradation in reconstruction performance is guaranteed by this intrinsic broadening of the observed time profile, with secondary optical effects, such as spectral dispersion, contributing further to the distortion.

Though Cherenkov light is produced by liquid scintillators and, indeed, all dielectric liquids, the number of detected Cherenkov photons is typically a small fraction of the overall light collected, and they are thus difficult to use for dedicated reconstruction purposes. Several avenues are being explored in order to achieve high-fidelity Cherenkov-tagging, which would thus enable hybrid photon detection. Three principal efforts are i) formulation of materials which intrinsically balance the Cherenkov and scintillation yields, including WbLS and slow-emitting scintillators [88, 89], ii) development of high-time-precision photodetectors that can better resolve the prompt Cherenkov contribution from the relatively delayed scintillation contribution [90], and iii) design of dichroic-filter-based structures to spectrally sort photons before detection [91], resulting in separate readout streams, which are either intrinsically Cherenkov- or scintillation-rich. Explicit reconstruction-level improvements, such as topologically-aware algorithms [92] and machine-learning based approaches [93] are under development, and would exhibit even greater performance when coupled to the aforementioned detector-level technologies.

Simultaneous to lab-scale studies, such technologies are being deployed in ton-scale demonstration detectors. The Accelerator Neutrino-Neutron Interaction Experiment (ANIE) [94], which nominally characterizes neutron-containing final-states of GeV-scale neutrino interactions in water, has deployed both high-time-precision photodetectors and a kg-scale inner vessel of WbLS to demonstrate neutrino detection with a novel scintillator. At Brookhaven National Laboratory, one ton and 30 t vessels of WbLS are operating under constant photomonitoring, in order to further improve recirculation and purification techniques, and demonstrate long-term stability at scale. The EOS detector [95] is currently under construction on the campus of the University of California, Berkeley, and will employ high-time-precision photodetectors and spectral sorting in analyzing radioactive source data using water, WbLS and pure scintillator target media, to demonstrate hybrid reconstruction techniques and detailed material modeling. Such demonstrations will support the design of THEIA, a 10s-of-kiloton-scale hybrid detector capable of a broad physics program, spanning measurements of CP-violation and neutrinoless double- β decay, as well precision

measurements of solar and reactor neutrinos [37].

In order to accurately model the ton-scale demonstrations and make robust predictions for larger-scale detectors, the inputs to detector simulations must be well-grounded in reality. To this end, lab-scale measurements which characterize the scintillation properties of WbLS and explore timing-based Cherenkov-tagging using state-of-the-art photodetectors are presented in Chapter 6. In particular, we present two sets of measurements. First, Section 6.2 presents a measurement of the scintillation light yields of WbLS and LAB+PPO in response to protons, which influences both studies of reactor-neutrino measurements, to which interactions of external neutrons with internal protons constitute a background, and elastic scattering of neutrinos off protons, which is a favorable channel for flavor-inclusive spectral measurements of supernova neutrinos. Second, Section 6.3 presents measurements of the scintillation emission time profiles of WbLS and LAB+PPO samples in response to electrons and α radiation, which allow for realistic predictions of not only the nominal reconstruction performance, but also the PID capabilities, achievable with different detector designs. High-time-precision photodetectors are employed for the electron measurements, which gives a first demonstration of timing-based Cherenkov-/scintillation discrimination at the small scale. These measurements each provide valuable input to the scaling of ton-scale demonstrators to large-scale detectors sensitive to modern physics measurements.

3.4 Particle astrophysics with neutrino detectors

A growing post-millennial endeavor is the development of so-called multimessenger astronomy — that is, studying astronomical systems through non-electromagnetic channels — which has seen great success in the past decade. Measurements of the properties of cosmic rays date back more than a century, but only in the last decade have significant advances been made in understanding their origins [96, 97]. More recently, the watershed detection of gravitational waves from black hole mergers has ushered in a new era in studying gravitational interactions of the densest objects in the known universe [98]. Neutrinos in particular, owing to their small interaction cross section, have emerged as a candidate for general-purpose astronomical messenger.

Building on the early detection of neutrinos produced by SN1987A [67, 68], which illustrated that neutrinos could be used as a tool for studying extraterrestrial phenomena, and the successful resolution of the solar neutrino problem, which has enabled genuine study of stellar content via neutrinos [99–101], modern large-scale neutrino detectors have been used to search for and characterize astrophysical processes. Large-scale Cherenkov detectors, such as IceCube [102] and ANTARES [103], have been purpose-built for the detection and directional reconstruction of ultra-high-energy neutrinos. Highlight results are the detection of the highest-energy neutrinos ever observed [104], the determination of neutrino emission from an active blazar [105], and the observation of a gross neutrino flux from the galactic plane of the Milky Way [106]. Still other detectors, optimized for measurements at lower energies, nevertheless constitute large calorimeters which are sensitive to a large class

of potential signals. Tests for correlations of the neutrino rate with astrophysical events are routinely made, and both model-(in)dependent searches for hypothetical astrophysical fluxes of neutrinos and particle dark matter are performed, many models for which have been proposed.

In particular, recent years have seen an expanded interest in searches for light dark matter using neutrino detectors [107, 108]. As discussed in Section 2.4, past generations of dedicated direct-detection dark matter detectors were typically designed to search for WIMPs of GeV-scale mass and weak-scale interaction cross sections, usually via elastic scattering off nuclei. With current cross section limits ruling out the conventional WIMP [55], and indirect searches for dark matter signals via optical channels yielding no significant signal [109], more attention has been given to indirect searches using neutrinos. Though relatively difficult to detect, the non-interacting nature of neutrinos makes for an attractive messenger, as spectral features in an observed signal would be preserved, which is important for model-dependent interpretation of an observation. Another possibility, which in the current observational landscape cannot be discounted, is that the principal connection between the Standard Model and dark sector is via couplings to neutrinos. In such a situation, neutrino-based investigation is the only plausible option.

Searches for dark matter with neutrino detectors include both direct and indirect detection. Due to the relatively high energy threshold compared to dedicated detectors, direct detection searches are generally only sensitive to scenarios where particle dark matter is boosted to relativistic energies before reaching Earth, e.g. as daughters of the decays of heavier dark particles [110] or by upscattering off high-energy cosmic rays [111]. Such searches have been performed by Super-Kamiokande, yielding no significant signal [112]. Indirect searches typically involve the conventional detection of neutrinos, which are ultimately a manifestation of dark matter as it exists in the universe, although analyses of more general final states of dark matter annihilation *inside* of the detector volume have been performed [113].

Historically, the preferred context for indirect searches is MeV-scale particle dark matter annihilation into neutrino-antineutrino pairs, $\chi\bar{\chi} \rightarrow \nu\bar{\nu}$, which follows from the assumption that any particle dark matter would be Majorana in nature, inferred from its being electrically neutral. At the MeV-scale, below the muon mass, no heavier annihilation products decay via neutrino emission, and hence the (anti)neutrino flux is comprised of direct decay products, and is thus a δ -function centered at the value of the dark matter mass. The flux from the local galaxy can be determined by integrating over a spatial model of the dark matter mass halo [107], and is usually written as

$$\phi(E_\nu) = \frac{1}{6} \frac{J_{\text{avg}} R_{\text{sc}} \rho_{\text{DM}}}{m_\chi^2} \langle \sigma v \rangle \delta(E_\nu - m_\chi), \quad (3.2)$$

where J_{avg} encodes the averaging of the flux intensity over the angular profile of the local dark matter halo, R_{sc} is the distance from the local solar system to the galactic center, m_χ is the dark matter mass, $\langle \sigma v \rangle$ is product of the dark matter velocity with the $\chi\bar{\chi}$ cross section averaged over the thermal energy distribution, and the factor of 6 results from a factor of

two, accounting for the assumed $\chi \leftrightarrow \bar{\chi}$ association, and a factor of three stemming from the assumption that annihilation proceeds to all three flavors of neutrino equally. A redshifted component to the spectrum from extragalactic dark matter has a broader spectral shape, but is subdominant and generally neglected in the context of neutrino datasets with few or zero candidate events. Constraints on self-annihilation resulting from searches for astrophysical sources have been established using the SNO, Borexino, KamLAND, Super-Kamiokande, and Super-Kamiokande+Gd detectors [114–118], which are discussed further in Section 5.9.

An alternative hypothesis to particle dark matter, which presents a similar experimental opportunity, is the widespread presence of sub-stellar-mass primordial black holes (PBHs) [119]. Similar to self-annihilation of particle dark matter, this would experimentally manifest as a correlated signature of particles and antiparticles, including neutrinos, created as Hawking radiation. Searches have been made for electromagnetic signatures of Hawking radiation, but thus far have not yielded any significance observations [120]. In the era of multi-messenger astronomy, searches for Hawking neutrinos have been proposed, particularly in the context of constraining the PBH contribution to dark matter [121, 122], with the only dedicated analysis to date being performed on data from Super-Kamiokande [122].

Two measurements which influence the experimental landscape of searches for astrophysical neutrino fluxes are presented in Chapter 4 and Chapter 5. As discussed in further detail in Chapter 5, a favorable channel for such searches is via IBD reactions of electron-type antineutrinos, for the final state allows for a coincidence signal which dramatically reduces background contamination. Chapter 4 presents a measurement of the production of neutrons by cosmic-ray muons in the SNO detector, which not only constitutes a generic background to low-energy physics analyses, but also a coincidence background in certain detectors, complicating the background-free picture usually associated with IBD searches. Chapter 5 presents a preliminary search for astrophysical antineutrinos using the SNO+ detector, the observation of which would convey new information about the larger universe, including interpretations of dark matter as self-annihilating particles or PBHs, as described above.

Chapter 4

Cosmogenic Neutrons in SNO

4.1 Introduction

High energy muons created in cosmic-ray interactions in the Earth’s atmosphere penetrate deep underground, where they induce electromagnetic and hadronic showers. These produce, among other particles of interest, free neutrons with an energy spectrum spanning several GeV. These cosmogenic neutrons form a direct background to searches for rare processes, including many of those described in Section 2.3 and Section 3.4.

The development and realization of next-generation detectors targeting these physics topics require unprecedented levels of background reduction. The prerequisite deep-underground location of such experiments reduces the rate of spallation backgrounds, but even the small number of remaining events can prove limiting to the potential physics reach of the experiments. It thus becomes critical to advance the understanding of the production and properties of cosmogenic neutrons. The average energy of the surviving cosmic muons increases with depth, and the extrapolation of cosmogenic neutron production rates from measurements made at shallow sites to greater depths is not well understood. Hence, measurements at deep locations are critical to the success of future experiments.

Many experimental collaborations have performed dedicated studies of cosmogenic neutrons using liquid targets [123–137], generally at relatively shallow depths. The deepest dedicated study to date was performed on data taken with the LSD detector, which was filled with liquid scintillator and located at a depth of 5200 meters water equivalent (m.w.e.) [125]. More recently, the Super-Kamiokande+Gd Collaboration recent published a measurement of cosmogenic neutrons in pure water loaded with gadolinium [138].

The Sudbury Neutrino Observatory (SNO) experiment offers a unique data set to study cosmogenic neutron production deep underground. The SNO detector was a kiloton-scale heavy water detector, located at a depth of 5890 ± 94 m.w.e. Using the parameterization found in [139], the average muon energy at this depth is (363.0 ± 1.2) GeV , higher than those in many other published studies [123, 124, 126–136], and comparable to that at LSD [125]. The SNO data can thus provide information in the high-energy regime, and further

the understanding of how models for neutron production scale with muon energy.

Here we present results derived from the observation of cosmogenic neutrons in the SNO detector, namely a comparison of observables to model predictions and a measurement of the neutron production rate. Section 4.2 describes the SNO detector; Section 4.3 describes the Monte Carlo simulation used; Section 4.4 describes the analysis methods, including the selection criteria for muons and neutrons, and backgrounds to this measurement; Section 4.5 presents comparisons of characteristic observables seen in the data to those predicted by simulations; and Section 4.6 presents the results of the cosmogenic neutron yield measurement.

4.2 The SNO Detector

The SNO detector was a water Cherenkov detector located in INCO’s (now Vale’s) Creighton mine, near Sudbury, Ontario, at a depth of (2.092 ± 0.033) km. It consisted of a spherical acrylic vessel (AV) 12 m in diameter, filled with 1000 metric tons of 99.92% isotopically pure heavy water ($^2\text{H}_2\text{O}$, or D_2O). Surrounding the AV were 9456 Hamamatsu R1408 photomultiplier tubes (PMTs), each 20 cm in diameter, arranged onto a support structure (PSUP) of diameter 17.8 m. Each PMT was outfitted with a light concentrator which increased the total photocoverage to approximately 55%. The AV was surrounded by 7.4 kt of ultra-pure H_2O , approximately 2 kt. of which resides within the PSUP. 96 outward-looking PMTs (OWLs) were arranged on the outer surface of the PSUP, which were used to detect muons which did not enter the PSUP. The detector arrangement is shown in Figure 4.3.

The primary goal of the SNO detector was the resolution of the SNP, which was achieved by overconstraining the fluxes of different flavor combinations of solar neutrinos, an option made available by the choice of D_2O as the primary target medium. Three reactions have detectable final states: elastic scattering (ES), in which a neutrino scatters off an electron (flavor-inclusive scattering is mediated via Z -boson exchange, but electron-type neutrinos can interact via W -boson exchange as well); charged-current (CC) nuclear interactions, in which $\nu_e + n \rightarrow e^- + p$ via W -exchange inside a deuteron, resulting in one electron and two free protons in the final state; and neutral-current (NC) nuclear interactions, in which a neutrino scatters elastically off a quark bound in a deuteron via Z -exchange, imparting enough energy to break up the deuteron and result in a free final-state neutron. For solar neutrino energies, which are strictly below the muon mass, only electron-type neutrinos participate in W -mediated interactions, which results in the three reaction channels having different cross sections for different neutrino flavors. The relevant Feynman diagrams are shown in Figure 4.1, and the cross section ratios are listed in Table 4.1. By measuring the rates of these three reaction channels, the ratio of the electron-type to flavor-inclusive solar fluxes was overconstrained, which allowed for an unambiguous demonstration that solar neutrinos change flavor from electron-type to muon/tau-type in transit to Earth [18, 140–143] — this is summarized graphically in Figure 4.2.

Data-taking proceeded in three phases, which employed different mechanisms for neutron detection. During Phase I, the inner volume was filled with pure D_2O , with the neutron

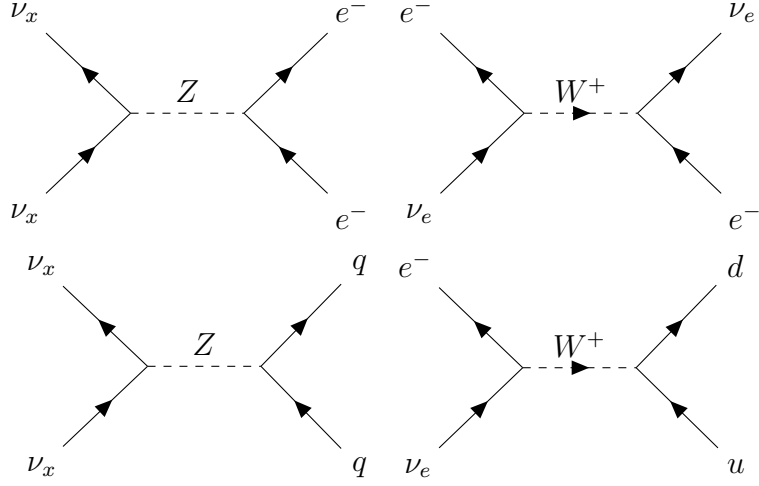


Figure 4.1: Feynman diagrams for main reaction channels at SNO: (top left) flavor-inclusive neutral-current elastic scattering, (top right) electron-type-exclusive charged-current elastic scattering, (bottom left) flavor-inclusive neutral-current reaction, (bottom right) electron-type exclusive charged-current reaction.

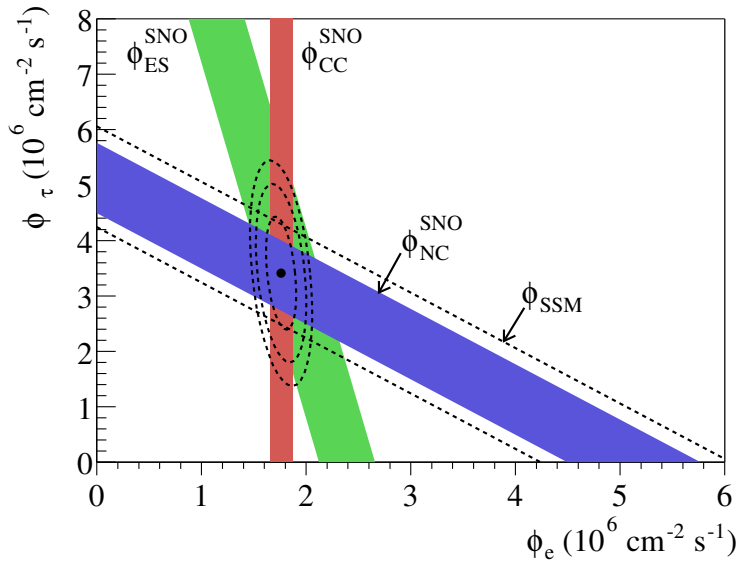


Figure 4.2: Final constraints on electron-type and muon-/tau-type solar neutrino fluxes from SNO. The measurement of three different reaction channels with different sensitivities to the electron flavor overconstrained the flux ratios, unambiguously demonstrating flavor transformation. Figure reproduced from [144].

	Reaction	$\nu_e : \nu_\mu : \nu_\tau$
Elastic scattering	$\nu_x + e^- \rightarrow \nu_x + e^-$	6 : 1 : 1
Charged-current	$\nu_e + D \rightarrow p + p + e^-$	1 : 0 : 0
Neutral-current	$\nu_x + D \rightarrow \nu_x + p + n$	1 : 1 : 1

Table 4.1: Approximate cross section ratios for different neutrino flavors at the \sim MeV-scale, for the three reaction channels observed in the SNO detector.

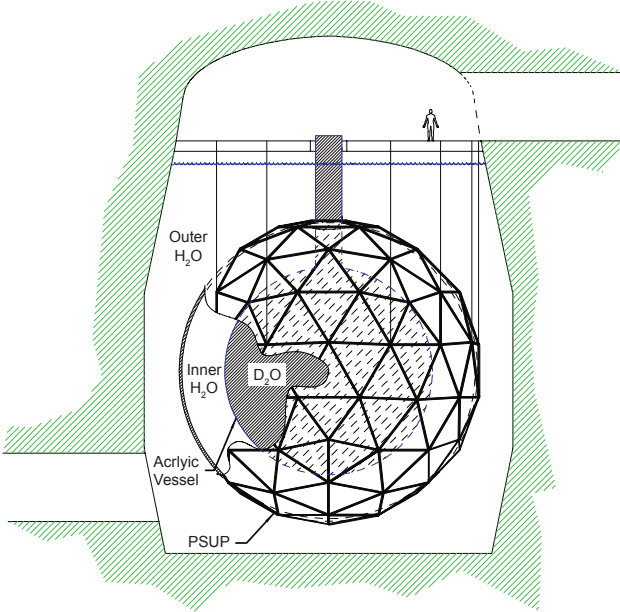


Figure 4.3: Schematic diagram of the SNO detector. Figure reproduced from [70].

detection signal being the emission of a 6.25-MeV gamma following radiative capture on the deuteron. In Phase II, neutron detection was enhanced with the addition of 2 tof NaCl. Chlorine-35 has a larger neutron capture cross section, and a cascade of photons totaling 8.6 MeV in energy is emitted upon neutron capture, further separating the signal from low-energy backgrounds. In Phase III, an array of 3He proportional counters was deployed for neutron detection. The present analysis considers data taken during the first two phases, in which the detector was filled with homogenous media. The livetimes of each phase were 337.25 ± 0.02 and 499.45 ± 0.02 days, respectively.

4.3 Simulating SNO: GEANT4 and SNOMAN

The historical **SNOMAN** Monte Carlo and analysis code [70] incorporates a detailed, high-precision model of the SNO detector, including geometry, material and optical properties, and the response of the PMTs and electronic readout system. This model was based on measurements of microphysical parameters, and tuned and verified using calibration data

from deployed radioactive and optical sources in the context of neutrino analyses [18, 140–143, 145–149]. However, the code relevant to the production and propagation of muons and neutrons evolved to become a compilation of algorithms from various sources. In particular, neutron propagation was based principally on the MCNP package [150], which in SNOMAN is applicable only for neutron energies below 20 MeV. For the purposes of both improved accuracy in the high-energy regime, and ease of interpretation by the scientific community, in the present analysis SNOMAN is used only for the purposes of modeling detector response and event reconstruction in the context of measuring the neutron yield; the propagation of muons and neutrons is performed using GEANT4 [151] version 10.00.p02 using the standard “Shielding” physics list with two modifications described below.

In the course of this analysis, two issues concerning the treatment of deuterons by the standard physics processes included in the Shielding list were discovered. One of the most prominent neutron-producing reactions relevant to this analysis is the photonuclear reaction $\gamma d \rightarrow pn$, which can occur in electromagnetic showers initiated by a cosmic muon. GEANT4 tabulates photonuclear cross sections as a function of the mass number of the nucleus, but, when calculating the cross section for a given isotope, uses a mass number corresponding to the average mass of the naturally occurring isotopes of the given element. For heavy isotopes of hydrogen, this incorrectly returns the cross section on a free proton, which, for energies below the threshold for pion production, is 0, as no nuclear breakup can occur for a single nucleon. This issue was reported to the GEANT4 development team and has been corrected in release version 10.5. In this work, a patch was implemented to disable this behavior for deuterons, for which a cross section tabulation already exists.

It was further discovered that the default model for photonuclear final state generation, the Bertini Intranuclear Cascade, fails to properly model photodisintegration of the deuteron below the pion threshold. Indeed, while $\gamma d \rightarrow \gamma\gamma d$ and similar reactions occur, $\gamma d \rightarrow pn$ reactions do not. For the present analysis, we reimplemented the deuteron photodisintegration model developed for SNOMAN [152] as a GEANT4 physics process, which is applied only to γd reactions below the pion threshold, as an alternative to the Bertini model. In short, this model treats deuteron breakup as a two-body problem subject to conservation of energy-momentum. A summary of the contributions of various cosmogenic neutron-producing processes in GEANT4 is shown in Table 4.2.

The first step in the full Monte Carlo is to generate muons on a spherical shell approximately 4 m outside the PSUP. Given the spherical geometry of the SNO detector, the track can be specified using three coordinates: the impact parameter, which is the distance from the center of the detector to the midpoint of the line connecting the entrance and exit points; the zenith angle, which is the angle of the track measured from vertical; and the corresponding azimuthal angle. The impact parameters and entrance angles are sampled from the muons reconstructed in data, convolved with the resolution of the muon track reconstruction algorithm used in previous cosmic analyses [153]. The initial muon energy is sampled from an analytic form taken from [139], namely

$$P(E) = Ae^{-bh(\gamma-1)} (E + \varepsilon(1 - e^{-bh}))^{-\gamma}, \quad (4.1)$$

Process	Phase I	Phase II
Photonuclear	48.3%	46.1%
Neutron inelastic	25.1%	25.7%
π inelastic	14.8%	16.1%
Proton inelastic	4.5%	4.7%
μ capture	3.3%	3.6%
μ -nuclear	2.7%	2.4%
Other	1.3%	2.4%

Table 4.2: Breakdown of cosmogenic neutron producing processes at SNO, as modeled by **GEANT4**. All processes labeled “inelastic” refer to inelastic scattering, and “ μ -nuclear” refers to direct muon-nucleus interactions via virtual photon exchange.

where $b = 0.4/\text{km.w.e.}$, $\varepsilon = 693 \text{ GeV}$, $\gamma = 3.77$, are constants which parameterize the shape of the spectrum taken from [154, 155], $h = 5.89 \text{ km.w.e.}/\cos \theta$ is the slant depth parameterized by the incident zenith angle θ , and A encodes the normalization of the probability to 1. This distribution is the result of propagating muons from surface [156], neglecting their angular dependence, through a depth h , in the approximation of continuous energy loss. While the angular dependence of the energy spectrum at surface is neglected, the angular dependence due to the flat rock overburden, which for deep detectors is the dominant contribution, is included.

The propagation of muons and all daughter particles is handled by **GEANT4**, subject to the two corrections to photonuclear reactions described above. To mitigate poor performance due to the great number of low-energy photons created by high-energy muons, optical photon tracking is disabled and no detector response is simulated. All high-level observables extracted from the Monte Carlo are thus taken as truth information, as output solely of the physics models. As described above, the detector response is modeled using **SNOMAN** in the context of measuring the neutron yield.

4.4 Analysis

There are two goals of this study. The first is to provide a detailed comparison of the data to model predictions across a number of observables, including the capture time and the reconstructed position of the captured neutrons, offering validation of the models implemented in **GEANT4**. The second goal is a measurement of the neutron yield, defined as the number of neutrons produced per unit muon track length per unit target material, in the D_2O target.

Use of a heavy water target in SNO offered a higher energy signature for neutron capture than the historically common light water and liquid scintillator: neutron capture on the deuteron results in a 6.25-MeV gamma, in comparison to the 2.2-MeV gamma from capture on hydrogen. As a result, the efficiency for detecting neutron captures is greater than 95% in the data set under consideration (see Section 4.4.6). The signal energy is also well above internal radioactive backgrounds, leading to effective neutron identification. The relatively

low muon flux at SNO translates to both unambiguous muon-neutron correlations and limited statistics, in comparison to studies performed at shallower sites.

4.4.1 Muon reconstruction

The reconstruction of a muon candidate event is performed under the through-going hypothesis, and estimates several parameters which specify the muon track, including the geometric impact parameter (b) and zenith angle (θ).

Details of the reconstruction algorithm are described in [148]. Briefly, reconstruction is performed in two stages, where a preliminary fit from the first stage is used as the seed to a more sophisticated algorithm in the second stage. The first stage is a purely geometric construction: the entrance point is identified with the cluster of earliest hit PMTs, and the exit point with the charge-weighted position of all hit PMTs. The second stage, which takes this seed track as input, is a likelihood fit containing terms for the number of detected photoelectrons, and the PMT multiphotoelectron charge and hit-times. Using an external muon-tracking system to validate the fits, the muon reconstruction algorithm was found to perform with a resolution of less than 4 cm in impact parameter and 0.5° in zenith angle [153].

4.4.2 Data set and event selection

The data considered in this analysis was collected during Phases I and II, with the AV filled with pure heavy water and salt-loaded heavy water, respectively. It is thus a subset of the data used in the SNO cosmic muon flux measurement [148], which also considered data taken during Phase III, and a 13-day period between Phases II and III when the detector contained pure heavy water. Phase I data was collected between November 2, 1999 and May 28, 2001, and Phase II data was collected between July 26, 2001 and August 28, 2003, for a combined livetime of 836.7 ± 0.03 days.

The selection criteria for muon events are designed to select through-going muons and reject instrumental backgrounds. Specifically, to qualify as a muon, events must have had at least 500 calibrated PMTs fired, with fewer than three of them in the neck of the AV, which is characteristic of external light entering from the top of the detector. Events that occur within 5 μ s of another event in which 250 PMTs fired, or within a 2-s window containing 4 or more such events, are identified as a class of instrumental events called “bursts,” and are removed from analysis. Furthermore, events with uncharacteristically low total PMT charge and/or broad timing distributions are inconsistent with the muon hypothesis, and are similarly identified as instrumental events. Further high-level cuts are made, among which are the requirements that the reconstructed impact parameter $b < 830$ cm to ensure the validity of the track fit, and the reconstructed energy loss $-dE/dX \geq 200$ MeV/m to reject muons that stop inside the detector volume. Finally, cuts are imposed on the fraction of photoelectrons geometrically contained inside the predicted Cherenkov cone for the muon track, and on the timing of these in-cone photons.

These criteria are identical with previous cosmic muon analyses and are described further in [148, 153, 157] with one exception. A Fisher discriminant was previously used to reject stopping muons, but was found to incorrectly exclude muons with high light production — potentially the most interesting from the standpoint of neutron production — from the analysis. For the present analysis, we omit this linear discriminant cut; stopping muons do not contaminate neutron selection due to their relatively prompt decays, as discussed below. A total cross-sectional area of 216.4 m^2 is considered in this analysis, for which Monte Carlo studies of cosmic muons in SNOMAN show the total event selection cut efficiency to be greater than 99% for through-going muons [148].

The average capture time for thermal neutrons is known to be on the order of tens of ms in pure D₂O, and was decreased to a few ms with the addition of NaCl in Phase II. We thus search for cosmogenic neutrons in a time window of $20 \mu\text{s} < \Delta t < \Delta t_{\max}$ following any through-going muon. The lower bound of $20 \mu\text{s}$ was chosen both to exclude Michel electrons from the decay of daughter muons from pions produced in hadronic showers, and to veto a period of several μs following particularly energetic muons in which the PMTs experienced significant afterpulsing. Imposing this lower bound reduces the livetime for neutron selection by less than 0.5%. The upper bound Δt_{\max} was chosen to accept $> 99\%$ of neutron captures in each phase, and is set to 300 ms in Phase I and 40 ms in Phase II. Low-level cuts to identify candidate events are identical to those used in previous analyses [18, 143, 147]. Neutron events are identified by reconstructing Compton scatters of the capture gammas under a single-scatter hypothesis, yielding a total effective electron energy E_{eff} and reconstructed radial position r . Neutron events are selected by requiring $4.0 \text{ MeV} < E_{\text{eff}} < 20.0 \text{ MeV}$ and $r < 550.0 \text{ cm}$.

These high-level selection criteria differ from previous neutron selection in using a widened energy window consistent between the two phases, compared to the 6-10 MeV window used previously for Phase II data [141], intended to maximize neutron acceptance. This extended acceptance window affects the purity of the selected neutron sample minimally due to the coincidence requirement with the stringent muon selection criteria. Table 4.3 shows the number of muons accepted for the cosmogenic neutron search, and the percentages for which a follower was detected in both the data and Monte Carlo. The scarcity of neutron followers as shown in the table results in fewer than 3000 muons with detected neutron followers across both phases.

	# Muons	% With followers in data	% With followers in Monte Carlo
Phase I	21485	$(2.9 \pm 0.12) \%$	$(3.2 \pm 0.01) \%$
Phase II	31898	$(5.8 \pm 0.13) \%$	$(5.7 \pm 0.01) \%$

Table 4.3: The specific size of the data set, i.e. the number of muons included in this analysis and fraction with followers, indicating the scarcity of neutrons. Uncertainties are statistical only.

4.4.3 Tests of model predictions

In order to validate the models of cosmogenic neutron production and propagation in the GEANT4 Shielding physics list at SNO depth and muon energies, we compare the data with model predictions for a number of observable distributions, including the properties of muons after which neutrons were observed, detected neutron multiplicity, neutron capture position, capture distance from the muon track, clustering of capture positions, and capture time.

These quantities offer benchmarks of different aspects of the models implemented in GEANT4, and unique measurements of the physics involved in neutron production. For example, measurement of the per-muon neutron multiplicity yields insight into the validity of the cross sections of different neutron-producing reactions, while the capture time is sensitive to different neutron energies. Understanding these complementary observables in the simulations and the data will lead to improved physics modeling, imperative for more precise physics measurements.

Furthermore, a measurement of the neutron production rate, using Monte Carlo information as input, requires the reliable simulation of several effects: both direct and secondary production of neutrons, typically through electromagnetic and hadronic channels; the energy spectrum of produced neutrons, which can range up to several GeV; the transport of neutrons both at high and thermal energies; and the detection of capture gammas.

As the neutrons are thermalized and then detected after radiative capture, this analysis is not directly sensitive to the energy of the neutrons, nor their production mechanisms. The observables listed above, however, allow a means to verify the reliability of the Monte Carlo implementations of neutron propagation and capture, in the context of measuring the neutron production rate.

4.4.4 Neutron yield

The “neutron yield” is defined as the production rate of neutrons per unit muon track length per unit material density. Here we measure yields in heavy water, both pure and with the NaCl loaded at 0.2% by weight. The track length through the target material, of density ρ , of a muon with impact parameter b can be written as $\ell_\mu = 2\sqrt{R_{AV}^2 - b^2}$, where $R_{AV} = 600$ cm is the radius of the AV. We define $N_n^{(\mu)}$ to be the number of neutrons produced by the muon, and define the yield to be

$$Y_n = \frac{1}{\rho} \frac{\sum_\mu N_n^{(\mu)}}{\sum_\mu \ell_\mu} = \frac{1}{\rho} \frac{\sum_\mu N_n^{(\mu)}}{N_\mu \ell_{avg}}. \quad (4.2)$$

where N_μ is the total number of muons and ℓ_{avg} is the average muon track length.

The number of neutrons can be determined simply by counting neutron-like events following muon-like events, subject to the following corrections. We express the probability for a neutron produced by a muon of impact parameter b to be captured in the fiducial volume, the “capture efficiency”, as $\varepsilon_{Cap}(b)$; and the probability for a neutron capture at radius r to trigger the detector and survive the event selection cuts, the “observation efficiency”, as

$\varepsilon_{\text{Obs}}(r)$. With a background count of $N_{\text{bkg}}^{(\mu)}$, the number of produced neutrons is then

$$N_n^{(\mu)} = \frac{1}{\varepsilon_{\text{Cap}}(b)} \left(\sum_{n=1}^{N_f^{(\mu)}} \frac{1}{\varepsilon_{\text{Obs}}(r_n)} - N_{\text{bkg}}^{(\mu)} \right), \quad (4.3)$$

where $N_f^{(\mu)}$ is the number of follower events, and we account for the relevant efficiencies on a per-neutron and per-muon basis, as appropriate. The number of background counts is

$$N_{\text{bkg}}^{(\mu)} = N_{\text{ext}}^{(\mu)} + N_{\text{coinc}}^{(\mu)} + N_{\text{radio}}^{(\mu)}, \quad (4.4)$$

comprised of neutrons originating external to the inner volume, radioactive backgrounds coincident with the follower selection window, and radioisotopic backgrounds also produced in spallation reactions, respectively. Estimates for the number of background counts in both phases are given in Section 4.4.7.

The first expression in Equation 4.2 is an idealized production rate, measured under the assumption that neutron production is a Poisson process, occurring constantly along the path of the muon. This is largely untrue, however, as the majority of production actually occurs during showering [158]. The Poisson rate is equal to the mean per-muon yield were each muon to have equal track length. This is, in general, distinct from the mean of the true per-muon yield values calculated using the track length appropriate to each muon, which we denote by \bar{Y}_n . Because SNO is able to reliably reconstruct individual muon tracks, we also calculate a per-muon yield

$$Y_n^{(\mu)} = \frac{N_n^{(\mu)}}{\rho \ell_\mu} \quad (4.5)$$

unique to each muon, and compute \bar{Y}_n as the mean $Y_n^{(\mu)}$. The two quantities Y_n and \bar{Y}_n are compared in Section 4.6.1.

4.4.5 Capture efficiency

The capture efficiency is defined as the fraction of neutrons produced by a muon that is captured in the fiducial volume, parameterized as a function of the impact parameter of the muon. A ^{252}Cf source was deployed in SNO to measure the capture efficiency of MeV-scale neutrons (see Figure 4.15), but the energy spectrum from cosmogenic production extends much higher, potentially invalidating the californium results. We thus evaluate this efficiency solely using GEANT4 simulations. An uncertainty on the capture efficiency due to the spectrum of starting neutron energies, shown in Figure 4.4, is calculated by computing the efficiency in ten bins in energy, ranging from 0 to 5 GeV, and computing the RMS difference of these binned efficiencies from the nominal value, weighted by each bin's integral of the energy spectrum. The capture efficiencies in both phases are shown in Figure 4.5. The cosmogenic capture efficiency curves differ from those measured with the ^{252}Cf source (see

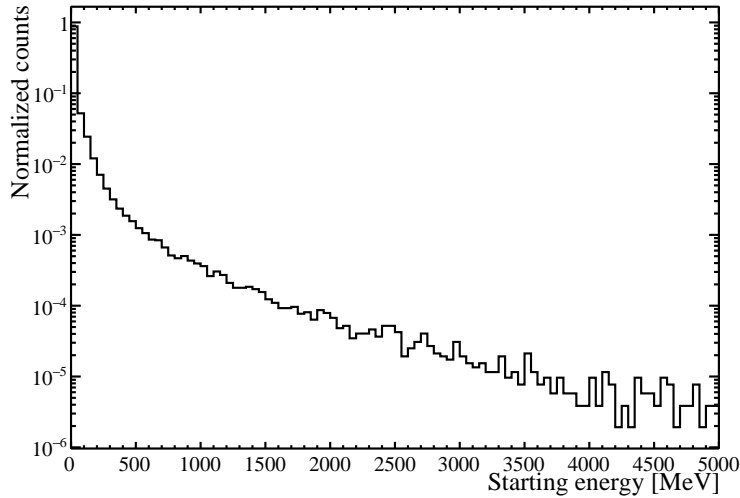


Figure 4.4: The spectrum of starting energies of muon-induced neutrons at SNO, as generated by GEANT4.

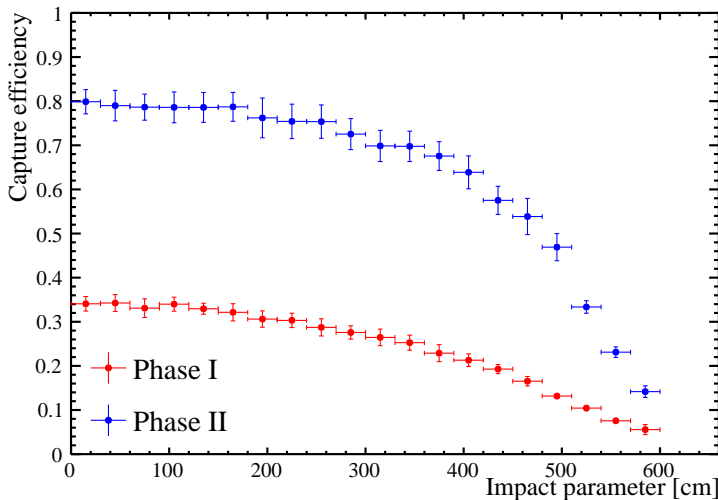


Figure 4.5: GEANT4-based capture efficiencies for cosmogenic neutrons in Phases I (red) and II (blue). Error bars represent the spread in efficiency due to the neutron energy spectrum.

Figure 4.15) for two reasons: principally, the cosmogenic capture efficiency is parameterized by the muon impact parameter, not neutron starting position, but also due to differences in the neutron energy spectra, as previously noted.

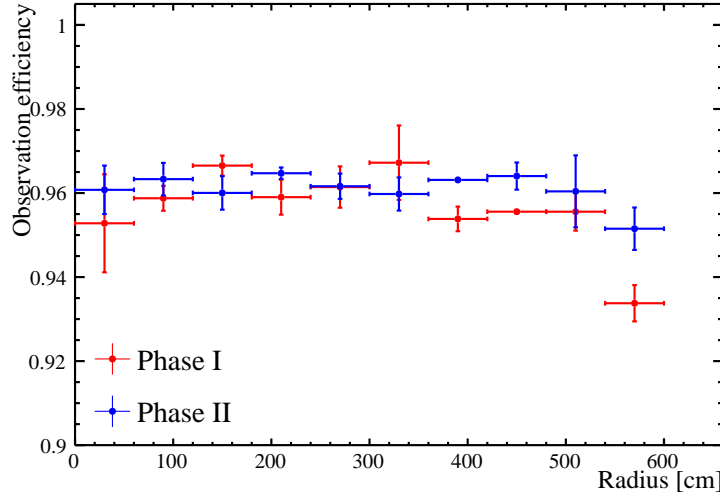


Figure 4.6: SNOMAN-based observation efficiency for neutron captures on D in Phase I (red), and ^{35}Cl in Phase II (blue). Error bars are statistical.

4.4.6 Observation efficiency

The observation efficiency is defined as the probability for a neutron capture through a visible capture mode to trigger the detector and pass the event selection criteria outlined in Section 4.4.2. We evaluate this efficiency by propagating and reconstructing capture gammas in SNOMAN. This efficiency is shown in Figure 4.6. Because the energy threshold used in this analysis is lower than that used in past solar neutrino analyses, this efficiency is comparable in both phases, and relatively stable with respect to position in the detector.

4.4.7 Backgrounds

The yield measurement as defined in Equation 4.2 and Equation 4.3 is subject to three general classes of background, namely cosmogenic neutrons from sources other than the detector target volume, cosmogenic radioisotopes produced in conjunction with neutrons, and random coincident events, each of which is discussed below.

External captures

One background to measuring the rate of neutron production in heavy water is contamination from cosmogenic neutrons produced in other materials, which we define as “external captures.” At SNO, the principal external sources are the AV and surrounding light water. We assess this contamination as a function of impact parameter, and find, using GEANT4, that the average number of external neutrons capturing in the fiducial volume per muon is

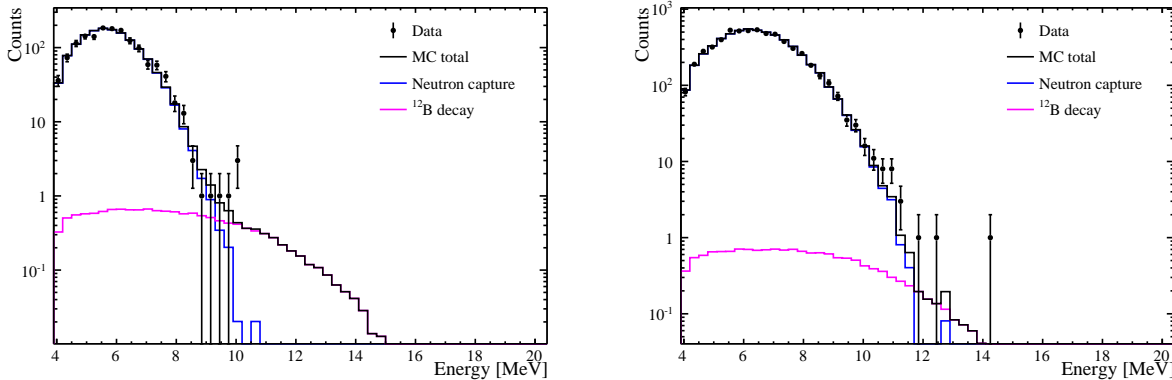


Figure 4.7: Determination of ^{12}B contamination, in Phases I (left) and II (right). The time delay and reconstructed energy (shown here) distributions are fit to a combination of exponentials, corresponding to neutron captures and ^{12}B decays.

at most $(5.3 \pm 0.2) \times 10^{-3}$ in Phase I and $(1.5 \pm 0.1) \times 10^{-2}$ in Phase II, where the larger capture efficiency in Phase II determines the difference.

Cosmogenic radioisotopes

The passage of a muon can result in the production of various unstable isotopes [159], as well as the neutrons that are the focus of this analysis. While the usual concern for cosmogenic production centers on long-lived isotopes, such as ^{16}N with a half-life of roughly 7 s, the timing cut used to select followers makes this analysis sensitive to the production of short-lived isotopes. From both calculations and measurements of isotope production at Super-Kamiokande [159, 160], we determine the expected dominant isotope background to be ^{12}B , which β -decays with a half-life of 20 ms and Q -value of ~ 13 MeV. Our approach to assessing the contribution of this background is data-driven: we search for contamination from ^{12}B decays using a maximum likelihood fit of both the timing and energy distributions of events following cosmic muons. Explicitly, where t and E are the time delay and energy of each event, we construct a likelihood function

$$L(\tau, f_{\text{B}}) = \prod_{\text{events}} \left(\frac{1 - f_{\text{B}}}{\tau} e^{-t/\tau} P_{\text{NC}}(E) + \frac{f_{\text{B}}}{\tau_1} e^{-t/\tau_1} P_{\text{B}}(E) \right), \quad (4.6)$$

where $\tau_1 = 20$ ms / $\ln 2$ is the ^{12}B lifetime, and P_{NC} and P_{B} are the reconstructed energy spectra for neutron captures and ^{12}B β -decays, respectively. The fit parameters are τ , the neutron capture time, and f_{B} , the fractional ^{12}B contamination. The fit is performed separately on the samples of follower events in each phase; the results of the fit in energy space are shown in Figure 4.7. The best fit capture time constants are consistent with those fit under the boron-free hypothesis (Section 4.5.6).

We compute an upper limit on the fractional ^{12}B contamination at the 90% confidence level after marginalizing over the capture time constant. This results in limits on the radioisotopic contamination of 2.4% and 0.67% in Phases I and II, respectively, which are included as uncertainties on the measured neutron yield.

Random coincidences

All remaining backgrounds are uncorrelated with the passage of a muon, and are classified as random coincidences. We assess this class of backgrounds by imposing neutron selection criteria on events in a 3-s time window immediately preceding the trigger time of each muon. The random-coincidence windows are chosen to directly precede each muon in order to most accurately reflect the detector state during the periods in which muons were observed; the window length of 3 s was chosen to balance the benefits of a long analysis window with a conservative time scale for changes in detector conditions, due e.g. to transient instrumental backgrounds. Doing so determines the average coincidence rates to be $7.89 \times 10^{-4} \text{ s}^{-1}$ and $9.73 \times 10^{-4} \text{ s}^{-1}$ in Phases I and II, respectively, which translate to average numbers of coincident events per muon of 2.4×10^{-2} and 3.9×10^{-3} , respectively.

4.5 Study of Event Distributions

To aid in the development and improvement of physical models, both strictly theoretical and those implemented in simulation packages, we present distributions of observables of cosmogenic neutrons and their relation to their leading muon in the data, and a comparison to **Shielding** model predictions. Specifically, we show distributions of the track parameters of muons for which neutron followers were observed, follower multiplicity, the capture positions measured both in the detector and in relation to the leading muon, and the time delay between the muon and follower event. In all cases, the Monte Carlo has been scaled to the normalization of the data, to facilitate comparison of the shapes of the distributions.

4.5.1 Follower selection

The number of muons that have follower events passing the selection criteria described in Section 4.4.2 is shown in Table 4.3. The higher proportion of muons for which followers were observed in Phase II reflects the higher capture cross section. Figure 4.8 shows the distributions of muon impact parameter, both for all muons and only those with followers. The pre-selection distributions agree because the input to the Monte Carlo is sampled from the population of muons observed in the data. The shapes of the post-selection distributions are roughly proportional to the muon track length in the detector. With regard to the zenith angle, the subset of muons with followers is representative of the larger population, and is shown in Figure 4.9.

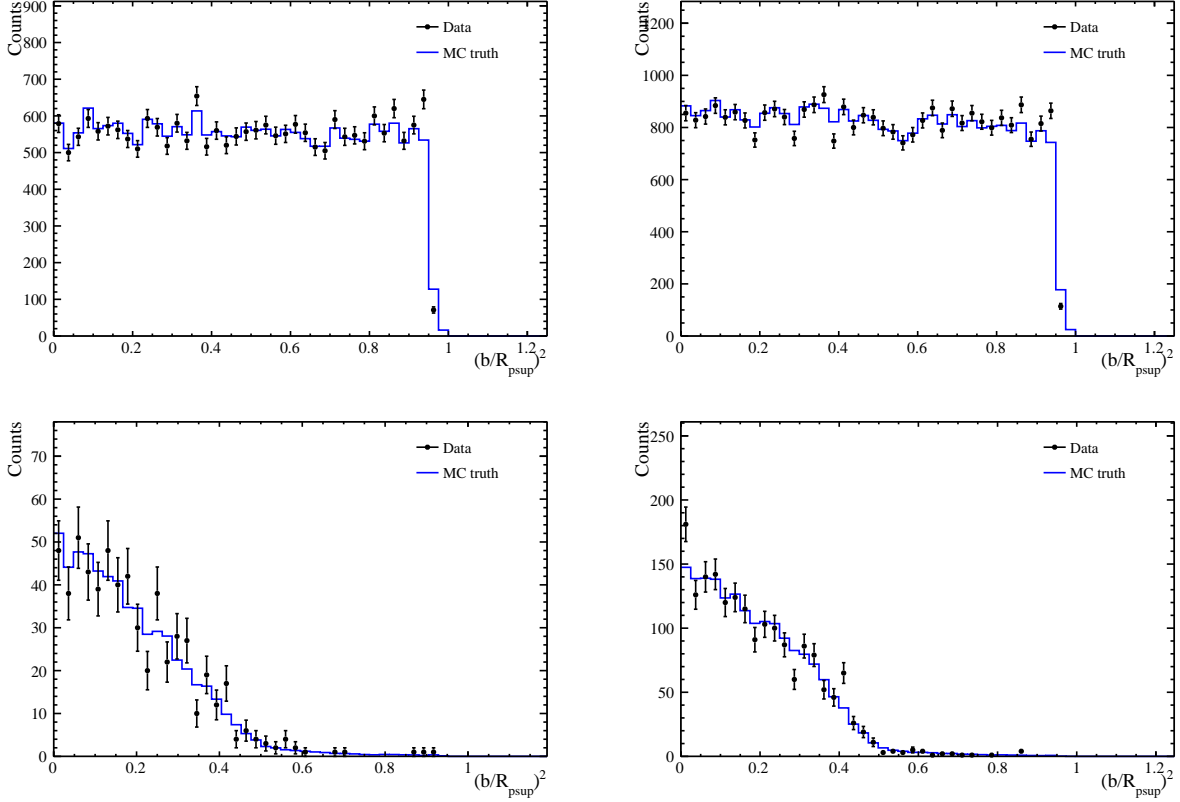


Figure 4.8: Area-normalized impact parameters b^2/R_{PSUP}^2 of all muons (top) and only muons with followers (bottom), in Phase I (left) and II (right). $R_{\text{PSUP}} = 850$ cm is the radius of the PSUP. The AV boundary is at abscissa value ≈ 0.5 . The MC reproduces the data adequately, demonstrating that muons through the center of the detector generically produce more neutrons than those passing near the boundary.

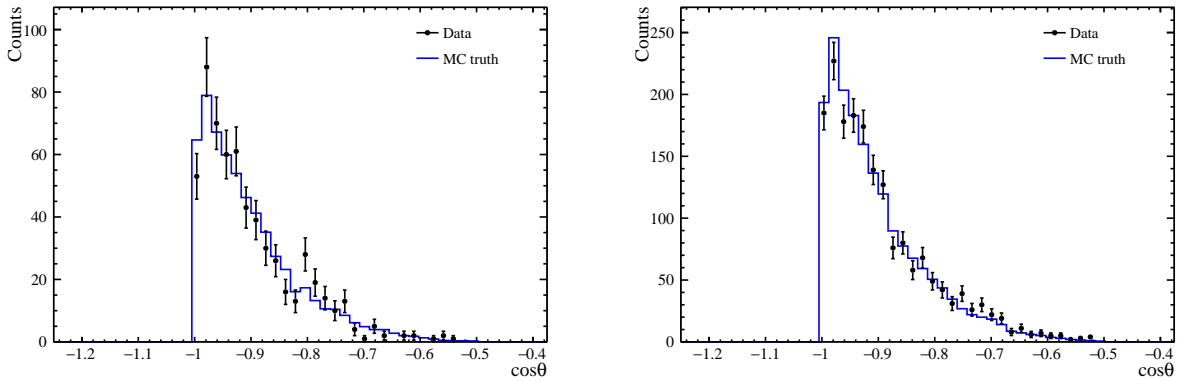


Figure 4.9: Entrance zenith angles of muons with detected followers, in Phases I (left) and II (right). The MC adequately reproduces the data.

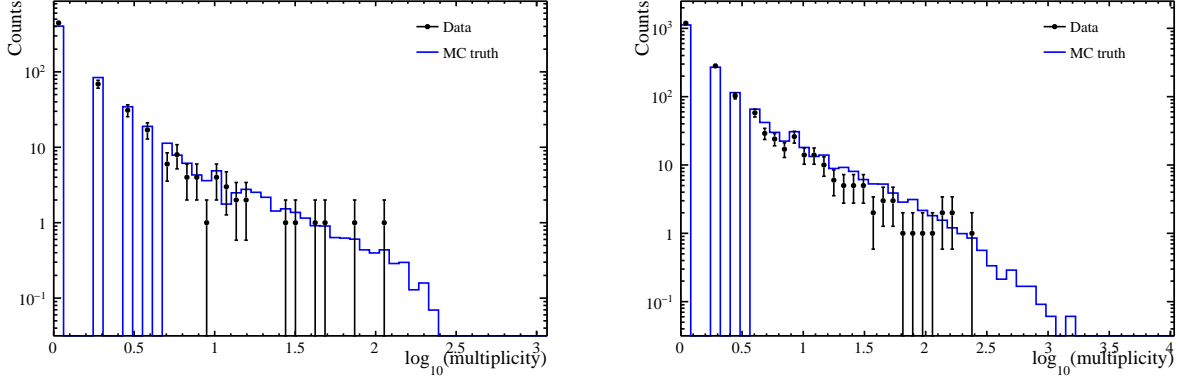


Figure 4.10: Number of detected neutron followers per muon, in Phases I (left) and II (right). Each entry to the histograms represents one muon. The MC reproduces the data well, save for the far tail of the Phase-II distribution, which may indicate mismodeling of reactions involving sodium and chlorine nuclei.

4.5.2 Follower multiplicity

The distributions of the number of neutron-like events following a muon are shown in Figure 4.10. Muons with hundreds of followers were observed in each phase; indeed, events of such high multiplicity are reproduced in simulation. The disagreement observed in the number of high-multiplicity events in Phase II, however, may indicate mismodeling of certain reactions on sodium and chlorine. This could be attributed to incorrect cross sections for the dominant, low-multiplicity, neutron-producing processes, i.e. photonuclear and neutron inelastic scattering, or incorrect final-state generation after near-complete nuclear breakup at high energies.

Distinct identification of cosmic muons as showering either electromagnetically or hadronically has been demonstrated by studying the distribution of multiplicities of neutron followers in high energy (> 90 GeV) muon-induced showers in liquid scintillator detectors [161]. When imposing shower selection criteria, the multiplicity distribution analogous to those shown in Figure 4.10 exhibited two peaks, corresponding to electromagnetic and hadronic showering, with the hadronic case corresponding to larger multiplicities. Our data set includes neutrons of all origins, and the distributions shown in Figure 4.10 do not exhibit the bimodal topography characteristic of such shower separation.

4.5.3 Capture position

Figure 4.11 shows the distributions of the radial position of neutron captures in the detector. Because the muon flux is uniform in area and, in aggregate, neutrons are produced uniformly along a track, they are, in aggregate, produced uniformly in the volume of the detector. This is reflected in Phase II, where there is a large capture cross section and the capture

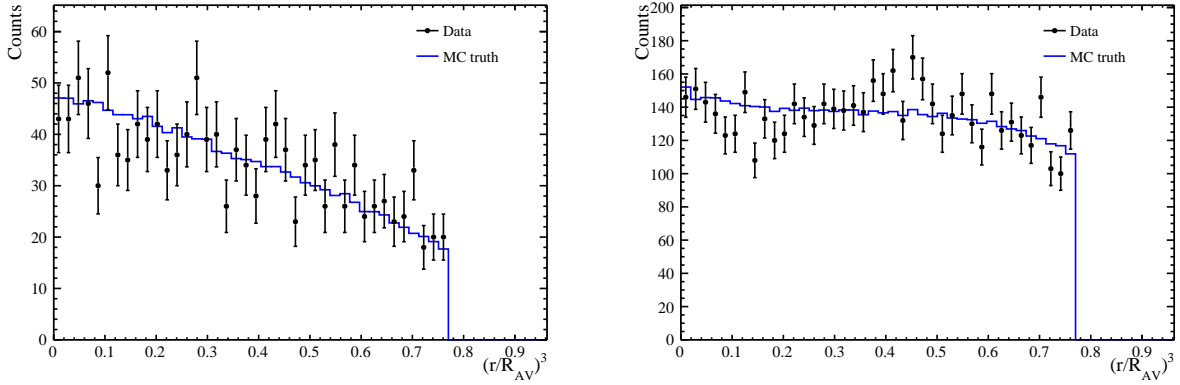


Figure 4.11: Volume-normalized capture position r^3/R_{AV}^3 of detected followers, in Phases I (left) and II (right). $R_{AV} = 600$ cm is the radius of the AV. The MC adequately reproduces the data, demonstrating largely uniform detection of neutrons, save for neutron escape from the fiducial volume, which is suppressed in Phase II.

position is more strongly correlated with production position. In Phase I, where the effective capture cross section is 2 orders of magnitude lower, neutrons are more likely to diffuse out of the fiducial volume; this effect grows as the muon and, hence, neutrons are located closer to the edge of the AV, which has a relatively high hydrogen content, and results in a deficiency of captures in the outer fiducial volume compared to the center. The agreement of the comparison shown in Figure 4.11 constitutes a partial validation of the propagation of neutrons in the **GEANT4** detector model, but is complicated by the finite size of the detector. More ideal tests would use large volumes where boundary effects are suppressed.

4.5.4 Capture clustering

The majority of neutron production occurs in electromagnetic showers. The initiation of a shower usually entails a localized energy deposition by the muon, in contrast to the smaller, constant ionization losses. In the electromagnetic case, this energy deposition has a characteristic profile in the direction of the muon track, which at cosmic-muon energies in light water has a width typically on the order of several meters; see [158] for a discussion.

To attempt to profile the energy deposition relevant to neutron production, we investigate the clustering of muon-induced neutrons. Specifically, we use the neutron capture positions as proxies for their production positions, which act as proxies for the location of energy deposition. We define a clustering metric, σ_{Long} , as the standard deviation in the coordinate of the followers' capture positions measured longitudinally along the muon track. Specifically, we define \vec{r}_n as the reconstructed position of a neutron capture event, $\vec{r}_{\mu \text{ entrance}}$ and $\vec{r}_{\mu \text{ exit}}$ as the positions where the muon enters and exits the PSUP, respectively, and x_n as the

coordinate of the neutron capture measured along the track. That is,

$$x_n = \frac{(\vec{r}_n - \vec{r}_{\mu \text{ entrance}}) \cdot (\vec{r}_{\mu \text{ exit}} - \vec{r}_{\mu \text{ entrance}})}{\|\vec{r}_{\mu \text{ exit}} - \vec{r}_{\mu \text{ entrance}}\|}, \quad (4.7)$$

$$\bar{x} = \frac{1}{N_f^{(\mu)}} \sum_n x_n, \quad (4.8)$$

and

$$\sigma_{\text{Long}} = \sqrt{\frac{1}{N_n^{(\mu)} - 1} \sum_n (x_n - \bar{x})^2}. \quad (4.9)$$

The distributions of this clustering metric in both phases are shown in Figure 4.12. The shapes of the distributions in the top panel are determined as the sum of χ -distributions; a well-known result states that the variance of n normally distribution samples follows a χ^2 -distribution for $n - 1$ degrees of freedom. Indeed, the bottom panel of Figure 4.12 shows the distributions of clustering metrics for muons broken down by multiplicity — those followed by 2 neutrons, and those followed by greater than 2 neutrons — and shows that the 2-neutron widths follow a falling distribution, unlike the bell-shaped curves shown for multi-neutron events.

The mean capture profile width is (1.28 ± 0.06) m in Phase I, and (1.08 ± 0.04) m in Phase II. If interpreted as a length scale over which energy is deposited into hadronic channels, this is smaller than the expected scale for electromagnetic deposition, which in light water occurs over a range of several meters [158].

4.5.5 Lateral capture distance

The distributions of the lateral capture distance from the leading track are shown in Figure 4.13, which follow an anticipated exponential form. The offset in exponential behavior from 0 is due both to neutrons being produced away from the track, and the distance traveled by the neutrons before thermalizing. The characteristic distances, both in data and simulation, in Phase II are reduced in comparison to Phase I, which is expected on the basis of the larger capture cross section for ^{35}Cl than that for ^2H . A single muon in Phase I preceeded a follower candidate observed more than 12 m away, an extreme not predicted by the Monte Carlo. The muon did not enter the AV, and traveled only through the surrounding light water.

The data from Phase II exhibit a rather gross difference in shape from the Monte Carlo prediction, a discrepancy not present for Phase I. Indeed, that this likely points to a problem with the treatment of *cosmogenic* neutrons in GEANT4. While validations of low energy neutron transport have been performed, opportunities to benchmark models of high energy transport are scarce. It is also possible that the energy spectrum of primary neutrons determined in GEANT4 is incorrect, or that the cross sections for scattering from chlorine at high energy are invalid. No such discrepancy is observed in Phase I because low energy neutrons

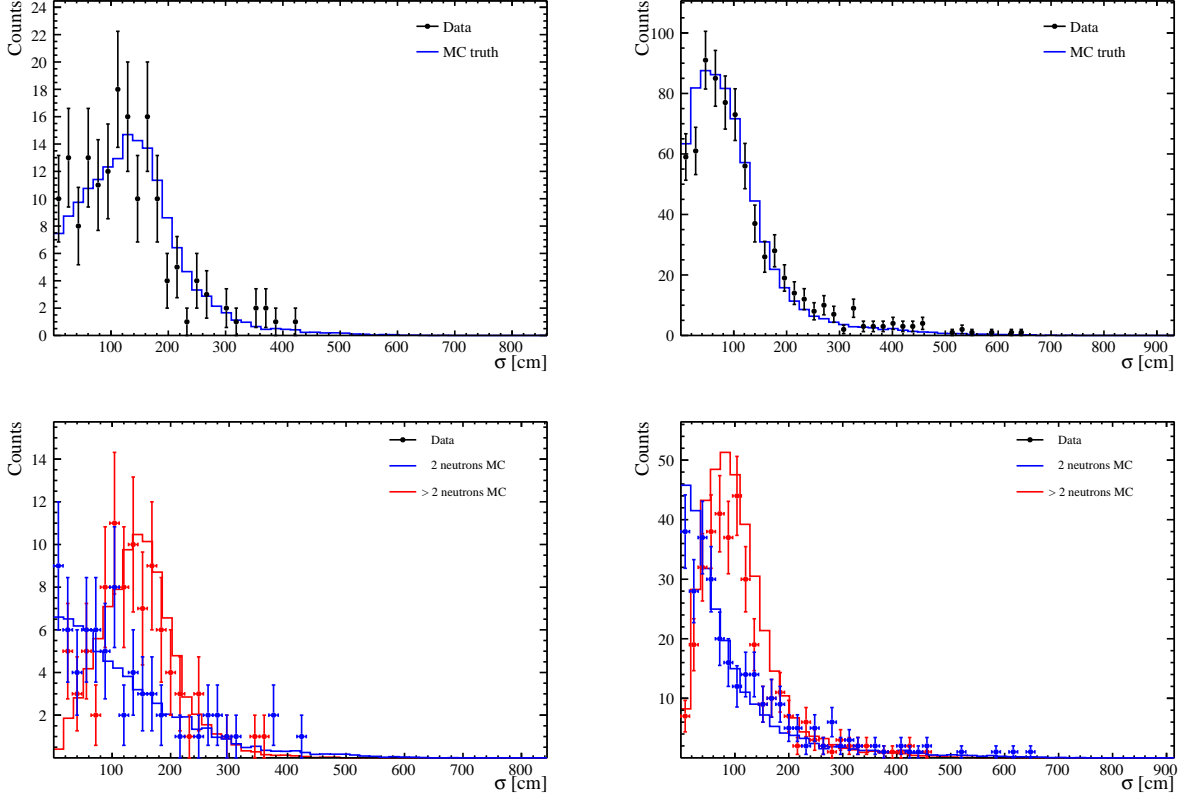


Figure 4.12: Per-muon spreads of capture position measured along the track, in Phases I (left) and II (right). The bottom row shows contributions from muons of different multiplicities. The MC reproduces the data well, indicating that the multiplicity of specific neutron-producing reactions is well-modeled.

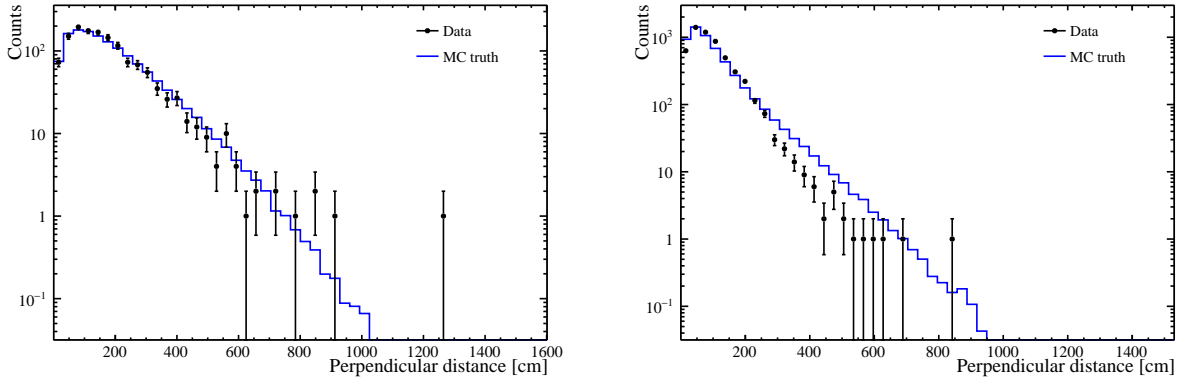


Figure 4.13: Lateral capture distances from track, in Phases I (left) and II (right). The MC reproduces the data adequately, save for the tail of the Phase-II distribution, which may indicate mismodeling of reactions involving sodium and chlorine nuclei.

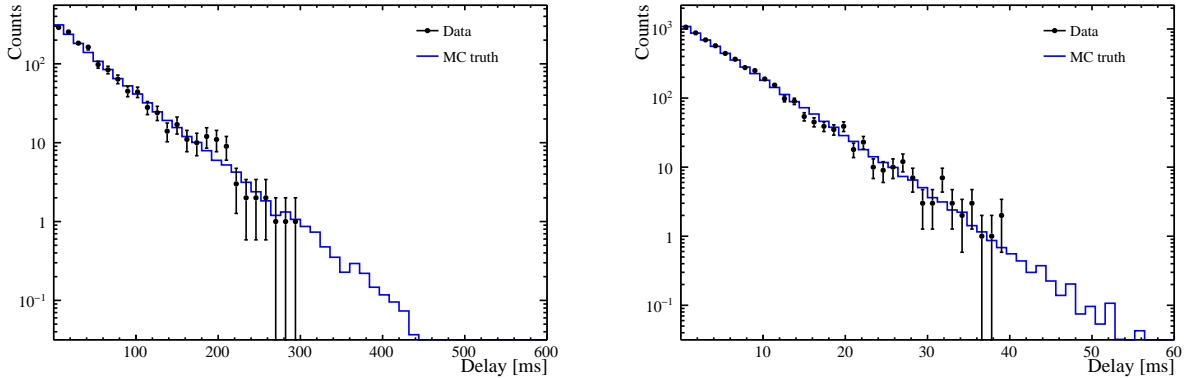


Figure 4.14: Follower delay from most recent muon, in Phases I (left) and II (right). The MC reproduces the data well, indicating that the neutron capture cross sections and material densities are implemented correctly.

in deuterium experience appreciable random walks, typically several meters in length, before capturing. Any sub-meter difference in the path length traveled at high energy is masked by the effect of this relatively long random walk. Indeed, using a simple toy Monte Carlo which samples high-energy transport lengths from the Phase II distributions in Figure 4.13 and low-energy transport lengths from the distribution of random walk lengths that a neutron may experience in pure D₂O, the resulting distributions exhibit a similar level of agreement as the data from Phase I.

4.5.6 Time delay

Distributions of the delay between a muon's passage through the detector and its follower captures are shown in Figure 4.14. The data during each phase may be fit with a pure exponential, yielding maximum-likelihood estimators of the characteristic capture times of 48.5 ± 1.3 ms in Phase I, and 5.29 ± 0.07 ms in Phase II. While muon-induced neutrons may be produced with very high energies, this is in agreement with the previously measured capture time for ²⁵²Cf neutrons in the salt phase of 5.29 ± 0.05 ms [141]. As the thermalization time is small in comparison to the overall capture time, this suggests that the modeling of low-energy neutron transport and capture are valid in the presence of chlorine, further indicating that the source of the discrepancy in lateral capture distance is in the high-energy regime.

4.6 Results for neutron yield

The measured neutron yield values in pure heavy water and salt-loaded heavy water are found to be, in units of 10^{-4} cm/(g · μ), 7.28 ± 0.09 (stat.)_{-1.12}^{+1.59} (syst.) and 7.30 ± 0.07 (stat.)_{-1.02}^{+1.40} (syst.), respectively. These are to be compared with the respective

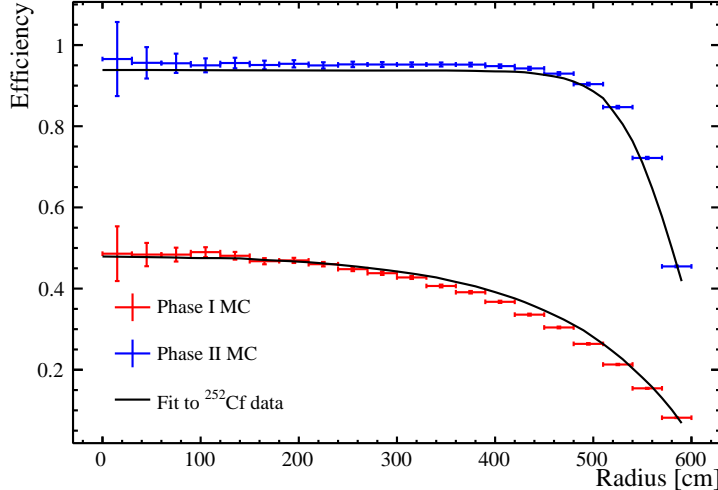


Figure 4.15: Low-energy capture efficiencies as calculated by simulating ^{252}Cf neutrons with GEANT4, compared with analytic fits performed to ^{252}Cf calibration data taken during Phases I and II.

values predicted by GEANT4 of 7.01 ± 0.014 (stat.) and 7.29 ± 0.014 (stat.), respectively, though it should be noted that systematic uncertainties on the simulated values may be quite large, up to $\sim 50\%$. See [133] for extensive discussion.

The systematic uncertainties for this measurement are shown in Table 4.4, including uncertainties from the Monte Carlo-based capture and observation efficiencies, as well as the number of neutron-like background counts coincident with a through-going muon.

The dominant uncertainty is due to the Monte Carlo-based capture efficiency. A ^{252}Cf fission source was deployed in both phases to measure a per-neutron capture efficiency for low energy (< 15 MeV) neutrons as a function of position in the detector [141]. We assess an additional uncertainty on the muon-induced capture efficiency by computing a volume-weighted average of the relative error between the capture efficiency for ^{252}Cf neutrons as reported by GEANT4 and the results of the calibration campaign, which are shown in Figure 4.15. While the simulation is able to reproduce the gross features of the low-energy capture efficiency in both phases, the disagreement at high radii, where the efficiency decreases substantially, causes this to be the dominant uncertainty.

4.6.1 Evaluation of the Poisson hypothesis

The yield values presented above are measurements of Y_n (see Equation 4.2), which is standard in the literature, and are the values appropriate when describing neutron production as a Poisson process. These can be compared to the mean per-muon yields, \bar{Y}_n (see Equation 4.5), which in units of $10^{-4} \text{ cm}/(\text{g} \cdot \mu)$ is 7.62 ± 0.89 (stat.) and 9.32 ± 1.22 (stat.), in

	Phase I	Phase II
Capture efficiency	+21.7% -15.2%	+19.1% -13.8%
Observation efficiency	$\pm 0.4\%$	$\pm 2.1\%$
Background counts	+0.0% -2.4%	+0.0% -0.7%
Total	+21.7% -15.3%	+19.2% -14.0%

Table 4.4: Relative uncertainties on the yield measurement.

Phases I and II, respectively. The two rates are consistent in pure heavy water, but not in Phase II, where the discrepancy is 24.4%. The mean per-muon yield is more sensitive to high-multiplicity muons than the idealized rate, and indeed the few muons in the tail of the Phase II distribution shown in Figure 4.10 are the source of this difference. Monte Carlo sampling indicates that a discrepancy this large is not unusual, which suggests that a Poisson rate, while useful for summarizing a gross production rate, should not be interpreted as a parameter fundamental to neutron production.

4.6.2 Comparison to other experiments

While no cosmogenic neutron yield measurements have been published for heavy water, Super-Kamiokande+Gd has recently published results for gadolinium-loaded light water [138], and several measurements have been performed using liquid scintillator targets. The nuclear composition of both light and, in particular, heavy water, abundant with weakly bound deuterons, differ from that of the carbon chains typically found in organic liquid scintillators, and so the results should not be compared directly. Still, the average numbers of nucleons per unit volume are comparable, and so the yields should be of similar scale. Figure 4.16 shows several yield measurements performed with liquid scintillator targets as a function of average muon energy, and a fit to a scaling law of the form $Y_n = aE_\mu^b$ recently performed by the Daya Bay Collaboration [136], with the LSD [125] and relatively recent Jinping [137] scintillator measurements, Super-Kamiokande+Gd light water measurement, as well as this heavy water measurement, overlaid. Repeating the power-law fit with and without the higher-energy measurements from LSD and Jinping yields consistent results within uncertainty. The average muon energy at SNO depth was determined using the parameterization in [139]. It is observed that while cosmogenic neutron production in heavy water occurs on a similar scale to the extrapolation from liquid scintillator measurements, it is enhanced, consistent with the greater average mass number. With the SNO+ experiment currently running in the original SNO cavern with plans to record data with both light water and liquid scintillator targets, it will be possible to perform additional yield measurements at this same site using multiple different materials, to further elucidate the nature of neutron production at such high energies and across different materials.

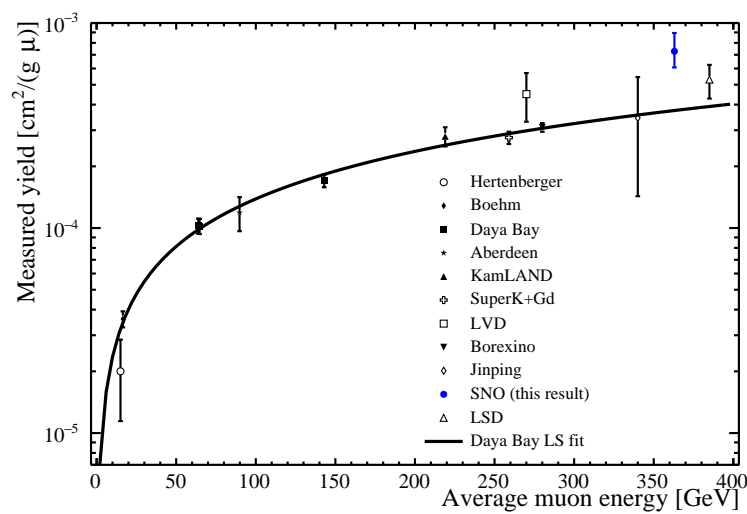


Figure 4.16: Power-law fit for the cosmogenic neutron yield in liquid scintillator, performed by the Daya Bay Collaboration [136], with the SNO Phase I, LSD, Jinping, and Super-Kamiokande+Gd measurements overlaid. The SNO, LSD, Jinping, and Super-Kamiokande measurements are not included in the fit, and the target materials used in SNO and Super-Kamiokande+Gd are not liquid scintillators.

Chapter 5

Extraterrestrial Antineutrinos in SNO₊

5.1 Introduction

All antineutrinos observed to date are believed to have originated on planet Earth — whether from radioactive decays in nuclear reactors [2, 19] or the Earth’s crust [162, 163], or from hadronic decays in the atmosphere [164–168]. Due to both their low interaction rate in transit, and apparent absence at Earth, astrophysical antineutrinos thus present a “smoking gun” opportunity for observations of new physics, varying from confirmation of predicted but unobserved phenomena, such as the detection of the diffuse supernova neutrino background (DSNB) [169, 170], to novelties in fundamental particle physics, such as electromagnetically-mediated neutrino-antineutrino transformation [171]. Due to the unique experimental signature offered by IBD reactions, namely the coincident detection of the final-state positron and neutron according to $\bar{\nu}_e + p \rightarrow e^+ + n$, experimental searches for antineutrinos are generally subject to relatively low backgrounds, which enhances their utility in searching for new phenomena.

Several large-scale neutrino detectors have recently performed searches for such an astrophysical antineutrino flux. The SNO collaboration published a search for electron antineutrinos using 647 kg-years of data in 2004, ultimately suffering from the low neutron detection efficiency generally achieved in a water-based detector, placing early limits on an astrophysical flux below 15 MeV [114]. The Borexino collaboration, which is ultimately limited by a relatively small detector size, has also focused on the low-energy region below 15 MeV, and as of 2019 reports no significant antineutrino excess with a total exposure of approximately 1.5 ton-year of scintillator data [115]. The use of a scintillator admits a much higher neutron detection efficiency, owing to reduced intrinsic radioactivity and increased light collection. In 2022, The KamLAND collaboration performed an analysis on 6.72 kton-year of scintillator data in an energy range below 30 MeV, also finding no significant excess of antineutrinos [116]. In 2021, the Super-Kamiokande collaboration reported improved limits up to 31 MeV

with an exposure of 183 kt-year, also utilizing a water-based detector with a relatively low neutron detection efficiency [117]. After a recent addition of gadolinium to the detector, which significantly improved the neutron detection efficiency, an analysis of 34 kt-year of Super-Kamiokande+Gd data has resulted in comparable limits to the 2021 pure water results, and are approaching values consistent within theoretical uncertainties of DSNB model predictions [118].

While there are several models that may explain any observed astrophysical antineutrino flux, the pertinent experimental question remains whether such a nonzero flux exists. This is thus the primary test we perform here: a model-independent search for an excess antineutrino flux.

Geological antineutrinos are produced predominantly in Uranium and Thorium decay, which occur below ~ 3 MeV. The flux of reactor antineutrinos is negligible above ~ 8 MeV, leaving atmospheric neutrino interactions as the only true background at higher energies. We present here a preliminary search for an excess of antineutrinos using 53 kg-year of scintillator data using the SNO+ detector, in the energy range between 10 MeV and 40 MeV, which is the first exploratory analysis of high energy data using the SNO+ detector. We present model-independent limits on the astrophysical flux, as well as limits on cross-section for dark matter self-annihilation into neutrino/antineutrino pairs, and sensitivity projections for future analyses of larger data sets.

5.2 The SNO+ detector

The SNO+ detector is an upgrade to the SNO detector described in Section 4.2, which is in the second phase of a three-phase experimental program, consisting of an initial phase operating with water, a second phase operating with liquid scintillator, and a third phase in which the liquid scintillator will be loaded with tellurium to search for neutrinoless double- β decay of ^{130}Te . The most prominent feature of these transitions is the replacement of the heavy water used in SNO, and the pure water used in the initial phase, with a liquid scintillator, comprised of linear alkylbenzene (LAB) as a base solvent with 2,5-diphenyloxazole (PPO) dissolved at a concentration of 2 g/L, which acts as a fluor with an emission spectrum better matched to the PMTs with which the detector is instrumented. The use of liquid scintillator allows for a lower energy threshold and improved energy resolution, compared to water-based detectors such as SNO and Super-Kamiokande. Other practical upgrades to the detector, such as improved data readout protocols and structural additions to accomodate the higher buoyancy of a scintillator-filled vessel, are detailed in [172]. The light yield of the scintillator with which the data analyzed in this work is ~ 11800 photons/MeV deposited [173], which manifests as approximately 250 PMT hits/MeV deposited at low energy. At higher energy, there is typically a significant proportion of multiphoton hits, wherein multiple photons are detected by a single PMT and are not resolved by the front-end electronics.

5.3 Simulating SNO+: RAT

The SNO+ detector is modeled using RAT, a GEANT4-based Monte Carlo simulation which evolved from the same code base as RAT-PAC. Generic interactions of particles with matter, as well as optical propagation of photons, is performed by GEANT4 [151], the scintillation process by custom routines based on GLG4Scint [174], and the detector response by a fully custom codebase. Calibration of the simulation model roughly factors into calibrations of the PMTs and electronics, which are performed offline, and of properties of the target medium, which are achieved through a combination of in-situ analyses of radioactive and optical source data (see, e.g. [172] for an overview and [175] for an example from the water phase).

5.4 Reconstruction

General-purpose tools, collaboratively developed by the SNO+ collaboration, are available to reconstruct the position and energy deposited in neutrino interactions from the record of PMTs hit in a given event. Nominal event reconstruction makes use of statistical models of the number and times of photons detected by individual PMTs, and is performed under the assumption that each PMT detects, on average, less than one photon (i.e., the detector is operating at “low occupancy”), and hence is optimized for relatively low energy measurements. Here we review the methodology underlying standard reconstruction techniques and discuss their predicted performance in a higher energy regime, where appreciable fractions of the detector may be hit.

5.4.1 Overview

Position, or vertex, reconstruction is achieved by determining a maximum-likelihood estimate of the position coordinates, where the likelihood is computed as a product over the probabilities of observing the given *hit time residuals* registered by each PMT, where the relevant probability distributions are tabulated from Monte Carlo. The hit time residual is defined as

$$t_r = t - t_0 - \sum_i \frac{L_i}{c_i} \quad (5.1)$$

where t is the time associated with the PMT signal, t_0 is the candidate time of the event, and L_i and c_i are the path lengths and effective speeds of light in the materials that the photon propagates through between the event vertex and PMT. The path lengths L_i are functions of the vertex coordinates and are computed online using the optical properties of the various detector media. Probability distributions of hit time residuals are tabulated using simulated electrons of energy 10 MeV and below.

Energy reconstruction is achieved by inverting the nonlinear mapping between the energy deposited in the scintillator and number of hit PMTs, the form of which is determined by

modeling the occupancy of the PMTs as a Poisson process. The following is a brief description which follows the excellent presentation found in [176].

Neglecting nonlinearities which appear at very low energies ($<< 1$ MeV), the mean number of photons, N_γ , produced by the scintillator is proportional to the energy deposited in the scintillator, E_{dep} :

$$\langle N_\gamma \rangle \propto E_{\text{dep}}. \quad (5.2)$$

The mean number of photoelectrons detected by the i^{th} PMT, μ_i , is proportional to the number of photons produced, according to quantum efficiency of the PMT and various optical effects at play in the detector:

$$\mu_i \propto \langle N_\gamma \rangle \propto E_{\text{dep}}, \quad (5.3)$$

and the mean number of photoelectrons detected across the detector is the sum over all PMTs present. Assuming that the proportionality in Equation 5.3 is uniform for all PMTs — that is, $\mu_i = \mu$ for all i (a fair assumption for, say, a central event in the spherical geometry of SNO+) — we then have

$$\langle N_{PE} \rangle = \sum_i \mu_i = N_{\text{PMT}} \cdot \mu \propto E_{\text{dep}}. \quad (5.4)$$

The proportionality in Equation 5.4 can be quantified using simulation, but the actual value of N_{PE} must be determined on an eventwise basis. In SNO+, the photoelectron count N_{PE} is not directly measured, but instead the number of distinct hits N_{hits} is reported. Assuming Poisson fluctuations, the probability of a PMT *not* being hit, that is, detecting 0 photoelectrons, is

$$P(\text{PMT } i \text{ not hit}) = e^{-\mu}, \quad (5.5)$$

and hence

$$P(\text{PMT } i \text{ hit}) = 1 - e^{-\mu}. \quad (5.6)$$

The total number of hits across the detector is then

$$\langle N_{\text{hits}} \rangle = N_{\text{PMT}} \cdot P(\text{PMT hit}) = N_{\text{PMT}} (1 - e^{-\mu}), \quad (5.7)$$

from which we estimate the mean per-PMT photoelectron count as

$$\mu = -\log \left(1 - \frac{N_{\text{hits}}}{N_{\text{PMT}}} \right), \quad (5.8)$$

and hence

$$N_{PE} = N_{\text{PMT}} \cdot \mu = -N_{\text{PMT}} \log \left(1 - \frac{N_{\text{hits}}}{N_{\text{PMT}}} \right), \quad (5.9)$$

to which the proportionality in Equation 5.4 can be inverted to estimate the energy deposited. In practice, where the assumption of a global mean photoelectron count μ does not hold, for example for a non-central event, the detector can be partitioned into distinct sets of PMTs

for which the assumption approximately holds, with the energy estimates obtained from each partition summed together. It is important to note that this technique can only be applied before the saturation point of the detector: fluctuations of N_{hits} cannot exceed N_{PMT} , and so as $\langle N_{\text{hits}} \rangle \rightarrow N_{\text{PMT}}$, become effectively one-sided and hence the mean energy estimate is biased low. As shown below, this imposes additional constraints on the analysis windows constructed for high energy analyses using hit-based energy reconstruction.

5.4.2 Performance at high energy

Reconstruction performance was investigated using RAT Monte Carlo simulations of electrons distributed throughout the scintillator volume. The results are summarized in Figure 5.1, which shows the mean error of reconstructed radial position and energy deposited as a function of electron energy, for six equal-volume radial shells in starting position. Three conclusions are evident: first, that vertex reconstruction becomes biased radially outward; second, that the energy of central events can be reconstructed up to approximately 40 MeV, at which point the detector saturates and reconstruction is biased, as discussed above; and third, that energy reconstruction above 10 MeV degrades rapidly with increasing radial position.

The first feature, the outward radial position bias, can be understood as a consequence of the distortion to the time-residual likelihood in the presence of multiphoton hits, the nature of which is discussed in detail in Section 6.3.4. The second feature, energy bias at high energy, is caused by global saturation of the detector. The third feature, energy bias at high radius, is attributed to *local* detector saturation, where appreciable portions of the detector nearby the event position saturate. This can be mediated to some extent by more sophisticated partitioning schemes, but it was found to provide very minor extensions of the analysis window offered by current energy reconstruction (namely, energy less than 40 MeV and radial position less than 3.3 m). Implementation of a PMT-charge-based reconstruction algorithm, which would effectively remove these limitations imposed by detector saturation is underway, but is not utilized in this work.

5.5 Data set and event selection

The data analyzed in this work was collected with the SNO+ detector filled with the nominal LAB + 2 g/L PPO scintillator cocktail, between April 29th, 2022, and March 10th, 2023, totaling a livetime of approximately 155.2 days. This livetime is subject to losses from veto periods to remove cosmogenic backgrounds, which is discussed below.

Event selection criteria are designed to identify two triggers which are correlated in time, corresponding to the prompt positron and delayed radiative capture of the neutron emitted in an IBD reaction. The associated “prompt” and “delayed” selection criteria, corresponding to positron and neutron selection, respectively, are outlined below.

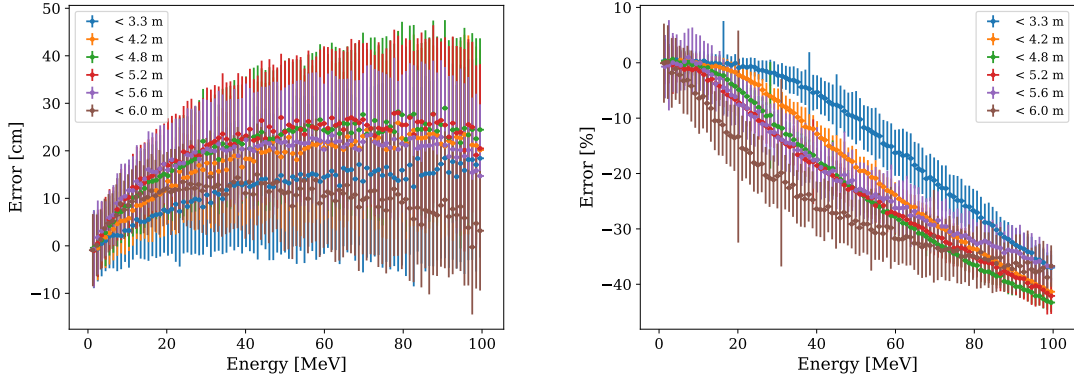


Figure 5.1: Reconstruction of hit-based position (left) and energy (right) reconstruction for electrons with energy up to 100 MeV. Different colors denote different radial shells in starting position. The energy of central electrons can be accurately reconstructed up to 40 MeV, with performance degrading at higher radii.

5.5.1 Prompt event selection criteria

Owing to kinematic considerations, the IBD positron is emitted with most of the available final-state kinetic energy [177], and as such the primary motivator of the prompt event selection is valid energy reconstruction. Accordingly, the prompt event selection is defined as a reconstructed energy in the region of interest (ROI) of 10 MeV to 40 MeV, and a reconstructed position within the 3.3 m fiducial volume. The lower bound of 10 MeV is chosen to avoid overlap with the reactor antineutrino regime; the upper bound of 40 MeV and fiducial volume are chosen to ensure that energy reconstruction is unbiased and any spectral features observed in the data can be meaningfully interpreted. The outward radial bias in position reconstruction results in a loss in signal efficiency, but, importantly, preservation of any observed spectral features.

5.5.2 Delayed event selection criteria

No kinematic information is reconstructable from neutron interactions in scintillator, as the light levels produced by recoil protons is typically very low. Nonetheless, IBD neutron detection acts as a background-suppression mechanism, removing the majority of non-IBD prompt-like events from consideration. Delayed event selection is implemented by detecting the 2.2-MeV γ ray emitted upon radiative neutron capture by a hydrogen nucleus, the dominant capture mode available in the scintillator. Because the neutron may diffuse some distance from the IBD interaction site, and the 2.2-MeV γ ray does not saturate the detector, an enlarged 5.7 m fiducial volume is utilized. The distribution of reconstructed energy of simulated neutron captures in this extended volume is shown in Figure 5.2, which justifies a selection window of 1.7 MeV to 2.5 MeV.

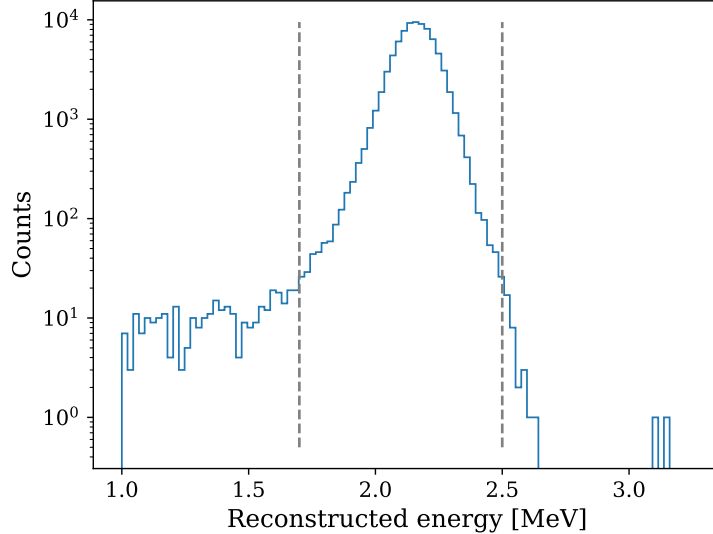


Figure 5.2: Reconstructed energy of simulated neutron captures on hydrogen which reconstruct within a 5.7 m fiducial volume, with the selection cuts used in this analysis demarcated.

Two additional delayed selection criteria are implemented as further background suppression mechanisms: the time measured from the last prompt event, and the number of delayed candidates in a surrounding time window. The definition of the former criterion is driven by two considerations. On short time scales after large light levels are present in the detector, such as after a through-going cosmic muon, the PMTs and frontend electronics suffer a period of instability caused by high rates of afterpulsing and oscillations of the electrical baseline of the trigger system. This period of instability was characterized using through-going muons in the water phase, finding that the detector returned to normal operations after a few microseconds, during which spurious triggers may reconstruct as low energy physics-like events in the detector [178]. In this work, we conservatively veto the first 10 μ s after any prompt-like event. On longer timescales, a maximum time-difference from the latest prompt event is enforced. In general, this maximum time value is chosen to optimize against accidental coincidence backgrounds, which are distributed uniformly in time, as opposed to the exponential distribution of neutron captures. As discussed in Section 5.6.2 below, this background is negligible in the ROI, and hence we choose a generous upper bound of 1 ms, roughly 5 times the characteristic capture time of ~ 200 μ s.

The second quality criterion, a “multiplicity” condition, is defined as the requirement that an identified neutron-like event is the only event, other than the prompt positron-like event, with reconstructed energy above 400 keV within a 2 ms window omitting the 10 μ s post-prompt-event veto window. The effect of this cut is to suppress false coincidences where a high-energy positron-like event accidentally coincides with a neutron produced by a low-energy atmospheric neutrino interaction. The atmospheric neutrino background is discussed

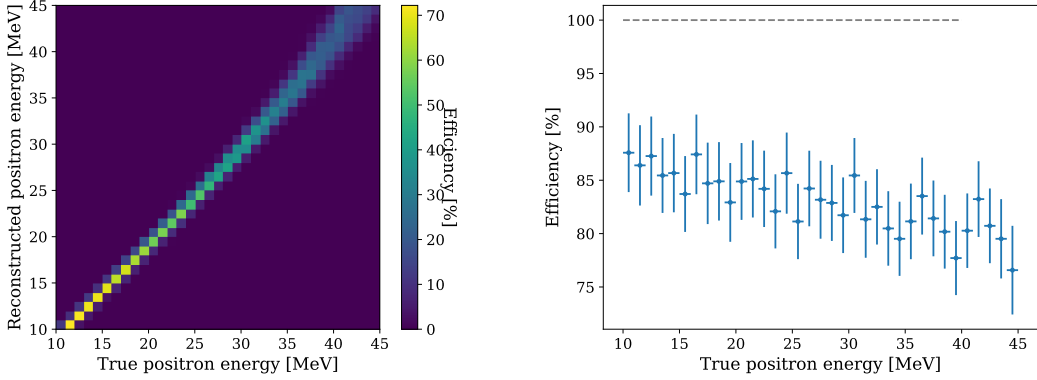


Figure 5.3: Detector response matrix (left) and detection efficiency (right) for positrons distributed within the central 3.3 m detector volume.

in further detail in Section 5.6.3.

5.5.3 Detector response matrix and signal efficiency

The detector response matrix, which encodes the efficiency for an IBD event of a given energy to validly reconstruct with a given energy, was quantified using RAT simulations, and is shown for events uniformly distributed within the central 3.3 m volume in Figure 5.3. Also shown in Figure 5.3 is the gross detection efficiency, defined as the detector response matrix summed along the reconstructed energy axis. The average detection efficiency is $\sim 83\%$, with losses dominated by misreconstruction of prompt events outside of the fiducial volume, which is a larger effect at higher energies owing to the radial bias discussed in Section 5.4.2. The 10 μ s post-muon veto window affects a uniform 6% efficiency loss.

5.6 High-energy backgrounds

5.6.1 Cosmic-ray muons

As discussed in Chapter 4, interactions of high-energy cosmic rays with the Earth's atmosphere initiate hadronic showers, which terminate with the copious production of pions, which promptly decay into muons which can penetrate deep underground. At SNO+, the overwhelming majority of these muons traverse the full detector volume, depositing up to 4 GeV of energy through ionization alone. These typically constitute the highest-energy genuine physics interactions in the detector, and can be accompanied by the production of both free neutrons and unstable radioisotopes which decay via $\beta + n$ emission, namely ${}^8\text{He}$ and ${}^9\text{Li}$, with spectral endpoints of 10.7 MeV and 13.6 MeV, respectively. Both isotopes have half-lives below 200 ms, and thus both coincidence pairs (primary muon / neutron and

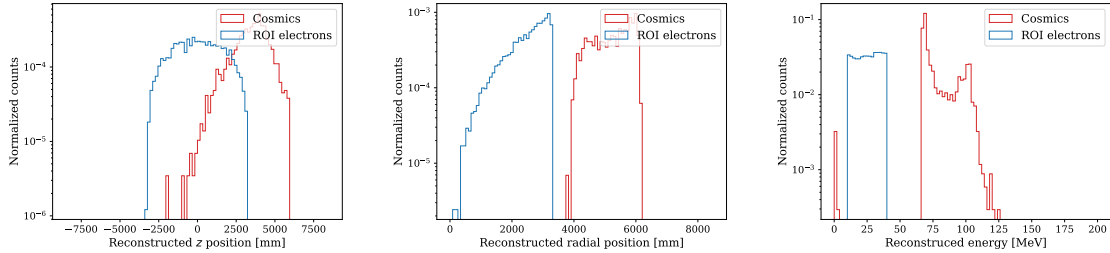


Figure 5.4: Distributions of reconstructed z -position (left), radial position (middle), and energy (right) for ROI electrons (blue) and cosmic-ray muons (red). Muons reconstruct toward the top of the detector and saturate energy reconstruction, and hence lie do not contribute to the ROI.

decay β / neutron) are efficiently rejected from analysis by applying a 20 s veto window after each muon.

Thus, to quantify the muon-induced background, the relevant quantity is the muon tagging efficiency. Due to changes in the electronics in transition from SNO to SNO+, and the nature of the timing and amount of light produced in the detector, the muon tagging criteria must be updated from that employed in Chapter 4. Optimization of general-purpose selection criteria is ongoing, and in this work we employ a conservative nominal tagging scheme of 5 or more OWL hits, which qualifies that a reasonable amount of light was present in the external cavity water. Preliminary investigations of the tagging efficiency of this simple criteria yield a value of roughly 95-97%, with the remaining muons eluding tagging due to low-probability trajectories through the cavity volume and fluctuations in energy deposition in the associated water, which conspire to circumvent the OWL threshold.

The detector response and reconstructed values of cosmic-ray muons were investigated using Monte Carlo simulations, to determine their potential contribution to the ROI defined in Section 5.5. Distributions of the reconstructed position and energy of muons with a primary energy spectrum similar to that described in Section 4.3, and which reconstruct inside of the AV, are shown in Figure 5.4, with analogous distributions for ROI electrons overlaid for comparison. Because muons enter the detector via the top of the PSUP, the first light detected is always at the top of the detector, and consequently they reconstruct (under the point-deposition hypothesis) toward the top of the detector. This translates to a minimal radial position of ~ 4 m, comfortably outside of the 3.3 m fiducial volume. Additionally, the passage of muons through scintillator generates enough light to saturate the detector, leading to a lower bound on the reconstructed energy of ~ 70 MeV, well above the analysis endpoint of 40 MeV.

With these considerations in mind, we extend the muon tagging to the logical-or of the following criteria:

1. 5 or more OWL hits

2. 60 MeV or larger reconstructed energy

The latter criteria is conservative in that it allows a reasonable tolerance for deficiencies in modeling of the response to muons, and results only in livetime losses due to atmospheric neutrino interactions, as discussed in Section 5.6.3. In a Monte Carlo data set consisting of roughly three times the detector livetime utilized in this analysis, the expected contribution of background events from cosmic-ray muons prediction is 0. This background is thus considered negligible, which was verified by verifying that the limits reported are robust to the inclusion of an associated background term uniform in energy with a conservative magnitude.

5.6.2 Accidental coincidences

Coincidence events can be formed by the random coincidence of uncorrelated prompt-like and delayed-like events. The rate of such “accidental coincidences” is often quantified by applying prompt-like and delayed-like selection criteria to the dataset under consideration without any coincidence requirement, and calculating the expected accidental rate R_a as

$$R_a = R_p R_d w, \quad (5.10)$$

where R_p and R_d are the observed prompt-like and delayed-like rates, respectively, and w is the length of the coincidence selection window (here, 990 μs). Such a scheme is only valid in the limit that the uncorrelated rates dominate over the rate of true coincidences, and otherwise is an overestimate. Nevertheless, using this figure as an upper bound, we find the expected accidental contribution for the dataset under consideration to be negligible. This is driven by a prompt-like rate of 4.5×10^{-7} Hz, which, coupled with a delayed-like rate of 1.4×10^{-2} Hz, yields an expected contribution of less than 10^{-4} events across the full dataset.

5.6.3 Atmospheric neutrino interactions

As discussed in Section 5.6.1, interactions of cosmic rays in the atmosphere result in a flux of high energy muons, which are the daughters of pion decay. A second product of these decays are muon-neutrinos. The decay of cosmic-ray muons into electrons also results in a flux of electron-neutrinos. Note that because muon decay itself results in the direct production of muon-type neutrinos, a single decay chain initiated by a pion produces twice as many muon-neutrinos as electron-type neutrinos. This rule-of-thumb serves as a first-order approximation, but is experimentally verified [179]. These so-called “atmospheric neutrinos” are produced over a broad energy spectrum, up to and above the TeV scale, and constitute the largest background in the search for astrophysical antineutrinos.

Estimates of the atmospheric neutrino flux at given coordinates at the Earth’s surface are generally made by means of simulation, which use balloon-borne magnetic spectrometer cosmic ray flux measurements as input. We follow recent treatments of atmospheric neutrinos [146, 180] at SNO by utilizing two distinct flux calculations: between 100 MeV and 10 GeV, the 2004 Bartol tables [181] tabulate the flux of electron- and muon-neutrinos as a function

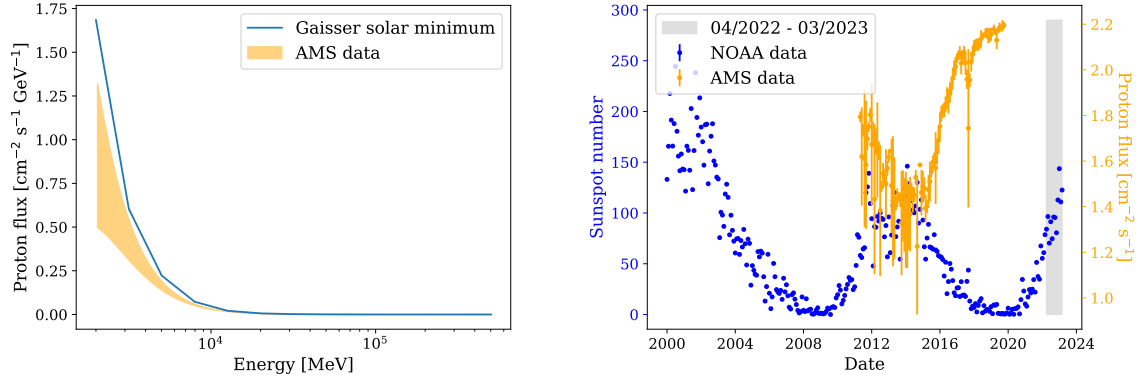


Figure 5.5: (Left) Primary cosmic ray energy spectrum used in solar minimum simulations of atmospheric neutrino production, and spread of measured cosmic proton flux values during data-taking. (Right) Sunspot number and integrated cosmic proton flux over the last decade, with data-taking period shaded. Simulated flux values are taken from [185], sunspot number records from [184], and proton flux measurements from [183].

of energy and zenith angle; between 10 MeV and 100 MeV, the exclusive electron-type flux is tabulated as a function of energy from the results of FLUKA simulations performed by Battistoni et al [182]¹. In the low energy region, between 10 MeV and 100 MeV, we approximate the muon-(anti)neutrino flux as twice the electron-(anti)neutrino flux, and the angular profile is assumed to be that calculated by Bartol et al. at 100 MeV.

The flux of cosmic rays and, hence, the rate of atmospheric neutrino production, modulates out-of-phase with the 11-year solar magnetic cycle, as solar wind intercepts cosmic rays en route to the Earth. The neutrino fluxes described above were produced using the cosmic ray flux at solar minimum, whereas the present data set was collected during a period of relatively high solar activity, comparable to the last solar maximum (see the right panel of Figure 5.5). To account for this, we reference daily measurements of the cosmic proton flux, which accounts for $\sim 80\%$ of the total cosmic ray flux by the Alpha Magnetic Spectrometer (AMS) collaboration [183], and tabulations of solar activity indicators from the National Oceanic and Atmospheric Administration (NOAA) [184]. The cosmic ray spectrum used in the Bartol simulation is compared with the spread of values measured by AMS between 2011 and 2019 in the left panel of Figure 5.5.

Ideally, one would convolve the appropriate cosmic ray spectrum with the cosmic-ray-energy/neutrino-energy correlation matrix inferred from simulation, to approximate the correct atmospheric neutrino spectrum, but no such correlation matrix is available in the literature. We thus scale the flux normalization to the appropriate integrated flux as measured by AMS. The appropriate value is determined by correlating the integrated flux with the avail-

¹The authors of [182] kindly produced simulations for SNO at the collaboration's request, although they were not included in the initial publication.

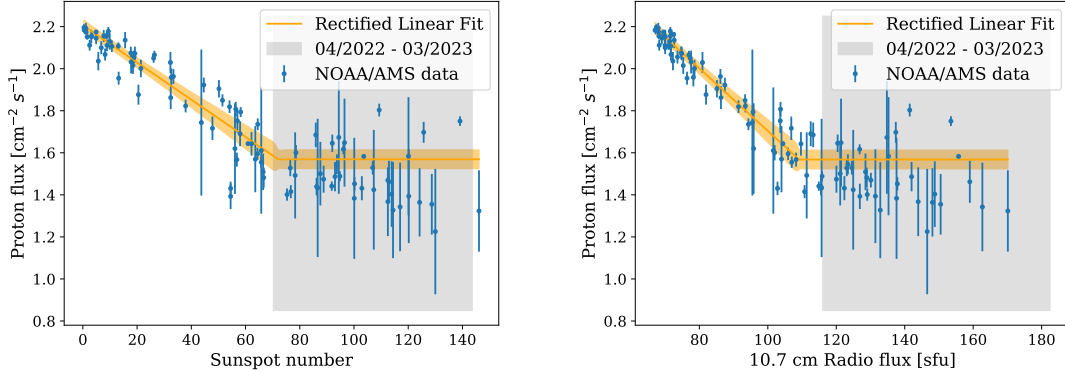


Figure 5.6: (Left) Correlation between observed sunspot number and integrated cosmic proton flux, with fit of rectified linear model overlaid and data-taking period shaded. (Right) Same, for observed 10.7 cm solar flux data. Uncertainty bands are scaled by a factor of 10 for visualization. Sunspot number and solar flux records are taken from [184], and proton flux measurements from [183].

able solar indicators, namely the sunspot number and flux of the 10.7 cm radio line. These correlations, and associated fits with a rectified linear function, are shown in Figure 5.6. The use of a rectified linear function accounts for the correlation at low solar activity and apparent plateau at high solar activity. The appropriate flux scalings are consistent between the two solar indicators, and yield a scaling of $(53.2 \pm 0.1)\%$.

With the normalization established, the surface fluxes are translated to underground fluxes via the standard neutrino oscillation formulae, i.e. Equation 2.10. Here we follow the method developed and described in [186]. In brief, a toy Monte Carlo is run which samples the flux of each (anti)neutrino flavor according to the available surface flux tables, with the selected angle interpreted as a relative latitude on surface; the sample is then weighted according to the transition probabilities according to the distance between the surface coordinates and SNOLAB:

$$\phi_{\beta}^{\text{und.}}(E, \theta) = \sum_{\text{flavors } \alpha} \phi_{\alpha}^{\text{surf.}}(E, \theta) P(\alpha \rightarrow \beta; E, \theta). \quad (5.11)$$

The atmospheric neutrino fluxes, both at surface and underground, are shown in Figure 5.7. The discontinuity at 100 MeV originates from a discrepancy in high- and low-energy tabulations of the atmospheric flux in the ~ 100 MeV region, which is well-within uncertainty on the flux normalization.

Final states of atmospheric neutrino interactions within the PSUP volume are sampled using the version 3.02.02 of the **GENIE** event generator [187], and the detector response to these final states is simulated using **RAT**. The event selection criteria of Section 5.5 is then applied. The resulting prompt energy spectrum of selected events is shown in Figure 5.8. The nominal total contribution of atmospheric neutrino interactions to the ROI is 7.5 events

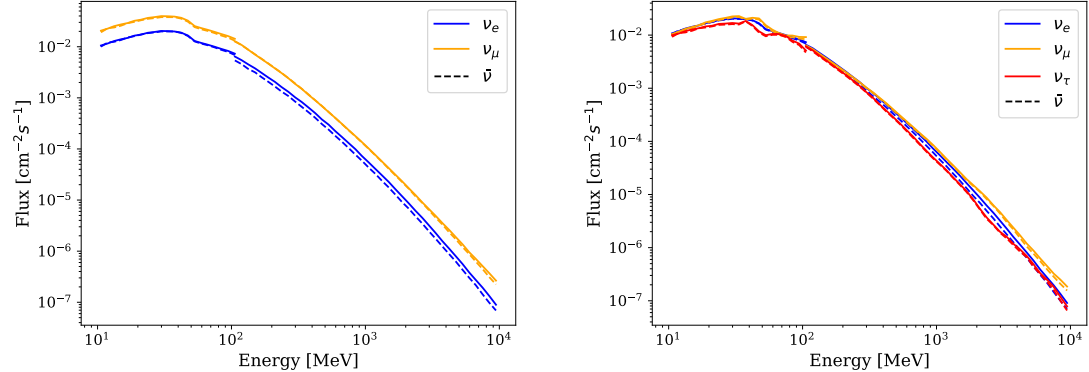


Figure 5.7: Nominal atmospheric neutrino fluxes at surface (left) and underground (right). The discontinuity in muon- and tau-neutrino oscillated fluxes originates from the discontinuity in muon-type oscillated fluxes at the transition between Bartol and Battistoni flux tables.

per year, translating to 3.3 events for the present data set. After accounting for systematic uncertainties on the interaction rate, as discussed in Section 5.7.1, the expected rate of atmospheric neutrino events is 3.2 events, with the difference well-within the systematic uncertainty.

5.7 Statistical analysis

5.7.1 Systematic uncertainties

The dominant systematic uncertainty is the number of atmospheric interactions in the ROI, and is comprised of two components: an uncertainty on the surface flux normalization, and uncertainties on the interaction cross sections and final states. The flux uncertainty is 20 – 25% in the energy range relevant to this work [188], driven by uncertainty in modeling hadronic interactions during showering. We thus conservatively include a 25% uncertainty, independent of energy. A small additional uncertainty of 0.1% is contributed by the uncertainty on the cosmic ray primary flux scaling due to solar modulation, as discussed in Section 5.6.3, though this neglects shape-related uncertainty arising from the unknown cosmic-ray/atmospheric-neutrino energy correlation matrix.

Uncertainty originating from cross sections and final-state generation is quantified using the **GENIE** event reweighting framework, which allows for the propagation of systematic uncertainties on **GENIE** model inputs through any analysis using **GENIE** interaction products. For each atmospheric (anti)neutrino flavor, an ensemble of one hundred-thousand prompt energy spectra is generated by sampling 75 **GENIE** input parameters, listed in Appendix A. The parameters are sampled normally and uncorrelated, within $\pm 3\sigma$ of their nominal values.

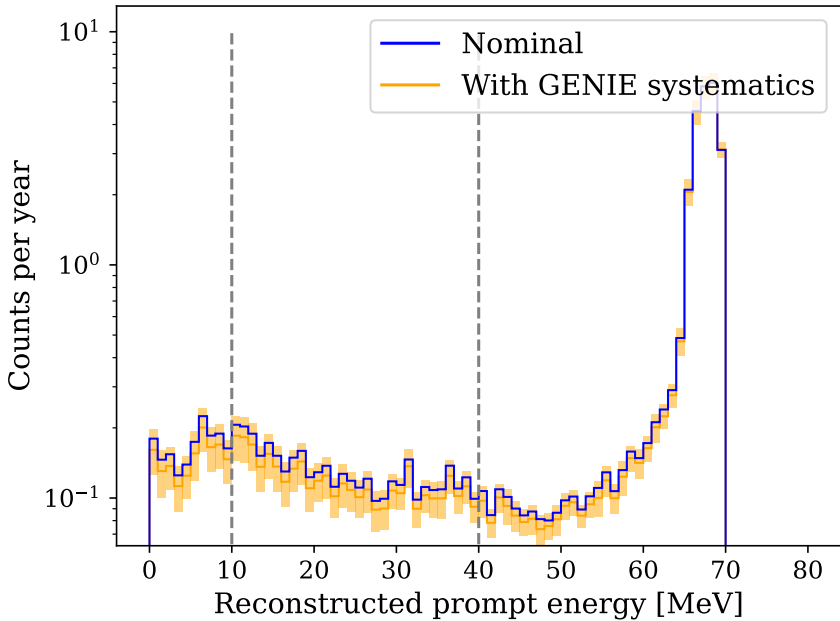


Figure 5.8: Gross prompt energy spectra, both nominal and after propagating uncertainties on GENIE inputs, of atmospheric neutrino interactions. The colored bands denote the systematic uncertainty due to interaction modeling, and the grey dashed lines demarcate the analysis ROI.

The resulting uncertainty on the expected detected spectrum is approximately 15-20% across the ROI, and is reflected in the uncertainty bands shown in Figure 5.8. The uncertainty on the detector response is taken as 4.2%, uniform across energy, derived from the precision of the simulations from which it was quantified.

5.7.2 Limit-setting routine

To set limits both on the astrophysical flux, a Markov-Chain-Monte-Carlo (MCMC), implemented in PyMC [189], is used to approximate posterior distributions by generating one million samples thereof, assuming a uniform prior on the flux in each energy bin. The model convolves the candidate input astrophysical spectrum with the detector response via the detector response matrix, and then adds the atmospheric background contribution, sampled with the covariance detailed in Appendix A. 90% credible limits are then computed following the Feldman-Cousins method [190], which here amounts to integrating the posterior up to 90% probability mass.

Model-independent limits on the astrophysical flux are also computed using a simpler method common in the literature, wherein limits are first placed on the number of observed events in each bin in reconstructed energy, after which the cross-section, exposure, and

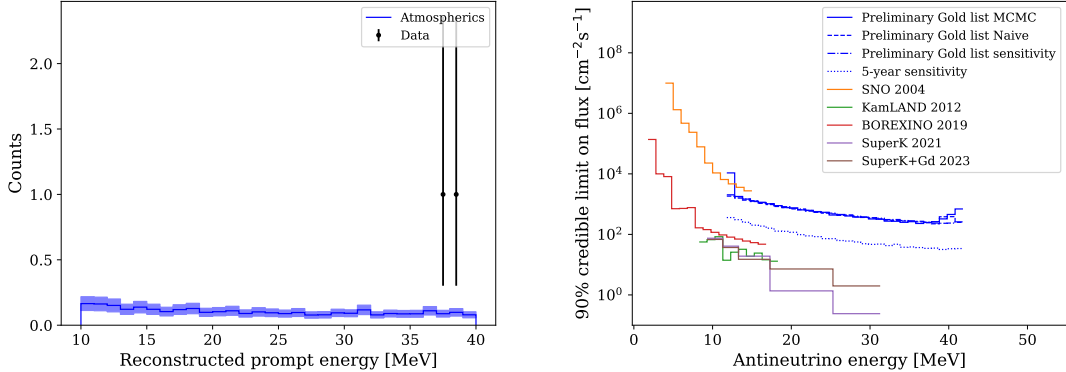


Figure 5.9: (Left) Observed prompt event energy spectrum, and expected atmospheric neutrino background, over 149.5 days of livetime. The shaded band denotes the systematic uncertainty on the background prediction. (Right) Corresponding model-independent limits on the flux of astrophysical $\bar{\nu}_e$. Existing limits from other detectors are overlaid [114–118], along with sensitivity projections for 5 years of exposure.

livetime are accounted for. We present these results to facilitate comparison with existing limits, but note that this method fails to properly account for the lower detection efficiency at the ROI boundaries, where events can misreconstruct out of the event selection window, and does not naturally account for uncertainties on other quantities, in particular the large uncertainty on the normalization of the atmospheric neutrino background.

5.8 Results

The total livetime remaining after applying the cosmic muon veto criteria defined in Section 5.5 is approximately 149.2 days. The observed prompt event energy spectrum after applying IBD event selection and the corresponding model-independent limit on the astrophysical $\bar{\nu}_e$ flux are shown in Figure 5.9. Also shown are existing limits from other detectors and the projected sensitivity, defined as the median limit in an ensemble of signal-free trials, for 5 years of livetime. Two candidate events are observed in the ROI, with an expectation of 3.2 background events. Posterior distributions for the excess number of IBD interactions in each energy bin are available in Appendix B.

5.9 Interpretation and discussion

No excess of IBD events, and hence of electron antineutrinos, is observed in the 155.2 days of data analyzed in this work, leading to model-independent astrophysical flux limits on the order of $10^2 - 10^3 \text{ cm}^{-2}\text{s}^{-1}\text{MeV}^{-1}$, dependent on energy. The two observed events are separated by approximately 1.3 MeV, an interesting spectral feature which is observed in

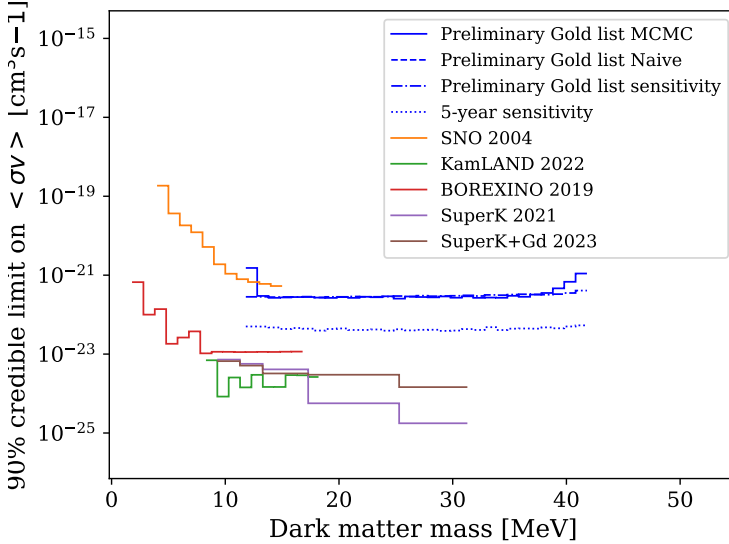


Figure 5.10: Limits on light dark matter thermally-averaged annihilation cross section and sensitivity projections for 5 years of data-taking, with limits derived from existing flux from SNO, KamLAND, Borexino, Super-Kamiokande, and Super-Kamiokande+Gd overlaid [114–118].

a higher energy than that studied in previous experiments. The relevant p -value — that is, the probability for two events sampled from the expected background spectrum to be separated by no greater than 1.3 MeV — is 8.8%. A mature interpretation of this and any other spectral features, however, must be deferred to an updated analysis performed on a larger data set.

The model-independent flux limits can be easily converted to limits on the thermally-averaged self-annihilation cross section of light dark matter. As discussed in Section 2.4 and Section 3.4, the spectral signature of neutrinos from dark matter annihilation, local to the galaxy, is monoenergetic below the muon mass, and hence we can limit the annihilation cross section as

$$\langle\sigma v\rangle = \frac{6m_\chi^2}{J_{\text{avg}}R_{\text{sc}}\rho_{\text{DM}}^2}\phi \quad (5.12)$$

where $m_\chi = E_\nu$ is the dark matter mass, $J_{\text{avg}} = 5.0$ is the canonical angular-averaged intensity, $R_{\text{sc}} = 8.5$ kpc is the galactic dark matter halo scale, and $\rho_{\text{DM}} = 223.2$ MeV/cm 3 is the local dark matter density, and $\phi = \phi(E_\nu)$ is the upper limit on the astrophysical flux. Limits from the current analysis and sensitivity projections for 5 years of data-taking are shown in Figure 5.10 with comparison to existing limit derived from the flux limits of SNO, Borexino, KamLAND, Super-Kamiokande, and Super-Kamiokande+Gd.

A feature unique to both light dark matter annihilation and black hole evaporative signatures is the opportunity for a correlated analysis: searches for a spectrally-correlated excess in

both neutrino and antineutrino event samples are at increased sensitivity beyond that achievable using e.g. an IBD-like event sample alone. Finally, it should be emphasized that the model-independent limits shown in Section 5.8 were established using an ultra-conservative fiducial volume — roughly one sixth of the full scintillator mass. With improvements to energy reconstruction techniques, an extended fiducial volume can be utilized to achieve limits comparable to the current-best from KamLAND and Super-Kamiokande+Gd with 5 years of data. Going further, the external water volume can be utilized to achieve a dramatic increase in target mass, a factor of ~ 10 , albeit with a lower signal efficiency [191]. Such an endeavor would require improvements to muon tagging and reconstruction to more efficiently reject this background in an extended fiducial volume, but would likely result in world-leading limits after 5 years of data-taking.

Chapter 6

R&D toward Hybrid Detectors

6.1 Introduction

As described in Section 3.3, there are three principal avenues of ongoing lab-scale development to enable hybrid Cherenkov/scintillation neutrino detection: i) the synthesis of novel materials in which the identification of Cherenkov photons is an easier task, ii) the realization of high-time-resolution photodetectors, and iii) the implementation of spectral photon sorting devices. These axes constitute a basis for a priori hybrid detection, but a conventional detector employing hybrid reconstruction techniques would be further aided by the addition of any one of these technologies.

We present here measurements relevant to the first principal direction, namely properties of a material known as water-based liquid scintillator (WbLS). The base solvent of the scintillator cocktail deployed in SNO+, and other experiments, LAB, is an organic compound similar to mineral oil. As such, its effective dilution in water was a novel chemical achievement [88], and results in an inexpensive liquid which scintillates with a relatively low, but tuneable, light yield, and has optical properties near the desirable limit of pure water. In order to evaluate the suitability of WbLS for deployment in a future hybrid detector, the properties of its scintillation light must be measured and characterized. The light yield and long time-scale emission profile in response to electrons, and emission spectrum have been previously measured [192, 193], but many properties remain unknown. We present here benchtop-scale measurements of: the light yield of 5% WbLS in response to protons; the early-time emission time profiles in response to electrons with a high-time-precision photodetector of 1%, 5%, and 10% WbLS; and the emission time profiles in response to α particles of WbLS and LAB+PPO samples.

6.2 Proton light yield

6.2.1 Introduction

While electrons are the principal candidate for detecting low-energy neutrino interactions in scintillators, protons play important roles of their own, both as signal and background. As an example of the former, the cross section of elastic scattering of neutrinos off protons is flavor-independent and, thus, offers a channel for undistorted flavor-inclusive spectral measurements, which is acknowledged as an important observation for neutrinos emitted from supernovae [194–196]. As to the latter, consider the following coincidence signal, which can mimic the signal of IBD reactions used to detect antineutrinos: a ~ 10 MeV external neutron which enters the detector volume and scatters off protons as it moderates to thermal energies and eventually captures. The scintillation light from the primary recoil protons is at MeV-scale-positron-equivalent light levels, and thus presents as a background to, e.g., reactor neutrino measurements. Because the fast neutron energy spectrum will generally differ from an expected IBD energy spectrum, this can be accounted for with spectral analysis if the proton light yield is known.

The proton light yield of LAB+PPO has been measured previously, at the Physikalisch-Technische Bundesanstalt (PTB) [196], but this is the first measurement of WbLS sample, which was made using a 5% scintillator-loaded sample. The proton light is here measured in collaboration with the Bay Area Neutron Group (BANG) using a double-time-of-flight technique [197, 198] at the 88-Inch Cyclotron at Lawrence Berkeley National Laboratory (LBNL) [199]. The results of the LAB+PPO measurement are then compared to those of the PTB measurement.

6.2.2 Experimental setup

A broad spectrum neutron beam was produced by a 33-MeV $^2\text{H}^+$ beam incident on a 3-mm-thick Be target. The LAB+PPO and WbLS samples to be characterized were placed, independently, in the focus of the beam, roughly 7 m downstream of the breakup target. Eleven auxiliary detectors, filled with EJ-309 [200], an organic liquid scintillator with pulse-shape-discrimination (PSD) capabilities, were positioned out-of-beam to detect forward-scattered neutrons from the target scintillator, each at a unique scattering angle. The geometry of the experimental setup is visualized in Figure 6.1. The relevant neutron-trajectory lengths and scattering angles for each measurement are listed in Table 6.1. The detector coordinates defining the geometry were established using a laser-based distance meter, and are each assigned a conservative 1 cm uncertainty. There is one exception in the z -position of the breakup target, which is known to 5 mm.

Further details of the experimental hall, Be target, and auxiliary detector shielding can be found in [201]. The neutron beam has a broad energy distribution dominated by breakup neutrons centered at ~ 15 MeV, which extends from ~ 0 to 37.4 MeV. The tail of the distribution is due mainly to compound and pre-equilibrium reactions, and the endpoint is defined by sum of the the incident deuteron energy and the reaction Q-value. Further discussion and measurements of comparable beams can be found in [202–205]. For each sample, data was

Channel	LAB+PPO		WbLS	
	Distance [cm]	Scattering angle [°]	Distance [cm]	Scattering angle [°]
Breakup to target	721.3 ± 1.4	–	716.6 ± 1.4	–
Target to	2	133.8 ± 1.8	80.0 ± 1.9	134.2 ± 1.8
	3	131.7 ± 2.1	65.0 ± 2.0	133.2 ± 2.1
	4	137.6 ± 2.2	52.2 ± 2.0	140.0 ± 2.1
	5	148.1 ± 2.2	41.9 ± 1.9	151.1 ± 2.1
	6	165.4 ± 2.1	32.3 ± 1.7	168.9 ± 2.0
	7	184.9 ± 2.0	25.1 ± 1.6	188.7 ± 1.9
	9	133.0 ± 1.7	78.1 ± 1.9	134.1 ± 1.6
	12	132.7 ± 1.9	61.4 ± 2.0	135.1 ± 1.9
	13	139.6 ± 2.0	48.7 ± 2.0	142.7 ± 1.9
	14	156.2 ± 2.0	35.9 ± 1.8	160.0 ± 1.9
	15	183.7 ± 1.8	24.4 ± 1.6	187.9 ± 1.8

Table 6.1: Distances between various experimental apparatus, and nominal scattering angles associated with each auxiliary detector.

acquired over a period of approximately 11 hours of constant beam running with a current of approximately 55 nA. The period between beam extractions was approximately 111 ns.

The LAB+PPO and WbLS target scintillators were contained in cylindrical quartz crucibles, of dimensions 50 mm diameter by 50 mm tall and 1 mm in wall thickness. A quartz disk of the same thickness was used to seal the open face using a two-part epoxy. The side wall and sealed face of the cells were wrapped in no less than 10 layers of polytetrafluoroethylene (PTFE) tape to improve internal reflectivity, and thus light collection. The remaining transparent face was optically coupled to a Hamamatsu H1949-51 photomultiplier tube (PMT) using EJ-550 silicone grease. The sealed cells, both before and after wrapping with PTFE, are shown in Figure 6.2.

The scintillator cells of the auxiliary detectors were right cylinders of diameter and height 50.8 mm, constructed of a thin aluminum housing and filled with EJ-309 [200], and were each coupled to a PMT via a borosilicate glass window and EJ-550 silicone grease. All PMTs used in these measurements were obtained from Hamamatsu Photonics (either Type No. 1949-50 or 1949-51), and were negatively biased using either a CAEN R1470ET or CAEN NDT1470 power supply.

The data acquisition system triggered on a coincidence between the target PMT and any of the auxiliary detectors within a 400 ns coincidence window. Upon triggering, digital waveforms of a total length of 800 ns from all channels, as well as a waveform digitizing a sinusoidal RF control signal provided by cyclotron operations, were recorded using a CAEN V1730 500 MS/s digitizer. The scintillator signal timing was determined using the CAEN digital constant fraction discrimination algorithm, with a 75% fraction and a 4 ns delay. The timing pickoff for the cyclotron RF signal was determined using leading-edge discrimination.

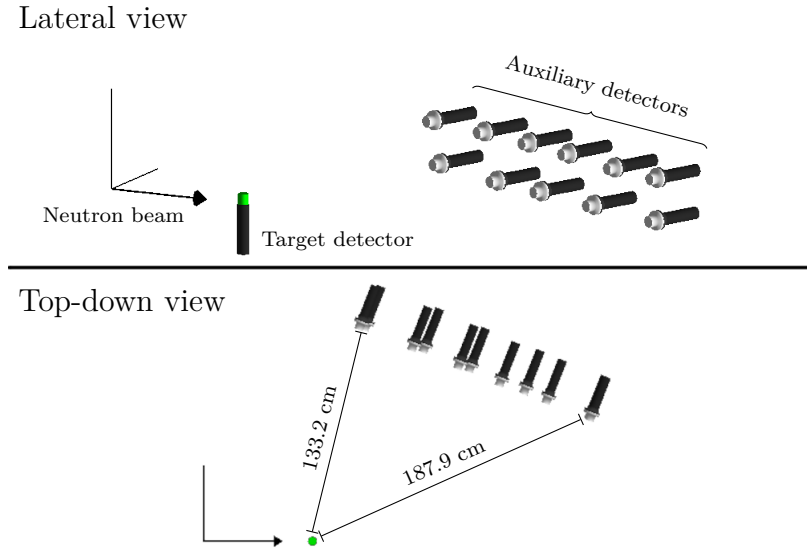


Figure 6.1: Experimental setup for proton light yield measurements. The neutron beam travels along the axis designated with an arrow to the target scintillator cell, shown in green. Eleven auxiliary detectors are positioned at forward scattering angles with respect to the incoming neutron beam. The shortest and longest target-to-auxiliary trajectories are shown, labeled as in the configuration for WbLS data-taking. The upper face and side walls of the target cell, highlighted in green, was wrapped with Teflon tape; the lower face was unwrapped and optically coupled to a PMT. Top and bottom panels show the experimental geometry from lateral and from-above vantage points.



Figure 6.2: (Left) Sealed target cell containing LAB+PPO before wrapping with PTFE tape. (Right) Both target cells after wrapping in PTFE.

6.2.3 Analysis methods

Waveforms from the target and auxiliary detectors were integrated to compute the charge collected in the associated PMT in units of summed analog-to-digital-converter readings (adc), after correcting for nonlinearity of the target PMT as described in Section 6.2.4. Waveforms in the target detectors were integrated for 140 ns, to ensure collection of $\geq 95\%$ of the observed charge. For the auxiliary detectors, waveforms were integrated for 300 ns, and a PSD-metric was obtained by calculating the ratio of the charge of the prompt region corresponding to the first 30 ns of the waveform, to the delayed region between 30 ns and 260 ns from the start of the waveform, providing good separation between γ -ray and neutron signals for high-charge producing events. For coincident events, the high-level observables are the charge and timing for the target and auxiliary detectors, a PSD-metric for the auxiliary detector, and a timestamp corresponding to the cyclotron RF signal. To measure the PLY as a function of energy, a conversion between charge in the target PMT and light produced by the sample must be established, γ and neutron interactions distinguished, and the energy deposited by neutron interactions reconstructed from the available timing and geometric information. The methods employed herein were originally introduced in [197, 198] and are further detailed below.

6.2.4 PMT linearity correction

A nonlinearity correction for the two PMTs coupled to the measurement samples was performed using the method of Friend et al. [206]. In brief, each PMT was placed in the view of two LEDs with peak wavelength 405 nm [207], which were flashed both independently and in coincidence, thus recording the PMT response to two independent fluxes, as well as the response to the summed flux. By repeating this procedure over a range of fluxes spanning the range of the digitizer used in this measurement, the deviation from linear operation was computed. A more detailed description of the methodology, and supplemental material showing the intermediate data quality, is available in Appendix C. The measured nonlinearities, interpreted as quartic polynomials, are shown in Figure 6.3 as a function of the true waveform voltage. The nonlinearity correction was applied on a sample-by-sample basis to waveforms collected during both reference charge calibration and neutron-beam running.

6.2.5 Reference charge calibration

To establish a measurement unit proportional to the number of scintillation photons, a reference charge is defined and used to calibrate all observed light levels. Specifically, the reference charge is that associated with a 477 keV electron, evaluated using the Compton edge of the 662 keV γ ray emitted following ^{137}Cs decay. Calibration data was collected using ^{137}Cs (662 keV γ) and ^{207}Bi (1.770 MeV γ) sealed sources, as well as a ^{24}Na (2.754 MeV γ) source created by beam-activation of a sample of natural aluminum, placed at a distance ≥ 10 cm from the center of each target scintillator cell. Because beam operation was required to

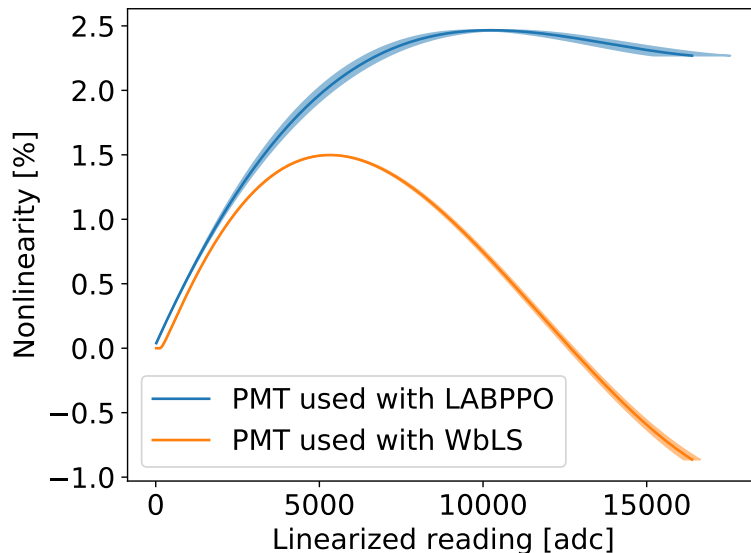


Figure 6.3: Deviation of output current from linear operation of the PMTs used in this measurement, as biased during runtime operations. The blue and orange curves correspond to the PMTs mounted to the LAB+PPO and WbLS samples, respectively. The abscissa spans the full scale range of the employed digitizer. The uncertainty bands are scaled up by a factor of 20 for visualization.

produce the sample of ^{24}Na , this source was not available before irradiation of the LAB+PPO sample. For each other source used with the LAB+PPO scintillator, and for all sources used with the WbLS, calibration data was taken both before and after irradiation. The ^{207}Bi and ^{24}Na sources were used to quantify systematic uncertainty on the reference charge, and facilitate comparisons with other measurements performed with different calibration schemes.

The charge associated with the Compton edge, the “Compton charge,” was determined by fitting a model to the measured calibration data. The model consists of an electron energy deposition spectrum following γ -ray interactions in the scintillator, generated using the **GEANT4** simulation toolkit [151], convolved with a three-parameter system resolution function [208], summed with a power-law background term [209]. A linear charge response was applied to the experimental data to convert the measured charge in units of summed adc, Q , to that associated with a given electron recoil energy, E . The energy-charge relation is an affine function, $E = aQ + b$, which assumes that the electron light yield is approximately linear in the energy range of interest, with b accounting for potential nonlinearity at lower energies, which manifest as $b \neq 0$. The minimization was performed using the SIMPLEX and MIGRAD algorithms from the ROOT Minuit2 package [210].

For each target scintillator, the measured calibration data before and after neutron irradiation were fit with the corresponding charge model independently, with the offset term, b , fixed to zero. The best-fit charge models are compared to pre-irradiation ^{137}Cs data in Fig-

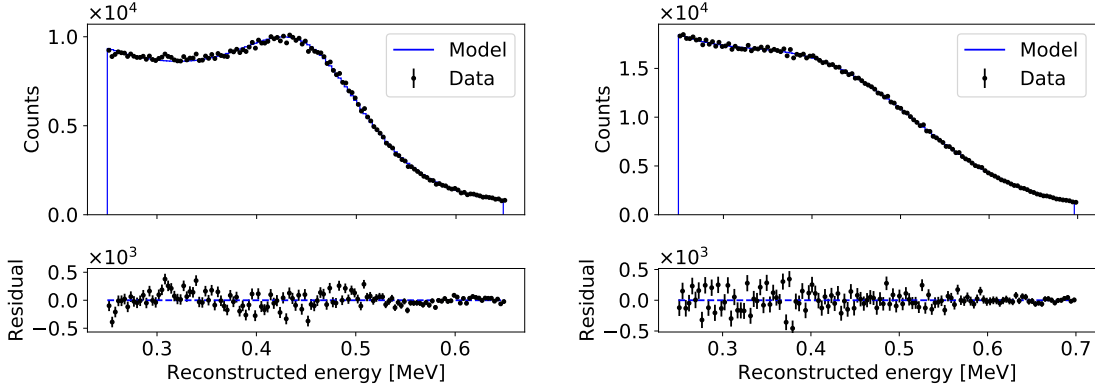


Figure 6.4: Best fit charge models compared to LAB+PPO (left) and WbLS (right) calibration data using a ^{137}Cs source. Best-fit model parameters courtesy of T. A. Laplace [211].

ure 6.4, and the resulting Compton charges are reported in Table 6.2 for each γ -ray source. Also reported is the statistical uncertainty, determined from the statistical uncertainty on a , and systematic uncertainty, which stems from the uncertainties in the background shape and electron light linearity, described in detail below.

The systematic uncertainty on the Compton charge is computed as the standard deviation of the Compton charge determined using all available combinations of pairs and triplets of calibration γ rays. Simultaneous fits to multiple Compton edges were performed without any constraint on b . This accounts for low-energy electron light nonlinearity, which at higher energies manifests as $b \neq 0$.

The gain stability of the target PMTs was investigated by chronologically partitioning the full beam dataset for each scintillator into 10 distinct datasets and analyzing each separately. No systematic trends or significant fluctuations were observed in the PLY results (see Appendix D). A strong ambient γ -ray background was present in the experimental hall due to activation from previous experiments, which biases the measured Compton charge. An associated systematic uncertainty was quantified by comparing the results of calibration before and after data collection, for which data were taken in different locations in the experimental hall. The difference in the ^{137}Cs Compton charge before and after irradiation is 1.8% and 1.5% for LAB+PPO and WbLS, respectively. Smaller differences were observed for the ^{207}Bi lines (0.1% and -0.3%) and the ^{24}Al data (0.6%), which are each in a higher energy region with lower background.

6.2.6 Auxiliary detector particle identification

The 11 auxiliary detectors located at forward scattering angles are filled with EJ-309 [200], a commercial liquid scintillator with established particle-identification (PID) capabilities achieved via PSD, in this case exploiting that γ -ray pulses have a higher ratio of prompt to delayed light relative to neutron pulses. For each auxiliary detector, a constraint on the total

Source	Compton edge energy [keV]	Compton charge [adc]	
		LAB+PPO	WbLS
^{137}Cs	477	$2525.4 \pm 1.3 \pm 21.2$	$2131.9 \pm 2.6 \pm 53.9$
^{207}Bi	1547	$8617.0 \pm 22.8 \pm 13.7$	$9741.2 \pm 82.8 \pm 94.7$
^{24}Na	2520	$14219.5 \pm 9.3 \pm 44.5$	$16795.5 \pm 15.7 \pm 71.5$

Table 6.2: Compton charges for both LAB+PPO and WbLS. The first uncertainty corresponds to the statistical uncertainty obtained from parameter fitting. The second uncertainty corresponds to the standard deviation of the Compton charge determined using simultaneous fits of multiple calibration spectra (i.e., all combinations of pairs and triplets). Best-fit model parameters courtesy of T. A. Laplace [211].

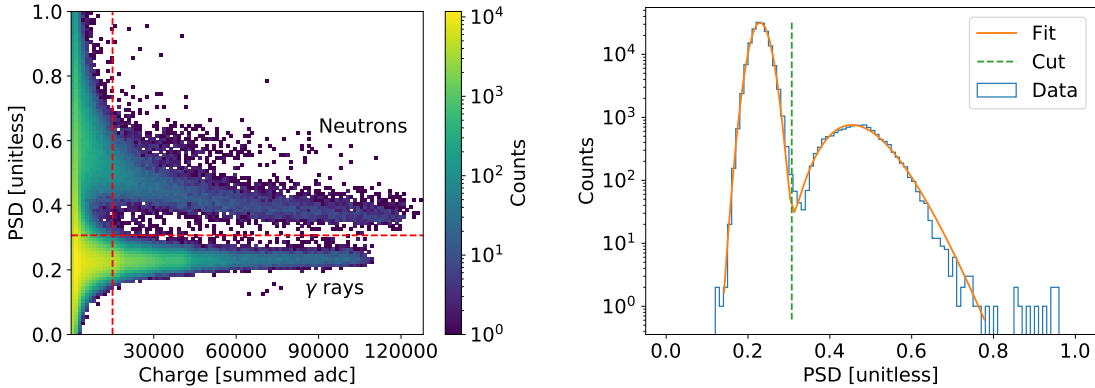


Figure 6.5: (Left) PSD metric vs charge collected in the PMT for beam events in an example auxiliary detector, showing separation between neutrons and γ -ray interactions at high charge. (Right) Projection onto the PSD-axis for events with charge above 15000adc, along with a normal-lognormal fit and subsequently optimized discrimination threshold.

charge collected is chosen to reject events in the low-charge region where the distributions of PSD values from pulses originating from neutron and γ -ray interactions overlap. These constraints are then imposed on beam data, after which the PSD metric, i.e., the ratio of delayed to prompt charge, is binned and fit with an empirical normal-plus-lognormal form, where the former term models the distribution of γ s and the latter neutrons. After performing the fit, an optimal PSD value for distinguishing between the two components is determined by minimizing the neutron contamination of γ selection, with the resultant purity above 98% for high-charge events. Visualizations of the PSD achieved in each detector, and normal-plus-lognormal fits used to optimize the PSD cut value, are available in Appendix D.

6.2.7 Time-of-flight calibration

In order to perform energy reconstruction, as described in Section 6.2.8, the time-of-flight (TOF) measurements must be calibrated to correct for cable and system delays; this cali-

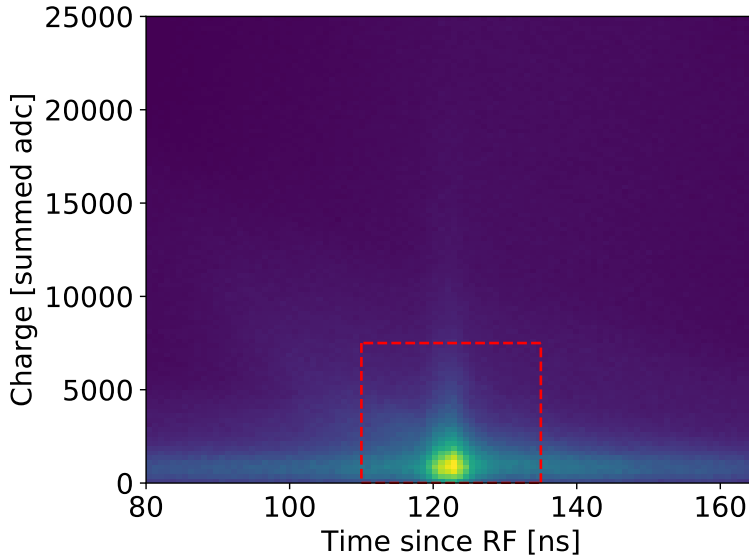


Figure 6.6: Charge collected in target PMT vs uncalibrated time since beam extraction during LAB+PPO data collection. Low energy beam-correlated γ rays appear as an isochronic population at low charge. The selection window is illustrated using the red dashed lines.

bration must be performed independently to establish time differences between interactions in the breakup target and the measurement cell (the “incoming TOF”), and from the measurement cell to each of the 11 auxiliary detectors (the “outgoing TOF”). In all cases, the calibration is achieved by selecting on beam-correlated γ rays and comparing the measured clock differences to the true TOF, given the known speed of light and measured detector positions. Selection of γ rays for the outgoing TOF is achieved by exploiting the PSD capabilities of EJ-309, as exemplified in Figure 6.5; γ -ray selection for the incoming TOF is achieved by selecting low-charge events in the target cell in a given time window, as exemplified in Figure 6.6. Efforts to apply PSD-based neutron/ γ -ray discrimination using the target scintillators were not fruitful, likely attributable to the dissolved oxygen content of the LAB+PPO sample, and the large water content of WbLS.

Example resultant distributions of measured γ -ray time differences are shown in Figure 6.7 and Figure 6.8 for the incoming and outgoing TOF, respectively. Each distribution is fit with an empirical function comprised of a Gaussian signal term and a polynomial background term. For the outgoing TOF, the background is modeled using a linear term and is dominated by uncorrelated γ rays uniformly distributed in time; a nonzero slope is allowed to account for a potential asymmetry around the γ -ray population introduced by beam-correlated contamination. For the incoming TOF, there is an additional background of beam-correlated neutrons from previous beam extractions, which have a nontrivial timing structure associated with their energy spectra, and thus a quadratic background term is allowed. The uncertainty in any measured neutron TOF, which propagates to uncertainty

in proton recoil energy, is determined both by the uncertainty on the mean of the Gaussian and its width. The width of the incoming TOF is dominated by the temporal profile of the beam pulse. All calibration uncertainties are significantly below 1%, and the best-fit standard deviations are provided in Table 6.3. The relatively poor quality of the fit to the incoming TOF data may be due to the relatively high background rate and shortcomings of the single-Gaussian signal model which, in reality, is modified by a number of effects, notably perturbations to the beam profile due to multiple-extraction from the main cyclotron ring. As neutron energy reconstruction is performed under the single beam extraction hypothesis, the relevant quantity for the incoming TOF calibration is the centroid of the γ -ray population, which is adequately quantified using the empirical model. A collection of the outgoing TOF calibrations for each auxiliary detector is available in Appendix D.

Channel	Standard deviation [ps]	
	LAB+PPO	WbLS
Incoming	2348.2	2608.8
Outgoing	406.6	811.1
2	431.7	914.1
3	448.5	727.9
4	430.3	943.4
5	399.9	896.3
6	420.7	899.5
7	502.8	1019.9
9	403.0	828.8
12	379.9	914.0
13	464.1	730.8
14	423.4	799.9
15		

Table 6.3: Standard deviations of best-fit Gaussian models for TOF distributions of all neutron trajectories, in both the LAB+PPO and WbLS datasets. Uncertainties on all Gaussian parameters are significantly below 1%.

6.2.8 Energy reconstruction

The neutron beam employed in this work has a broad energy distribution, as discussed in Section 6.2.2. While advantageous in allowing simultaneous measurement over a broad energy range, this necessitates event-wise energy reconstruction, which is achieved via two time-of-flight measurements, which translate to the neutron energy both before, and after, interacting with the target scintillator volume. The detection of the scattered neutron in an auxiliary detector establishes a scattering angle which, for single elastic scatters, kinematically overconstrains the system. For single scatters, the kinetic energy of the recoil proton, T_p , may be reconstructed using the incoming neutron energy, T_n , outgoing neutron energy

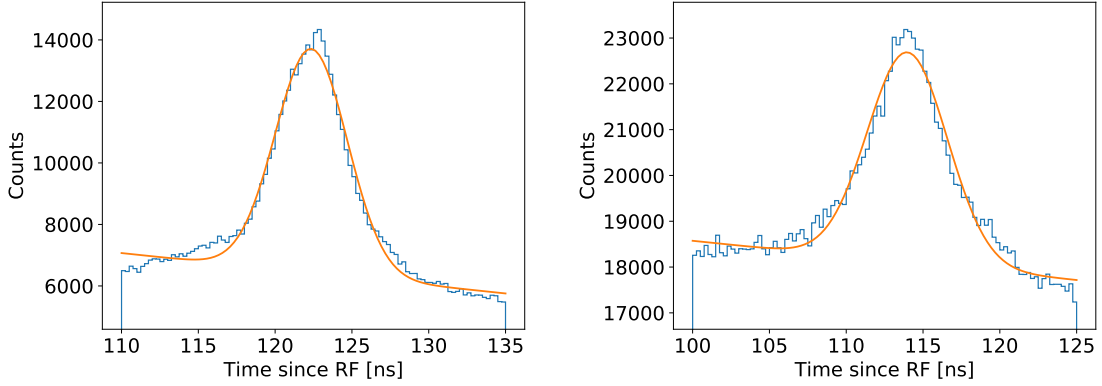


Figure 6.7: Distribution of measured time differences between the cyclotron RF signal and γ -ray events in the measurement sample, with empirical fit overlaid, during LAB+PPO (left) and WbLS (right) data collection.

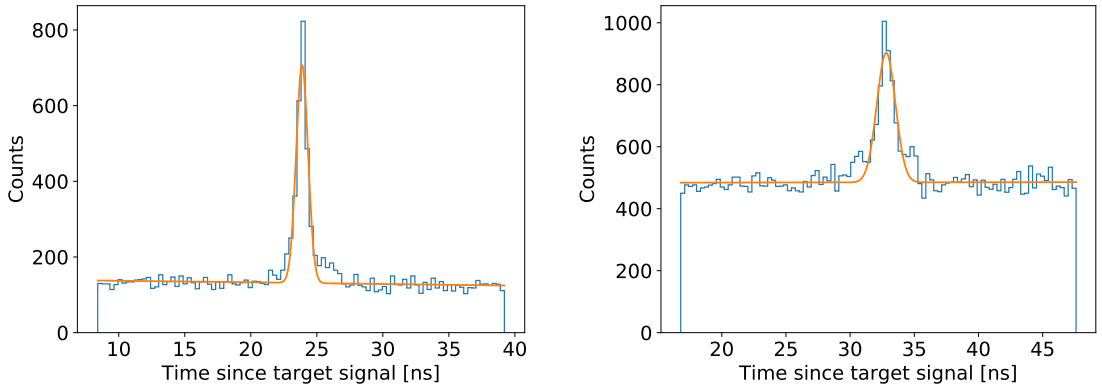


Figure 6.8: Distribution of measured time differences between γ -ray events in the measurement sample and a representative auxiliary detector, with empirical fit overlaid, during LAB+PPO (left) and WbLS (right) data collection. The data for each material is shown for channel 2, which is located at nominal scattering angles of 80° and 78° , respectively. Analogous figures for all auxiliary detectors are available in Appendix D.

T'_n , and scattering angle, θ , in three ways:

$$T_p = T_n \sin^2 \theta \quad (6.1)$$

$$= T'_n \tan^2 \theta \quad (6.2)$$

$$= T_n - T'_n. \quad (6.3)$$

Each method of reconstruction is subject to a different uncertainty, owing to the different uses of the fundamental timing and spatial observables:

$$\begin{aligned} \delta T_p^2 &= \left(\frac{\partial T_p}{\partial T_n} \delta T_n \right)^2 + \left(\frac{\partial T_p}{\partial T'_n} \delta T'_n \right)^2 + \left(\frac{\partial T_p}{\partial \theta} \delta \theta \right)^2 \\ &= \begin{cases} (\sin^2 \theta \delta T_n)^2 + (2T_n \sin \theta \delta \theta)^2 \\ (\tan^2 \theta \delta T'_n)^2 + (2T'_n \tan \theta \sec^2 \theta \delta \theta)^2 \\ (\sin^2 \theta \delta T_n)^2 + (\tan^2 \theta \delta T'_n)^2 \end{cases}. \end{aligned} \quad (6.4)$$

The uncertainty on the scattering angle associated with each auxiliar detector is listed in Table 6.1. The uncertainty on the neutron energy is driven by uncertainty on both its time-of-flight and distance traveled; for a neutron detected twice with separation and uncertainty in time t_0 , δt , and space x_0 , δx , the uncertainty on the kinetic energy

$$T = m \left(\frac{1}{\sqrt{1 - (x_0/t_0)^2}} - 1 \right) = m(\gamma - 1), \quad (6.5)$$

can be written:

$$\delta T^2 = \left(\frac{\partial T}{\partial x} \delta x \right)^2 + \left(\frac{\partial T}{\partial t} \delta t \right)^2, \quad (6.6)$$

$$\frac{\partial T}{\partial x} = m\gamma^3 \cdot \frac{x_0}{t_0^2}, \quad (6.7)$$

$$\frac{\partial T}{\partial t} = -m\gamma^3 \cdot \frac{x_0^2}{t_0^3}, \quad (6.8)$$

$$\frac{\delta T}{T} = \frac{\gamma^3}{\gamma - 1} \sqrt{\frac{x_0^2 \delta x^2}{t_0^4} + \frac{x_0^4 \delta t^2}{t_0^6}}, \quad (6.9)$$

where δt is taken as the width of the relevant TOF distribution (dominated by either the beam profile or electronics), and δx is taken as the uncertainty on the path length between detectors. This latter value is quantified conservatively, by combining a “center-to-center” uncertainty, found by propagating a 1 cm uncertainty on all measured cell coordinates, with an additional 3 cm uncertainty on the detection coordinates, which is slightly more than half of the longest dimension of any cell used in this measurement. The resulting uncertainties on

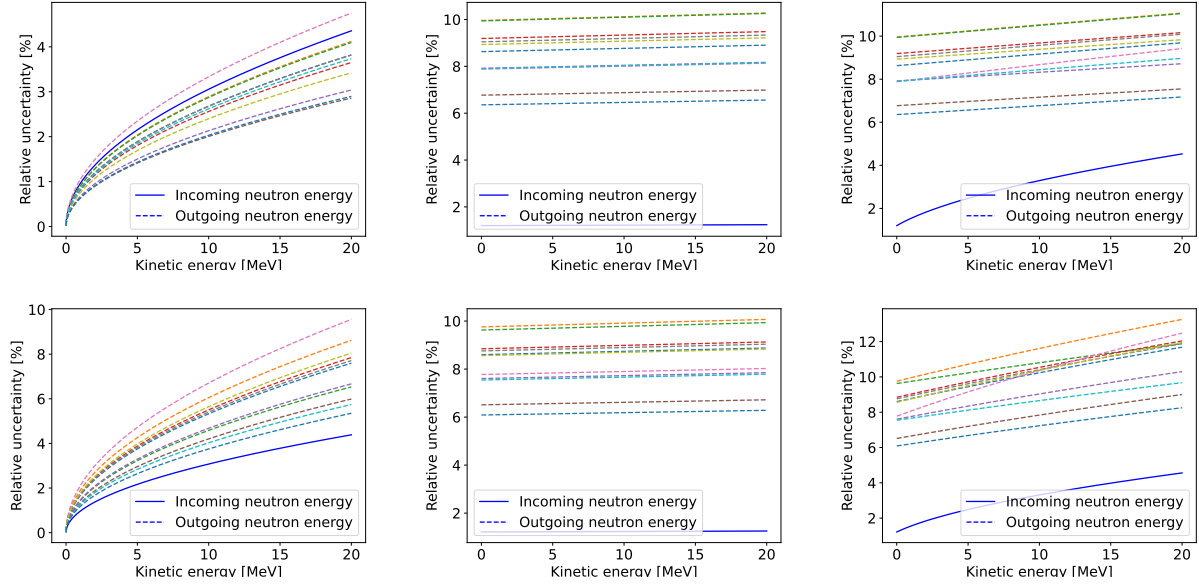


Figure 6.9: Uncertainty on neutron energy due to timing (left), cell coordinates (middle), and both sources (right), for LABPPO (top) and WbLS (bottom) data. Differently colored dashed lines refer to outgoing trajectories established using different auxiliary detectors.

both the incoming and outgoing neutron uncertainties and proton kinetic energy are shown, as functions of energy, in Figure 6.9. The difference in resolution between the two datasets is driven principally by the difference in the widths of measured γ time-of-flight distributions.

Due to its relatively long baseline, the incoming trajectory offers the most precise measurement of neutron energy. In both datasets, it admits a resolution of $\lesssim 5\%$, depending on the energy scale. Outgoing paths suffer from resolutions of several percent in LABPPO, and higher in WbLS.

The resolution on the proton recoil energy for the three different reconstruction methods in Equation 6.3, i.e. the expressions in Equation 6.4, are shown in Figure 6.10, Figure 6.11, and Figure 6.12, respectively. Reconstructing the recoil proton energy using the incident neutron energy and nominal scattering angle generally provides the best available resolution, owing to the relatively long neutron trajectory from production to target. The optimality is corroborated by simulations performed for similar experimental geometries, such as those described in [197].

There is ambiguity as to which beam extraction a given neutron detected in the target cell was produced by, associated with the relatively short cyclotron extraction period of ~ 111 ns. For comparison, the time for a 10 MeV neutron to travel from the production target to the target scintillator cell is approximately 165 ns. A measured incoming TOF can thus be interpreted only as measured modulo the cyclotron period. This ambiguity is resolved by kinematically reconstructing an expected incoming TOF using the outgoing TOF and the known scattering angle. If there is a multiple of the cyclotron period by which

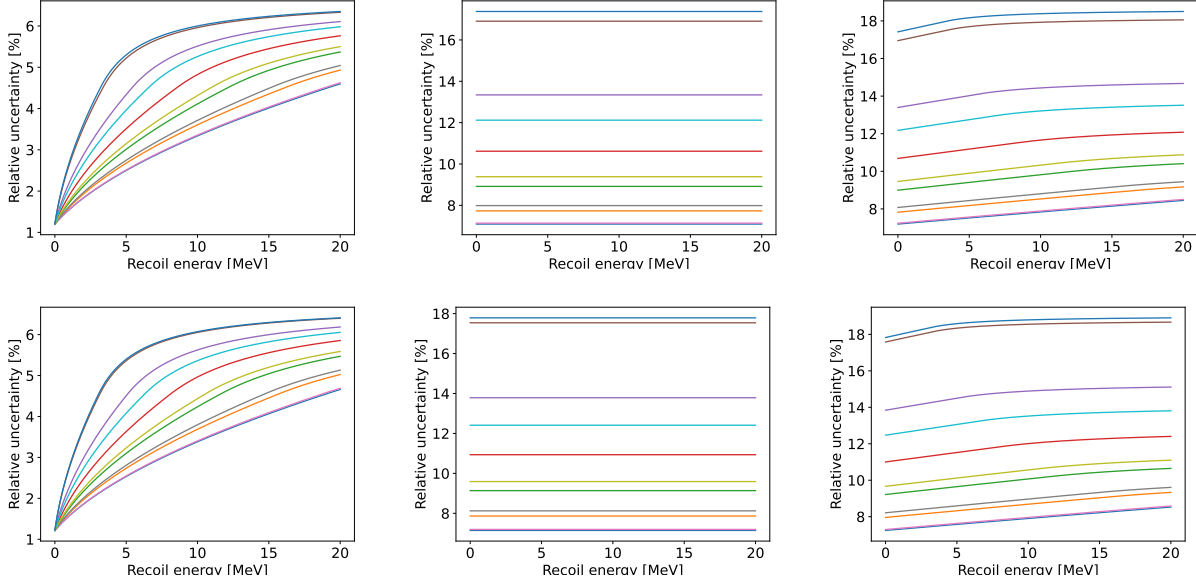


Figure 6.10: Uncertainty on proton energy calculated using the incoming neutron energy due to neutron energy (left), scattering angle (middle), and both sources (right), for LABPPO (top) and WbLS (bottom) data. Differently colored lines refer to trajectories established using different auxiliary detectors.

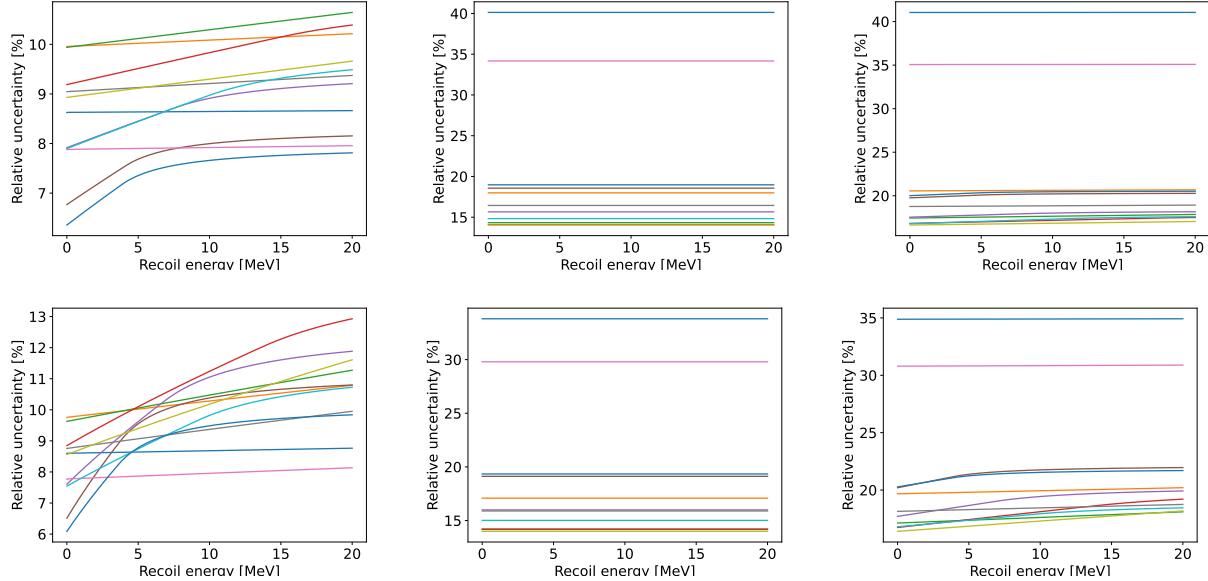


Figure 6.11: Uncertainty on proton energy calculated using the post-scatter neutron energy due to neutron energy (left), scattering angle (middle), and both sources (right), for LABPPO (top) and WbLS (bottom) data. Differently colored lines refer to trajectories established using different auxiliary detectors.

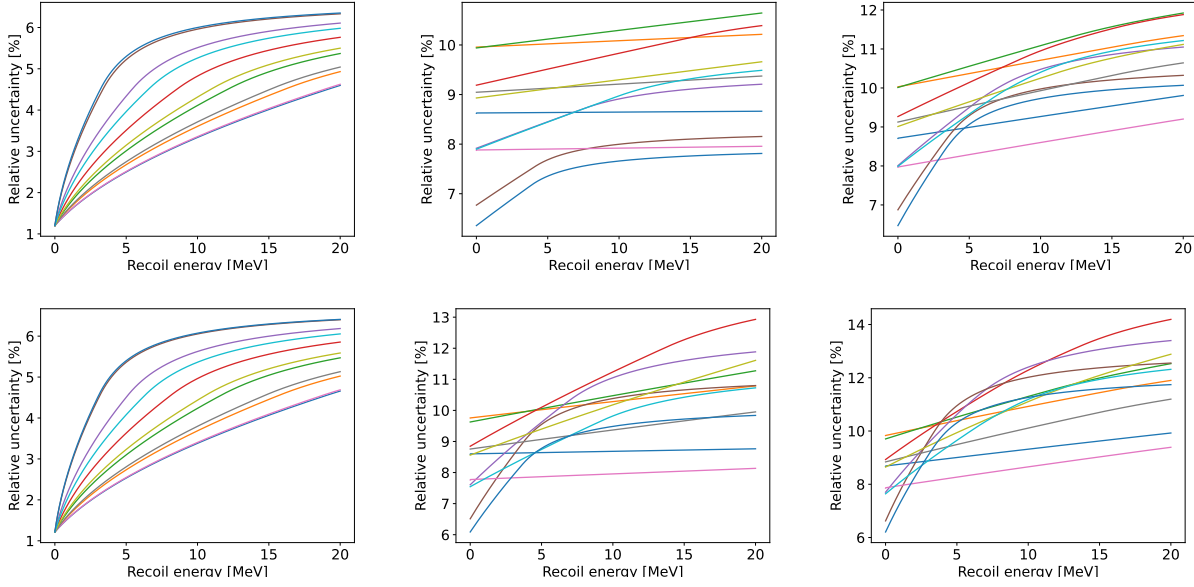


Figure 6.12: Uncertainty on proton energy calculated as the difference between pre- and post-scatter neutron energies due to the pre-scatter energy (left), post-scatter energy (middle), and both sources (right), for LABPPO (top) and WbLS (bottom) data. Differently colored lines refer to trajectories established using different auxiliary detectors.

the measured and reconstructed incoming TOFs agree to within less than 10 ns, the event is considered kinematically consistent and the ambiguity resolved. An example distribution showing the charge collected in the target PMT and the resolved incoming time-of-flight is shown in Figure 6.13.

6.2.9 Proton light yield extraction

Signal events are selected by applying the kinematic consistency criteria described in Section 6.2.8 and selecting neutron events via PID in each auxiliary detector. Two-dimensional distributions of charge and deposited energy for the selected events are shown in Figure 6.14. To extract the PLY relation, events are partitioned into energy bins, the widths of which are guided by the resolution of single-scatter energy reconstruction presented in Section 6.2.8. A representative charge is assigned to each energy bin by fitting its population of charge values with an empirical distribution comprised of a Gaussian signal term and two exponential background terms. The centroid of each Gaussian is the representative charge for a given energy bin and, relative to the reference charge defined in Section 6.2.5, establishes the scale of the relative proton light yield observed. Examples of such fits are shown in Figure 6.15; a full collection of per-bin charge fits for each energy bin is available in Appendix D.

The fit is formulated as an unbinned maximum likelihood fit, and performed using a two-step minimization wherein a global minimization based on a simulated-annealing technique

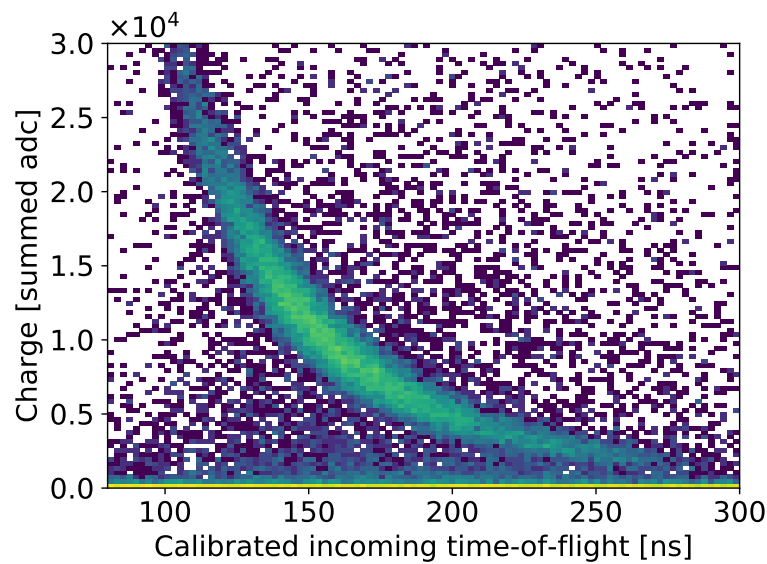


Figure 6.13: Charge collected in the target PMT vs incoming time-of-flight for neutron-like events in WbLS, which were tagged in channel 5.

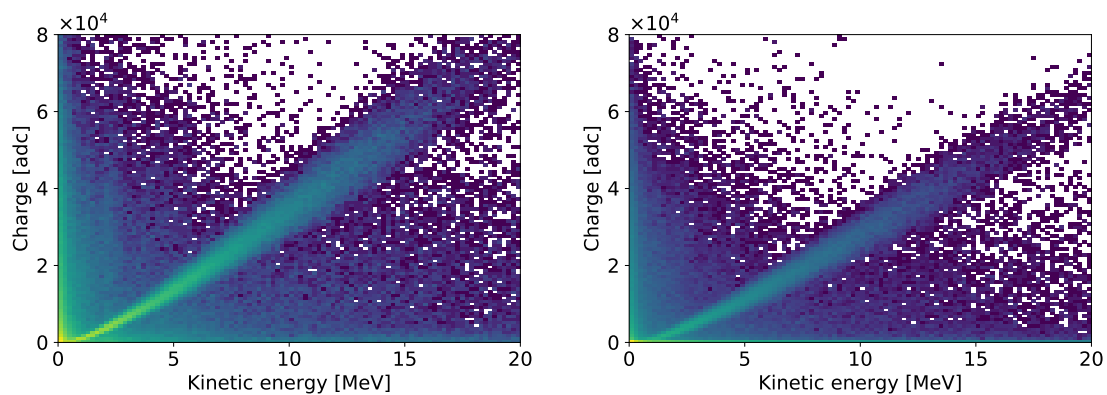


Figure 6.14: Charge collected in the target PMT vs energy deposited in the scintillator for kinematically-consistent events in LAB+PPO (left) and WbLS (right) data.

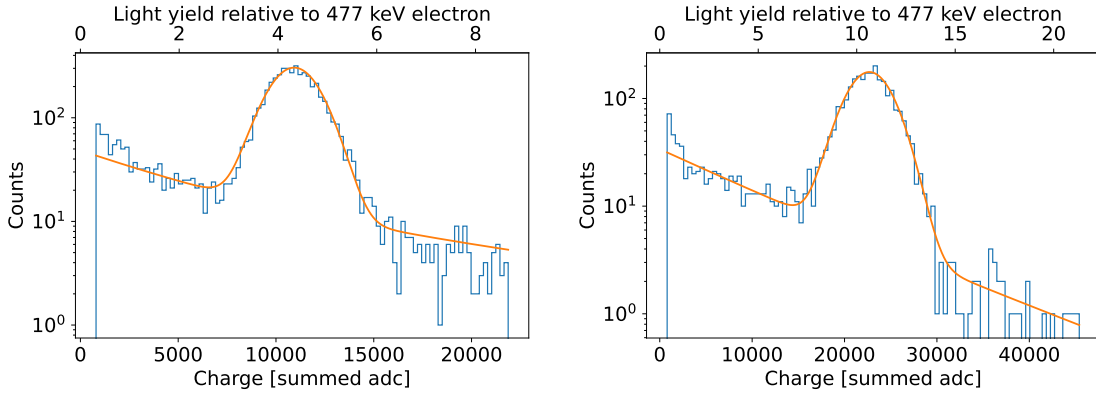


Figure 6.15: Distributions of charge values for kinematically consistent events, with empirical fits overlaid, of individual proton energy bins: 4.0–4.5 MeV events in LAB+PPO (left) and 8.0–9.0 MeV events in WbLS (right). Analogous figures for all energy bins are available in Appendix D.

(provided by SciPy [212]) is followed by a simplex-based local minimization (provided by NLOpt [213]). Uncertainties are computed using a resampling technique: the statistical uncertainty is computed via bootstrapping [214], wherein the dataset is repeatedly refit under resampling with replacement, and the total uncertainty, which includes systematic effects, is computed similarly, but with analysis parameters which act as sources of uncertainty simultaneously resampled at each iteration. The sources of systematic uncertainty included are the experimental geometry and timing calibrations: the coordinates of the breakup target, measurement cell, and each auxiliary detector, as well as the calibration value for each possible neutron trajectory. Each is sampled from a normal distribution centered on its nominal value, with standard deviations equal to its associated uncertainty. For each trial, energy reconstruction of all events in the dataset is performed and each energy bin is refit to extract a representative charge. This procedure generates a non-diagonal covariance matrix reflecting correlations between energy bins, which stem from the different, but broad, energy spectra associated with different auxiliary detectors.

6.2.10 Modeling ionization quenching

Ionization quenching refers to a reduction in scintillation output resulting from high excitation and ionization densities produced by a recoiling ion in a scintillating medium. Birks proposed the first phenomenological description for organic scintillators in 1951 [215], which remains widely used today. For a charged particle stopping along a distance x in a scintillating material, the rate of production of scintillation photons, L , is given by

$$\frac{dL}{dx} = \frac{S \frac{dE}{dx}}{1 + kB \frac{dE}{dx}}, \quad (6.10)$$

where dE/dx is the stopping power of material to the particle, S establishes the conversion between light produced and energy deposited in the limit of an unquenched system, and kB , termed the Birks constant of the material, introduces nonlinearity with respect to primary particle energy. Discrepancies have been observed between the Birks model and measured PLY data, particularly below 1 MeV, for a variety of organic scintillators [216–218]. More recently, it has been shown that the model fails to accurately describe the PLY of four different samples for energies above 1 MeV when lower energy data are considered [66]. Chou extended the model by introducing an additional quenching term quadratic in the stopping power [219], often interpreted as accounting for energy loss through bimolecular interactions:

$$\frac{dL}{dx} = \frac{S \frac{dE}{dx}}{1 + kB \frac{dE}{dx} + C \left(\frac{dE}{dx} \right)^2}. \quad (6.11)$$

Using either model, the total photon yield for a fully stopped ion can be found by numerically integrating the quenching relation using a table of stopping powers.

Quenching parameters are extracted by fitting each model to the measured PLY data via χ^2 minimization, with χ^2 defined as:

$$\chi^2 = \sum_{i,j} \Delta_i H_{ij} \Delta_j, \quad (6.12)$$

where Δ_i is given by:

$$\Delta_i = (Y_i - f(E_i; S, kB, C)). \quad (6.13)$$

Here, E_i and Y_i are the centroid and relative PLY value of the i^{th} proton energy bin, respectively; $f(E; S, kB, C)$ denotes the integration of the model up to energy E ; and H is the inverse of the covariance matrix of the dataset under consideration. Stopping power tables were generated using the Stopping Range of Ions in Matter (**SRIM**) software package [220], in which the stopping power of a compound material is calculated as a linear combination of those of its atomic constituents, as suggested by [221]. For table-defined energies E , the integral is performed using the trapezoidal rule. For non-table-defined energies, the yield is computed by linearly interpolating between adjacent table-defined yields. Parameter uncertainties and correlations are computed from the covariance matrix associated with the curvature about minimum χ^2 .

6.2.11 Results

6.2.12 Proton light yield

The light yields of LAB+PPO and WbLS as a function of proton recoil energy are shown in Figure 6.16 and listed in Table 6.4 and Table 6.5, respectively. The horizontal error bars denote the energy bin widths and do not represent uncertainty. The relative PLY of WbLS is consistently lower than that of LAB+PPO by 3.8%, although some energy bins below 9.5 MeV are individually consistent to within 1σ . Systematic uncertainty generally

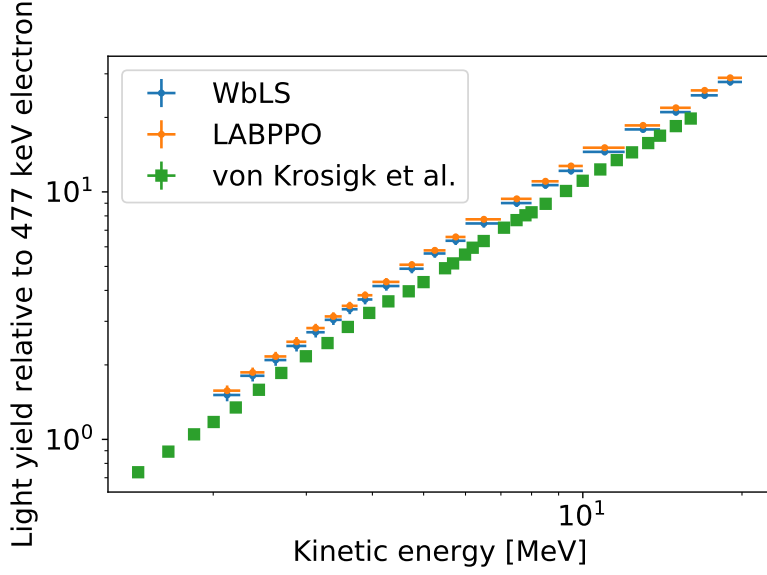


Figure 6.16: Proton light yield of LAB + 2 g/L PPO and 5% WbLS, relative to that of a 477 keV electron. A previous measurement of deoxygenated 2 g/L LAB+PPO by von Krosigk et al. [196] is overlaid.

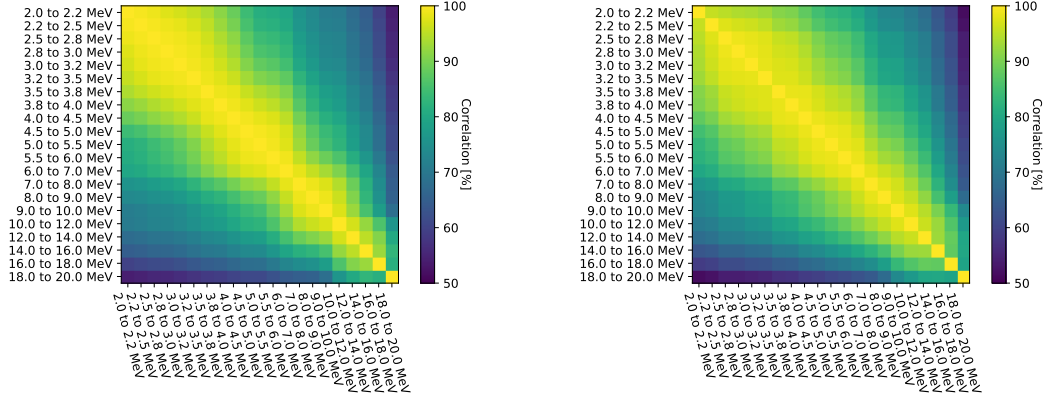


Figure 6.17: Correlation matrices of proton light yield uncertainties in different energy bins, for LAB+PPO (left) and WbLS (right) data.

dominates over statistical uncertainty, and is driven by the uncertainties on the experimental geometry tabulated in Table 6.1. Correlation matrices for the proton light yield values are tabulated in Table 6.6 and Table 6.7, and are visualized in Figure 6.17. Per-energy-bin time-dependent results, which exhibit no systematic trends during data-taking, are available in Appendix D.

Previous PLY measurements of several LAB+PPO formulations were performed by von Krosigk et al. using a neutron beam at the Physikalisch-Technische Bundesanstalt (PTB)

Energy range [MeV]	Relative LY	Stat. uncertainty [%]	Ref. uncertainty [%]	Total uncertainty [%]
2.00 – 2.25	1.57	±0.27	±0.84	±4.85
2.25 – 2.50	1.87	±0.25	±0.84	±4.51
2.50 – 2.75	2.16	±0.24	±0.84	±4.32
2.75 – 3.00	2.48	±0.25	±0.84	±4.47
3.00 – 3.25	2.82	±0.24	±0.84	±4.00
3.25 – 3.50	3.14	±0.25	±0.84	±3.89
3.50 – 3.75	3.46	±0.25	±0.84	±3.82
3.75 – 4.00	3.82	±0.26	±0.84	±3.55
4.00 – 4.50	4.33	±0.20	±0.84	±3.60
4.50 – 5.00	5.08	±0.19	±0.84	±3.19
5.00 – 5.50	5.80	±0.19	±0.84	±3.17
5.50 – 6.00	6.57	±0.19	±0.84	±2.96
6.00 – 7.00	7.74	±0.16	±0.84	±2.84
7.00 – 8.00	9.38	±0.17	±0.84	±2.59
8.00 – 9.00	11.05	±0.20	±0.84	±2.68
9.00 – 10.00	12.72	±0.21	±0.84	±2.27
10.00 – 12.00	15.09	±0.19	±0.84	±1.99
12.00 – 14.00	18.56	±0.25	±0.84	±1.91
14.00 – 16.00	21.86	±0.34	±0.84	±1.89
16.00 – 18.00	25.71	±0.49	±0.84	±1.87
18.00 – 20.00	28.84	±0.76	±0.84	±1.75

Table 6.4: Light yield of proton recoils, relative to that of a 477 keV electron, in LAB + 2 g/L PPO, and associated uncertainties (from left to right): statistical uncertainty, uncertainty on reference charge, and total uncertainty including systematic effects.

[196]. The PTB measurement for a deoxygenated 2 g/L LAB+PPO scintillator is also shown in Figure 6.16. The relative PLY data are systematically lower than the LAB+PPO PLY obtained in this work by 15 – 20%. A discrepancy between the PLY of the two samples is not unexpected, as the LAB+PPO measured at PTB was deoxygenated via bubbling with gaseous argon, which removes molecular oxygen, whereas the sample measured in this work was not. Such deoxygenation has been shown to impact ionization quenching [65, 222], though the relative proton light yield would be expected to decrease in aerated samples, opposite to the increase observed here. This is ultimately due to the preferential impact of oxygen quenching on triplet states, given the higher fraction of delayed light for proton recoils relative to electrons.

A number of factors may explain this discrepancy. The simple use of different integration lengths in waveform processing can lead to significant differences in measured light yields [198, 223], due to differences in the scintillation temporal profiles of electrons and protons, as well as potential variation in the proton pulse shape with recoil energy. Use of an integration length that is too short results in a pulse integral that is not proportional to the total number of scintillation photons. The integration length used in this work is 140 ns, which was chosen to ensure that $\geq 95\%$ of the light was collected. The integration length used in the PTB measurement is not reported in [196].

Energy range [MeV]	Relative LY	Stat. uncertainty [%]	Ref. uncertainty [%]	Total uncertainty [%]
2.00 – 2.25	1.51	±0.58	±2.54	±5.68
2.25 – 2.50	1.81	±0.45	±2.54	±5.15
2.50 – 2.75	2.10	±0.43	±2.54	±5.23
2.75 – 3.00	2.39	±0.40	±2.54	±5.05
3.00 – 3.25	2.71	±0.37	±2.54	±4.78
3.25 – 3.50	3.04	±0.37	±2.54	±4.66
3.50 – 3.75	3.36	±0.40	±2.54	±4.49
3.75 – 4.00	3.68	±0.38	±2.54	±4.45
4.00 – 4.50	4.17	±0.28	±2.54	±4.25
4.50 – 5.00	4.90	±0.29	±2.54	±4.18
5.00 – 5.50	5.64	±0.28	±2.54	±3.92
5.50 – 6.00	6.34	±0.28	±2.54	±3.90
6.00 – 7.00	7.45	±0.24	±2.54	±3.88
7.00 – 8.00	9.01	±0.24	±2.54	±3.60
8.00 – 9.00	10.65	±0.25	±2.54	±3.35
9.00 – 10.00	12.17	±0.27	±2.54	±3.39
10.00 – 12.00	14.51	±0.26	±2.54	±3.10
12.00 – 14.00	17.87	±0.32	±2.54	±3.01
14.00 – 16.00	21.00	±0.39	±2.54	±3.14
16.00 – 18.00	24.54	±0.64	±2.54	±3.05
18.00 – 20.00	27.89	±0.90	±2.54	±3.14

Table 6.5: Light yield of proton recoils, relative to a 477 keV electron, in 5% WbLS, and associated uncertainties (from left to right): statistical uncertainty, uncertainty on reference charge, and total uncertainty including systematic effects.

The reference charge calibration also represents a potential source of bias. The electron light yield of LAB+PPO has been shown to deviate from linearity below ~ 400 keV [224]. The PTB group used multiple γ -ray sources and assumed perfect electron light linearity, equivalent to fixing the offset parameter $b = 0$ in the model described in Section 6.2.5. For LAB+PPO, the multi-source calibration performed in this work leads to an offset parameter, $b = 34.7 \pm 1.2$ keV, indicative of electron light nonlinearity. The average charge per unit energy can be calculated for the single Compton edge fits described in Section 6.2.5. This charge per unit energy is 5.2% greater when using the 1547 keV Compton edge from ^{207}Bi compared to the 477 keV Compton edge from ^{137}Cs ; this value is 6.6% greater if the 2520 keV Compton edge from ^{24}Na is used.

Finally, the edge characterization method employed in [196] to extract the PLY is known to be subject to bias [198, 225]. In particular, the importance of neutron response modeling to the PTB measurement necessitates the need to extrapolate the light yield curve to lower energies in order to properly account for multiple neutron scatters, whereas the kinematic consistency and signal extraction methods employed in this work are model independent.

Bin #	Bin 0	Bin 1	Bin 2	Bin 3	Bin 4	Bin 5	Bin 6	Bin 7	Bin 8	Bin 9	Bin 10	Bin 11	Bin 12	Bin 13	Bin 14	Bin 15	Bin 16	Bin 17	Bin 18	Bin 19	Bin 20
Bin 0	100.0	99.2	98.7	97.7	96.8	95.6	93.9	91.3	88.6	84.4	81.4	80.8	79.5	75.8	73.5	71.3	70.9	67.7	65.0	60.0	54.2
Bin 1		100.0	99.4	98.8	98.2	97.0	95.2	92.5	89.8	85.5	82.4	81.7	80.3	76.4	74.0	71.8	71.4	68.3	65.6	60.6	54.8
Bin 2			100.0	99.4	99.0	98.1	96.4	94.1	91.5	87.4	84.3	83.6	81.9	77.7	75.1	72.7	72.3	69.2	66.4	61.4	55.6
Bin 3				100.0	99.4	98.7	97.4	95.1	92.8	88.9	85.9	85.0	83.2	78.5	75.7	73.1	72.6	69.4	66.7	61.6	55.8
Bin 4					100.0	99.2	98.1	96.4	94.2	90.8	87.9	86.9	84.9	80.0	76.8	74.1	73.5	70.2	67.4	62.4	56.5
Bin 5						100.0	98.8	97.8	96.0	93.1	90.6	89.6	87.5	82.4	78.9	75.9	75.0	71.7	68.8	63.7	57.5
Bin 6							100.0	98.8	98.1	95.9	94.0	92.9	90.6	85.2	81.2	78.0	76.7	73.1	70.1	64.9	58.6
Bin 7								100.0	99.0	97.7	96.2	95.1	92.7	87.1	82.6	79.2	77.5	73.8	70.6	65.5	59.0
Bin 8									100.0	99.0	98.2	97.3	95.0	89.5	85.0	81.6	79.7	75.6	72.2	66.9	60.2
Bin 9										100.0	99.3	98.7	97.0	92.0	87.4	84.0	81.7	77.5	73.6	68.1	61.0
Bin 10											100.0	99.2	97.6	93.0	88.5	85.1	82.6	78.1	73.9	68.3	61.1
Bin 11												100.0	98.8	95.4	91.7	88.7	86.0	81.2	76.3	70.3	62.6
Bin 12													100.0	98.1	95.6	93.2	90.3	85.2	79.4	72.7	64.3
Bin 13														100.0	98.7	97.3	94.3	88.8	81.7	74.3	65.1
Bin 14															100.0	98.7	96.0	90.5	83.0	75.2	65.8
Bin 15																100.0	97.3	92.6	85.5	77.8	68.3
Bin 16																	100.0	96.7	92.2	86.0	76.0
Bin 17																		100.0	95.0	90.7	80.4
Bin 18																			100.0	92.5	83.0
Bin 19																				100.0	81.6
Bin 20																					100.0

Table 6.6: Correlation matrix of proton light yield uncertainties in different energy bins, for LAB+PPO data. Bins are ordered as in Table 6.4.

Bin #	Bin 0	Bin 1	Bin 2	Bin 3	Bin 4	Bin 5	Bin 6	Bin 7	Bin 8	Bin 9	Bin 10	Bin 11	Bin 12	Bin 13	Bin 14	Bin 15	Bin 16	Bin 17	Bin 18	Bin 19	Bin 20
Bin 0	100.0	95.7	94.8	94.0	93.6	92.8	90.9	90.3	87.9	84.8	83.0	82.1	79.8	76.1	73.2	72.8	70.4	67.9	63.3	58.9	51.6
Bin 1		100.0	97.6	96.8	96.3	95.3	92.9	92.2	89.8	86.5	84.6	83.4	81.1	77.2	74.4	73.9	71.4	68.9	64.2	59.6	52.3
Bin 2			100.0	98.7	98.2	97.5	95.9	95.2	93.1	90.1	88.0	86.9	84.3	80.0	76.9	76.4	73.8	71.3	66.2	61.7	54.2
Bin 3				100.0	98.7	97.9	96.6	96.1	94.2	91.1	88.9	87.8	85.1	80.6	77.2	76.9	74.0	71.3	66.4	61.7	54.2
Bin 4					100.0	98.1	97.4	96.9	95.4	92.8	90.9	89.6	87.0	82.5	79.1	78.5	75.6	72.6	67.5	62.5	54.8
Bin 5						100.0	97.6	97.5	96.3	93.7	91.8	90.7	87.9	83.0	79.6	79.0	76.0	73.2	67.8	62.9	55.4
Bin 6							100.0	98.4	98.1	96.7	95.3	94.1	91.6	86.8	83.1	82.4	79.0	75.7	70.2	64.8	57.0
Bin 7								100.0	98.5	97.1	95.7	94.8	92.4	87.4	83.7	83.1	79.6	76.2	70.6	65.2	57.3
Bin 8									100.0	98.6	97.7	96.9	94.9	90.3	86.6	86.0	82.3	78.6	72.9	67.0	58.9
Bin 9										100.0	98.7	98.1	96.4	92.1	88.5	87.8	83.9	80.0	74.1	67.9	59.6
Bin 10											100.0	98.6	97.7	94.1	91.1	90.0	86.2	82.2	75.9	69.3	60.7
Bin 11												100.0	98.6	95.9	93.2	92.0	88.3	84.0	77.6	70.8	61.6
Bin 12													100.0	98.0	95.9	94.5	91.0	86.5	79.8	72.6	62.8
Bin 13														100.0	98.1	96.6	93.5	89.0	82.2	74.5	64.1
Bin 14															100.0	97.5	95.5	91.7	85.3	78.0	67.5
Bin 15																100.0	97.5	94.7	90.0	83.5	73.7
Bin 16																	100.0	96.0	92.4	86.4	76.8
Bin 17																		100.0	92.8	88.1	79.6
Bin 18																			100.0	87.9	80.0
Bin 19																				100.0	78.9
Bin 20																					100.0

Table 6.7: Correlation matrix of proton light yield uncertainties in different energy bins, for WbLS data. Bins are ordered as in Table 6.5.

6.2.13 Model compatibility

Figure 6.18 shows the best-fit quenching models for the LAB+PPO and WbLS relative proton light yield data obtained using the Birks and Chou parameterizations (see Equation 6.10 and Equation 6.11, respectively). The best-fit model parameters are listed in Table 6.8. The Chou model provides a better fit for each material, and significant deviations are observed for the Birks fit of the WbLS data below 3 MeV proton recoil energy. The parameter correlation between S and kB in Birks' model is 87.2% and 87.4% for the LAB+PPO and WbLS datasets, respectively. Correlation matrices associated with the Chou model are provided in Table 6.9.

The PLY of LAB + 2 g/L PPO (+ 15 mg/L bis-MSB, a secondary fluor) was measured using a proton beam at the NASA Space Radiation Laboratory at Brookhaven National Laboratory, and fit with Birks' law in [226]. The reported best-fit Birks' constant of $kB =$

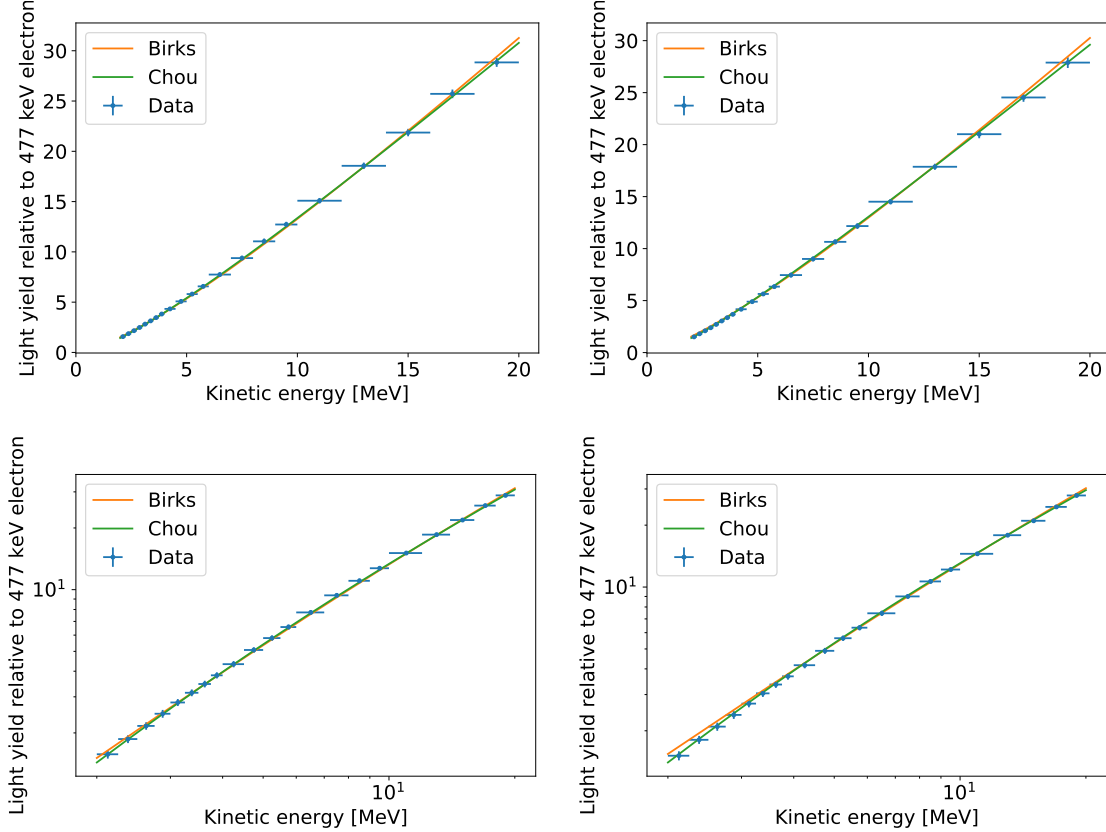


Figure 6.18: Best-fit quenching models compared to the measured PLY for LAB+PPO (left) and WbLS (right), shown with both linear (top) and logarithmic (bottom) axes. The Birks model fails to reproduce the low-energy behavior of both materials, which is better modeled with the inclusion of the Chou bimolecular quenching term.

	Birks		Chou	
	LAB+PPO	WbLS	LAB+PPO	WbLS
S [MeV $^{-1}$]	2.193 ± 0.053	2.082 ± 0.071	1.963 ± 0.074	1.776 ± 0.079
kB [cm/GeV]	7.08 ± 0.45	5.95 ± 0.43	3.76 ± 0.91	1.65 ± 0.81
C [cm 2 /GeV 2]	-	-	9.88 ± 2.74	13.30 ± 2.70
χ^2/ndf	36.6/19	44.7/19	22.8/18	17.3/18

Table 6.8: Best-fit model parameters for the LAB+PPO and WbLS proton light yields, relative to that of a 477 keV electron. Neither material is well modeled using the Birks formalism, but both are adequately described using the Chou model.

(7.0 ± 0.1) cm/GeV) is consistent with the present result, although it should be noted that the Brookhaven measurement was performed at energies above 20 MeV. The PTB study investigated ionization quenching in LAB+PPO using the Chou model [196]. In that work, scintillation light was quantified using an electron-equivalent energy in units of MeVee/MeV,

LAB+PPO	<i>S</i>	<i>kB</i>	<i>C</i>	WbLS	<i>S</i>	<i>kB</i>	<i>C</i>
<i>S</i>	100.0	93.9	-73.5	<i>S</i>	100.0	93.7	-70.2
<i>kB</i>		100.0	-87.0	<i>kB</i>		100.0	-84.9
<i>C</i>			100.0	<i>C</i>			100.0

Table 6.9: Correlation matrices of parameter uncertainties for the Chou quenching model, in units of percent.

and S was fixed to a value of 1 MeVee/MeV. In this work, scintillation light was determined relative to that produced by a 477 keV electron, which gives a value of $S = (477 \text{ keV})^{-1} = 2.095 \text{ MeV}^{-1}$ in the absence of electron light quenching. This is equivalent to the value of $S = 1 \text{ MeVee/MeV}$ used in [196]. The best-fit model in the PTB study was consistent with a quadratic coefficient, C , of zero, i.e., equivalent to the model provided in Equation 6.10, although a metric directly quantifying the goodness-of-fit was not reported. In contrast, in this work, a nonzero quadratic coefficient is preferred. The Birks constant extracted in the PTB study, $kB = 9.8 \text{ cm/GeV}$, is larger than that found in this work, while the fixed value of S is smaller (though consistent to within 1σ). As the S and kB parameter errors are positively correlated, a decrease in the estimate of S would result in a decreased estimate of kB for the same predicted light yield. Hence, fixing $S = 2.095 \text{ MeV}^{-1}$ in this work would result in a smaller value of kB for the Birks fit, representing an even larger discrepancy with the PTB quenching parameter.

The PTB measurement extended a few hundred keV below the 2 MeV floor used in this work, but the best-fit model failed in the high energy region, systematically predicting an excess light yield above 12 MeV. Additional PLY measurements, particularly at lower energy and with deoxygenated samples, would help resolve tension with the PTB study.

6.3 Precision scintillator time-profile measurements

6.3.1 Introduction

As described in Section 6.1, the scintillation emission time profile critically influences the reconstruction of neutrino interactions in large-scale detectors. Determining the time profile in-situ, however, is generally difficult. For example, the observed time profile is distorted by optical effects, such as self-absorption and reemission by the scintillator itself — see, e.g. [87] for concrete examples of this at play. Such effects are averaged over different path lengths throughout the detector, and as such cannot be generally be factored out of the observed timing. Scintillator time profiles hence must be measured ex-situ, using relatively small volumes.

The scintillation time profile of two-component systems, containing a primary solvent and secondary fluor, are typically modeled as a sum of exponentially-decaying terms, each modified by a common “rise time,” which accounts for excitation of fluor molecules via

non-radiative energy transfer from solvent molecules, as described in [65]:

$$S(t) = \sum_{i=1}^N A_i \frac{e^{-t/\tau_i} - e^{-t/t_R}}{\tau_i - t_R}, \quad (6.14)$$

$$\sum_{i=1}^N A_i = 1, \quad (6.15)$$

where t is the time of photon emission relative to solvent excitation, τ_i are the lifetimes of the N observable decay modes, t_R is the rise time, and S is normalized so that $\int_0^\infty dt' S(t') = 1$.

The theory of organic scintillators usually associates the observed scintillation with primary excitation and ionization of π -electrons [65]. Direct excitation is into a singlet state; in the case of full ionization, electron pairs recombine preferentially into a relatively long-lived triplet state [65]. The larger stopping power for heavier ions, such as α s relative to electrons, thus translates to a higher proportion of triplet states, and hence a generically slower scintillation time profile. This is the basis for timing-based PID, which allows for *a priori* background rejection, without reliance on any spectral features.

In order to enable explorations timing-based PID capabilities, the time profiles of WbLS and LAB+PPO samples in response to both electrons and α particles were measured. Measurements of the response to electrons were made for 1%, 5%, and 10% WbLS formulations, as well as LAB loaded with PPO at 0.6 g/L, 1.5 g/L, and 2.0 g/L. Measurements in response to α particles were made for 5% and 10% WbLS formulations, and LAB + 2 g/L PPO.

6.3.2 Experimental setup and waveform processing

The experimental setup used to measure the emission time profiles, shown in Figure 6.19, is built around a 1-inch right cylindrical acrylic vessel, which contains a hollow volume in which the sample under study resides. There is no top face to the vessel; instead, a radioactive button source, purchased from Spectrum Techniques [227], acts as a lid for the container. Such a windowless design is necessary for α measurements — even a thin acrylic window will stop the majority of decay α s before entering the sample. For electrons, the windowless design has the benefit of maximizing the energy deposited in the sample, allowing for maximal Cherenkov light collection.

The acrylic vessel is viewed by a collection of photodetectors, namely two PMTs and one Large-Area Picosecond Photodetector (LAPPD), which operate in tandem to measure the emission time profile. Each PMT is a Hamamatsu H11934-200 [229], which operate with individual time resolutions of ~ 115 ps. One PMT, termed the “trigger PMT,” is directly coupled to the outer surface of the acrylic vessel using EJ-550 optical grease [230], and for a typical source decay detects multiple photons. The other PMT is placed at a standoff distance from the sample, such that for a typical decay, on average less than one photon is detected. The sample itself sits on top of the face of the LAPPD, which is produced by INCOM [231]. The face of the LAPPD glass is masked off, with only a residual hole of

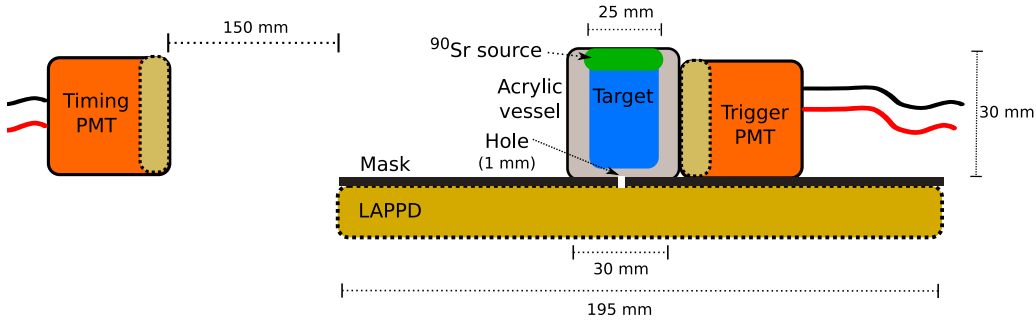


Figure 6.19: Experimental setup used in scintillator time profile measurements, exemplifying a sample, β -decay source, and available photodetectors. Figure borrowed from [228].

~ 1 mm diameter open to light, to similarly reduce the occupancy of the LAPPD to less than one photon per event.

Signals from all photodetectors are digitized using a CAEN V1742 [232] collecting 1024 samples each at 5 GS/s, and triggering is accomplished by applying a fixed threshold to the trigger PMT signal. Waveforms are processed to identify pulses by first applying a 5 mV threshold to each signal; if a signal is above-threshold, a time value is assigned according to the following: for the trigger PMT, waveforms from which are comprised of multi-photoelectron (multi-PE) pulses, the time value is the threshold-crossing time of a 3 mV threshold, which corresponds to the time-of-arrival of the first detected photon; for the single-PE PMT and LAPPD, waveforms from which contain a single pulse associated with a single photon, time values are calculated using a constant-fraction-discrimination (CFD) algorithm — specifically, the time value is defined as the time at which the waveform reaches 60% of its maximum amplitude. Further details relevant in defining “a time value” for LAPPD data are given in Appendix E. The use of a CFD time for the single-PE channels improves the effective time resolution by suppressing the effects of electronic noise on waveform processing, whereas the use of a constant-threshold time for the multi-PE trigger channel allows for the system reference time to be interpreted as the time of the first detected photon, which, as discussed below, is important for modeling the system response. A charge value is assigned to each waveform by integrating the waveform over a 120 ns window following the arrival of the pulse. Examples of single- and multi-PE waveforms are shown in Figure 6.20.

For electron measurements, the radioactive source employed was an effective ${}^{90}\text{Y}$ source: the active material contains ${}^{90}\text{Sr}$, which β -decays to the ground state of ${}^{90}\text{Y}$ with a 29-year half-life and Q -value of 546 keV, which itself decays with a 64-hour half-life and Q -value of ~ 2.3 MeV. The primary strontium decays are removed from analysis using a cut on trigger PMT charge, which is discussed below. For α particle measurements, a sample of ${}^{210}\text{Po}$ was employed, which overwhelmingly decays directly to the ground state of ${}^{206}\text{Pb}$ via the emission of 5.3 MeV α , with a half-life of 138 days.

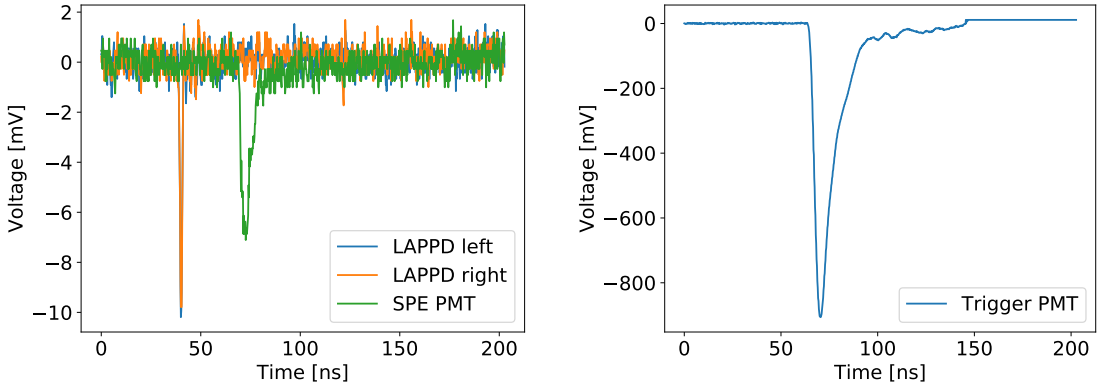


Figure 6.20: Example single-PE waveforms from the LAPPD and SPE PMT (left), and multi-PE waveform from the trigger PMT (right), sampled from ^{90}Sr data taken with a LAB + 2 g/L PPO target.

6.3.3 Analysis strategy

The emission time profile of each sample under study is determined by fitting an analytic model to the observed time profile, with particular attention paid to the form of the system response, which is determined by the trigger scheme. At the finest level of detail, this entails both modeling the effect on the system response of the occupancy levels of the trigger PMT and the independent determination of the occupancy levels — though this level of precision is only necessary in certain regimes, and approximations can be made in others. With the form of the response taken as input, however, its dependence on the scintillation emission time profile can be modeled. This improves sensitivity to the scintillation rise time, which is often degenerate with features of the system response, and is important in assessing the purity of detected Cherenkov light, emitted when the rise time dominates the strength of scintillation emission.

The distribution of observed, or “measured,” SPE photodetector times, relative to the system trigger, can conceptually be written as

$$M(t) = P(t) \otimes R(t) \odot T(t) \otimes \delta(t - t_0) \quad (6.16)$$

where P is the emission time profile; R is the response function of the photodetector; T is the *trigger profile*, i.e. the distribution of times between data acquisition triggering and the deposition of energy into the sample; t_0 is an overall system delay; \otimes denotes convolution, i.e. $F \otimes G = \int_{-\infty}^{+\infty} dt' F(t') G(t - t')$; \odot denotes truncated anticonvolution, i.e. $F \odot G = \int_0^{+\infty} dt' F(t + t') G(t')$; and all operators are applied in the order reading from left to right. The anticonvolution with the trigger profile must be truncated to respect causality, as the system cannot trigger before any photons are detected. The photodetector response function R is approximately Gaussian for both the PMTs and LAPPD [229, 233], but the trigger profile T is, in general, asymmetric. Details of the techniques used to model the trigger

profile are given in Section 6.3.4; what is important, generally, is that its shape depends on the emission time profile of the sample, which should be accounted for when modeling the shape of the observed time profile.

Details of the emission time profile, P , depend on the nature of the sample and source. For α particles, which here are far below the threshold for Cherenkov production, $P(t) = f \cdot S(t) + (1 - f) \cdot U(t)$, where f is the fraction of events due to scintillation light, S is the scintillation emission time profile defined in Equation 6.15, and $U(t)$ is a uniform distribution, which models the constant “dark rate” of pulses generated by thermal electrons inside the photodetector, which are uncorrelated with source decays. That is, for an analysis window of length w ,

$$U(t) = \frac{1}{w}. \quad (6.17)$$

The emission time profile of electrons is defined similarly, with an additional term (and accompanying fractional weighting) to model the presence of Cherenkov light: the time scale for Cherenkov production is at the level of picoseconds, far below the scale of other shape features, and we thus approximate the Cherenkov component as a simple δ -function, $\delta(t)$. For both electrons and α particles, we allow for two scintillator deexcitation modes (i.e. $N = 2$ in Equation 6.15).

Given this model and a histogram of observed time values, we define the joint negative log-likelihood of the photodetectors participating in the measurement, often simply referred to as “the likelihood” for brevity, as

$$-\log L = \sum_{\text{photodetectors } j} \sum_{\text{bins } i} \mu_i^{(j)} - n_i^{(j)} + n_i^{(j)} \log \left(\frac{n_i^{(j)}}{\mu_i^{(j)}} \right), \quad (6.18)$$

where μ and n are the expected and observed counts in a bin, respectively, and i and j label the histogram bins and photodetectors used in the measurement, respectively. In the limit that the bin widths are small in comparison to the shape features of the model, the expected counts for a bin centered with center time t and width Δ and can be approximated as

$$\mu = \int_{t - \frac{1}{2}\Delta}^{t + \frac{1}{2}\Delta} dt' M(t') \approx M(t) \cdot \Delta, \quad (6.19)$$

which aids in evaluating the likelihood quickly and, ideally, analytically. The parameters of the emission time profile are then determined by minimizing the joint likelihood.

6.3.4 Modeling the trigger profile

The reference time used in these measurements is, conceptually, the time that the first photon reaches the multi-PE trigger PMT. The trigger profile $T(t)$, is the distribution of such times relative to the energy deposition in the sample, and as such is a function of the emission time profile: the longer the time scale on which a scintillator emits light, the more time

typically elapses before the system triggers. To be precise, T can be written in terms of the first order-statistic (see, e.g., [234] for mathematical context) of the emission time profile P – that is, given n photons detected by the trigger PMT, the probability density function of the time the first detected photon. This can be written analytically: if $Q(t)$ is the cumulative distribution function associated with the probability distribution function $P(t)$, then the first order-statistic of P given n detected photons is

$$P_1^{(n)}(t) = nP(t)(1 - Q(t))^{n-1}. \quad (6.20)$$

Using a scintillation time profile with a principal decay time of $\tau_1 = 3$ ns as an example, the trigger profiles and resultant observed timing distributions in a single-PE photodetector are shown for a variety of increasing trigger occupancies in Figure 6.21. Two features are apparent: first, that the trigger profile narrows and becomes more symmetric as the trigger occupancy increases; and second, that the degree of symmetry of the trigger profile correlates with the slope of the rising edge of the observed time profile. The latter observation is critical when interpreting scintillator rise time estimates and Cherenkov/scintillation separation in such small-scale setups.

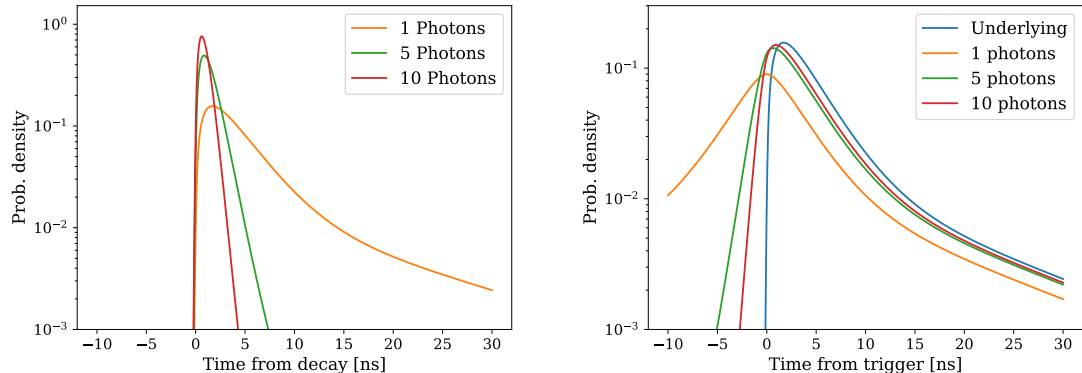


Figure 6.21: Example trigger profiles (left) and observed time profiles (right) for increasing trigger occupancy levels, for a pure scintillation emission time profile with the following parameters: $t_R = 100$ ps, $\tau_1 = 3$ ns, $\tau_2 = 15$ ns, $A_1 = 0.75$. As the trigger occupancy increases, the trigger profile becomes symmetric, and the rising edge of the observed time profile steepens.

In the electron measurements presented here, accomplished using ^{90}Y β -decays, high-enough light levels are available in which the trigger profile can be approximated as a Gaussian with a single free parameter, the standard deviation. Data in this regime is selected for analysis by means of a cut on the trigger charge, which removes the primary strontium and low-energy yttrium decays from analysis. The lower bounds on the trigger charge employed for each material are listed in Table 6.10. In this regime, Equation 6.16 can be evaluated analytically, using the expressions presented in Appendix F.

	WbLS			LAB+PPO		
	1% WbLS	5% WbLS	10% WbLS	0.61 g/L	1.1 g/L	2.0 g/L
Trigger charge cut [pC]	> 14.0	> 18.1	> 25.7	> 25.7	> 25.7	> 25.7

Table 6.10: Lower bound on charge collected in trigger PMT in electron data, to remove low-energy yttrium and strontium decays from analysis. Lower values are used for 1% and 5% WbLS to recover statistics from the body of the β spectrum and establish reasonably-sized data sets.

For measurements of α particles, which produce significantly less light than electrons, owing to differences in energy deposition in the sample, the Gaussian approximation does not hold and more detailed modeling is necessary. If the trigger PMT operated at a fixed occupancy, then the trigger profile would simply be the first order-statistic defined in Equation 6.20. In practice, however, the number of photons collected by the trigger PMT is not constant, but varies event-to-event. This owes fundamentally to Poisson statistics, but there are higher-order effects which contribute to a non-Poisson shape, such as energy losses of the α in the air and source surface, as well as contamination of thermal photoelectrons (“dark hits”) which are uncorrelated with the scintillation response. If W_i is the fraction of events in which the trigger PMT detected i photons, then the trigger profile can be written generally as

$$T(t) = R'(t) \otimes \sum_{n=1}^{\infty} W_n P_1^{(n)}(t), \quad (6.21)$$

$$\sum_{n=1}^{\infty} W_n = 1, \quad (6.22)$$

where $R'(t)$ is the response function of the trigger PMT. The occupancy fractions (or occupancy spectrum) $\{W_i\}$ can be determined by calibrating the SPE charge of the trigger PMT, as described in Section 6.3.5, and fitting the observed multi-PE charge spectrum during data-taking, as described in Section 6.3.6. With this formulation, the anticonvolution in Equation 6.16 is then evaluated numerically, modeling the combined photodetector response of the two PMTs, $R \otimes R'$, as a Gaussian with $\sigma = \sqrt{2} \cdot 115 \text{ ps} \approx 163 \text{ ps}$, corresponding to the combined response of two identical devices operating at manufacturer specification [229]. The remaining dependence of the trigger profile $T(t) = T(t; t_R, \tau_1, \tau_2, A_1)$ on the candidate emission time profile, however, is explicitly modeled.

6.3.5 Trigger PMT Calibration

In order to determine the distribution of trigger PMT occupancies, as described in Section 6.3.6, the SPE charge response of the trigger PMT must be parameterized and calibrated. This was accomplished using single-photon pulses provided by a blue LED. The LED was pulsed so as to establish a low detection rate in the trigger PMT, which suppresses

multiphoton contamination. Charge values were computed from the resulting waveforms using an integration window of 18 ns, which captures the full width of SPE pulses but circumvents the degradation in resolution intrinsic to integrating over longer windows, due to the inclusion of more electronic noise. No threshold is applied to the data so as to avoid biasing the calibration.

The distribution of SPE charge is shown in Figure 6.22, and is fit with a two-Gaussian model, corresponding to pure noise, i.e. empty waveforms, and a single-photon signal. This simple model adequately describes the observed charge distribution with best-fit signal parameters of $\mu = (0.731 \pm 0.009)$ pC and standard deviation $\sigma = (0.538 \pm 0.007)$ pC; these values are consistent with cross-check calibrations performed using longer integration lengths, though the latter provide weaker constraints due to the higher level of electronic noise included in the integration.

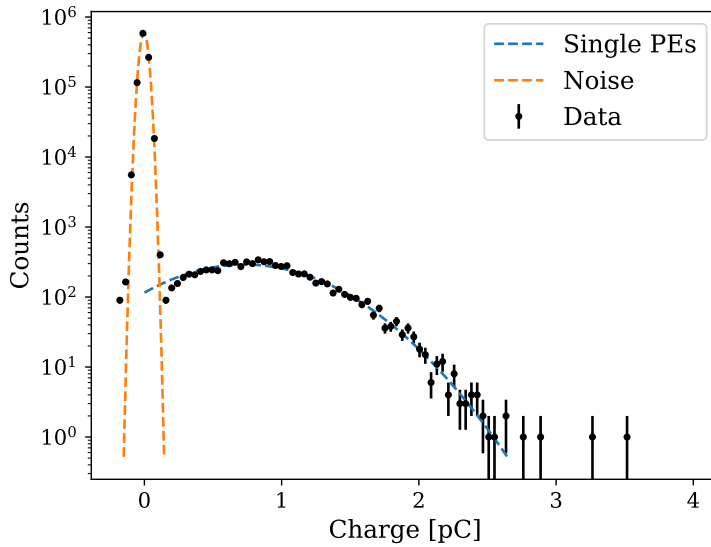


Figure 6.22: Distributions of trigger PMT charge when flashing an LED, calculated using 18 ns integration window.

6.3.6 Determining the Occupancy Spectrum

The trigger occupancy spectrum, i.e. the distribution of the number of photons detected by the trigger PMT, can be extracted from the trigger PMT charge spectrum collected during data-taking, given models for both the SPE charge response and charge summation. As discussed in Section 6.3.5, the distribution of SPE charge q is approximately a Gaussian function $G(q; \mu, \sigma)$, with mean μ and standard deviation σ . We assume that SPE pulses add perfectly linearly, so that the charge response associated with an n -PE pulse is also a Gaussian $G(q; n\mu, \sqrt{n}\sigma)$ in accordance with the central limit theorem. Given an observed

distribution $P(q)$ of charge q , we can write

$$P(q; \{W_i\}) = \sum_{n=1}^{\infty} W_n G(q; n\mu, \sqrt{n}\sigma) \quad (6.23)$$

as a sum over multi-PE charge distributions, and identify the fractions $\{W_i\}$ with those which appear in Equation 6.22.

Regarding the fractions $\{W_i\}$ as free parameters, Equation 6.23 can be fit to the distribution of trigger PMT charge observed during data-taking. The fit is formulated as a least-square-difference minimization between the binned charge data and model. In practice, the infinite sum must be truncated at some finite maximum mode, n_{\max} . In developing the results presented in this work, several choices for n_{\max} were used, and it was found that the fit results are robust to changes to the exact value, as long as the mean charge of the maximum mode, $n_{\max}\mu$, is well-above the endpoint of the observed charge distribution. The high dimensionality associated with the generality of this model (choosing $n_{\max} = 200$, for example, requires a 200-dimensional minimization) is dealt with by evaluating the model using the `JAX` [235] library, which allows the cost function, C_0 , to be differentiated analytically via automatic differentiation. This allows for efficient minimization using gradient descent, without the presence of the numerical error which accrues when approximating the gradient using finite difference methods. In this work, we employ a basin-hopping algorithm, in which simulated annealing is applied to repeated local gradient-descent-based minimizations.

It was observed that the best-fit occupancy spectra exhibit oscillatory behavior, wherein the preferred occupancy varies between several local maxima and minima, as opposed to a unimodal distribution, as might be expected from a monoenergetic source. This is believed to be an artifact of imperfect minimization owing to the combinatorics of high-dimensionality and large correlations between neighboring occupancy modes, intrinsic to the general model defined by Equation 6.23: because neighboring occupancies are nearly-degenerate, there are many minima, which we term “impostor minima,” in which one occupancy representative of its neighborhood contains an excess weighting, but only one minima where the weighting is correctly allocated between neighboring modes. Whether the minima identified are sufficient to properly model the trigger response was studied by manually enforcing unimodality in the occupancy spectrum via a constraint term in the cost function, which penalizes spectra according to the difference between neighboring modes. That is, we instead minimize a penalized cost function

$$C_{\lambda}(\{W_i\}) = C_0 + \lambda \sum_{n=1}^{\infty} (W_{n+1} - W_n)^2, \quad (6.24)$$

where the penalization strength λ controls level of constraint on the spectrum shape: $\lambda = 0$ results in the ordinary least-squares cost function defined previously, whereas in the limit $\lambda \rightarrow \infty$ the preferred occupancy spectrum is uniform across all allowed modes. The scintillation time profile results presented in this work are robust to machine precision for different choices

of λ spanning 10 orders of magnitude, indicating that the small difference between the impostor and true global minima is below the sensitivity of our timing data to the trigger profile.

Observed trigger charge spectra and best-fit models are shown in Figure 6.23, which demonstrate that a single Gaussian adequately models the SPE charge response. A small mismodeling is present in the transition region between pure noise and SPE pulses, which this does not affect this analysis as the data is collected in a strictly multi-PE regime, wherein the small discrepancy is further suppressed by repeated self-convolutions of the SPE spectrum with itself. Best-fit occupancy spectra, for a selection of penalization strengths, are shown in Figure 6.24. Note that the heavily penalized spectra interpolate the weakly penalized spectra, but maintain probability mass in the same occupancy regions.

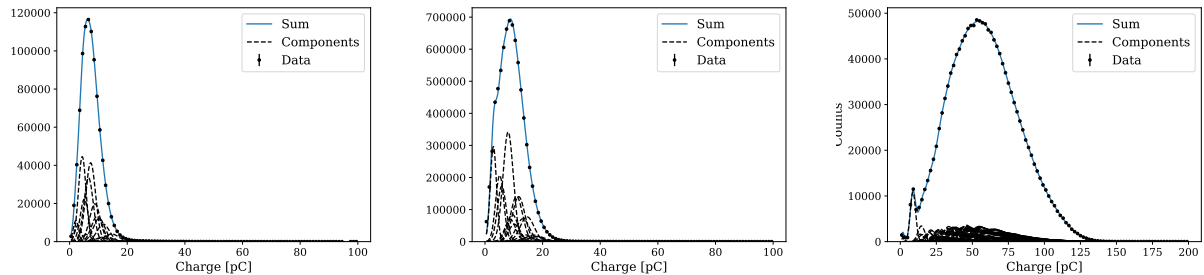


Figure 6.23: Distribution of trigger PMT charge during α data-taking, with best-fit multi-PE charge model overlaid, for 5% WbLS (left), 10% WbLS (middle), and LAB+PPO (right).

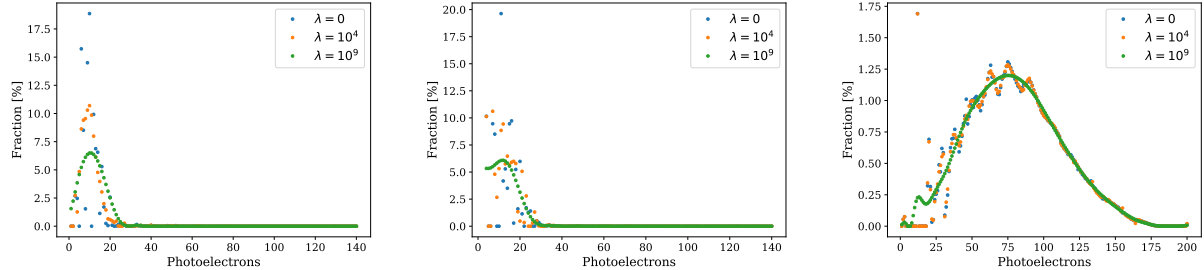


Figure 6.24: Best-fit spectra of trigger PMT occupancies during α data-taking, for 5% WbLS (left), 10% WbLS (middle), and LAB+PPO (right), under different modality-penalization strengths.

6.3.7 Results

The collected timing data and best-fit time profile models are shown for electrons in WbLS and LAB+PPO samples in Figure 6.25 and Figure 6.26, respectively, and for α particles in Figure 6.27. The best-fit model parameters are listed in Table 6.11 and Table 6.12.

Of particular note are the features of the Cherenkov light observed in the electron data. The value of the effective system resolution in each channel, σ_X , is determined principally by the shape of the observed Cherenkov contribution, and decreases with increasing scintillator fraction in WbLS samples, or PPO concentration in pure-LAB based samples. This is due to the increased scintillation light yield in higher-loaded samples, which increases the trigger occupancy and hence narrows the trigger profile, as described in Section 6.3.4. The magnitude of the Cherenkov contribution follows the reverse trend, in that samples with lower-scintillator/fluor loadings naturally produce less scintillation light, and the Cherenkov contribution is more pronounced. This leads to improved Cherenkov selection, as quantified in Section 6.3.8. Note also that the PMT detects less Cherenkov light, in all cases, than does the LAPPD — this is due to the geometry of the setup, wherein the β is, on average, directed downward toward the LAPPD.

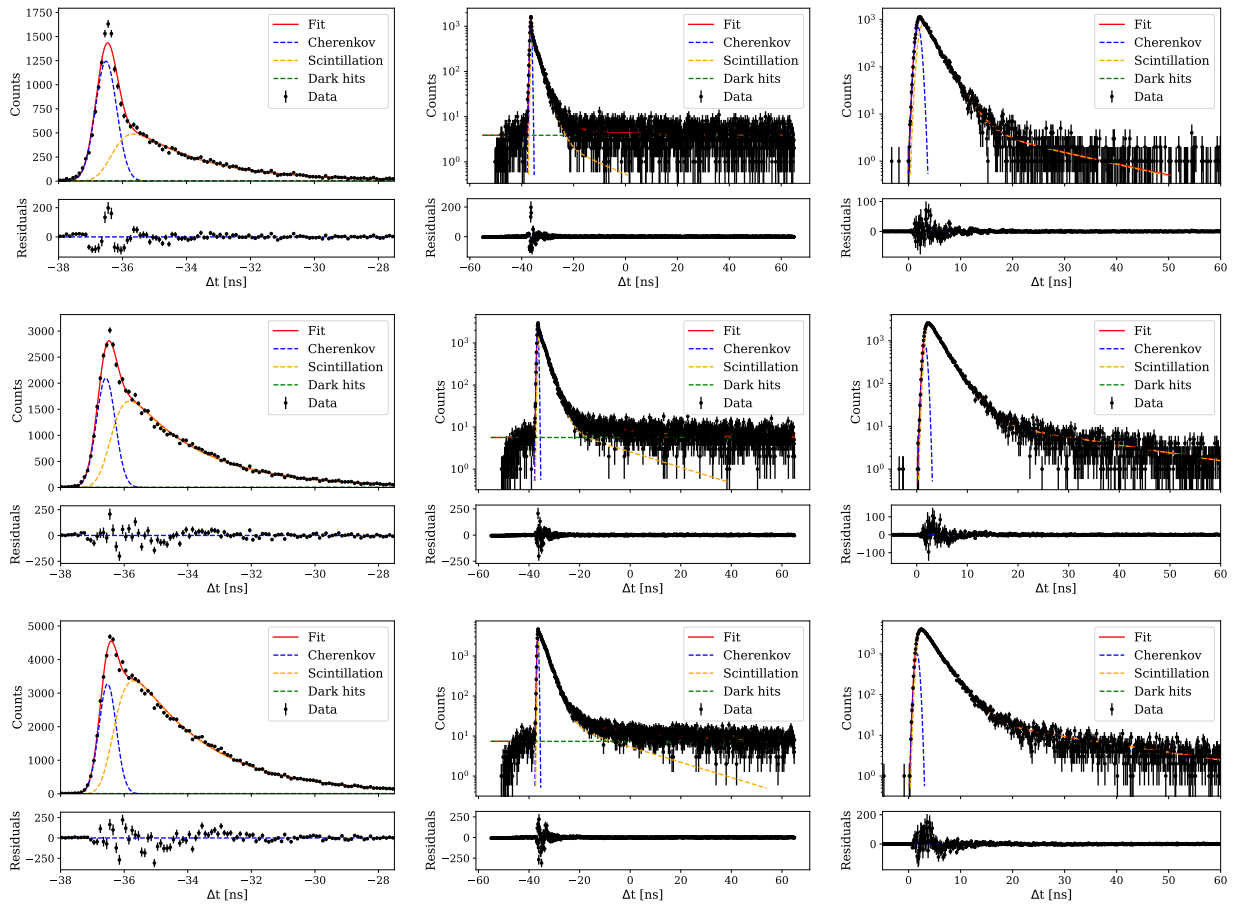


Figure 6.25: Distribution of detected times relative to trigger, with best-fit Cherenkov/scintillation model overlaid, for 1% (top), 5% (middle), and 10% (bottom) WbLS data, in the peak region of the LAPPD (left), full analysis window of the LAPPD (middle), and full analysis window of the timing PMT (right).

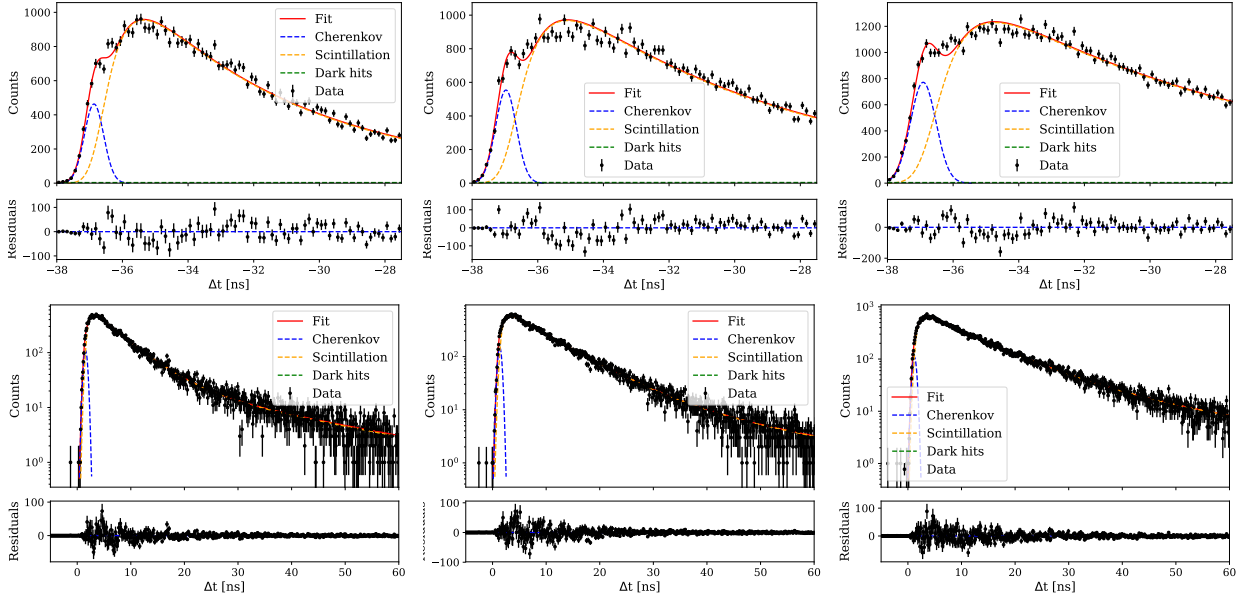


Figure 6.26: Distribution of detected times relative to trigger, with best-fit Cherenkov/scintillation model overlaid, for LAB loaded with PPO at 2.0 g/L (left), 1.1 g/L (middle), and 0.61g/L (right), in response to electrons, in the LAPPD (top) and PMT (bottom) channels.

	WbLS			LAB+PPO		
	1%	5%	10%	0.61 g/L	1.1 g/L	2.0 g/L
σ_L [ps]	334^{+4}_{-4}	298^{+4}_{-3}	273^{+3}_{-3}	390^{+8}_{-8}	317^{+8}_{-10}	294^{+11}_{-12}
σ_P [ps]	495^{+13}_{-7}	381^{+8}_{-5}	372^{+5}_{-4}	373^{+13}_{-16}	370^{+9}_{-34}	341^{+16}_{-12}
$f_{C,L}$ [%]	$38.8^{+0.7}_{-0.6}$	$22.3^{+0.5}_{-0.5}$	$16.1^{+0.3}_{-0.3}$	$4.6^{+0.1}_{-0.2}$	$4.3^{+0.2}_{-0.2}$	$4.2^{+0.3}_{-0.3}$
$f_{C,P}$ [%]	$22.4^{+1.9}_{-1.0}$	$8.4^{+1.5}_{-0.7}$	$6.2^{+0.6}_{-0.6}$	$1.2^{+0.2}_{-0.2}$	$2.5^{+0.2}_{-0.7}$	$2.1^{+0.5}_{-0.5}$
τ_R [ps]	270^{+26}_{-20}	209^{+10}_{-11}	276^{+7}_{-7}	756^{+19}_{-17}	672^{+28}_{-14}	577^{+17}_{-20}
τ_1 [ns]	$2.22^{+0.02}_{-0.02}$	$2.25^{+0.01}_{-0.01}$	$2.36^{+0.01}_{-0.01}$	$8.77^{+0.08}_{-0.09}$	$7.15^{+0.07}_{-0.08}$	$5.06^{+0.07}_{-0.05}$
τ_2 [ns]	$17.7^{+1.3}_{-1.1}$	$23.5^{+1.0}_{-0.9}$	$22.8^{+0.7}_{-0.7}$	$28.9^{+0.9}_{-0.9}$	$25.7^{+1.1}_{-1.1}$	$23.1^{+1.1}_{-0.8}$
A_1 [%]	$95.6^{+0.3}_{-0.3}$	$94.8^{+0.1}_{-0.1}$	$94.9^{+0.1}_{-0.1}$	$80.9^{+0.8}_{-0.8}$	$87.8^{+0.7}_{-0.7}$	$78.6^{+0.8}_{-0.6}$
χ^2	2967.6	3031.1	3373.2	2586.8	2563.2	2664.1
ndf	2388	2388	2388	2388	2388	2388

Table 6.11: Best-fit electron time profile model parameters for WbLS and LAB+PPO samples. Subscripts L and P refer to the LAPPD and PMT channels, respectively; σ refers to the effective system resolution; and f_C refers to fractional contribution of Cherenkov light.

6.3.8 Cherenkov/Scintillation Separation

It is instructive to quantify the level of Cherenkov/Scintillation separation achievable for electron interactions in each material, so as to gain insight into how different materials may compare when deployed in a hybrid detector aiming to use advanced reconstruction

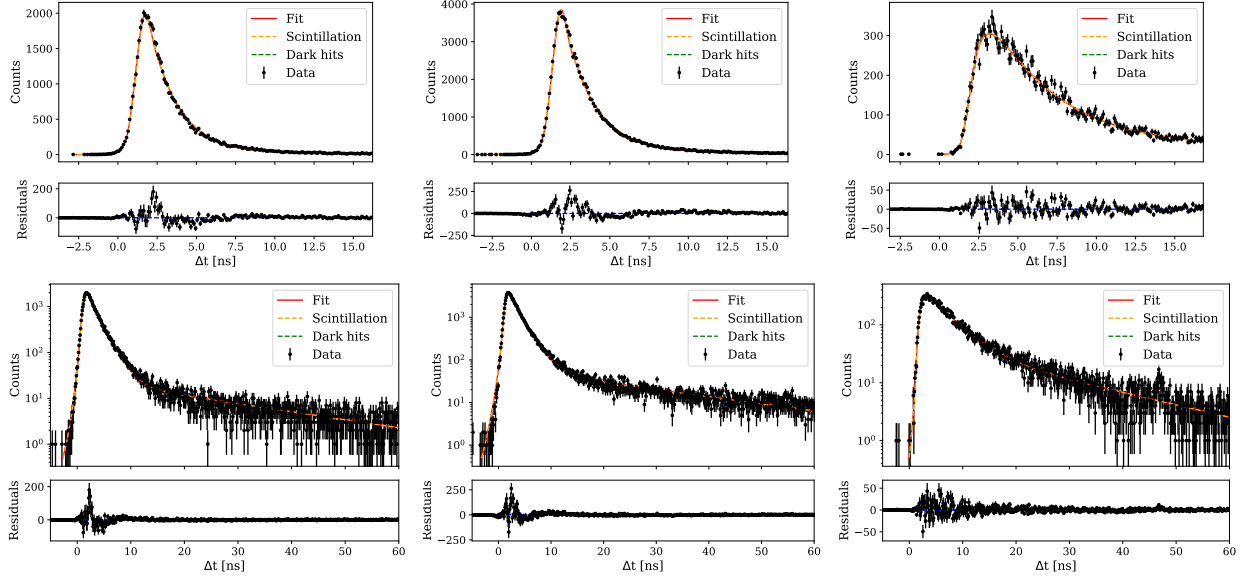


Figure 6.27: Distribution of detected times relative to trigger, with best-fit scintillation model overlaid, for 5% WbLS (left), 10% WbLS (middle), and LAB+PPO (right), in response to α radiation, in linear (top) and logarithmic (bottom) scales.

	5% WbLS	10% WbLS	LAB + 2 g/L PPO
τ_R [ps]	169^{+15}_{-15}	129^{+13}_{-13}	709^{+49}_{-49}
τ_1 [ns]	$1.82^{+0.01}_{-0.01}$	$1.92^{+0.01}_{-0.01}$	$4.13^{+0.13}_{-0.13}$
τ_2 [ns]	$24.7^{+0.8}_{-0.8}$	$26.1^{+0.5}_{-0.5}$	$20.3^{+0.8}_{-0.8}$
A_1 [%]	$89.6^{+0.1}_{-0.1}$	$88.1^{+0.1}_{-0.1}$	$79.8^{+0.4}_{-0.4}$
χ^2	1430.3	1685.0	1316.3
ndf	1194	1194	1194

Table 6.12: Best-fit α time profile model parameters for WbLS and LAB+PPO samples.

techniques. The appropriate metric is context-dependent — depending on how photon classification is achieved, what is considered “optimal” may change. For example, applying spectral sorting in a pure scintillator detector may be more tolerant to losses of scintillation light, since it is relatively abundant compared to a WbLS deployment. Because only timing information is considered in this work, we consider the performance achieved with classification using a simple timing-cut: for a threshold time t_c , we classify light arriving with $t < t_c$ as Cherenkov light, and at later times $t \geq t_c$ as scintillation light. Under this classification method, we calculate the maximum statistical significance of the selected Cherenkov light as a metric for separation. This significance, and the associated Cherenkov purity, is compared across different materials. To be concrete, we define $C(t)$ and $S(t)$ as the Cherenkov and

scintillation time profiles comprising the best-fit models of Section 6.3.7, and determine

$$t_c = \max_t \frac{\int_{-\infty}^t C(t') dt'}{\sqrt{\int_{-\infty}^t (C(t') + S(t')) dt'}}, \quad (6.25)$$

from which we calculate an associated purity

$$\mathcal{P} = \frac{\int_{-\infty}^{t_c} C(t') dt'}{\int_{-\infty}^t (C(t') + S(t')) dt'}. \quad (6.26)$$

This is performed independently for the time profiles observed in the LAPPD and PMT, which reflect “best-case” and “baseline” levels of performance, respectively, owing to the different timing characteristics and geometric Cherenkov acceptances of the two photodetectors. The significances, as a function of the timing cut value, are shown in Figure 6.28, and the optimal significances and associated purities are listed in Table 6.13 and Table 6.14. The dominant determinant of the Cherenkov significance and purity is, naturally, the scintillation light yield of the material. Secondary is the rise time of the scintillator, as slower rise times allow for a longer Cherenkov-dominant regime and more generous selection cut to be used. The PMT exhibits lower performance than the LAPPD principally because of the lower geometric acceptance, but also because of its relatively poor timing resolution.

It should be noted that, while the normalized-significance and purity quantities provide a comparison between different materials, care should be taken in extrapolating to different scenarios, such as large-scale detectors. Putting aside time profile distortions from optical effects, the significance, being a statistical quantity, scales proportionally with \sqrt{N} , where N is the total number of photons collected in any detector deployment, and this depends on many factors: the light yield of the material, the length scales present in and photocoverage of the detector, etc. The purity is properly normalized across light levels, and so offers a more transparent extrapolation in certain scenarios, though care should still be taken to consider how optical effects may impact the observed timing, and e.g. the absolute amount of Cherenkov light collected.

	WbLS			LAB+PPO		
	1%	5%	10%	0.61 g/L	1.1 g/L	2.0 g/L
t_c [ps]	553	409	352	500	387	352
Significance / \sqrt{N}	0.548	0.383	0.319	0.174	0.165	0.162
Purity [%]	81.6	71.7	70.3	73.1	71.1	69.9

Table 6.13: Maximal statistical significance of Cherenkov selection, and associated Cherenkov purity, for electron time profiles detected in WbLS and LAB+PPO samples using the LAPPD. The cut time t_c is defined relative to the peak of the Cherenkov time profile.

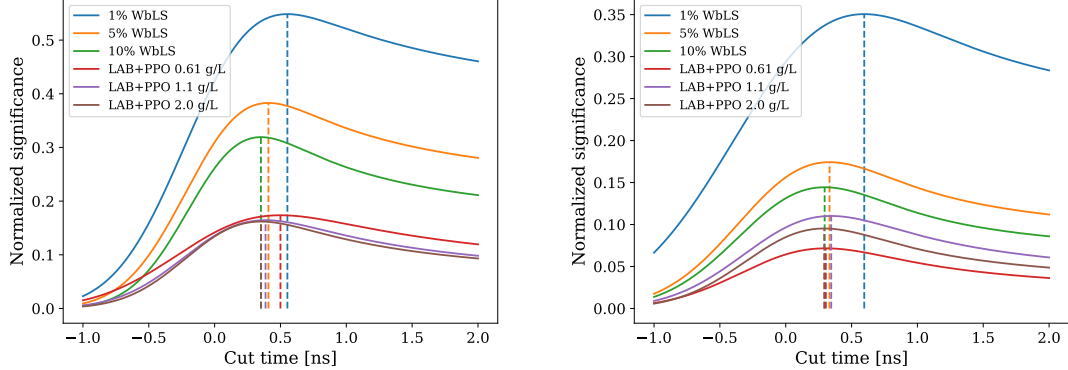


Figure 6.28: Statistical significance of Cherenkov selection, as a function of the timing cut value, for WbLS and LAB+PPO samples observed with the LAPPD (left) and PMT (right). The dashed lines denote the optimal cut value for each material.

	WbLS			LAB+PPO		
	1%	5%	10%	0.61 g/L	1.1 g/L	2.0 g/L
t_c [ps]	596	333	296	304	346	293
Significance / \sqrt{N}	0.351	0.174	0.144	0.072	0.110	0.095
Purity [%]	61.8	44.6	42.4	52.1	57.8	53.2

Table 6.14: Maximal statistical significance of Cherenkov selection, and associated Cherenkov purity, for electron time profiles detected in WbLS and LAB+PPO samples using the PMT. The cut time t_c is defined relative to the peak of the Cherenkov time profile.

6.4 Summary of R&D measurements

The development of new technology, generally, is an iterative process — prototype behavior must be characterized and assessed for fitness, before refining the design to iterate closer to an optimum. In the case of material formulation for hybrid Cherenkov/scintillation neutrino detectors, assessment for fitness includes Monte Carlo simulations of detector performance and medium-scale deployments in a real detector, both of which require material characterizations as input. We have presented measurements of the scintillation light yield in response to protons and the scintillation time profile in response to electrons and α particles, for samples of WbLS and LAB+PPO, the former being a candidate for hybrid detection. This includes the first demonstration of high-purity Cherenkov selection in WbLS, using only timing information. Such high-purity selection is a prerequisite for directional reconstruction, one of the core goals of hybrid technology. The quantitative results of this characterization, in conjunction with additional measurements of the scintillation light yields in response to electrons and α particles, are currently being used as input to simulations and analysis of data from EOS, a ton-scale detector which will demonstrate advanced reconstruction using hybrid detection technology [95], as well simulations to predict the performance of THEIA,

a tons-of-kiloton-scale hybrid detector currently under design which will address a broad physics program [37].

Chapter 7

Concluding Remarks

Once thought to have been inconsequential beyond the nature of β -decay spectra, neutrinos have come to support a vast research program, spanning fundamental physics to terrestrial applied science and searches for new astrophysical phenomena in the cosmos. The resolution of the SNP at the turn of the century revealed the first definitive shortcoming of the Standard Model of Particle Physics, the correction for which the scientific community is still in pursuit of. In the years since, the nature of neutrino flavor transformation has been robustly characterized and quantified to a precision level. This means that, on the one hand, the detection of neutrinos can confidently be used as a probe of both man-made and natural phenomena, including nuclear reactor activity and astrophysical processes and, on the other, that future experimental programs will be limited intrinsically by their backgrounds and detector designs. This dissertation addresses both limitations in presenting a characterization of the dominant cosmogenic background in large-scale neutrino detectors using a new target material, a search for new astrophysics manifesting as high-energy antineutrinos, and a lab-scale R&D program toward hybrid detector technology via characterization of the scintillation properties of WbLS.

The measurement of cosmogenic neutrons in SNO presents a distinct data point — while systematic studies of neutron production in muon interactions in have been performed in high- Z / thin-geometry targets, little is known about its general nature over large length scales, and virtually all existing studies utilize similar organic liquid scintillators as target media. The neutron yield result from SNO offers both a novel test point for nuclear modeling, as the deuteron is uniquely the most weakly bound of all stable nuclei, and establishes the first in a program of measurements to be made in the same detector, as the SNO+ experiment has completed operations with pure water and is currently operating with a liquid scintillator. The eventual establishment of three data sets taken with three different materials in the same detector will allow for the first systematic study of the neutron production rate as a function of material over large distances, which will doubtless be of use in the design and analysis of data from ultra-large-scale detectors with exchangeable target material, such as THEIA.

Farther from Earth, impressive high-energy processes occurring out in the universe have

made themselves known via new experimental signatures, including neutrinos. This, coupled with the absence of significant signals of dark matter in direct-detection, collider-based, and indirect optical measurement campaigns have positioned neutrinos as a modern candidate for probing the presence of dark matter indirectly, either as annihilation products of new particles or Hawking radiation from black holes formed early in the universe. The search for an excess of high-energy antineutrinos in SNO+ has yielded no significant excess above background, consistent with the results of previous searches, but the two events detected are outside of the energy ranges considered in previous work and are closely-spaced in energy. The interpretation of this spectral feature must be deferred to after the accumulation of more data, which will be achieved with increased livetime and an expanded fiducial volume made available by improved reconstruction algorithms.

Finally, the dream of a hybrid optical detector, which consciously detects both Cherenkov and scintillation photons to be treated preferentially with novel reconstruction techniques, is fast becoming a reality. As part of a larger campaign to develop high-timing-resolution photodetectors suitable for a large detector volume, and spectral sorting devices to produce Cherenkov- and scintillation-rich data streams chromatically, using optical hardware, characterization of candidate scintillators to be used as target material is underway.

The investigation both of new formulations, such as WbLS, and conventional scintillator cocktails, such as LAB+PPO, using state-of-the-art LAPPD technology has demonstrated an impressive level of Cherenkov/scintillation separation, using timing information alone, at the benchtop scale — and such results will only improve with refinements to the material composition and in combination with spectral sorting. Such Cherenkov/scintillation separation is key to achieving directional reconstruction in a scintillator detector, which then enables the selection of a high-purity signal in real detector data, for applications including searches for neutrinoless double- β decay, solar neutrinos, and potentially reactor neutrino monitoring.

The scintillation time profiles of both WbLS and LAB+PPO samples in response to electrons and α particles have been measured, which is a prerequisite for modeling real detectors and performing event reconstruction. Differences in the time profiles can be used to distinguish between the two species, enabling background rejection via particle-identification, studies of which are ongoing. Additionally, the scintillation light yields in response to protons have been measured using the 88-Inch Cyclotron at LBNL, which enables flavor-inclusive spectral measurements of supernova neutrinos via $\nu - p$ elastic scattering, and enhances reactor neutrino measurements by allowing for efficient rejection of fast neutron backgrounds.

The results of the measurements presented in this work advance the sensitivities of future detectors by enabling more accurate predictions of background rates and studies of signal selection, on the basis of vertex and directional reconstruction. As part of a larger hybrid R&D campaign, the characterization of scintillation properties of WbLS have led to imminent ton-scale demonstrations of hybrid technology. This includes deployment of WbLS in the ANNIE detector, and the construction of the EOS detector, both of which will adapt the results of this lab-scale work to prepare for scaling to larger volumes.

Bibliography

- [1] W. Pauli, “Letter to L. Meitner and her colleagues”, 1930.
- [2] C. L. Cowan et al., “Detection of the free neutrino: a confirmation”, *Science* **124**, 103–104 (1956) 10.1126/science.124.3212.103, eprint: <https://www.science.org/doi/pdf/10.1126/science.124.3212.103>, <https://www.science.org/doi/abs/10.1126/science.124.3212.103>.
- [3] R. L. Workman et al. (Particle Data Group), “Review of particle physics”, *Prog. Theor. Exp. Phys.* **2022**, 083C01 (2022).
- [4] S. Weinberg, “A model of leptons”, *Phys. Rev. Lett.* **19**, 1264–1266 (1967) 10.1103/PhysRevLett.19.1264, <https://link.aps.org/doi/10.1103/PhysRevLett.19.1264>.
- [5] F. Englert and R. Brout, “Broken symmetry and the mass of gauge vector mesons”, *Phys. Rev. Lett.* **13**, 321–323 (1964) 10.1103/PhysRevLett.13.321, <https://link.aps.org/doi/10.1103/PhysRevLett.13.321>.
- [6] P. W. Higgs, “Broken symmetries and the masses of gauge bosons”, *Phys. Rev. Lett.* **13**, 508–509 (1964) 10.1103/PhysRevLett.13.508, <https://link.aps.org/doi/10.1103/PhysRevLett.13.508>.
- [7] G. S. Guralnik et al., “Global conservation laws and massless particles”, *Phys. Rev. Lett.* **13**, 585–587 (1964) 10.1103/PhysRevLett.13.585, <https://link.aps.org/doi/10.1103/PhysRevLett.13.585>.
- [8] J. N. Bahcall, “Solar Neutrinos. I. Theoretical”, *Phys. Rev. Lett.* **12**, 300–302 (1964), <https://link.aps.org/doi/10.1103/PhysRevLett.12.300>.
- [9] R. Davis et al., “Search for neutrinos from the sun”, *Phys. Rev. Lett.* **20**, 1205–1209 (1968) 10.1103/PhysRevLett.20.1205, <https://link.aps.org/doi/10.1103/PhysRevLett.20.1205>.
- [10] Y. Totsuka, “Recent results on solar neutrinos from Kamiokande”, *Nucl. Phys. B - Proceedings Supplements* **19**, 69–76, ISSN: 0920-5632 (1991) [https://doi.org/10.1016/0920-5632\(91\)90189-L](https://doi.org/10.1016/0920-5632(91)90189-L), <https://www.sciencedirect.com/science/article/pii/092056329190189L>.

- [11] J. N. Abdurashitov et al., “Solar neutrino flux measurements by the Soviet-American gallium experiment (SAGE) for half the 22-year solar cycle”, *Jour. of Exp. and Theo. Phys.* **95**, 181–193 (2002) 10.1134/1.1506424, <https://doi.org/10.1134%2F1.1506424>.
- [12] M. Altmann et al., “Complete results for five years of GNO solar neutrino observations”, *Phys. Lett. B* **616**, 174–190 (2005) 10.1016/j.physletb.2005.04.068, <https://doi.org/10.1016%2Fj.physletb.2005.04.068>.
- [13] F. Kaether et al., “Reanalysis of the GALLEX solar neutrino flux and source experiments”, *Phys. Lett. B* **685**, 47–54, ISSN: 0370-2693 (2010) <https://doi.org/10.1016/j.physletb.2010.01.030>, <https://www.sciencedirect.com/science/article/pii/S0370269310000729>.
- [14] L. Wolfenstein, “Neutrino oscillations in matter”, *Phys. Rev. D* **17**, 2369–2374 (1978) 10.1103/PhysRevD.17.2369, <https://link.aps.org/doi/10.1103/PhysRevD.17.2369>.
- [15] S. P. Mikheyev and A. Y. Smirnov, “Resonant amplification of ν oscillations in matter and solar-neutrino spectroscopy”, *Nuovo Cimento* **9**, 17–26 (1986) 10.1007/BF02508049, <https://doi.org/10.1007/BF02508049>.
- [16] Y. Fukuda et al. (Super-Kamiokande Collaboration), “Evidence for oscillation of atmospheric neutrinos”, *Phys. Rev. Lett.* **81**, 1562–1567 (1998) 10.1103/PhysRevLett.81.1562, <https://link.aps.org/doi/10.1103/PhysRevLett.81.1562>.
- [17] H. H. Chen, “Direct approach to resolve the solar-neutrino problem”, *Phys. Rev. Lett.* **55**, 1534–1536 (1985) 10.1103/PhysRevLett.55.1534, <https://link.aps.org/doi/10.1103/PhysRevLett.55.1534>.
- [18] B. Aharmim et al. (SNO Collaboration), “Combined analysis of all three phases of solar neutrino data from the Sudbury Neutrino Observatory”, *Phys. Rev. C* **88**, 025501 (2013).
- [19] T. Araki et al. (KamLAND Collaboration), “Measurement of Neutrino Oscillation with KamLAND: Evidence of Spectral Distortion”, *Phys. Rev. Lett.* **94**, 081801 (2005) 10.1103/PhysRevLett.94.081801, <https://link.aps.org/doi/10.1103/PhysRevLett.94.081801>.
- [20] B. Pontecorvo, “Inverse beta decay processes and nonconservation of lepton charge”, *Zhurnal Èksperimental'noi i Teoreticheskoi Fiziki* **34**, 247 (1959).
- [21] Z. Maki et al., “Remarks on the Unified Model of Elementary Particles”, *Progress of Theoretical Physics* **28**, 870–880, ISSN: 0033-068X (1962) 10.1143/PTP.28.870, <https://doi.org/10.1143/PTP.28.870>.
- [22] T. Yanagida, “Horizontal symmetry and mass of the t quark”, *Phys. Rev. D* **20**, 2986–2988 (1979) 10.1103/PhysRevD.20.2986, <https://link.aps.org/doi/10.1103/PhysRevD.20.2986>.

- [23] T. Yanagida, “Horizontal Symmetry and Masses of Neutrinos”, *Progress of Theoretical Physics* **64**, 1103–1105, ISSN: 0033-068X (1980) 10.1143/PTP.64.1103, <https://doi.org/10.1143/PTP.64.1103>.
- [24] E. W. Kolb and M. S. Turner, “Grand unified theories and the origin of the baryon asymmetry”, *33*, 645–696 (1983) 10.1146/annurev.ns.33.120183.003241, eprint: <https://doi.org/10.1146/annurev.ns.33.120183.003241>, <https://doi.org/10.1146/annurev.ns.33.120183.003241>.
- [25] J. Schechter and J. W. F. Valle, “Neutrinoless double- β decay in $SU(2)\times U(1)$ theories”, *Phys. Rev. D* **25**, 2951–2954 (1982) 10.1103/PhysRevD.25.2951, <https://link.aps.org/doi/10.1103/PhysRevD.25.2951>.
- [26] W. Buchmüller et al., “Leptogenesis as the origin of matter”, *55*, 311–355 (2005) 10.1146/annurev.nucl.55.090704.151558, eprint: <https://doi.org/10.1146/annurev.nucl.55.090704.151558>, <https://doi.org/10.1146/annurev.nucl.55.090704.151558>.
- [27] K. Abe et al. (The T2K Collaboration), “Constraint on the matter-antimatter symmetry-violating phase in neutrino oscillations”, *Nature* **580**, 339–344 (2020) 10.1038/s41586-020-2177-0.
- [28] M. A. Acero et al. (The NO ν A Collaboration), “Improved measurement of neutrino oscillation parameters by the nova experiment”, *Phys. Rev. D* **106**, 032004 (2022) 10.1103/PhysRevD.106.032004, <https://link.aps.org/doi/10.1103/PhysRevD.106.032004>.
- [29] U. Rahaman et al., “A review of the tension between the T2K and NO ν A appearance data and hints to new physics”, *Universe* **8**, 109 (2022) 10.3390/universe8020109, <https://doi.org/10.3390%2Funiverse8020109>.
- [30] B. Abi et al., “Long-baseline neutrino oscillation physics potential of the DUNE experiment”, *Eur. Phys. Jour. C* **80**, 10.1140/epjc/s10052-020-08456-z (2020) 10.1140/epjc/s10052-020-08456-z, <https://doi.org/10.1140%2Fepjc%2Fs10052-020-08456-z>.
- [31] A. A. Abud et al. (DUNE Collaboration), “Low exposure long-baseline neutrino oscillation sensitivity of the DUNE experiment”, *Phys. Rev. D* **105**, 072006 (2022) 10.1103/PhysRevD.105.072006, <https://link.aps.org/doi/10.1103/PhysRevD.105.072006>.
- [32] K. Abe et al. (Hyper-Kamiokande Proto-Collaboration), “Hyper-Kamiokande Design Report”, 2018, arXiv:1805.04163 [physics.ins-det].
- [33] M. J. Dolinski et al., “Neutrinoless double-beta decay: status and prospects”, *69*, 219–251 (2019) 10.1146/annurev-nucl-101918-023407, eprint: <https://doi.org/10.1146/annurev-nucl-101918-023407>, <https://doi.org/10.1146/annurev-nucl-101918-023407>.

- [34] S. A. Kharusi et al. (nEXO Collaboration), “nEXO Pre-Conceptual Design Report”, 2018, [arXiv:1805.11142 \[physics.ins-det\]](https://arxiv.org/abs/1805.11142).
- [35] The CUPID Interest Group, “CUPID pre-CDR”, 2019, [arXiv:1907.09376](https://arxiv.org/abs/1907.09376).
- [36] N. Abgrall et al. (LEGEND Collaboration), “LEGEND-1000 Preconceptual Design Report”, 2021, [arXiv:2107.11462 \[physics.ins-det\]](https://arxiv.org/abs/2107.11462).
- [37] M. Askins et al., “THEIA: an advanced optical neutrino detector”, *Eur. Phys. Jour. C* **80**, 416, ISSN: 1434-6052 (2020) 10.1140/epjc/s10052-020-7977-8.
- [38] M. Aker et al. (KATRIN Collaboration), “KATRIN: status and prospects for the neutrino mass and beyond”, *Nature* **49**, 100501 (2022) 10.1088/1361-6471/ac834e, <https://doi.org/10.1088%2F1361-6471%2Fac834e>.
- [39] A. A. Esfahani et al. (Project 8 Collaboration), “Tritium beta spectrum and neutrino mass limit from cyclotron radiation emission spectroscopy”, 2023, [arXiv:2212.05048 \[nucl-ex\]](https://arxiv.org/abs/2212.05048).
- [40] P. B. Denton and J. Gehrlein, “A survey of neutrino flavor models and the neutrinoless double beta decay funnel”, 2023, [arXiv:2308.09737 \[hep-ph\]](https://arxiv.org/abs/2308.09737).
- [41] V. V. Barinov et al. (BEST Collaboration), “Results from the baksan experiment on sterile transitions (BEST)”, *Phys. Rev. Lett.* **128**, 10.1103/physrevlett.128.232501 (2022) 10.1103/physrevlett.128.232501, <https://doi.org/10.1103%2Fphysrevlett.128.232501>.
- [42] V. V. Barinov et al. (BEST Collaboration), “Search for electron-neutrino transitions to sterile states in the BEST experiment”, *Phys. Rev. C* **105**, 10.1103/physrevc.105.065502 (2022) 10.1103/physrevc.105.065502, <https://doi.org/10.1103%2Fphysrevc.105.065502>.
- [43] A. Aguilar et al. (LSND Collaboration), “Evidence for neutrino oscillations from the observation of $\bar{\nu}_e$ appearance in a $\bar{\nu}_\mu$ beam”, *Phys. Rev. D* **64**, 112007 (2001) 10.1103/PhysRevD.64.112007, <https://link.aps.org/doi/10.1103/PhysRevD.64.112007>.
- [44] A. A. Aguilar-Arevalo et al. (MiniBooNE Collaboration), “Updated MiniBooNE neutrino oscillation results with increased data and new background studies”, *Phys. Rev. D* **103**, 052002 (2021) 10.1103/PhysRevD.103.052002, <https://link.aps.org/doi/10.1103/PhysRevD.103.052002>.
- [45] P. Abratenko et al. (MicroBooNE Collaboration), “First constraints on light sterile neutrino oscillations from combined appearance and disappearance searches with the MicroBooNE detector”, *Phys. Rev. Lett.* **130**, 10.1103/physrevlett.130.011801 (2023) 10.1103/physrevlett.130.011801, <https://doi.org/10.1103%2Fphysrevlett.130.011801>.

- [46] P. Bakhti and M. Rajaei, “Sensitivities of future solar neutrino observatories to nonstandard neutrino interactions”, *Phys. Rev. D* **102**, 035024 (2020) 10.1103/PhysRevD.102.035024, <https://link.aps.org/doi/10.1103/PhysRevD.102.035024>.
- [47] A. Giannetti and D. Meloni, “Probing source and detector nonstandard interaction parameters at the DUNE near detector”, *Phys. Rev. D* **104**, 10.1103/physrevd.104.015027 (2021) 10.1103/physrevd.104.015027, <https://doi.org/10.1103/physrevd.104.015027>.
- [48] N. Aghanim et al. (Planck Collaboration), “Planck 2018 results”, *Astron. and Astrophys.* **641**, A6 (2020) 10.1051/0004-6361/201833910, <https://doi.org/10.1051/0004-6361%2F201833910>.
- [49] F. Zwicky, “On the masses of nebulae and of clusters of nebulae”, *The Astrophys. Jour.* **86**, 217 (1937) 10.1086/143864.
- [50] V. C. Rubin et al., “Rotational properties of 21 SC galaxies with a large range of luminosities and radii, from NGC 4605 (R=4 kpc) to UGC 2885 (R=122 kpc).”, *The Astrophys. Jour.* **238**, 471–487 (1980) 10.1086/158003.
- [51] A. Refregier, “Weak gravitational lensing by large-scale structure”, *Ann. Rev. of Astron. and Astrophys.* **41**, 645–668 (2003) 10.1146/annurev.astro.41.111302.102207, <https://doi.org/10.1146%2Fannurev.astro.41.111302.102207>.
- [52] G. Bertone and D. Merritt, “Dark matter dynamics and indirect detection”, *Mod. Phys. Lett. A* **20**, 1021–1036 (2005) 10.1142/s0217732305017391, <https://doi.org/10.1142%2Fs0217732305017391>.
- [53] J. L. Feng, “Dark matter candidates from particle physics and methods of detection”, *Ann. Rev. of Astron. and Astrophys.* **48**, 495–545 (2010) 10.1146/annurev-astro-082708-101659, eprint: <https://doi.org/10.1146/annurev-astro-082708-101659>, <https://doi.org/10.1146/annurev-astro-082708-101659>.
- [54] G. Jungman et al., “Supersymmetric dark matter”, *Physics Reports* **267**, 195–373 (1996) 10.1016/0370-1573(95)00058-5, <https://doi.org/10.1016/0370-1573%2895%2900058-5>.
- [55] J. Aalbers et al. (LUX-ZEPLIN (LZ) Collaboration), “First dark matter search results from the LUX-ZEPLIN (LZ) experiment”, *Phys. Rev. Lett.* **131**, 10.1103/physrevlett.131.041002 (2023) 10.1103/physrevlett.131.041002, <https://doi.org/10.1103/physrevlett.131.041002>.
- [56] J. M. Lorenz, “Supersymmetry and the collider dark matter picture”, *Mod. Phys. Lett. A* **34**, 1930005 (2019) 10.1142/s0217732319300052, <https://doi.org/10.1142%2Fs0217732319300052>.
- [57] S. Hawking, “Black hole explosions?”, *Nature* **248**, 30–31 (1974) 10.1038/248030a0, <https://doi.org/10.1038/248030a0>.

- [58] D. N. Page, “Information in black hole radiation”, *Phys. Rev. Lett.* **71**, 3743–3746 (1993) [10.1103/physrevlett.71.3743](https://doi.org/10.1103/physrevlett.71.3743).
- [59] S. Hawking, “Particle creation by black holes”, *Commun. Math. Phys.* **43**, 199–220 (1975) [10.1007/BF02345020](https://doi.org/10.1007/BF02345020), <https://doi.org/10.1007/BF02345020>.
- [60] S. C. Curran, *Counting tubes: theory and applications* (Academic Press, New York, 1949).
- [61] K. Fang et al., “The Giant Radio Array for Neutrino Detection (GRAND): Present and Perspectives”, 2017, [arXiv:1708.05128 \[astro-ph.IM\]](https://arxiv.org/abs/1708.05128).
- [62] P. Cherenkov, “Visible emission of clean liquids by action of γ -rays”, *Doklady Akad. Nauk* **2**, 451 (1934).
- [63] I. E. Frank and I. M. Tamm, “Coherent visible radiation of fast electrons passing through matter”, *Doklady Akad. Nauk* **14**, 105 (1937).
- [64] *Nobel lectures, physics 1901 - 1921*, See chapter on Henri Becquerel (Elsevier Publishing Company, Amsterdam, 1967).
- [65] J. Birks, *The theory and practice of scintillation counting*, International Series of Monographs in Electronics and Instrumentation (Pergamon Press, New York, 1964) Chap. 6, pp. 185–234, ISBN: 978-0-08-010472-0.
- [66] T. A. Laplace et al., “Modeling ionization quenching in organic scintillators”, *Materials Advances* **3**, 5871–5881 (2022) [10.1039/D2MA00388K](https://doi.org/10.1039/D2MA00388K).
- [67] R. M. Bionta et al., “Observation of a neutrino burst in coincidence with supernova 1987A in the Large Magellanic Cloud”, *Phys. Rev. Lett.* **58**, 1494–1496 (1987) [10.1103/PhysRevLett.58.1494](https://doi.org/10.1103/PhysRevLett.58.1494), [https://link.aps.org/doi/10.1103/PhysRevLett.58.1494](https://doi.org/10.1103/PhysRevLett.58.1494).
- [68] K. Hirata et al., “Observation of a neutrino burst from the supernova SN1987A”, *Phys. Rev. Lett.* **58**, 1490–1493 (1987) [10.1103/PhysRevLett.58.1490](https://doi.org/10.1103/PhysRevLett.58.1490), [https://link.aps.org/doi/10.1103/PhysRevLett.58.1490](https://doi.org/10.1103/PhysRevLett.58.1490).
- [69] K. Hirata et al., “Experimental study of the atmospheric neutrino flux”, *Phys. Lett. B* **205**, 416–420, ISSN: 0370-2693 (1988) [https://doi.org/10.1016/0370-2693\(88\)91690-5](https://doi.org/10.1016/0370-2693(88)91690-5), <https://www.sciencedirect.com/science/article/pii/0370269388916905>.
- [70] J. Boger et al. (SNO Collaboration), “The Sudbury Neutrino Observatory”, *Nucl. Inst. and Meth. in Phys. Res. Sect. A: Accel., Spect., Det. and Assoc. Equip.* **449**, 172–207 (2000) [10.1016/s0168-9002\(99\)01469-2](https://doi.org/10.1016/s0168-9002(99)01469-2), <https://doi.org/10.1016%2Fs0168-9002%2899%2901469-2>.
- [71] F. Suekane et al., “Recent status of the KamLAND experiment”, *Nucl. Phys. B - Proceedings Supplements* **111**, 128–132, ISSN: 0920-5632 (2002) [https://doi.org/10.1016/S0920-5632\(02\)01694-8](https://doi.org/10.1016/S0920-5632(02)01694-8), <https://www.sciencedirect.com/science/article/pii/S0920563202016948>.

- [72] C. Athanassopoulos et al., “The Liquid Scintillator Neutrino Detector and LAMPF neutrino source”, *Nucl. Inst. and Meth. in Phys. Res. Sect. A: Accel., Spect., Det. and Assoc. Equip.* **388**, 149–172 (1997) 10.1016/s0168-9002(96)01155-2, <https://doi.org/10.1016%2Fs0168-9002%2896%2901155-2>.
- [73] G. Drexlin et al., “The high resolution neutrino calorimeter KARMEN”, *Nucl. Inst. and Meth. in Phys. Res. Sect. A: Accel., Spect., Det. and Assoc. Equip.* **289**, 490–495, ISSN: 0168-9002 (1990) [https://doi.org/10.1016/0168-9002\(90\)91521-C](https://doi.org/10.1016/0168-9002(90)91521-C), <https://www.sciencedirect.com/science/article/pii/016890029091521C>.
- [74] A. G. Piepke et al., “Development of a Gd loaded liquid scintillator for electron anti-neutrino spectroscopy”, *Nucl. Inst. and Meth. in Phys. Res. Sect. A: Accel., Spect., Det. and Assoc. Equip.* **432**, 392–398 (1999) 10.1016/s0168-9002(99)00530-6, <https://doi.org/10.1016%2Fs0168-9002%2899%2900530-6>.
- [75] D. B. Collaboration, “A Precision Measurement of the Neutrino Mixing Angle θ_{13} using Reactor Antineutrinos at Daya Bay”, 2007, arXiv:hep-ex/0701029 [hep-ex].
- [76] W. Beriguete et al., “Production of a gadolinium-loaded liquid scintillator for the Daya Bay reactor neutrino experiment”, *Nucl. Inst. and Meth. in Phys. Res. Sect. A: Accel., Spect., Det. and Assoc. Equip.* **763**, 82–88, ISSN: 0168-9002 (2014) <https://doi.org/10.1016/j.nima.2014.05.119>, <https://www.sciencedirect.com/science/article/pii/S0168900214006834>.
- [77] G. Bellini et al. (BOREXINO Collaboration), “Final results of Borexino Phase-I on low-energy solar neutrino spectroscopy”, *Phys. Rev. D* **89**, 10.1103/physrevd.89.112007 (2014) 10.1103/physrevd.89.112007, <https://doi.org/10.1103%2Fphysrevd.89.112007>.
- [78] M. Anderson et al. (SNO+ Collaboration), “Search for invisible modes of nucleon decay in water with the SNO+ detector”, *Phys. Rev. D* **99**, 032008 (2019) 10.1103/PhysRevD.99.032008, <https://link.aps.org/doi/10.1103/PhysRevD.99.032008>.
- [79] A. Allega et al. (SNO+ Collaboration), “Improved search for invisible modes of nucleon decay in water with the SNO + detector”, *Phys. Rev. D* **105**, 112012 (2022) 10.1103/PhysRevD.105.112012, <https://link.aps.org/doi/10.1103/PhysRevD.105.112012>.
- [80] M. Anderson et al. (SNO+ Collaboration), “Measurement of the ${}^8\text{B}$ solar neutrino flux in SNO+ with very low backgrounds”, *Phys. Rev. D* **99**, 012012 (2019) 10.1103/PhysRevD.99.012012, <https://link.aps.org/doi/10.1103/PhysRevD.99.012012>.
- [81] A. Allega et al. (SNO+ Collaboration), “Evidence of antineutrinos from distant reactors using pure water at SNO+”, *Phys. Rev. Lett.* **130**, 091801 (2023) 10.1103/PhysRevLett.130.091801, <https://link.aps.org/doi/10.1103/PhysRevLett.130.091801>.

- [82] A. Aguilar-Arevalo et al., “The MiniBooNE detector”, *Nucl. Inst. and Meth. in Phys. Res. Sect. A: Accel., Spect., Det. and Assoc. Equip.* **599**, 28–46, ISSN: 0168-9002 (2009) <https://doi.org/10.1016/j.nima.2008.10.028>, <https://www.sciencedirect.com/science/article/pii/S0168900208015404>.
- [83] R. Patterson et al., “The extended-track event reconstruction for MiniBooNE”, *Nucl. Inst. and Meth. in Phys. Res. Sect. A: Accel., Spect., Det. and Assoc. Equip.* **608**, 206–224 (2009) [10.1016/j.nima.2009.06.064](https://doi.org/10.1016/j.nima.2009.06.064), <https://doi.org/10.1016%2Fj.nima.2009.06.064>.
- [84] M. Agostini et al. (Borexino Collaboration), “First directional measurement of sub-MeV solar neutrinos with borexino”, *Phys. Rev. Lett.* **128**, [10.1103/physrevlett.128.091803](https://doi.org/10.1103/physrevlett.128.091803) (2022) [10.1103%2Fphysrevlett.128.091803](https://doi.org/10.1103%2Fphysrevlett.128.091803), <https://doi.org/10.1103%2Fphysrevlett.128.091803>.
- [85] L. Lebanowski, *Neutrino physics with large liquid scintillator detectors*, American Physical Society April Meeting, New York City, 2022.
- [86] S. Andringa et al. (SNO+ Collaboration), “Current status and future prospects of the SNO+ experiment”, *Adv. in High Energy Phys.* **2016**, 1–21 (2016) [10.1155/2016/6194250](https://doi.org/10.1155/2016/6194250), <https://doi.org/10.1155%2F2016%2F6194250>.
- [87] B. J. Land et al., “MeV-scale performance of water-based and pure liquid scintillator detectors”, *Phys. Rev. D* **103**, [10.1103/physrevd.103.052004](https://doi.org/10.1103/physrevd.103.052004) (2021) [10.1103%2Fphysrevd.103.052004](https://doi.org/10.1103%2Fphysrevd.103.052004), <https://doi.org/10.1103%2Fphysrevd.103.052004>.
- [88] M. Yeh et al., “A new water-based liquid scintillator and potential applications”, *Nucl. Inst. and Meth. in Phys. Res. Sect. A: Accel., Spect., Det. and Assoc. Equip.* **660**, 51–56 (2011) [10.1016/j.nima.2011.08.040](https://doi.org/10.1016/j.nima.2011.08.040).
- [89] S. D. Biller et al., “Slow fluors for effective separation of Cherenkov light in liquid scintillators”, *Nucl. Inst. and Meth. in Phys. Res. Sect. A: Accel., Spect., Det. and Assoc. Equip.* **972**, 164106 (2020) [10.1016/j.nima.2020.164106](https://doi.org/10.1016/j.nima.2020.164106), <https://doi.org/10.1016%2Fj.nima.2020.164106>.
- [90] B. W. Adams et al. (LAPPD Collaboration), “A Brief Technical History of the Large-Area Picosecond Photodetector (LAPPD) Collaboration”, Mar. 2016, [arXiv:1603.01843 \[physics.ins-det\]](https://arxiv.org/abs/1603.01843).
- [91] T. Kaptanoglu et al., “Spectral photon sorting for large-scale Cherenkov and scintillation detectors”, *Phys. Rev. D* **101**, [10.1103/physrevd.101.072002](https://doi.org/10.1103/physrevd.101.072002) (2020) [10.1103%2Fphysrevd.101.072002](https://doi.org/10.1103%2Fphysrevd.101.072002), <https://doi.org/10.1103%2Fphysrevd.101.072002>.
- [92] J. Sawatzki et al., “Detecting the diffuse supernova neutrino background in the future water-based liquid scintillator detector THEIA”, *Phys. Rev. D* **103**, [10.1103/physrevd.103.023021](https://doi.org/10.1103/physrevd.103.023021) (2021) [10.1103%2Fphysrevd.103.023021](https://doi.org/10.1103%2Fphysrevd.103.023021), <https://doi.org/10.1103%2Fphysrevd.103.023021>.

- [93] A. Li et al., “KamNet: an integrated spatiotemporal deep neural network for rare event searches in KamLAND-Zen”, *Phys. Rev. C* **107**, 10.1103/physrevc.107.014323 (2023) 10.1103/physrevc.107.014323, <https://doi.org/10.1103/physrevc.107.014323>.
- [94] A. R. Back et al. (ANNIE), “Accelerator Neutrino Neutron Interaction Experiment (ANNIE): Preliminary Results and Physics Phase Proposal”, (2017), [arXiv:1707.08222 \[physics.ins-det\]](https://arxiv.org/abs/1707.08222).
- [95] T. Anderson et al., “Eos: conceptual design for a demonstrator of hybrid optical detector technology”, *Jour. of Inst.* **18**, P02009 (2023) 10.1088/1748-0221/18/02/P02009, <https://dx.doi.org/10.1088/1748-0221/18/02/P02009>.
- [96] M. Ackermann et al. (Fermi-LAT Collaboration), “Detection of the characteristic pion-decay signature in supernova remnants”, *Science* **339**, 807–811 (2013) 10.1126/science.1231160, <https://doi.org/10.1126/science.1231160>.
- [97] A. A. others (Pierre Auger Collaboration), “Observation of a large-scale anisotropy in the arrival directions of cosmic rays above 8×10^{18} ev”, *Science* **357**, 1266–1270 (2017) 10.1126/science.aan4338, <https://doi.org/10.1126/science.aan4338>.
- [98] B. P. Abbott et al. (LIGO and Virgo Collaborations), “GWTC-1: a gravitational-wave transient catalog of compact binary mergers observed by LIGO and virgo during the first and second observing runs”, *Phys. Rev. X* **9**, 10.1103/physrevx.9.031040 (2019) 10.1103/physrevx.9.031040, <https://doi.org/10.1103/physrevx.9.031040>.
- [99] T. B. Collaboration, “Experimental evidence of neutrinos produced in the CNO fusion cycle in the Sun”, *Nature* **587**, 577–582 (2020) 10.1038/s41586-020-2934-0, <https://doi.org/10.1038/s41586-020-2934-0>.
- [100] S. Appel et al., “Improved measurement of solar neutrinos from the carbon-nitrogen-oxygen cycle by Borexino and its implications for the standard solar model”, *Phys. Rev. Lett.* **129**, 10.1103/physrevlett.129.252701 (2022) 10.1103/physrevlett.129.252701, <https://doi.org/10.1103/physrevlett.129.252701>.
- [101] D. Basilico et al., “Final results of Borexino on CNO solar neutrinos”, 2023, [arXiv:2307.14636 \[hep-ex\]](https://arxiv.org/abs/2307.14636).
- [102] J. Ahrens et al. (IceCube Collaboration), “IceCube Preliminary Design Document”, 2001, <https://icecube.wisc.edu/wp-content/uploads/2020/11/IceCubeDesignDoc.pdf>.
- [103] The ANTARES Collaboration, *A deep sea telescope for high energy neutrinos*, 1999, [arXiv:astro-ph/9907432 \[astro-ph\]](https://arxiv.org/abs/astro-ph/9907432).
- [104] M. G. Aartsen et al. (IceCube Collaboration), “Detection of a particle shower at the glashow resonance with IceCube”, *Nature* **591**, 220–224 (2021) 10.1038/s41586-021-03256-1, <https://doi.org/10.1038/s41586-021-03256-1>.

- [105] M. Aartsen et al. (IceCube Collaboration), “Neutrino emission from the direction of the blazar TXS 0506+056 prior to the IceCube-170922A alert”, *Science* **361**, 147–151 (2018) 10.1126/science.aat2890, <https://doi.org/10.1126/science.aat2890>.
- [106] R. Abbasi et al. (IceCube Collaboration), “Observation of high-energy neutrinos from the galactic plane”, *Science* **380**, 1338–1343 (2023) 10.1126/science.adc9818, <https://doi.org/10.1126/science.adc9818>.
- [107] S. Palomares-Ruiz and S. Pascoli, “Testing MeV dark matter with neutrino detectors”, *Phys. Rev. D* **77**, 10.1103/physrevd.77.025025 (2008) 10.1103/physrevd.77.025025, <https://doi.org/10.1103/physrevd.77.025025>.
- [108] C. A. Argüelles et al., “Dark matter annihilation to neutrinos”, *93*, 10.1103/revmodphys.93.035007 (2021) 10.1103/revmodphys.93.035007, <https://doi.org/10.1103/revmodphys.93.035007>.
- [109] M. Ackermann et al. (Fermi-LAT Collaboration), “Updated search for spectral lines from galactic dark matter interactions with pass 8 data from the Fermi Large Area Telescope”, *Phys. Rev. D* **91**, 10.1103/physrevd.91.122002 (2015) 10.1103/physrevd.91.122002, <https://doi.org/10.1103/physrevd.91.122002>.
- [110] L. Necib et al., “Boosted dark matter at neutrino experiments”, *Phys. Rev. D* **95**, 075018 (2017) 10.1103/PhysRevD.95.075018, <https://link.aps.org/doi/10.1103/PhysRevD.95.075018>.
- [111] C. V. Cappiello et al., “Reverse direct detection: cosmic ray scattering with light dark matter”, *Phys. Rev. D* **99**, 10.1103/physrevd.99.063004 (2019) 10.1103/physrevd.99.063004, <https://doi.org/10.1103/physrevd.99.063004>.
- [112] K. Abe et al. (Super-Kamiokande Collaboration), “Search for cosmic-ray boosted sub-GeV dark matter using recoil protons at Super-Kamiokande”, *Phys. Rev. Lett.* **130**, 10.1103/physrevlett.130.031802 (2023) 10.1103/physrevlett.130.031802, <https://doi.org/10.1103/physrevlett.130.031802>.
- [113] D. McKeen et al., “Dark matter annihilation inside large-volume neutrino detectors”, *Phys. Rev. Lett.* **131**, 10.1103/physrevlett.131.011005 (2023) 10.1103/physrevlett.131.011005, <https://doi.org/10.1103/physrevlett.131.011005>.
- [114] B. Aharmim et al. (SNO Collaboration), “Electron antineutrino search at the Sudbury Neutrino Observatory”, *Phys. Rev. D* **70**, 093014 (2004) 10.1103/PhysRevD.70.093014, <https://link.aps.org/doi/10.1103/PhysRevD.70.093014>.
- [115] M. Agostini et al. (Borexino Collaboration), “Search for low-energy neutrinos from astrophysical sources with borexino”, *Astropart. Phys.* **125**, 102509, ISSN: 0927-6505 (2021) <https://doi.org/10.1016/j.astropartphys.2020.102509>, <https://www.sciencedirect.com/science/article/pii/S0927650520300815>.

- [116] S. Abe et al., “Limits on astrophysical antineutrinos with the KamLAND experiment”, *The Astrophys. Jour.* **925**, 14 (2022) 10.3847/1538-4357/ac32c1, <https://doi.org/10.3847%2F1538-4357%2Fac32c1>.
- [117] K. Abe et al. (Super-Kamiokande Collaboration), “Diffuse supernova neutrino background search at Super-Kamiokande”, *Phys. Rev. D* **104**, 122002 (2021) 10.1103/PhysRevD.104.122002, <https://link.aps.org/doi/10.1103/PhysRevD.104.122002>.
- [118] M. Harada et al. (Super-Kamiokande Collaboration), “Search for astrophysical electron antineutrinos in Super-Kamiokande with 0.01% gadolinium-loaded water”, *The Astrophys. Jour. Lett.* **951**, L27 (2023) 10.3847/2041-8213/acdc9e, <https://dx.doi.org/10.3847/2041-8213/acdc9e>.
- [119] B. Carr and F. Kühnel, “Primordial black holes as dark matter: recent developments”, **70**, 355–394 (2020) 10.1146/annurev-nucl-050520-125911, eprint: <https://doi.org/10.1146/annurev-nucl-050520-125911>, <https://doi.org/10.1146/annurev-nucl-050520-125911>.
- [120] M. Ackermann et al. (Fermi-LAT Collaboration), “Search for gamma-ray emission from local primordial black holes with the Fermi Large Area Telescope”, *The Astrophys. Jour.* **857**, 49 (2018) 10.3847/1538-4357/aaac7b, <https://dx.doi.org/10.3847/1538-4357/aaac7b>.
- [121] S. Wang et al., “Constraining primordial black holes as dark matter at JUNO”, *Phys. Rev. D* **103**, 10.1103/physrevd.103.043010 (2021) 10.1103/physrevd.103.043010, <https://doi.org/10.1103%2Fphysrevd.103.043010>.
- [122] N. Bernal et al., “Current and future neutrino limits on the abundance of primordial black holes”, **2022**, 068 (2022) 10.1088/1475-7516/2022/10/068, <https://dx.doi.org/10.1088/1475-7516/2022/10/068>.
- [123] L. B. Bezrukov et al., “Investigation of depth-intensity curve of nuclear events induced by muons”, *Sov. J. Nucl. Phys.* **17**, 51 (1973), <https://www.osti.gov/biblio/4281237>.
- [124] R. I. Enikeev et al., “Hadrons generated by cosmic-ray muons underground”, *Sov. J. Nucl. Phys.* **46:5**, 883 (1987), <https://www.osti.gov/biblio/5160630>.
- [125] M. Aglietta et al., “Neutron flux generated by cosmic-ray muons at 5200 hg/cm² s.r. underground. depth-neutron intensity curve.”, *Il Nuovo Cimento C* **12**, 467–477 (1989).
- [126] M. Aglietta et al. (LVD Collaboration), “Measurement of the neutron flux produced by cosmic-ray muons with LVD at Gran Sasso”, Proceedings, 26th International Cosmic Ray Conference (1999).
- [127] R. Hertenberger et al., “Muon-induced neutron and pion production in an organic liquid scintillator at a shallow depth”, *Phys. Rev. C* **52**, 3449 (1995).

- [128] T. Hagner et al., “Muon-induced production of radioactive isotopes in scintillation detectors”, *Astropart. Phys.* **14**, 33–47, ISSN: 0927-6505 (2000) [https://doi.org/10.1016/S0927-6505\(00\)00103-1](https://doi.org/10.1016/S0927-6505(00)00103-1), <https://www.sciencedirect.com/science/article/pii/S0927650500001031>.
- [129] F. Boehm et al. (Palo Verde Collaboration), “Neutron production by cosmic-ray muons at shallow depth”, *Phys. Rev. D* **62**, 092005 (2000).
- [130] H. M. Araujo et al., “Measurements of neutrons produced by high-energy muons at the Boulby Underground Laboratory”, *Astropart. Phys.* **29**, 471 (2008).
- [131] S. Abe et al. (KamLAND Collaboration), “Production of radioactive isotopes through cosmic muon spallation in KamLAND”, *Phys. Rev. C* **81**, 025807 (2010).
- [132] G. Bellini et al. (Borexino Collaboration), “Cosmogenic backgrounds in Borexino at 3800 m water-equivalent depth”, **2013**, 049 (2013).
- [133] H. M. Kluck, “Measurement of the cosmic-induced neutron yield at the Modane Underground Laboratory”, PhD thesis (Karlsruhe Institute of Technology, 2013).
- [134] L. Reichhart et al., “Measurement and simulation of the muon-induced neutron yield in lead”, *Astropart. Phys.* **29**, 67 (2007).
- [135] S. C. Blyth et al. (Aberdeen Tunnel Experiment Collaboration), “Measurement of cosmic-ray muons and muon-induced neutrons in the Aberdeen Tunnel Underground Laboratory”, *Phys. Rev. D* **93**, 072005 (2016).
- [136] F. P. An et al. (Daya Bay Collaboration), “Cosmogenic neutron production at daya bay”, *Phys. Rev. D* **97**, 052009 (2018).
- [137] L. Zhao et al. (JNE Collaboration), “Measurement of muon-induced neutron yield at the China Jinping Underground Laboratory”, *Chinese Physics C* **46**, 085001 (2022) [10.1088/1674-1137/ac66cc](https://dx.doi.org/10.1088/1674-1137/ac66cc), <https://dx.doi.org/10.1088/1674-1137/ac66cc>.
- [138] M. Shinoki et al. (The Super-Kamiokande Collaboration), “Measurement of the cosmogenic neutron yield in Super-Kamiokande with gadolinium loaded water”, *Phys. Rev. D* **107**, 092009 (2023) [10.1103/PhysRevD.107.092009](https://doi.org/10.1103/PhysRevD.107.092009), <https://link.aps.org/doi/10.1103/PhysRevD.107.092009>.
- [139] D.-M. Mei and A. Hime, “Muon-induced background study for underground laboratories”, *Phys. Rev. D* **73**, 053004 (2006).
- [140] B. Aharmim et al. (SNO Collaboration), “Determination of the ν_e and total ^8B solar neutrino fluxes with the Sudbury Neutrino Observatory Phase I data set”, *Phys. Rev. C* **75**, 045502 (2007).
- [141] B. Aharmim et al. (SNO Collaboration), “Electron energy spectra, fluxes, and day-night asymmetries of ^8B solar neutrinos from measurements with NaCl dissolved in the heavy-water detector at the Sudbury Neutrino Observatory”, *Phys. Rev. C* **72**, 055502 (2005).

- [142] B. Aharmim et al. (SNO Collaboration), “Measurement of the ν_e and total ^8B solar neutrino fluxes with the sudbury neutrino observatory phase-iii data set”, Phys. Rev. C **87**, 015502 (2013).
- [143] B. Aharmim et al. (SNO Collaboration), “Low energy threshold analysis of the Phase I and Phase II data sets of the Sudbury Neutrino Observatory”, Phys. Rev. C **81**, 055504 (2010).
- [144] A. Bellerive et al., “The Sudbury Neutrino Observatory”, Nucl. Phys. B **908**, 30–51 (2016) 10.1016/j.nuclphysb.2016.04.035, <https://doi.org/10.1016/j.nuclphysb.2016.04.035>.
- [145] S. N. Ahmed et al. (SNO Collaboration), “Measurement of the total active ^8B solar neutrino flux at the Sudbury Neutrino Observatory with enhanced neutral current sensitivity”, Phys. Rev. Lett. **92**, 181301 (2004).
- [146] B. Aharmim et al. (SNO Collaboration), “Search for *hep* solar neutrinos and the diffuse supernova neutrino background using all three phases of the Sudbury Neutrino Observatory”, Phys. Rev. D **102**, 062006 (2020) 10.1103/PhysRevD.102.062006, <https://link.aps.org/doi/10.1103/PhysRevD.102.062006>.
- [147] B. Aharmim et al. (SNO Collaboration), “An independent measurement of the total active ^8B solar neutrino flux using an array of ^3He proportional counters at the Sudbury Neutrino Observatory”, Phys. Rev. Lett. **101**, 111301 (2008).
- [148] B. Aharmim et al. (SNO Collaboration), “Measurement of the cosmic ray and neutrino-induced muon flux at the Sudbury Neutrino Observatory”, Phys. Rev. D **80**, 012001 (2009).
- [149] B. Aharmim et al. (SNO Collaboration), “Search for neutron-antineutron oscillations at the Sudbury Neutrino Observatory”, Phys. Rev. D **96**, 092005 (2017).
- [150] J. F. Briesmeister, MCNP – A General Monte Carlo N-particle Transport Code Version 4A, *Los Alamos National Laboratory Report*, LA-12625-M, (1993).
- [151] S. Agostinelli et al. (GEANT4), “GEANT4—a simulation toolkit”, Nucl. Inst. and Meth. in Phys. Res. Sect. A: Accel., Spect., Det. and Assoc. Equip. **506**, 250–303 (2003) 10.1016/S0168-9002(03)01368-8.
- [152] M. J. Lyon, “Neutron transport in the Sudbury Neutrino Observatory”, PhD thesis (Oxford University, 1996).
- [153] R. Abruzzio et al., “Calibration of muon reconstruction algorithms using an external muon tracking system at the sudbury neutrino observatory”, Nucl. Inst. and Meth. in Phys. Res. Sect. A: Accel., Spect., Det. and Assoc. Equip. **648**, 92 (2011).
- [154] G. Battistoni, *Study of photo-nuclear interaction of muons in rock with the macro experiment*, 1998, arXiv:hep-ex/9809006 [hep-ex].
- [155] D. Groom et al., Atomic Data and Nuclear Data Tables **78**, 183 (2001).

- [156] T. Gaisser et al., *Cosmic rays and particle physics* (Cambridge University Press, 2016).
- [157] C. Kyba, “Measurement of the atmospheric neutrino induced muon flux at the sudbury neutrino observatory”, PhD thesis (University of Pennsylvania, 2006).
- [158] S. W. Li and J. F. Beacom, “Spallation backgrounds in Super-Kamiokande are made in muon-induced showers”, Phys. Rev. D **91**, 105005 (2015).
- [159] S. W. Li and J. F. Beacom, “First calculation of cosmic-ray muon spallation backgrounds for MeV astrophysical neutrino signals in Super-Kamiokande”, Phys. Rev. C **89**, 045801 (2014).
- [160] Y. Zhang et al. (Super-Kamiokande Collaboration), “First measurement of radioactive isotope production through cosmic-ray muon spallation in Super-Kamiokande IV”, Phys. Rev. D **93**, 0122004 (2016).
- [161] A. S. Malgin and O. G. Ryazhskaya, “Neutrons from muons underground”, Physics of Atomic Nuclei **71**, 1769–1781 (2008).
- [162] T. Araki et al. (KamLAND Collaboration), “Experimental investigation of geologically produced antineutrinos with KamLAND”, Nature **436**, 499–503 (2005) 10 . 1038/nature03980.
- [163] M. Agostini et al. (Borexino Collaboration), “Comprehensive geoneutrino analysis with Borexino”, Phys. Rev. D **101**, 012009 (2020) 10 . 1103/PhysRevD.101.012009, <https://link.aps.org/doi/10.1103/PhysRevD.101.012009>.
- [164] D. Casper et al. (IMB Collaboration), “Measurement of atmospheric neutrino composition with the IMB-3 detector”, Phys. Rev. Lett. **66**, 2561–2564 (1991) 10 . 1103/PhysRevLett.66.2561, <https://link.aps.org/doi/10.1103/PhysRevLett.66.2561>.
- [165] W. Allison et al. (Soudan Detector Collaboration), “Measurement of the atmospheric neutrino flavour composition in Soudan 2”, Nucl. Phys. B **391**, 491–500, ISSN: 0370-2693 (1997) [https://doi.org/10.1016/S0370-2693\(96\)01609-7](https://doi.org/10.1016/S0370-2693(96)01609-7), <https://www.sciencedirect.com/science/article/pii/S0370269396016097>.
- [166] T. Kajita et al. (Super-Kamiokande and KamiokaNDE Collaborations), “Atmospheric neutrino results from Super-Kamiokande and Kamiokande — evidence for ν_μ oscillations”, Nucl. Phys. B - Proceedings Supplements **77**, 123–132, ISSN: 0920-5632 (1999) [https://doi.org/10.1016/S0920-5632\(99\)00407-7](https://doi.org/10.1016/S0920-5632(99)00407-7), <https://www.sciencedirect.com/science/article/pii/S0920563299004077>.
- [167] S. Adrián-Martínez et al. (ANTARES Collaboration), “Measurement of atmospheric neutrino oscillations with the ANTARES neutrino telescope”, Phys. Lett. B **714**, 224–230, ISSN: 0370-2693 (2012) <https://doi.org/10.1016/j.physletb.2012.07.002>, <https://www.sciencedirect.com/science/article/pii/S037026931200740X>.

- [168] M. G. Aartsen et al. (IceCube Collaboration), “Measurement of atmospheric neutrino oscillations with IceCube”, *Phys. Rev. Lett.* **111**, 081801 (2013) 10.1103/PhysRevLett.111.081801, <https://link.aps.org/doi/10.1103/PhysRevLett.111.081801>.
- [169] S. Ando and K. Sato, “Relic neutrino background from cosmological supernovae”, *New Jour. of Phys.* **6**, 170–170 (2004) 10.1088/1367-2630/6/1/170, <https://doi.org/10.1088%2F1367-2630%2F6%2F1%2F170>.
- [170] J. F. Beacom, “The diffuse supernova neutrino background”, *60*, 439–462 (2010) 10.1146/annurev.nucl.010909.083331, <https://doi.org/10.1146/annurev.nucl.010909.083331>.
- [171] K. Fujikawa and R. E. Shrock, “Magnetic moment of a massive neutrino and neutrino-spin rotation”, *Phys. Rev. Lett.* **45**, 963–966 (1980) 10.1103/PhysRevLett.45.963, <https://link.aps.org/doi/10.1103/PhysRevLett.45.963>.
- [172] V. Albanese et al. (SNO+ Collaboration), “The SNO+ experiment”, *Jour. of Inst.* **16**, P08059 (2021) 10.1088/1748-0221/16/08/P08059, <https://dx.doi.org/10.1088/1748-0221/16/08/P08059>.
- [173] M. Anderson et al. (SNO+ Collaboration), “Development, characterisation, and deployment of the SNO+ liquid scintillator”, *Jour. of Inst.* **16**, P05009 (2021) 10.1088/1748-0221/16/05/P05009, <https://dx.doi.org/10.1088/1748-0221/16/05/P05009>.
- [174] G. Horton-Smith, *GLG4Sim source code*, https://www.phys.ksu.edu/personal/gahs/GLG4sim/docs/html_latest/GLG4Scint_8hh.html.
- [175] M. Anderson et al., “Optical calibration of the SNO+ detector in the water phase with deployed sources”, *Jour. of Inst.* **16**, P10021 (2021) 10.1088/1748-0221/16/10/p10021, <https://doi.org/10.1088%2F1748-0221%2F16%2F10%2Fp10021>.
- [176] J. Dunger, “Topological and time based event classification for neutrinoless double beta decay in liquid scintillator”, PhD thesis (Christ Church College, University of Oxford, 2018).
- [177] P. Vogel and J. F. Beacom, “Angular distribution of neutron inverse beta decay, $\bar{\nu}_e + p \rightarrow e^+ + n$ ”, *Phys. Rev. D* **60**, 10.1103/physrevd.60.053003 (1999) 10.1103/physrevd.60.053003, <https://doi.org/10.1103%2Fphysrevd.60.053003>.
- [178] B. Liggins, “Cosmic muon induced neutrons in the SNO+ water phase”, PhD thesis (Queen Mary University of London, 2020).
- [179] T. Kajita, “The measurement of neutrino properties with atmospheric neutrinos”, *64*, 343–362 (2014) 10.1146/annurev-nucl-102313-025402, eprint: <https://doi.org/10.1146/annurev-nucl-102313-025402>, <https://doi.org/10.1146/annurev-nucl-102313-025402>.

- [180] B. Aharmim et al. (SNO Collaboration), “Measurement of neutron production in atmospheric neutrino interactions at the Sudbury Neutrino Observatory”, *Phys. Rev. D* **99**, 112007 (2019) 10.1103/PhysRevD.99.112007, <https://link.aps.org/doi/10.1103/PhysRevD.99.112007>.
- [181] G. D. Barr et al., “Three-dimensional calculation of atmospheric neutrinos”, *Phys. Rev. D* **70**, 023006 (2004) 10.1103/PhysRevD.70.023006, <https://link.aps.org/doi/10.1103/PhysRevD.70.023006>.
- [182] G. Battistoni et al., “The atmospheric neutrino flux below 100 MeV: the FLUKA results”, *Astropart. Phys.* **23**, 526–534, ISSN: 0927-6505 (2005) <https://doi.org/10.1016/j.astropartphys.2005.03.006>, <https://www.sciencedirect.com/science/article/pii/S0927650505000526>.
- [183] M. Aguilar et al. (AMS Collaboration), “Periodicities in the daily proton fluxes from 2011 to 2019 measured by the Alpha Magnetic Spectrometer on the International Space Station from 1 to 100 GV”, *Phys. Rev. Lett.* **127**, 271102 (2021) 10.1103/PhysRevLett.127.271102, <https://link.aps.org/doi/10.1103/PhysRevLett.127.271102>.
- [184] U.S. Dept. of Commerce, NOAA, Space Weather Prediction Center (SWPC), *Solar cycle progression*, Accessed August 1, 2023., <https://www.swpc.noaa.gov/products/solar-cycle-progression>.
- [185] G. Barr et al., “Flux of atmospheric neutrinos”, *Phys. Rev. D* **39**, 3532–3534 (1989) 10.1103/PhysRevD.39.3532, <https://link.aps.org/doi/10.1103/PhysRevD.39.3532>.
- [186] A. Mastbaum, “Constraining the hep solar neutrino and diffuse supernova neutrino background fluxes with the Sudbury Neutrino Observatory”, PhD thesis (University of Pennsylvania, 2016).
- [187] C. Andreopoulos et al., “The GENIE neutrino monte carlo generator”, *Nucl. Inst. and Meth. in Phys. Sect. A: Accel., Spect., Det. and Assoc. Equip.* **614**, 87–104 (2010) 10.1016/j.nima.2009.12.009, arXiv:0905.2517 [hep-ph].
- [188] T. K. Gaisser and M. Honda, “Flux of atmospheric neutrinos”, *52*, 153–199 (2002) 10.1146/annurev.nucl.52.050102.090645, <https://doi.org/10.1146%2Fannurev.nucl.52.050102.090645>.
- [189] J. Salvatier et al., *Probabilistic programming in Python using PyMC*, 2015, arXiv:1507.08050 [stat.CO].
- [190] G. J. Feldman and R. D. Cousins, “Unified approach to the classical statistical analysis of small signals”, *Phys. Rev. D* **57**, 3873–3889 (1998) 10.1103/PhysRevD.57.3873, <https://link.aps.org/doi/10.1103/PhysRevD.57.3873>.

- [191] M. R. Anderson et al. (SNO Collaboration), “Measurement of neutron-proton capture in the SNO+ water phase”, *Phys. Rev. C* **102**, 10.1103/physrevc.102.014002 (2020) 10.1103/physrevc.102.014002, <https://doi.org/10.1103/physrevc.102.014002>.
- [192] D. R. Onken et al., “Time response of water-based liquid scintillator from X-ray excitation”, *Materials Advances* **1**, 71–76 (2020) 10.1039/d0ma00055h, <https://doi.org/10.1039/d0ma00055h>.
- [193] J. Caravaca et al., “Characterization of water-based liquid scintillator for Cherenkov and scintillation separation”, *Eur. Phys. Jour. C* **80**, 10.1140/epjc/s10052-020-8418-4 (2020) 10.1140/epjc/s10052-020-8418-4, <https://doi.org/10.1140/epjc/s10052-020-8418-4>.
- [194] J. F. Beacom et al., “Detection of supernova neutrinos by neutrino-proton elastic scattering”, *Phys. Rev. D* **66**, 033001 (2002) 10.1103/PhysRevD.66.033001, <https://link.aps.org/doi/10.1103/PhysRevD.66.033001>.
- [195] B. Dasgupta and J. F. Beacom, “Reconstruction of supernova ν_μ , ν_τ , $\bar{\nu}_\mu$, and $\bar{\nu}_\tau$ neutrino spectra at scintillator detectors”, *Phys. Rev. D* **83**, 113006 (2011) 10.1103/PhysRevD.83.113006, <https://link.aps.org/doi/10.1103/PhysRevD.83.113006>.
- [196] B. von Krosigk et al., “Measurement of the proton light response of various LAB based scintillators and its implication for supernova neutrino detection via neutrino-proton scattering”, *Eur. Phys. Jour. C* **73**, 10.1140/epjc/s10052-013-2390-1, ISSN: 1434-6052 (2013) 10.1140/epjc/s10052-013-2390-1, <http://dx.doi.org/10.1140/epjc/s10052-013-2390-1>.
- [197] J. A. Brown, “A double time of flight method for measuring proton light yield”, PhD thesis (University of California, Berkeley, Dec. 2017).
- [198] J. A. Brown et al., “Proton light yield in organic scintillators using a double time-of-flight technique”, *Jour. of Appl. Phys.* **124**, 045101 (2018) 10.1063/1.5039632.
- [199] M. Kireeff Covo et al., “The 88-Inch Cyclotron: a one-stop facility for electronics radiation and detector testing”, **127**, 580–587, ISSN: 0263-2241 (2018) <https://doi.org/10.1016/j.measurement.2017.10.018>, <https://www.sciencedirect.com/science/article/pii/S0263224117306401>.
- [200] *Neutron/Gamma PSD Liquid Scintillator EJ-301, EJ-309*, Eljen Technology (July 2021), https://eljentechnology.com/images/products/data_sheets/EJ-301_EJ-309.pdf.
- [201] K. P. Harrig et al., “Neutron spectroscopy for pulsed beams with frame overlap using a double time-of-flight technique”, *Nucl. Inst. and Meth. in Phys. Res. Sect. A: Accel., Spect., Det. and Assoc. Equip.* **877**, 359–366, ISSN: 0168-9002 (2018) <https://doi.org/10.1016/j.nima.2017.09.051>, <https://www.sciencedirect.com/science/article/pii/S0168900217310215>.

- [202] J. P. Meulders et al., “Intensity measurements and shielding of a fast-neutron beam for biological and medical applications”, *Nuclear Instruments and Methods* **126**, 81–85, ISSN: 0029-554X (1975) [https://doi.org/10.1016/0029-554X\(75\)90234-7](https://doi.org/10.1016/0029-554X(75)90234-7), <https://www.sciencedirect.com/science/article/pii/0029554X75902347>.
- [203] J. Morrell, “Nex-generation isotope production via deuteron breakup”, PhD thesis (University of California, Berkeley, Spring 2021).
- [204] K. A. Weaver et al., “Neutron spectra from deuteron bombardment of D, Li, Be, and C”, *Nucl. Sci. and Eng.* **52**, 35–45 (1973) 10.13182/NSE73-A23287, <https://doi.org/10.13182/NSE73-A23287>.
- [205] J. E. Bevins et al., “Performance evaluation of an energy tuning assembly for neutron spectral shaping”, *Nucl. Inst. and Meth. in Phys. Res. Sect. A: Accel., Spect., Det. and Assoc. Equip.* **923**, 79–87, ISSN: 0168-9002 (2019) <https://doi.org/10.1016/j.nima.2019.01.049>, <https://www.sciencedirect.com/science/article/pii/S0168900219300968>.
- [206] M. Friend et al., “An LED pulser for measuring photomultiplier linearity”, *Nucl. Inst. and Meth. in Phys. Res. Sect. A: Accel., Spect., Det. and Assoc. Equip.* **676** (2011).
- [207] *High efficiency violet LED emitter LZ1-00UB00*, OSRAM LED Engin (2018), https://dammedia.osram.info/im/bin/osram-dam-5412887/LED%5C%20Engin_Datasheet_LuxiGen_LZ1-00UB00_rev2.1_20181120.pdf.
- [208] G. Dietze and H. Klein, “Gamma-calibration of NE 213 scintillation counters”, *Nuclear Instruments and Methods in Physics Research* **193**, 549–556, ISSN: 0167-5087 (1982) [https://doi.org/10.1016/0029-554X\(82\)90249-X](https://doi.org/10.1016/0029-554X(82)90249-X).
- [209] T. A. Laplace et al., “Low energy light yield of fast plastic scintillators”, *Nucl. Inst. and Meth. in Phys. Res. Sect. A: Accel., Spect., Det. and Assoc. Equip.* **954**, Symposium on Radiation Measurements and Applications XVII, 161444, ISSN: 0168-9002 (2020) <https://doi.org/10.1016/j.nima.2018.10.122>, <http://www.sciencedirect.com/science/article/pii/S0168900218314360>.
- [210] R. Brun and F. Rademakers, “ROOT – An object oriented data analysis framework”, *Nucl. Inst. and Meth. in Phys. Res. Sect. A: Accel., Spect., Det. and Assoc. Equip.* **389**, 81–86, ISSN: 0168-9002 (1997) [http://dx.doi.org/10.1016/S0168-9002\(97\)00048-X](http://dx.doi.org/10.1016/S0168-9002(97)00048-X), <http://www.sciencedirect.com/science/article/pii/S016890029700048X>.
- [211] T. A. Laplace, *Private communication*, Oct. 2021.
- [212] P. Virtanen et al., “SciPy 1.0: Fundamental Algorithms for Scientific Computing in Python”, *Nature Methods* **17**, 261–272 (2020) 10.1038/s41592-019-0686-2.
- [213] S. G. Johnson, *The NLOpt nonlinear optimization package*, <http://github.com/stevengj/nlopt>.
- [214] R. R. Rhinehart and R. M. Bethea, *Applied engineering statistics* (CRC Press, 2021).

- [215] J. B. Birks, “Scintillations from organic crystals: specific fluorescence and relative response to different radiations”, Proc. of the Phys. Society: Sect. A **64**, 874–877 (1951) 10 . 1088 / 0370 - 1298 / 64 / 10 / 303, <https://doi.org/10.1088/0370-1298/64/10/303>.
- [216] S. Yoshida et al., “Light output response of KamLAND liquid scintillator for protons and ^{12}C nuclei”, Nucl. Inst. and Meth. in Phys. Res. Sect. A: Accel., Spect., Det. and Assoc. Equip. **622**, 574–582, ISSN: 0168-9002 (2010) <https://doi.org/10.1016/j.nima.2010.07.087>, <https://www.sciencedirect.com/science/article/pii/S0168900210017018>.
- [217] J. Hong et al., “The scintillation efficiency of carbon and hydrogen recoils in an organic liquid scintillator for dark matter searches”, Astron. and Astrophys. **16**, 333–338 (2002).
- [218] J. F. Williamson et al., “Plastic scintillator response to low-energy photons”, Phys. in Med. and Bio. **44**, 857–871 (1999) 10 . 1088 / 0031 - 9155 / 44 / 4 / 004, <https://doi.org/10.1088/0031-9155/44/4/004>.
- [219] C. Chou, “The nature of the saturation effect of fluorescent scintillators”, Physical Review **87**, 904 (1952).
- [220] J. F. Ziegler, *Stopping Range of Ions in Matter*, <http://srim.org>.
- [221] W. H. Bragg and R. Kleeman, “On the α particles of radium, and their loss of range in passing through various atoms and molecules”, The London, Edinburgh, and Dublin Philosophical Magazine and Journal of Science **10**, 318–340 (1905) 10 . 1080/14786440509463378, <https://doi.org/10.1080/14786440509463378>.
- [222] I. B. Berlman, “Luminescence in a scintillation solution excited by α and β particles and related studies in quenching”, The Jour. of Chem. Phys. **34**, 598–603 (1961) 10 . 1063/1.1700992, <https://doi.org/10.1063/1.1700992>.
- [223] T. A. Laplace et al., “Scintillator light yield measurements with waveform digitizers”, Nucl. Inst. and Meth. in Phys. Res. Sect. A: Accel., Spect., Det. and Assoc. Equip. **959**, 163485, ISSN: 0168-9002 (2020) 10 . 1016 / j . nima . 2020 . 163485, <http://dx.doi.org/10.1016/j.nima.2020.163485>.
- [224] H. Wan Chan Tseung et al., “Measurement of the dependence of the light yields of linear alkylbenzene-based and EJ-301 scintillators on electron energy”, Nucl. Inst. and Meth. in Phys. Res. Sect. A: Accel., Spect., Det. and Assoc. Equip. **654**, 318–323, ISSN: 0168-9002 (2011) <https://doi.org/10.1016/j.nima.2011.06.095>, <https://www.sciencedirect.com/science/article/pii/S0168900211013908>.
- [225] R. Weldon et al., “Measurement of EJ-228 plastic scintillator proton light output using a coincident neutron scatter technique”, Nucl. Inst. and Meth. in Phys. Res. Sect. A: Accel., Spect., Det. and Assoc. Equip. **953**, 163192, ISSN: 0168-9002 (2020) <https://doi.org/10.1016/j.nima.2019.163192>, <https://www.sciencedirect.com/science/article/pii/S0168900219314871>.

- [226] L. J. Bignell et al., “Characterization and modeling of a water-based liquid scintillator”, *Jour. of Inst.* **10**, 12009–12009 (2015).
- [227] S. Techniques, *Beta Disk Sources*, <https://www.spectrumtechniques.com/products/sources/disk-sources-and-source-sets/>, Accessed Sep. 17, 2021.
- [228] T. Kaptanoglu, E. J. Callaghan, et al., “Cherenkov and scintillation separation in water-based liquid scintillator using an LAPPDTM”, *Eur. Phys. Jour. C* **82**, 10.1140/s10052-022-10087-5 (2022) 10.1140/s10052-022-10087-5.
- [229] Hamamatsu, *Datasheet for R11265U series / H11934 series*, Accessed June 16, 2022, 2019.
- [230] E. Technology, *Silicone Grease EJ-550*, <https://eljentechnology.com/products/accessories/ej-550-ej-552>, Accessed Sep. 17, 2021.
- [231] M. J. Minot et al., “Large Area Picosecond Photodetector (LAPPDTM) - Pilot production and development status”, *Nucl. Inst. and Meth. in Phys. Res. Sect. A: Accel., Spect., Det. and Assoc. Equip.* **936**, 10.1016/j.nima.2018.11.137 (2018) 10.1016/j.nima.2018.11.137.
- [232] CAEN, *V1742 digitizer*, Accessed Sep. 17, 2021, <https://www.caen.it/products/v1742/>.
- [233] Incom, “Measurement and test report for LAPPD 93”, *Private Communication* (2021).
- [234] H. A. David and H. . Nagaraja, *Order statistics* (John Wiley and Sons, Inc., 2003), ISBN: 9780471389262.
- [235] J. Bradbury et al., *JAX: composable transformations of Python+NumPy programs*, version 0.3.13, 2018, <http://github.com/google/jax>.
- [236] T. A. Laplace, *Private communication*, July 2019.
- [237] J. A. Brown, *Private communication*, Jan. 2020.
- [238] S. Malace and S. Wood, “Single photoelectron identification with Incom LAPPD 38”, *Jour. of Inst.* **16**, P08005 (2021) 10.1088/1748-0221/16/08/p08005, <https://doi.org/10.1088%2F1748-0221%2F16%2F08%2Fp08005>.

Appendix A

GENIE systematic uncertainties

The input parameters to GENIE which are considered sources of uncertainty are listed in Table A.1. The prompt-energy-bin-wise correlations are shown in Figure A.1.

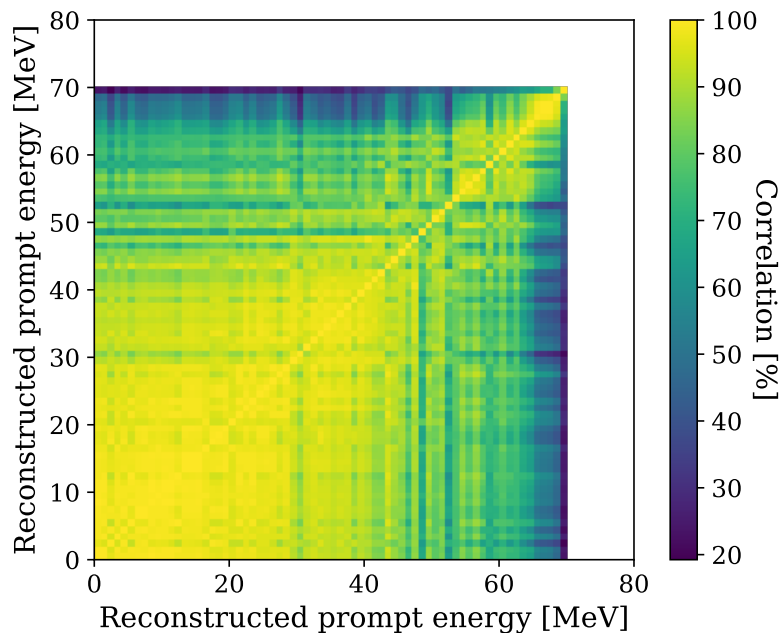


Figure A.1: Correlation matrix of bin-wise correlations of systematic uncertainties on atmospheric neutrino event rates.

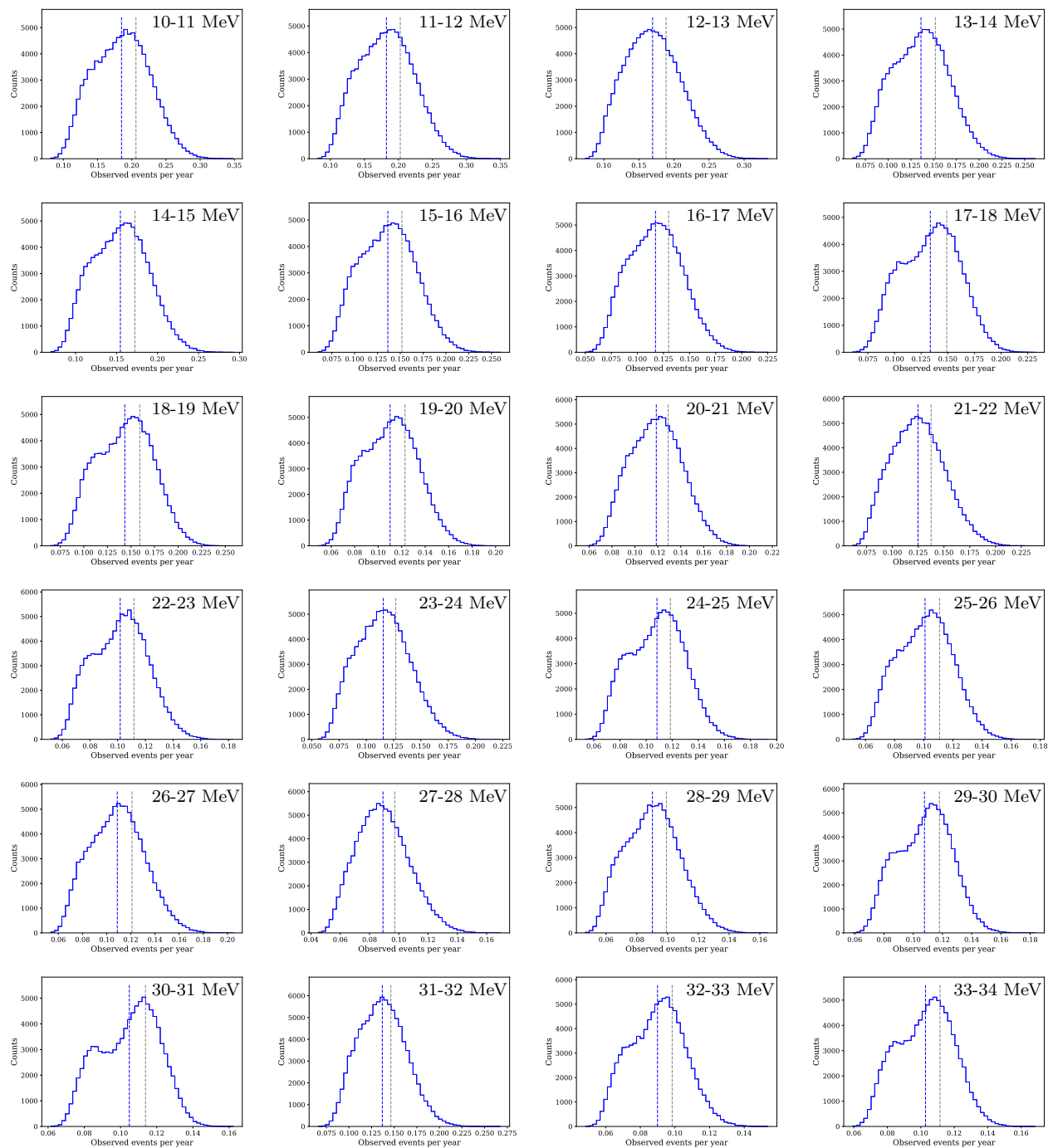
GENIE identifier	Description
MaNCEL	NCEL axial mass, affects $d\sigma_{NCEL}/dQ^2$ both in shape and normalization
EtaNCEL	NCEL η , affects $d\sigma_{NCEL}/dQ^2$ both in shape and normalization
NormCCQE	Energy-independent CCQE normalization
NormCCQEenu	Energy-dependent CCQE normalization
E0CCQE	CCQE E_0 running axial mass, affects $d\sigma_{CCQE}/dQ^2$ both in shape and normalization
ZNormCCQE	Energy-independent CCQE Z-expansion CCQE normalization
ZExpA1CCQE	CCQE Z-expansion coefficient 1, affects $d\sigma_{CCQE}/dQ^2$ both in shape and normalization
ZExpA2CCQE	CCQE Z-expansion coefficient 2, affects $d\sigma_{CCQE}/dQ^2$ both in shape and normalization
ZExpA3CCQE	CCQE Z-expansion coefficient 3, affects $d\sigma_{CCQE}/dQ^2$ both in shape and normalization
ZExpA4CCQE	CCQE Z-expansion coefficient 4, affects $d\sigma_{CCQE}/dQ^2$ both in shape and normalization
NormCCRES	CCRES normalization
MaCCRES	CCRES axial mass, affects $d\sigma_{CCRES}/dWdQ^2$ both in shape and normalization
MvCCRES	CCRES vector mass, affects $d\sigma_{CCRES}/dWdQ^2$ both in shape and normalization
NormNCRES	NCRES normalization
MaNCRES	NCRES axial mass, affects $d\sigma_{NCRES}/dWdQ^2$ both in shape and normalization
MvNCRES	NCRES vector mass, affects $d\sigma_{NCRES}/dWdQ^2$ both in shape and normalization
MaCOHpi	Axial mass in coherent π production
R0COHpi	R_0 in coherent π production
NonRESBGvpCC1pi	Non-resonant CC νp background 1- π weighing
NonRESBGvpCC2pi	Non-resonant CC νp background 2- π weighing
NonRESBGvpNC1pi	Non-resonant NC νp background 1- π weighing
NonRESBGvpNC2pi	Non-resonant NC νp background 2- π weighing
NonRESBGvnCC1pi	Non-resonant CC $\bar{\nu}n$ background 1- π weighing
NonRESBGvnCC2pi	Non-resonant CC $\bar{\nu}n$ background 2- π weighing
NonRESBGvnNC1pi	Non-resonant NC $\bar{\nu}n$ background 1- π weighing
NonRESBGvnNC2pi	Non-resonant NC $\bar{\nu}n$ background 2- π weighing
NonRESBGvbarpCC1pi	Non-resonant CC $\bar{\nu}\bar{p}$ background 1- π weighing
NonRESBGvbarpCC2pi	Non-resonant CC $\bar{\nu}\bar{p}$ background 2- π weighing
NonRESBGvbarpNC1pi	Non-resonant NC $\bar{\nu}\bar{p}$ background 1- π weighing
NonRESBGvbarpNC2pi	Non-resonant NC $\bar{\nu}\bar{p}$ background 2- π weighing
NonRESBGvbarnCC1pi	Non-resonant CC $\bar{\nu}n$ background 1- π weighing
NonRESBGvbarnCC2pi	Non-resonant CC $\bar{\nu}n$ background 2- π weighing
NonRESBGvbarnNC1pi	Non-resonant NC $\bar{\nu}n$ background 1- π weighing
NonRESBGvbarnNC2pi	Non-resonant NC $\bar{\nu}n$ background 2- π weighing
AhtBY	Bodek-Yang DIS parameter A_{ht} , including both shape and normalization effects
BhtBY	Bodek-Yang DIS parameter B_{ht} , including both shape and normalization effects
CV1uBY	Bodek-Yang DIS parameter $C_{V,1}^{(u)}$, including both shape and normalization effect
CV2uBY	Bodek-Yang DIS parameter $C_{V,2}^{(u)}$, including both shape and normalization effect
NormDISCC	Inclusive CC DIS normalization
RnubarunuCC	Ratio of CC (anti)neutrino cross sections, i.e. $\sigma(\bar{\nu})/\sigma(\nu)$
NC	Non-resonant non-quasi-elastic non-DIS NC event weighting
AGKYxF1pi	AGKY DIS model x_F distribution for low multiplicity $N + \pi$ final-state production
AGKYpT1pi	AGKY DIS model p_T distribution for low multiplicity $N + \pi$ final-state production
MFP_pi	INUKE model π intranuclear mean free path
MFP_N	INUKE model nucleon intranuclear mean free path
FrCEx_pi	Incident π charge exchange probability, for given total rescattering probability
FrInel_pi	Incident π inelastic probability, for given total rescattering probability
FrAbs_pi	INUKE model incident π absorption probability, for given total rescattering probability
FrPiProd_pi	INUKE model incident $\pi\pi$ -production probability, for given total rescattering probability
FrCEx_N	INUKE model incident nucleon charge exchange probability, for given total rescattering probability
FrInel_N	INUKE model incident nucleon inelastic probability, for given total rescattering probability
FrAbs_N	INUKE model incident nucleon absorption probability, for given total rescattering probability
FrPiProd_N	INUKE model incident nucleon π production probability, for given total rescattering probability
CCQEPAuliSupViaKF	Pauli suppression in Fermi gas nuclear modeling
CCQE Mom Distro FG to SF	Momentum distribution of Fermi gas nuclear modeling
RDecBR1gamma	Branching ratio for nuclear resonant production of single γ
RDecBR1eta	Branching ratio for nuclear resonant production of single η
Theta_Delta2Npi	Distortion of π angular distribution in $\Delta \rightarrow N + \pi$ resonance

GENIE identifier	Description
EmpMEC_Mq2d	Empirical meson-exchange cross section Mq2d parameter
EmpMEC_Mass	Empirical meson-exchange cross section mass parameter
EmpMEC_Width	Empirical meson-exchange cross section width parameter
EmpMEC_FracPN_NC	Fraction of empirical NC meson-exchange events with initial $p + n$ pair
EmpMEC_FracPN_CC	Fraction of empirical CC meson-exchange events with initial $p + n$ pair
EmpMEC_FracCCQE	Fraction of empirical meson-exchange events which are CCQE-mediated
EmpMEC_FracNCQE	Fraction of empirical meson-exchange events which are NCQE-mediated
EmpMEC_FracPN_EM	Fraction of empirical meson-exchange events which are electromagnetically-mediated
EmpMEC_FracEMQE	Fraction of empirical meson-exchange events which are EMQE-mediated
NormCCMEC	CC via meson-exchange cross section normalization
NormNCMEC	NC via meson-exchange cross section normalization
NormEMMEC	Electromagnetic meson-exchange cross section normalization
DecayAngMEC	Distortion of nucleon angular distribution in meson-exchange nucleon cluster decay
FracPN_CCMEC	Fraction of CC meson-exchange events with initial $p + n$ pair
FracDelta_CCMEC	Fraction of CC meson-exchange events with internal Δ resonance
XSecShape_CCMEC	CC via meson-exchange cross section shape parameter
ThetaDelta2NRad	Distortion of photon angular distribution in $\Delta \rightarrow N + n\gamma$

Table A.1: List of identifiers and descriptions of systematic uncertainties in GENIE modeling. Reproduced as a subset of [187].

Lower energy [MeV]	10	11	12	13	14	15	16	17	18	19	20	21	22	23	24	25	26	27	28	29	30	31	32	33	34	35	36	37	38	39																				
10	100.0	99.7	98.9	99.4	99.4	99.6	98.3	97.8	97.6	98.7	96.9	98.7	98.2	98.6	97.1	97.5	97.6	96.1	97.5	92.5	87.6	93.8	95.4	94.4	94.4	92.7	93.8	93.8	88.8	93.0																				
11		100.0	99.4	99.1	99.2	99.4	98.2	96.7	96.8	98.2	96.7	99.1	98.0	99.1	96.6	96.9	97.6	96.6	97.5	91.8	86.5	94.2	95.6	93.6	94.1	92.9	93.1	94.1	87.7	92.9																				
12			100.0	98.0	98.3	98.5	97.7	94.4	94.5	96.6	96.8	99.3	96.7	98.9	95.3	95.5	97.1	98.0	97.5	89.7	83.7	94.0	95.3	91.0	92.9	91.3	91.3	93.1	84.2	91.6																				
13				100.0	99.9	99.9	98.2	98.7	98.8	99.6	96.3	98.7	98.9	98.8	98.3	98.7	98.6	95.9	97.8	94.4	90.1	94.4	96.2	96.3	96.0	94.1	95.2	94.9	91.8	94.3																				
14					100.0	99.9	98.3	98.5	98.7	99.6	96.5	98.9	99.0	99.0	98.7	98.8	98.6	96.2	98.0	94.5	90.1	95.0	96.5	96.3	96.3	94.6	95.3	95.4	91.8	94.5																				
15						100.0	98.5	98.2	98.5	99.4	96.8	99.9	98.8	99.0	98.7	98.8	98.6	96.2	98.0	94.5	90.1	95.0	96.5	96.3	96.3	94.6	95.3	95.4	91.8	94.5																				
16							100.0	96.5	96.9	97.6	98.9	98.0	97.5	97.8	97.2	97.5	97.0	96.6	96.9	93.8	87.7	95.8	95.3	93.9	93.9	94.8	95.0	90.8	94.0																					
17								100.0	99.0	99.3	94.5	95.8	98.1	95.8	98.2	98.4	96.3	91.5	95.3	95.2	92.1	92.6	94.2	97.5	95.4	93.9	95.8	93.6	94.7	93.6																				
18									100.0	99.4	94.6	95.8	98.3	96.4	98.9	99.0	96.6	92.0	95.5	96.0	92.6	93.8	94.5	97.9	96.2	94.4	95.8	94.6	95.1	95.9																				
19										100.0	95.6	97.6	98.8	97.8	98.9	98.8	97.9	94.3	96.9	95.1	91.1	94.2	95.8	97.2	96.2	94.6	95.8	94.7	93.5	94.2																				
20											100.0	96.9	96.5	96.6	95.5	96.1	95.6	96.3	96.7	92.7	87.3	95.9	94.9	92.4	94.9	92.2	93.6	94.1	86.8	93.4																				
21												100.0	97.7	99.5	96.6	97.1	98.9	98.8	98.2	95.9	94.0	92.5	87.1	95.0	96.9	93.5	95.3	93.2	93.8	95.4	87.7	94.2																		
22													100.0	98.5	99.1	98.7	98.2	95.9	95.9	98.4	97.0	93.6	96.8	97.9	97.8	98.1	97.3	97.2	97.6	94.3	96.7																			
23														100.0	97.8	97.3	98.6	98.5	99.0	93.8	88.6	96.6	97.6	94.9	96.7	95.3	94.3	96.5	89.3	95.0																				
24															100.0	99.0	97.4	94.4	97.1	97.4	93.9	96.6	97.3	98.4	98.4	97.5	97.2	97.5	95.4	95.4	96.1																			
25																100.0	98.4	94.7	97.6	96.9	94.1	94.9	96.9	97.9	97.6	95.3	97.3	96.5	94.9	96.5	96.5																			
26																	100.0	97.5	99.3	95.2	92.0	94.2	98.1	95.9	97.1	94.7	96.6	96.3	91.4	96.8																				
27																		100.0	98.4	91.4	85.2	95.6	97.1	91.2	94.9	92.9	92.2	95.4	84.7	93.9																				
28																			100.0	95.2	91.8	95.9	99.0	95.5	97.8	96.0	96.6	97.3	90.8	97.4																				
29																				100.0	97.4	95.1	96.4	98.1	98.1	97.3	98.1	97.8	96.9	96.5																				
30																					100.0	97.4	93.7	96.4	95.5	94.9	97.4	95.7	97.0	96.3																				
31																						100.0	95.8	94.2	97.4	96.7	93.2	97.1	89.9	93.9																				
32																							100.0	96.3	98.4	97.9	97.9	98.5	92.5	98.2																				
33																								100.0	98.4	97.3	97.9	96.9	98.2	96.9																				
34																									100.0	98.7	98.0	98.6	95.6	98.3																				
35																										100.0	97.3	98.2	95.3	97.1																				
36																											100.0	97.4	96.4	98.3																				
37																												100.0	94.1	97.6																				
38																													100.0	94.7																				
39																															100.0																			
Uncertainty [%]	19.6	19.9	20.6	19.7	19.4	19.8	19.5	18.1	18.4	18.8	17.3	18.5	17.6	19.1	17.6	16.7	18.4	18.2	17.6	15.4	14.3	17.7	15.9	14.8	16.1	16.7	14.7	14.6	14.5	14.0																				

Table A.2: Correlation matrix of per-bin systematic uncertainties on atmospheric neutrino events, labeled by the energy of the lower bin edges. The bottom row quotes the uncertainty for each bin.



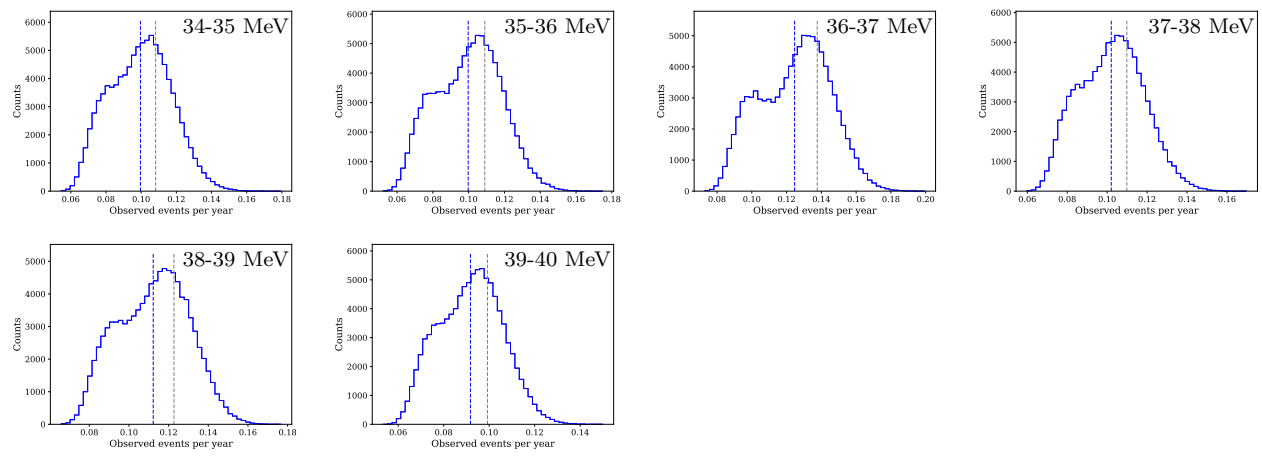
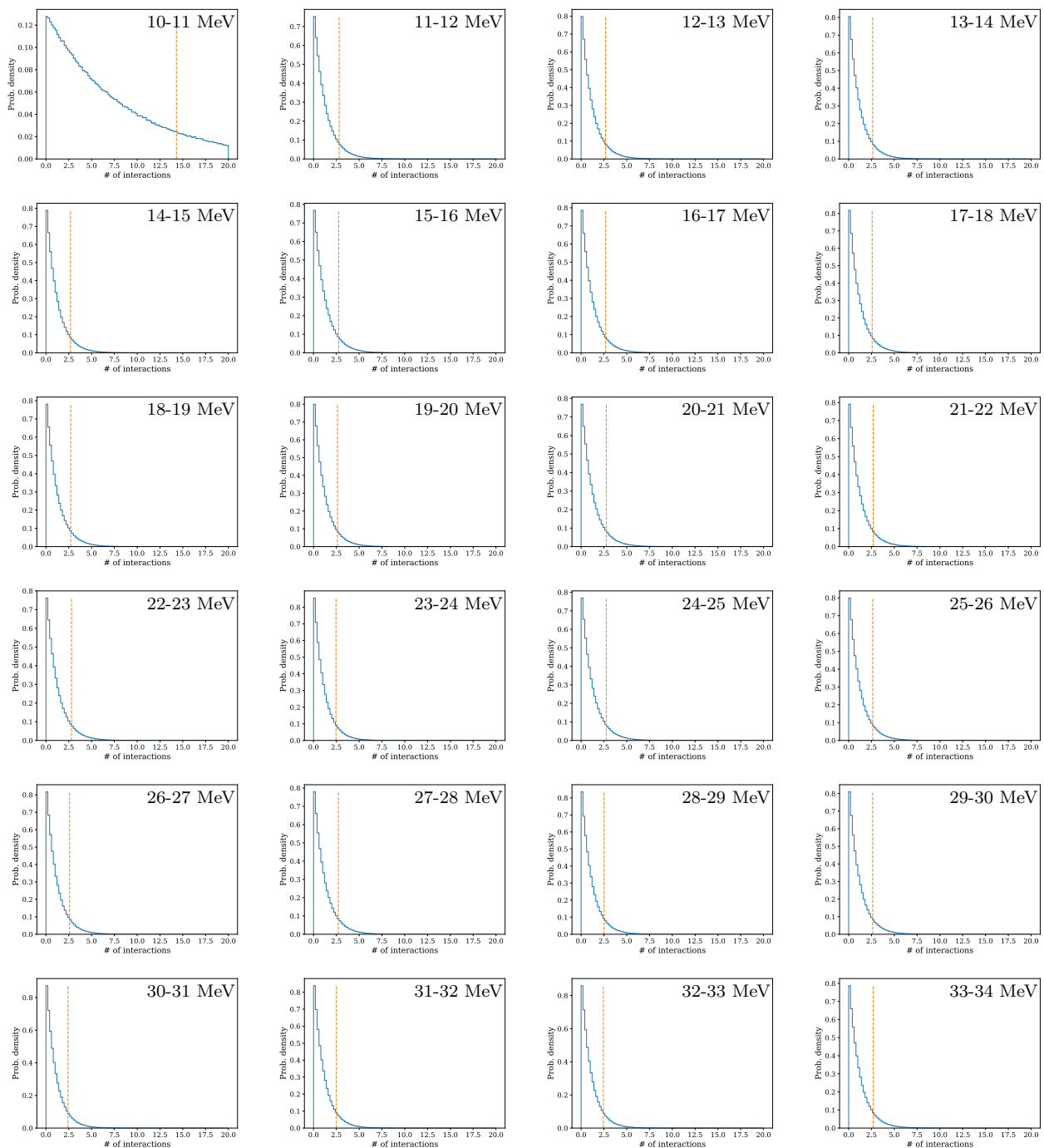


Figure A.2: Distribution of atmospheric neutrino events in various energy bins, under resamplings of GENIE inputs. The grey dashed line denotes the nominal prediction, and the blue dashed line denotes the mean resampled prediction.

Appendix B

Excess IBD interaction posterior distributions

Posterior distributions for the number of excess antineutrino interactions in each energy bin are shown in Figure [B.1](#).



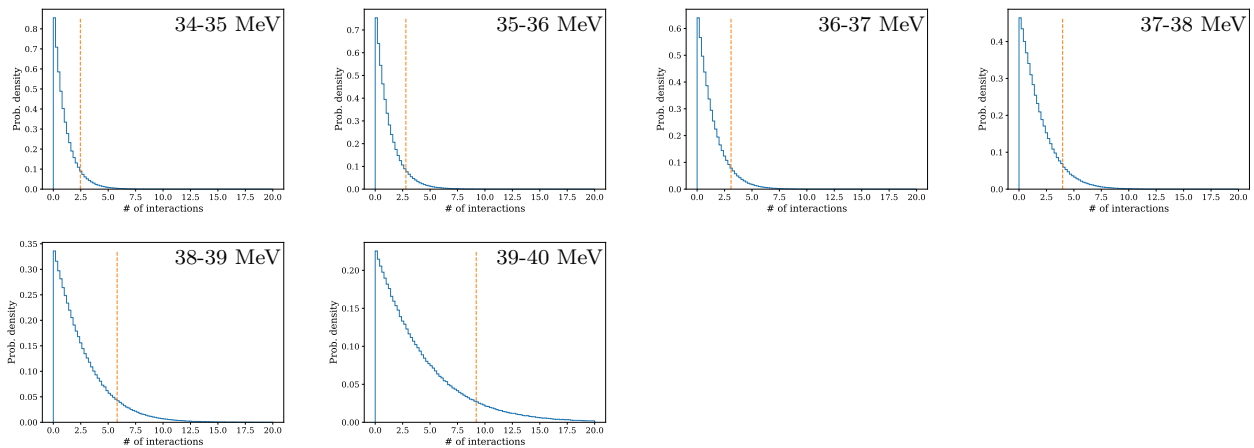


Figure B.1: Posterior distribution of excess atmospheric neutrino interactions in various energy bins, sampled using MCMC. The dashed line denotes the 90% probability mass upper limit.

Appendix C

Proton light yield PMT linearity measurement

C.1 Overview of methodology

In the context of the PLY measurement, the fundamental observable measured in-beam and with calibration sources must be proportional to the number of photons incident on the PMT. For a perfect PMT, the total charge collected at the anode would be such a quantity. A number of effects, however, prevent this from being the case. One principal imperfection are space-charge effects at the anode: the presence of existing charge acts to retard further charge collection, which affects a degradation in marginal PMT response. Critically, this narrative implies that the degradation in charge collected is a function not just of the total light collected, but also of how that light is distributed in time, i.e. the pulse shape. Such these effects should clear on a smaller time scale than the typical transit time of the PMT, which on the order of nanoseconds. This means that due to the 500 MS/s sampling rate used in this measurement, the nonlinearity exhibited in different samples are effectively uncorrelated. Coupled with the understanding that a charge-coordinated correction is only valid if measured using pulse-shapes compatible with those encountered during measurement, this demands that the nonlinearity be measured as a departure of individual sample response from ideal.

The methodology applied to measure the nonlinearity is adapted from Friend et al [206], who suggest the use of two LEDs, fired both simultaneously and out-of-phase, to measure the response to two distinct numbers of photons separately, and also the response to the summed photon count. Analytically, these photon counts *do not need to be known a priori*. One postulates the existence of a response function, f , which maps the number of photons incident on the PMT to “the response,” which is some property of the pulse output from the digitizer. For a given configuration of the two LEDs, producing m and n photons, respectively, one measures $f(m)$, $f(n)$, and $f(m + n)$. If one assumes some particular (and invertible) form for f , its incompatibility with the measured responses can be quantified

via the difference $\Delta(m, n) = f_{m+n} - f(f^{-1}(f_m) + f^{-1}(f_n))$, where the terms $f_x = f(x)$ are measured quantities. By making measurements at various (m, n) and parameterizing (visualized by ξ) a sufficiently flexible $f(x; \xi)$, one can fit f to the data by minimizing the gross incompatibility, e.g. $D(\xi) = \sum_{m,n} \Delta(m, n; \xi)^2$.

In the present context, we choose the maximum sample of the pulse as “the response,” as it encodes only single-sample information, as is required by the above, is easily identifiable for a given pulse, and, generally, is unique within each pulse (though this may be due, in some part, to the particular LEDs used in this work). The difficulty brought by this choice is the necessity to, for coincident measurements (i.e. $f(m+n)$), accurately and reliably align the two pulses in time. Of course, the three response measurements which constitute a single “data point,” i.e. $f(m)$, $f(n)$, and $f(m+n)$, are each measured statistically, as the mean of a population of individual measurements. In practice, m was varied so as to cover the full dynamic range of the digitizer used, and n was fixed to a relatively small value, $\sim 5\%$ of the dynamic range.

C.2 Hardware

Two LEDs, each with peak wavelength 405 nm [207], are arranged inside of a dark box containing the PMT to be characterized. The LEDs are driven by custom-soldered circuits, in which a capacitor is charged by a constant power supply, and discharged via the breakdown of a transistor subject to a trigger signal. An approximate schematic of the circuit design is shown in Figure C.1. The circuits were constructed principally by Josh Brown and Gino Gabella. Each circuit is arranged as follows: an external power supply (BK Precision 9174B) holds a capacitor at some positive voltage, with a path to ground intercepted by a transistor. The opposite side of the capacitor is connected to an LED. An external driving pulse fed directly to the transistor “opens the gate,” and the capacitor drains to ground. The draining of the opposite side of the capacitor powers the LED with a prompt pulse, upwards of 10 V in magnitude. One important feature of the circuits is that because they are fundamentally capacitors, there is a characteristic recharge time associated with each. If driven on timescales less than or comparable to this recharge time, but not at a constant frequency, then the pulses generated will be of systematically different sizes, which would introduce a bias into the measurement.

Two DG535 pulse generators, here also called “delay boxes,” produced by Stanford Research Systems (SRS) provide the heart of the electronics chain. Each box is capable of producing two square pulses of variable magnitude (< 4 V) and duration ($\gtrsim 1$ ns), each delayed from a trigger signal (generated either internally or externally). In order to generate two pulse trains, one for each driving circuit, such that the two LEDs alternately fire in and out of coincidence, the following scheme was implemented, developed by Josh Brown [237]: a third function generator provides logic pulses at a constant system frequency f_0 , or, put another way, with system period t_0 . Each input pulse is 5-way multiplexed; three of the fan-outs are delayed in NIM boxes by 0 , $\frac{1}{3}t_0$, and $\frac{2}{3}t_0$, and fed into one delay box; the

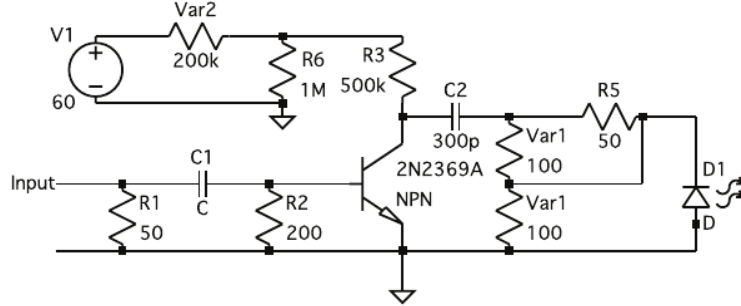


Figure C.1: Schematic for the LED-driving circuitry. Note that the passive component specifications may differ from those used in the final measurement. Figure courtesy of T. L. Laplace [236].

other two fan-outs are delayed by 0 and $\frac{1}{2}t_0$ and fed into the other delay box. Each delay triggers externally, with constant frequencies $\frac{3}{2}f_0$ and $2f_0$, respectively. Because the pulses ultimately originate from a single source, the delay-box output associated with the 0-delayed copy from each route are, up to small differences in cable length (which are accounted for), naturally aligned in time (up to a time-walk effect, which is discussed in detail below). The delayed copies then constitute the rest of a pulse train of length 3, which in total provide one measurement of the coincident response, one measurement of the response to one LED, and two measurements of the response to the other LED. The resulting pulse trains are shown in Figure C.2. If each LED were truly driven at a constant frequency, there would be no expected bias due to recharge-time effects. However, the NIM-level delays are hand-tuned, and as such there are biases in the interpulse timing for each separate pulse train. The system frequency is thus set to 30 Hz, which makes the fastest period encountered 10 ms — this is roughly the full recharge-time associated with the slower of the two circuits used in this measurement.

The strength of each pulse (i.e. m and n) is set by the voltage used to bias the associated driving circuitry. As n is held fixed, the size of the pulse associated with m is controlled using a single voltage setting, termed the supply voltage.

C.3 Time walk

A source of bias is the degree of coincidence to which the two LEDs fire simultaneously. Because the response metric used here is the pulse maximum, if the individual photon pulses do not reach maximum at the same time, then the measured maximum in coincidence is biased low relative to the true sum. This was investigated by repeating measurement at a single data point (i.e. (m, n) pair), systematically changing the delay on the output of one of the SRS boxes, to see how precisely the pulse alignment could be performed. This revealed that the proper alignment changes as a function of (m, n) . This is because the time for a pulse to transition from 0 to maximum is a function of the amplitude of the pulse, and

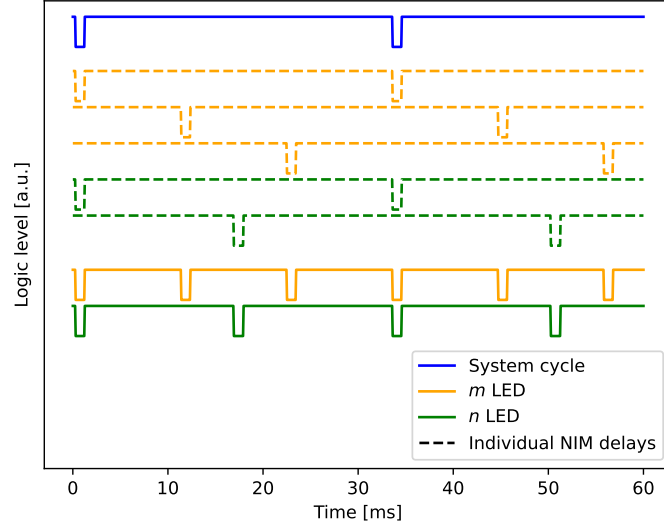


Figure C.2: Diagram visualizing the construction of interweaving pulse trains via multiplexing a common system signal. Reproduced from [237].

only the beginning of the transition can be explicitly triggered. In order to eliminate the bias this introduces to nonlinearity measurements, data is taken, for each (m, n) , in dedicated scans over the interpulse delay. The fully-aligned amplitude deficit $\Delta(m, n)$ is then taken as the maximum deficit of a quadratic fit to the measured deficits, as a function of delay. The expected (assuming perfect linearity) and observed coincident pulse heights, and associated amplitude deficits and quadratic fits, are available in Appendix D.

Appendix D

Supplementary material for proton light yield measurement

Per-auxiliary-detector particle-ID capabilites are summarized in Figure D.1, Figure D.2, Figure D.3, and Figure D.4. Outgoing TOF calibrations are shown in Figure D.5 and Figure D.6. Nominal per-energy-bin fits of proton recoil charge models are shown in Figure D.7 and Figure D.8, and time-series of the associated representative charges are shown in Figure D.9 and Figure D.10.

Scans of the predicted and measured coincident pulse amplitudes relevant to the PMT linearity characterization, as a function of the interpulse delay, are shown in Figure D.11 and Figure D.12. Quadratic fits to the deficit, in the neighborhood of the minimum, are shown in Figure D.13 and Figure D.14.

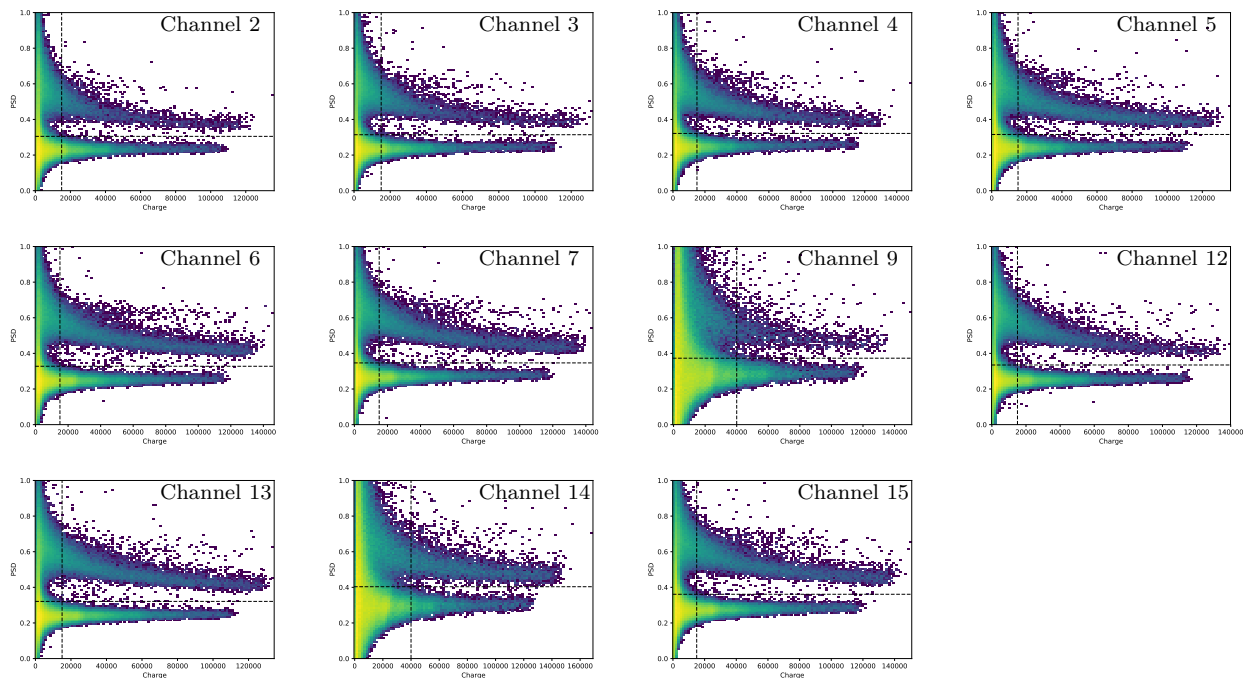


Figure D.1: Two-dimensional distributions of charge and PSD metric in each scatter cell, in LAB+PPO data, with semi-optimized PID discriminants overlaid.

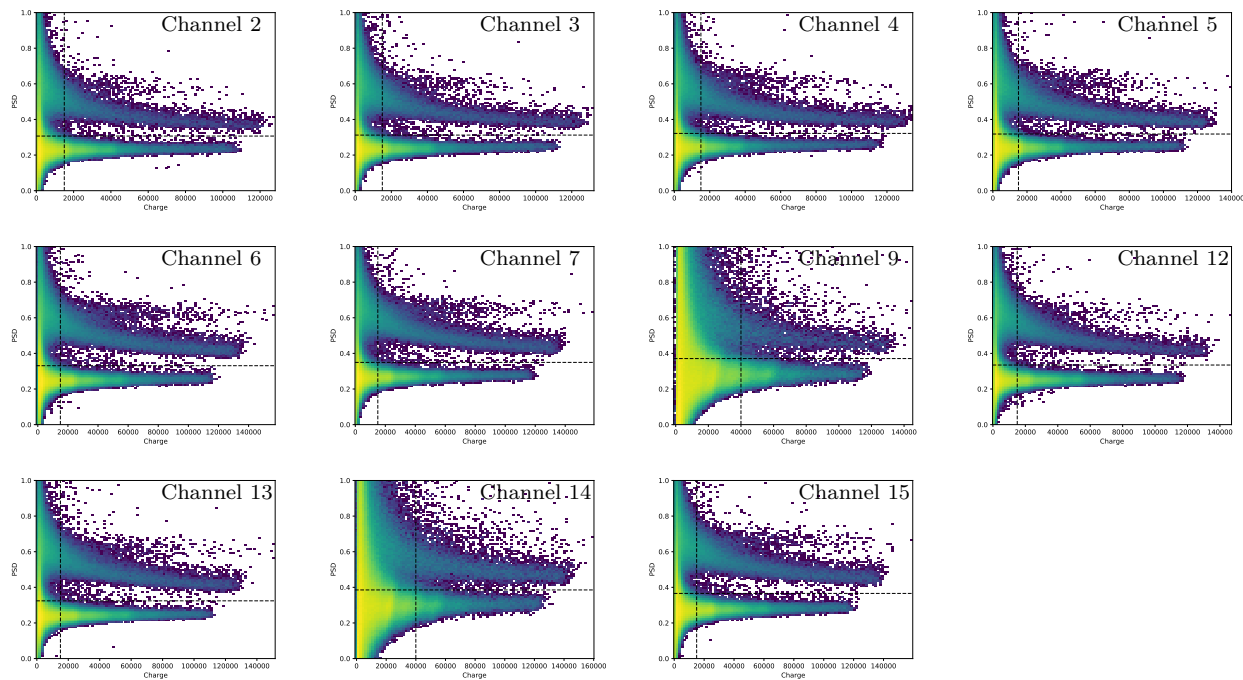


Figure D.2: Two-dimensional distributions of charge and PSD metric in each scatter cell, in WbLS data, with semi-optimized PID discriminants overlaid.

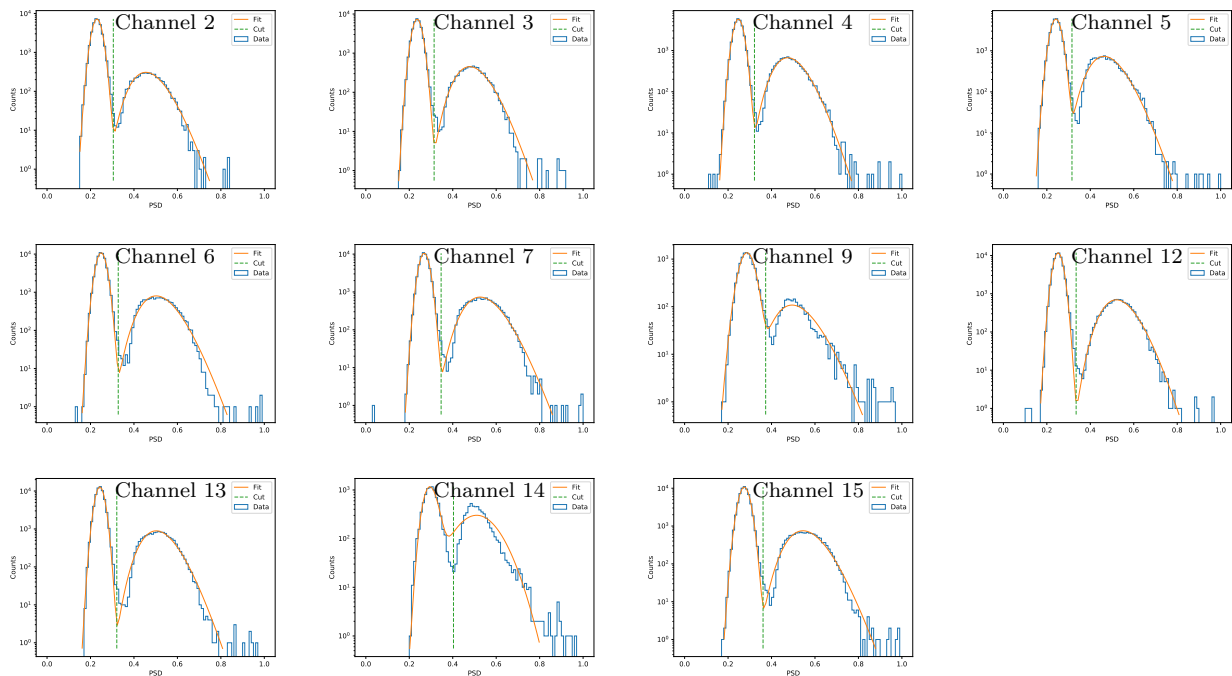


Figure D.3: Normal/log-normal fits to charge-selected PSD metrics in each scatter cell, in LAB+PPO data.

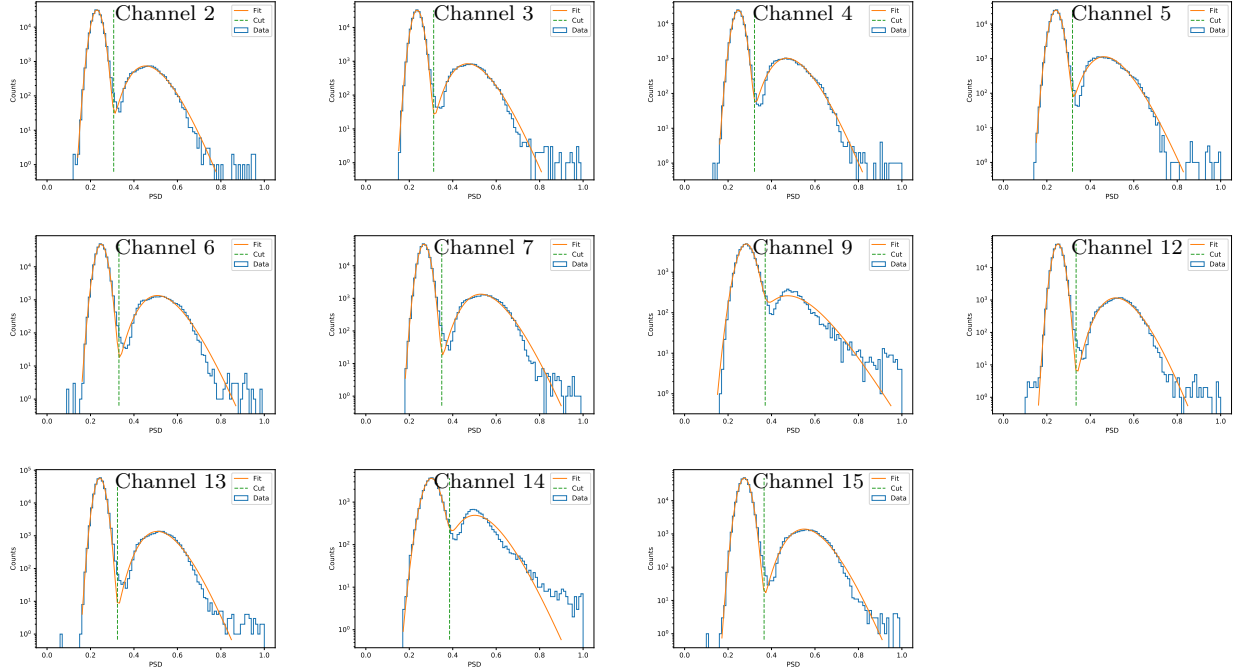


Figure D.4: Normal/log-normal fits to charge-selected PSD metrics in each scatter cell, in WbLS data.

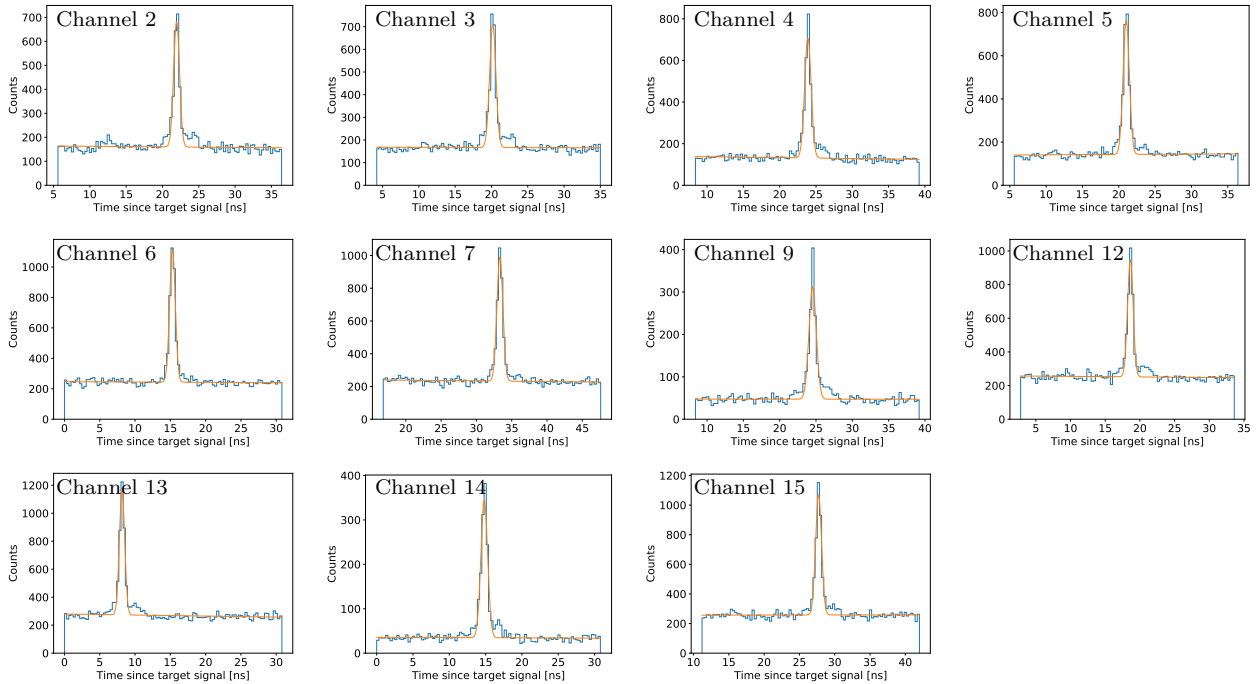


Figure D.5: Gaussian signal and linear background fits to LAB+PPO coincidence data.

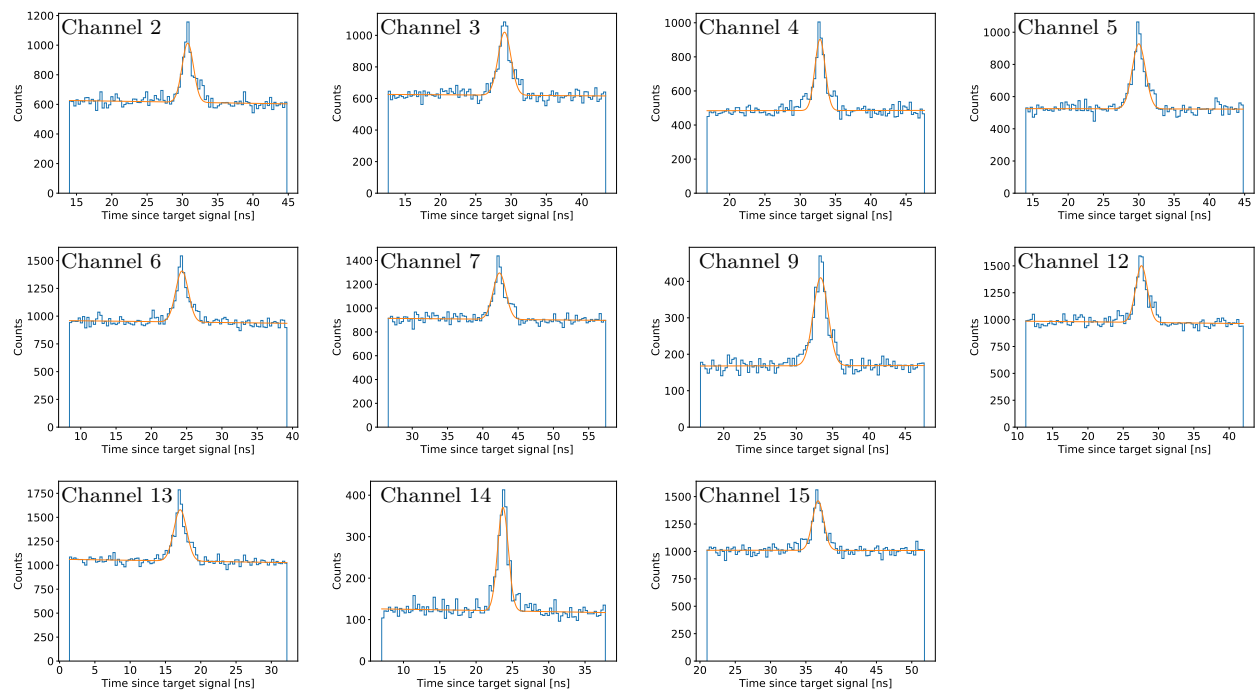


Figure D.6: Gaussian signal and linear background fits to WbLS coincidence data.

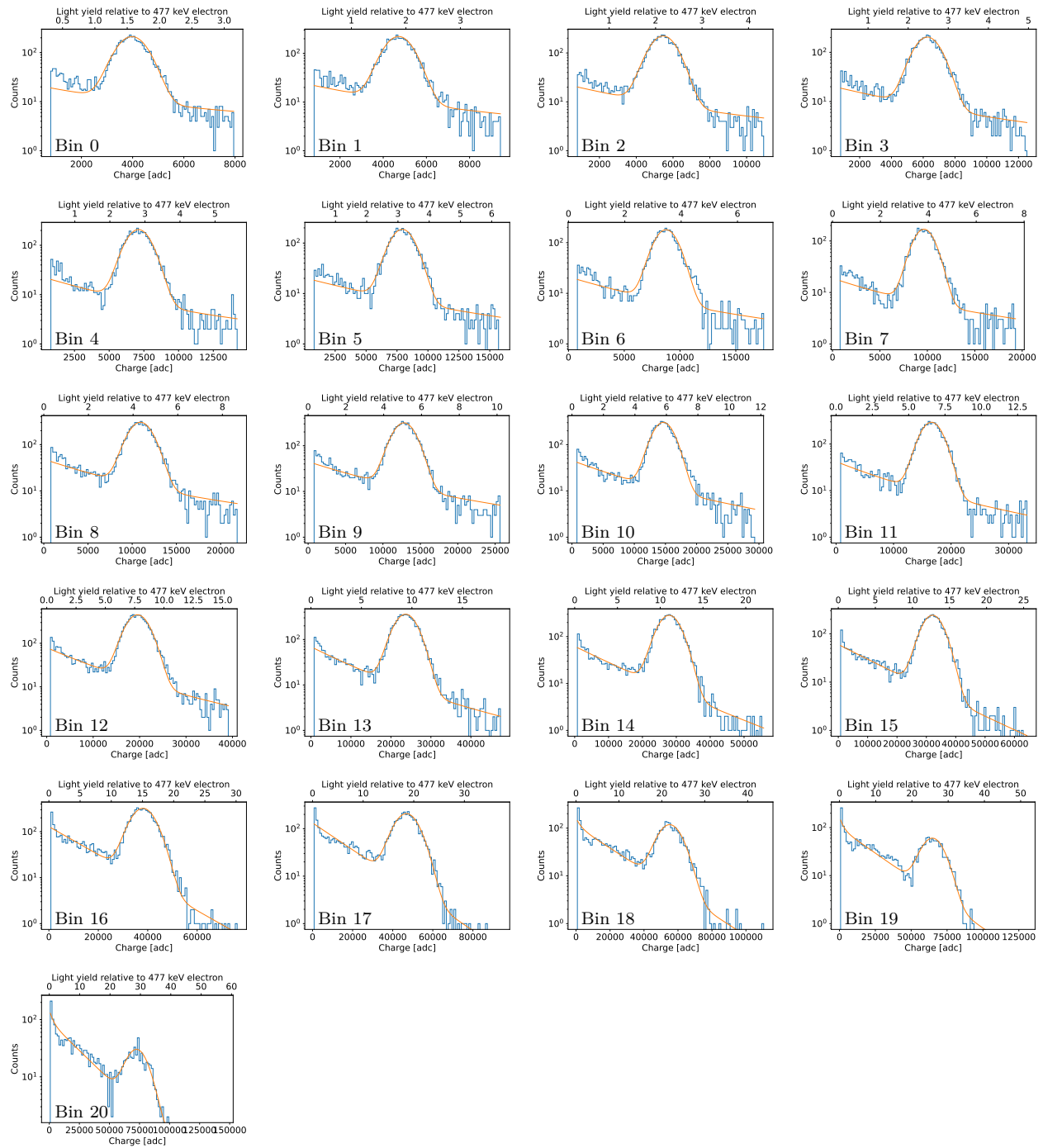


Figure D.7: Gaussian signal and double-exponential background fits to LAB+PPO proton charge data.

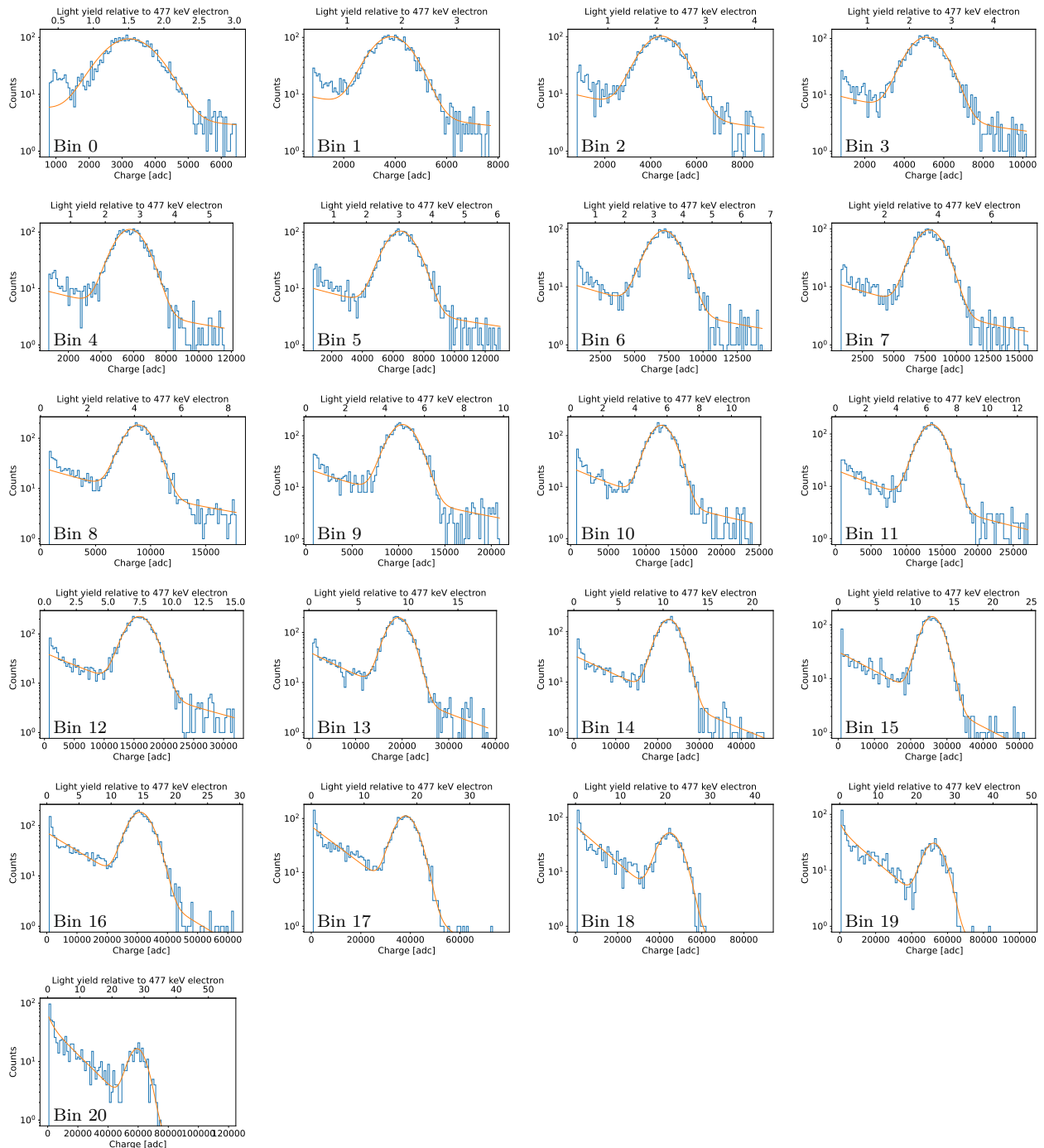


Figure D.8: Gaussian signal and double-exponential background fits to WbLS proton charge data.

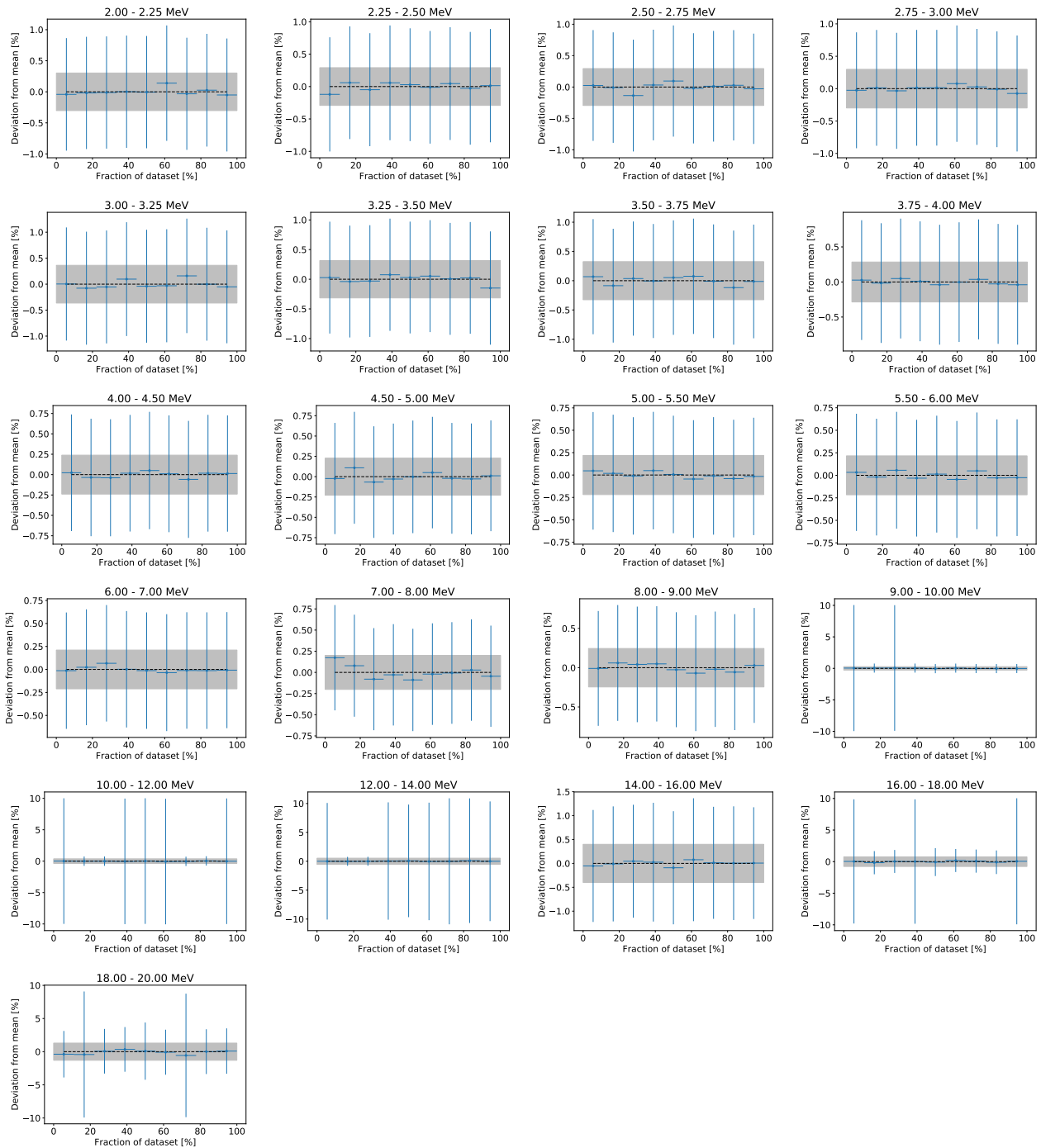


Figure D.9: Difference in LAB+PPO per-energy-bin relatively PLY as a function of chronological place in data set.

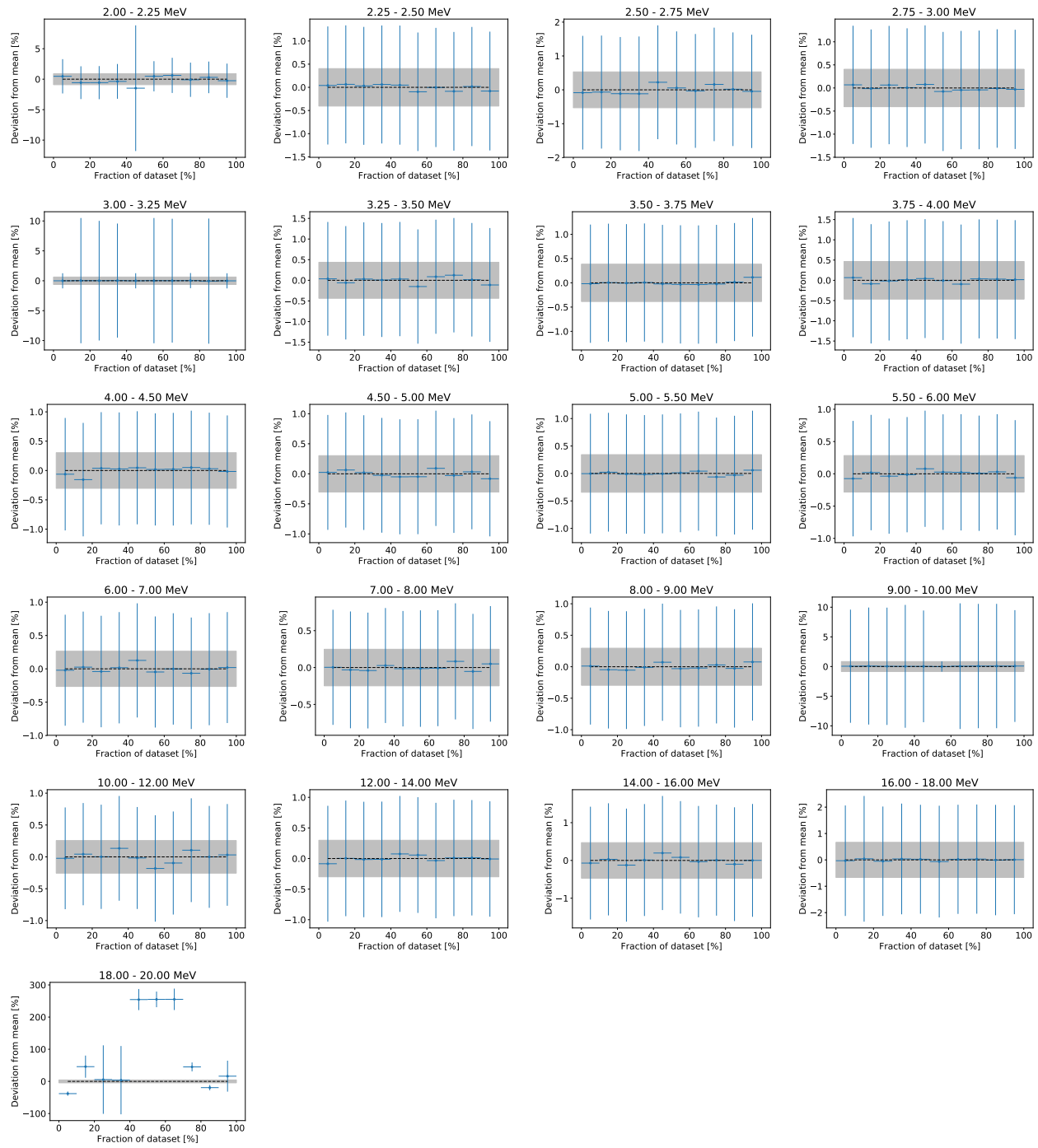
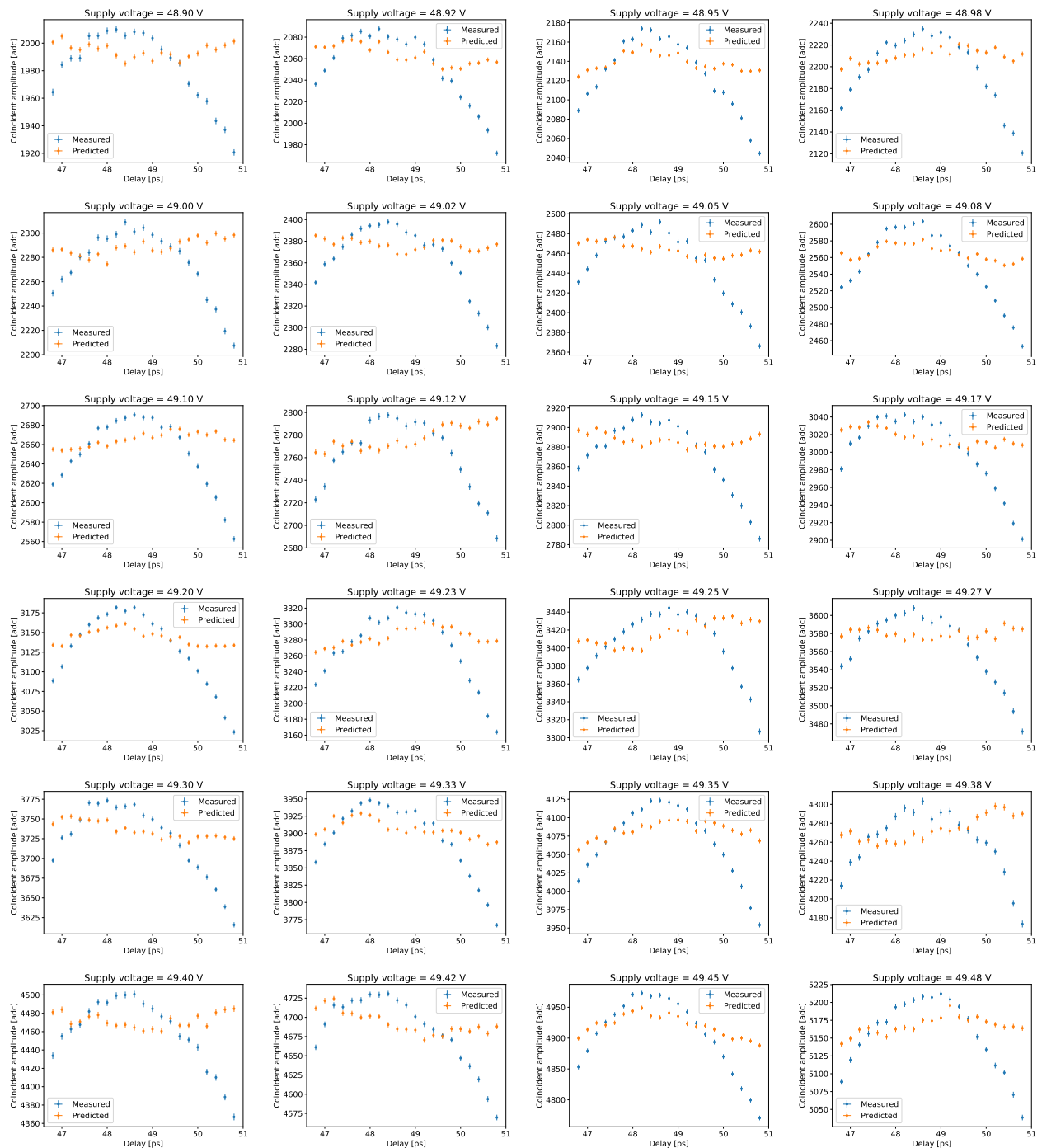


Figure D.10: Difference in WbLS per-energy-bin relatively PLY as a function of chronological place in data set.



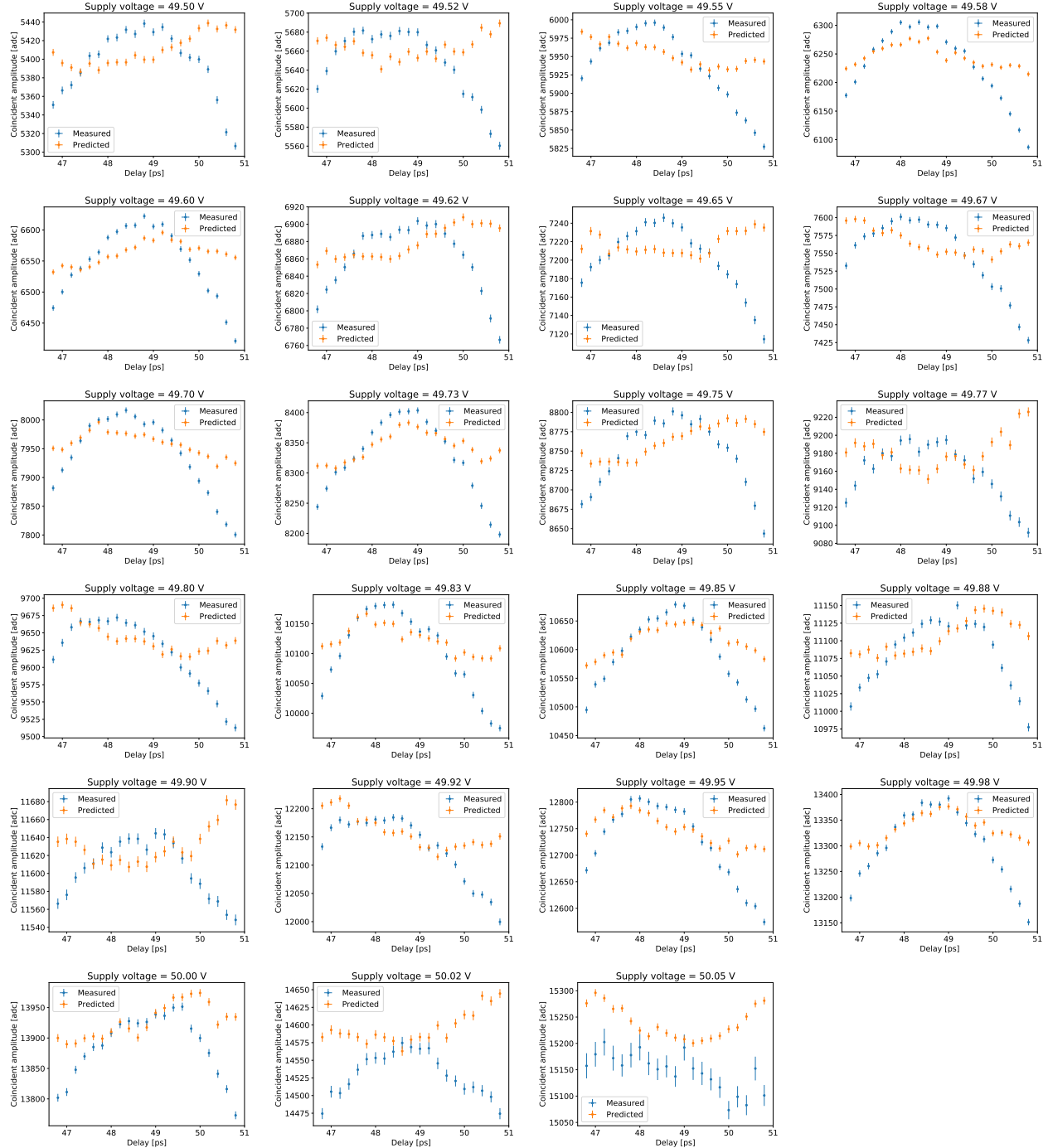
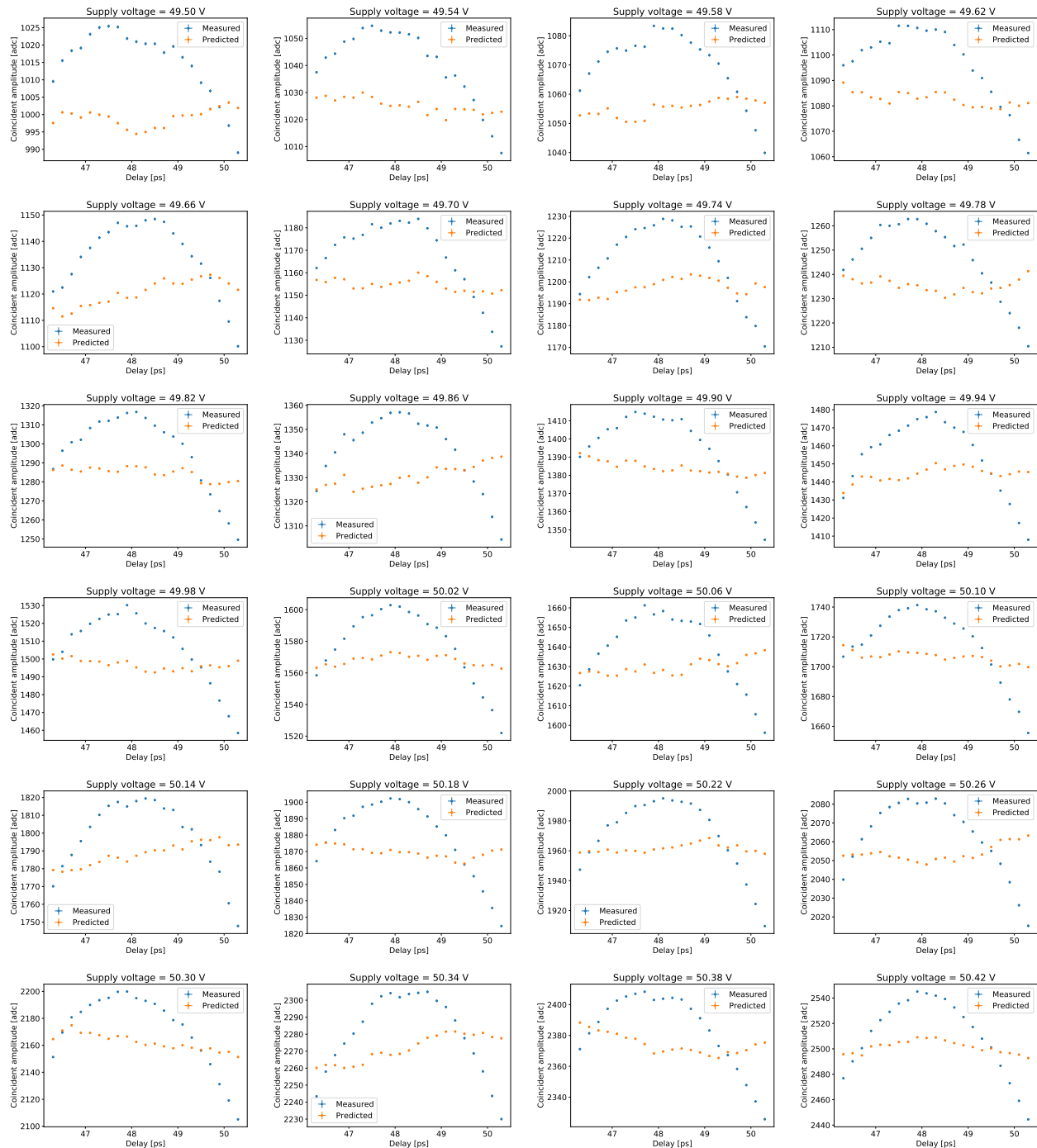
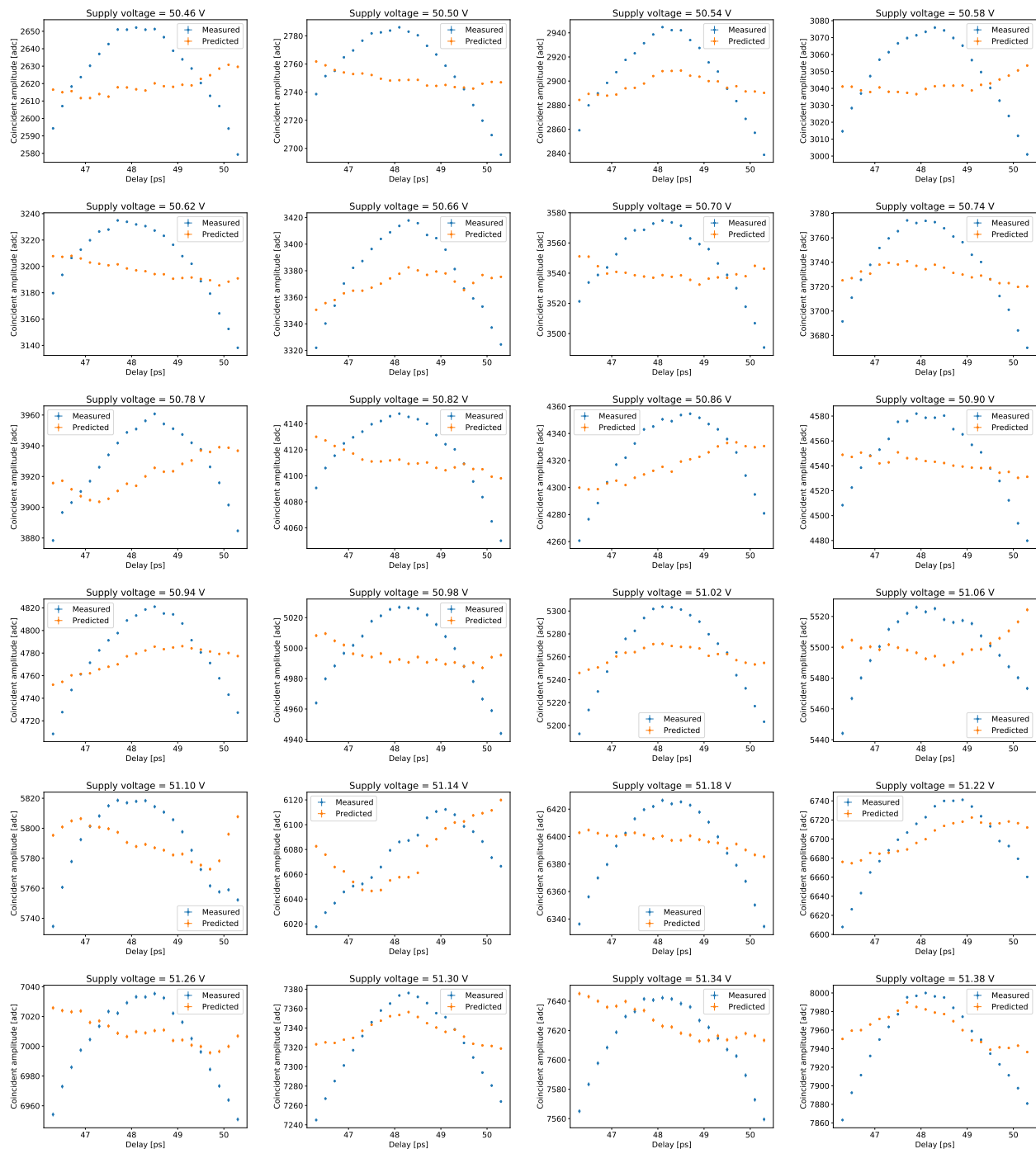


Figure D.11: Predicted and measured coincident pulse amplitudes, as a function of the interpulse delay, for the PMT used in LAB+PPO data-taking, at various supply voltages.





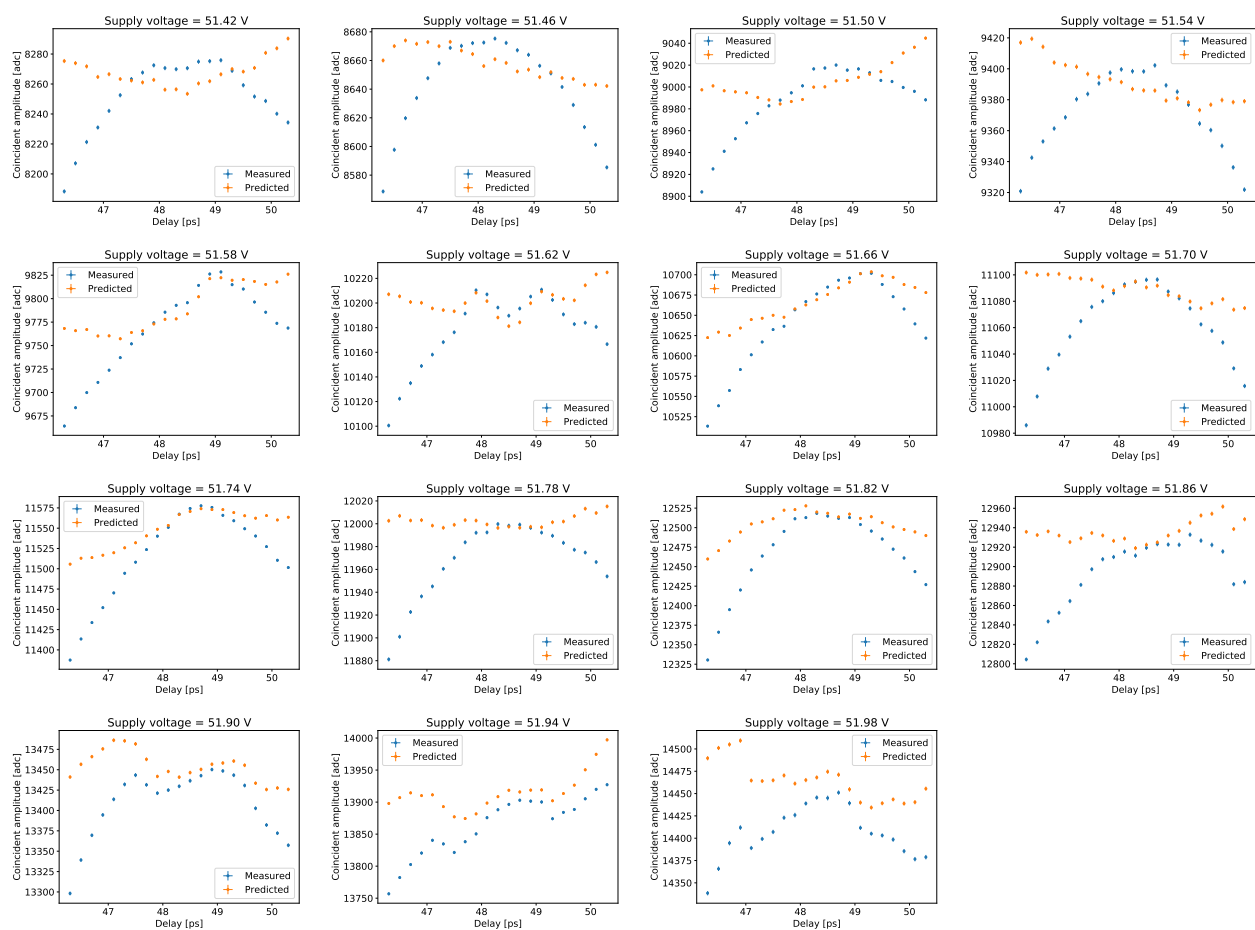
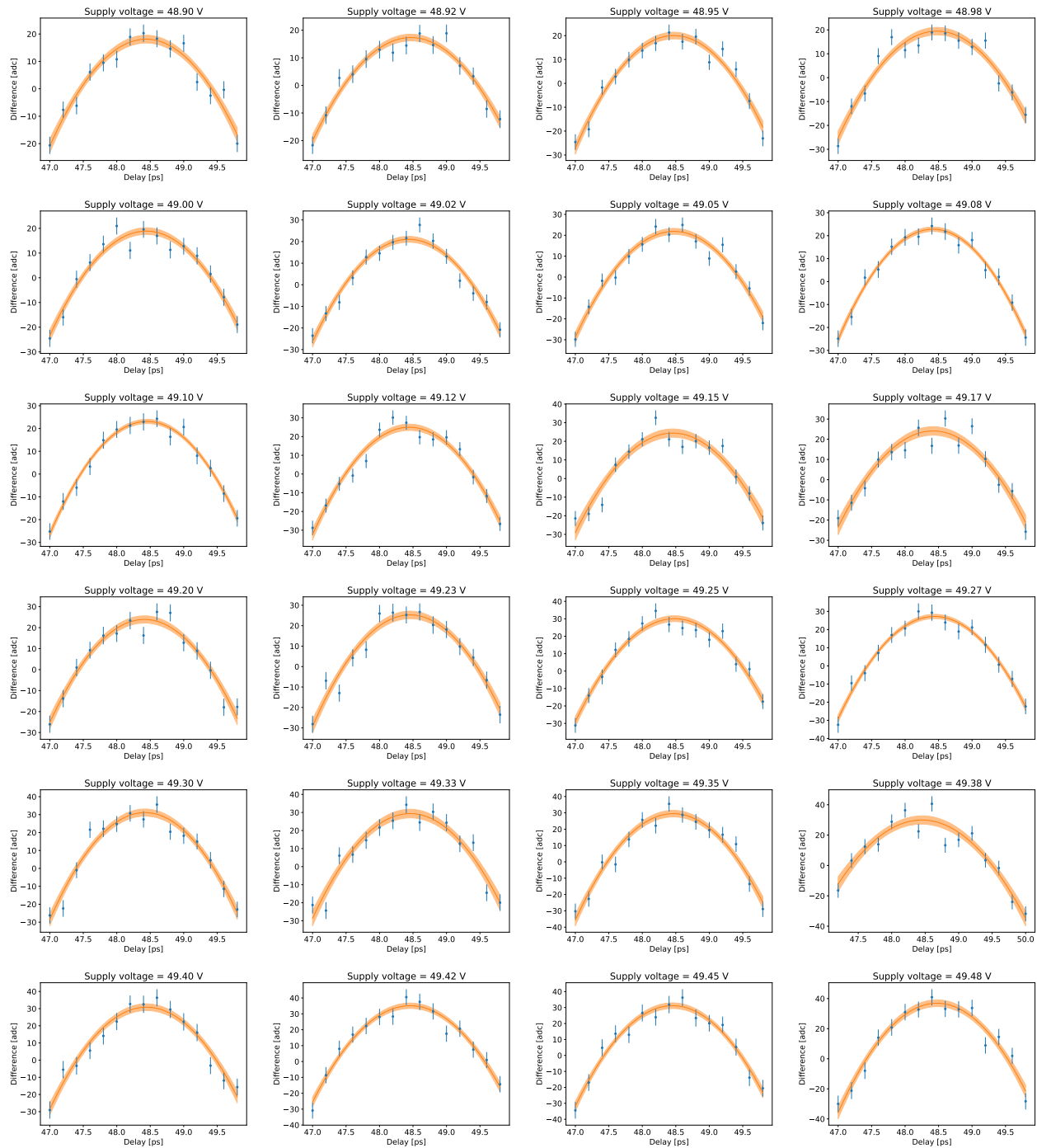


Figure D.12: Predicted and measured coincident pulse amplitudes, as a function of the interpulse delay, for the PMT used in WbLS data-taking, at various supply voltages.



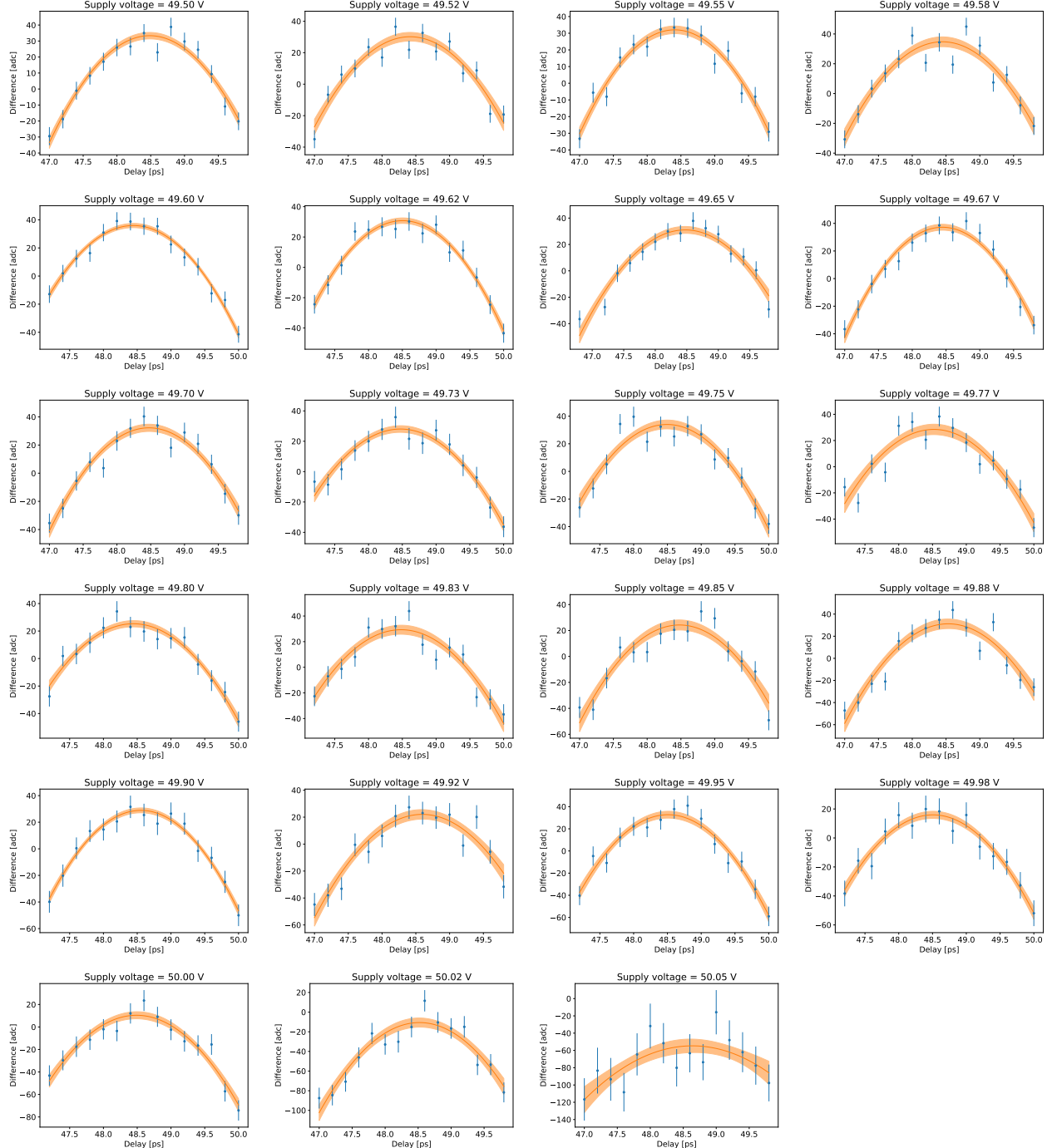
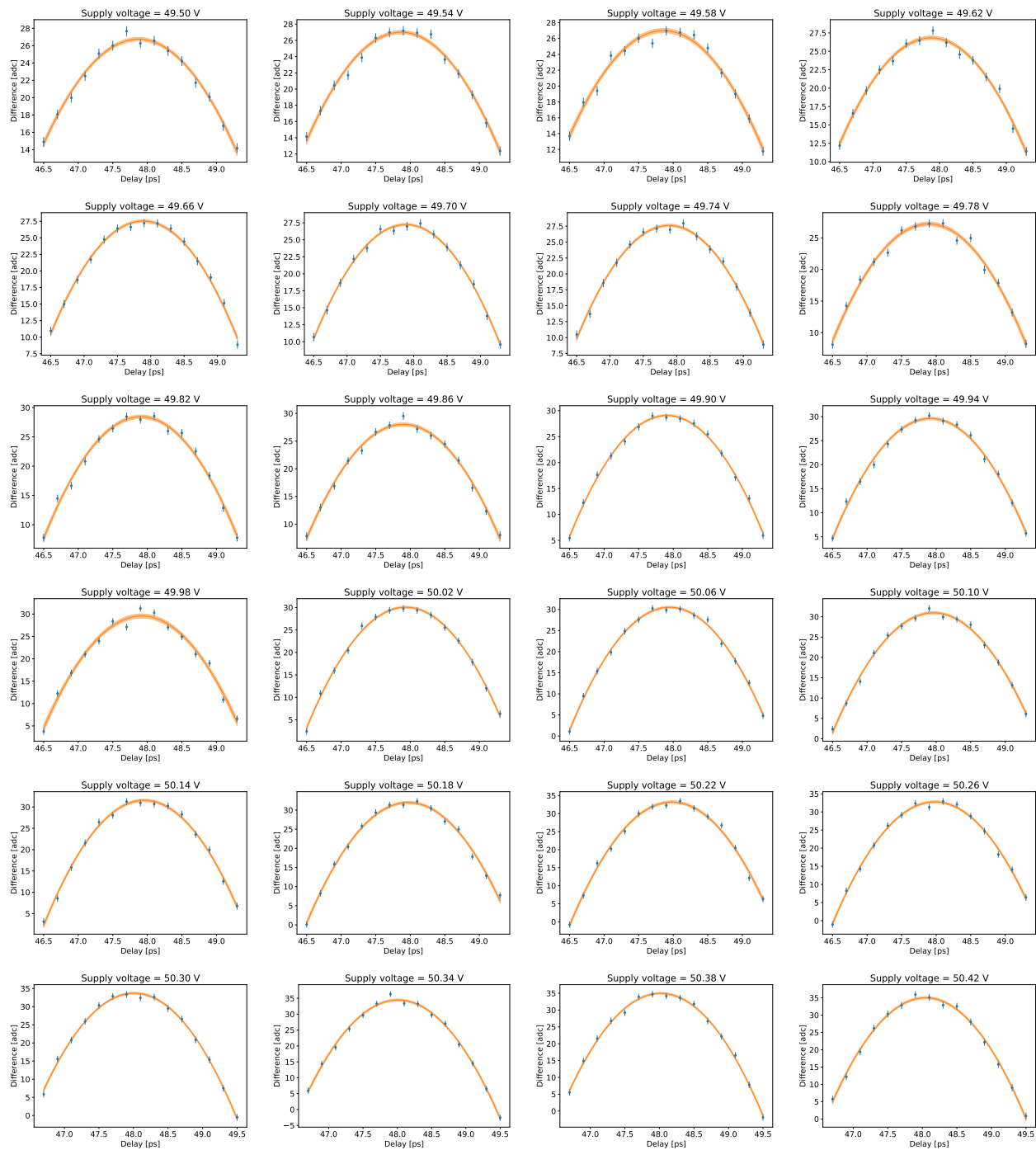
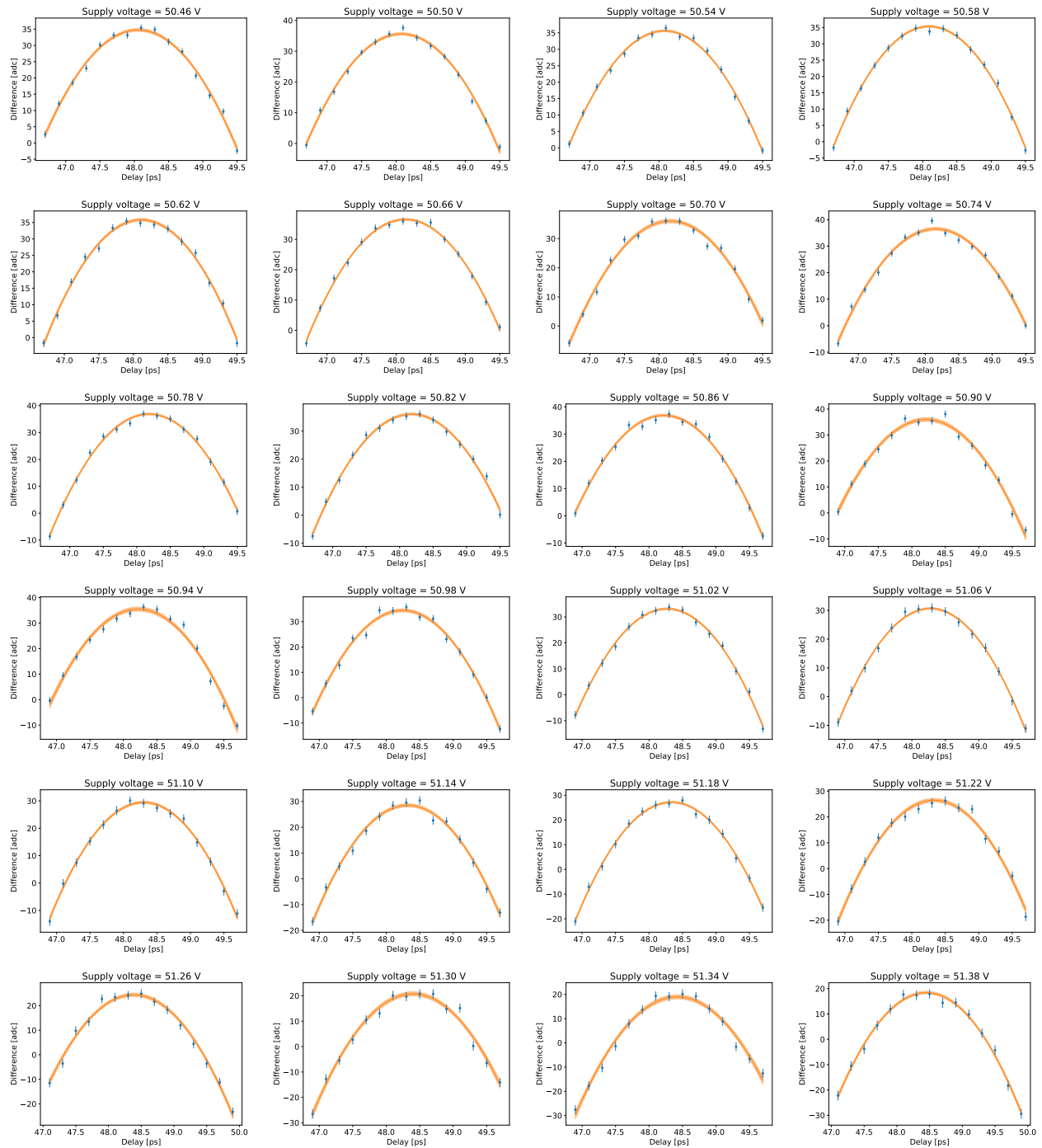


Figure D.13: Deficit of measured coincident pulse amplitudes, and quadratic fit as a function of interpulse delay, for the PMT used in LAB+PPO data-taking, at various supply voltages. The fit is performed over the 15 central data-points about the maximum pulse amplitude.





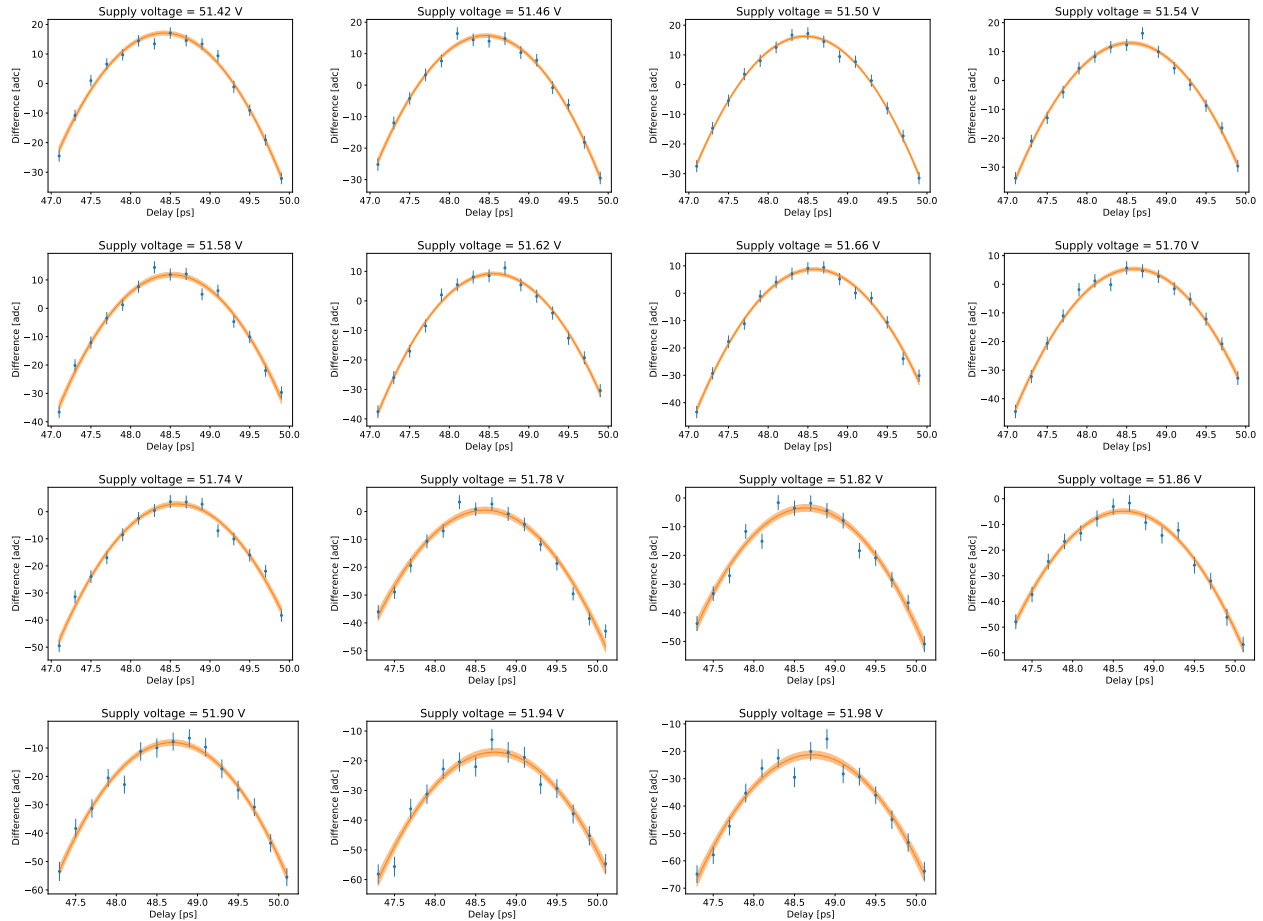


Figure D.14: Deficit of measured coincident pulse amplitudes, and quadratic fit as a function of interpulse delay, for the PMT used in WbLS data-taking, at various supply voltages. The fit is performed over the 15 central data-points about the maximum pulse amplitude.

Appendix E

LAPPD strip-level reconstruction

Large-area Picosecond Photodetectors are the product of a nearly decade-long effort to extend the picosecond-scale timing resolution of microchannel plate (MCP) photodetectors to larger sensitive areas [90]. Current models [231] offer timing resolution below 100 ps over sensitive areas of nearly 400 cm [231]. A modular design decouples the microchannel plates, in which signal multiplication occurs, from the anode configuration, which allows for various readout schemes implementing different degrees of pixelation across the sensitive area.

The LAPPD used in this work employed the conventional strip-line anode design, in which the anode is partitioned into 28 discrete strips, which run the full 20 cm length of one dimension and are ~ 5 mm wide (see Figure E.1). Dual readout of both ends of each strip allows for reconstruction of the time and position of the photoelectron cloud touchdown, improving the effective timing resolution.

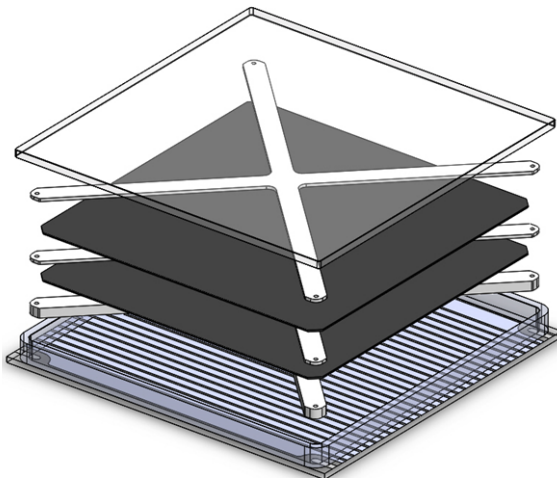


Figure E.1: Diagram of typical LAPPD layered construction, showing (from top to bottom): glass window and multialkali photocathode, structural spacer, first MCP, structural spacer, second MCP, structural spacer, silver strip-line anode. Figure reproduced from [238].

Let L be the full length of the strip; t_0 and x_0 the global time and position of the PE cloud touchdown, where x_0 is measured relative to the strip center; $\Delta_L = x_0$, $\Delta_R = L - x_0$ the touchdown position measured relative to the left and right terminals, respectively; t_L and t_R the global times of signal detection on at the left and right terminals (“channel times”), respectively; τ_L and τ_R the signal propagation times from the touchdown location to the left and right terminals, respectively; and v the signal propagation speed along the stripline. We then have

$$\begin{aligned} t_L &= t_0 + \tau_L \\ t_R &= t_0 + \tau_R \end{aligned} \tag{E.1}$$

relating the propagation and channel times, and

$$\begin{aligned} \Delta_L &= v\tau_L \\ \Delta_R &= v\tau_R \end{aligned} \tag{E.2}$$

relating the propagation times and distances. The average channel time is

$$\begin{aligned} \frac{t_L + t_R}{2} &= \frac{2t_0 + \tau_L + \tau_R}{2} \\ &= t_0 + \frac{\Delta_L + \Delta_R}{2v} \\ &= t_0 + \frac{L}{2v}, \end{aligned} \tag{E.3}$$

i.e. the global touchdown time, shifted by a constant offset. The difference in channel times is

$$\begin{aligned} t_R - t_L &= \tau_R - \tau_L \\ &= \frac{\Delta_R - \Delta_L}{v} \\ &= \frac{x_0}{v}, \end{aligned} \tag{E.4}$$

i.e. the touchdown location. All LAPPD detection times used in the scintillator time profile measurements presented in this work refer to global times reconstructed using Equation E.4. The timing response of the device used in this work, measured using a picosecond laser with trigger resolution ~ 30 ps, admits a Gaussian resolution of ~ 40 ps, and is shown in Figure E.2. An exponential tail accounts for $\sim 25\%$ of the response, and is associated with primary photoelectrons which backscatter off the upper MCP before amplifying within a microchannel.

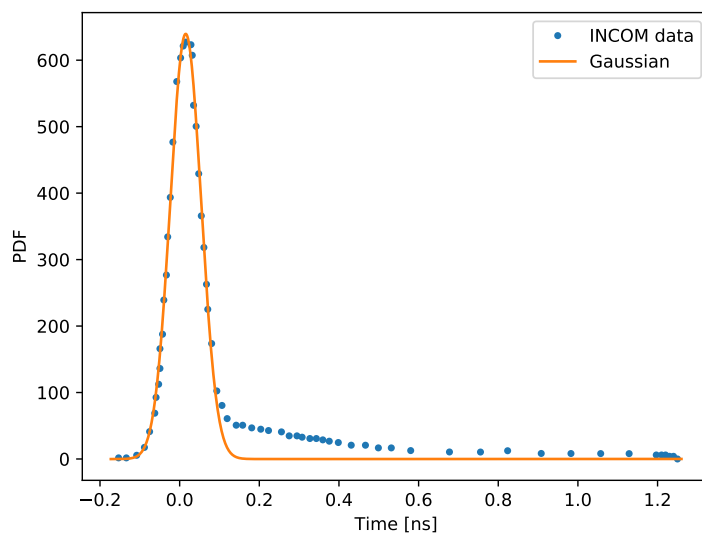


Figure E.2: Single-PE time response of LAPPD # 93, with a Gaussian fit to the prompt region overlaid. Data courtesy of INCOM [233].

Appendix F

Analytic scintillator timing model

The generic model outlined in Equation 6.16 can be evaluated analytically when the photodetector response function and trigger profile are both Gaussian, as is the case for the electron measurements presented in Section 6.3.7. In the case that the trigger profile is non-Gaussian, the other factors of the model can be evaluated efficiently by performing the convolutions analytically, and implementing only the anticonvolution with the trigger profile numerically. The core mathematical element is the convolution of a Gaussian distribution $G(t; \sigma)$ with an exponential distribution $E(t; \tau)$. This can be evaluated by “completing the square” in the exponent:

$$\begin{aligned}
G(t; \sigma) \otimes E(t; \tau) &= \int_0^\infty dx \frac{1}{\sqrt{2\pi}\sigma} e^{-\frac{1}{2}(\frac{t-x}{\sigma})^2} \cdot \frac{1}{\tau} e^{-\frac{x}{\tau}} \\
&= \frac{1}{\tau} \int_0^\infty dx \frac{1}{\sqrt{2\pi}\sigma} e^{-\frac{1}{2\sigma^2}(t^2+x^2-2tx)-\frac{x}{\tau}} \\
&= \frac{1}{\tau} e^{-\frac{t^2}{2\sigma^2}} \int_0^\infty dx \frac{1}{\sqrt{2\pi}\sigma} e^{-\frac{1}{2\sigma^2}(x^2-2tx)-\frac{x}{\tau}} \\
&= \frac{1}{\tau} e^{-\frac{t^2}{2\sigma^2}} \int_0^\infty dx \frac{1}{\sqrt{2\pi}\sigma} e^{-\frac{1}{2\sigma^2}(x^2-2(t-\frac{\sigma^2}{\tau})x)} \\
&= \frac{1}{\tau} e^{-\frac{t^2}{2\sigma^2}} \int_0^\infty dx \frac{1}{\sqrt{2\pi}\sigma} e^{-\frac{1}{2\sigma^2}((x-(t-\frac{\sigma^2}{\tau}))^2-(t-\frac{\sigma^2}{\tau})^2)} \\
&= \frac{1}{\tau} e^{-\frac{t^2}{2\sigma^2}} e^{\frac{1}{2\sigma^2}(t-\frac{\sigma^2}{\tau})^2} \int_0^\infty dx \frac{1}{\sqrt{2\pi}\sigma} e^{-\frac{1}{2\sigma^2}(x-(t-\frac{\sigma^2}{\tau}))^2} \\
&= \frac{1}{\tau} e^{\frac{\sigma^2}{2\tau^2}-\frac{t}{\tau}} \int_{\frac{1}{2\tau}-\frac{t}{2\sigma^2}}^\infty dx \frac{1}{\sqrt{2\pi}\sigma} e^{-\frac{1}{2}(\frac{x}{\sigma})^2}.
\end{aligned} \tag{F.1}$$

We recognize the remaining integral as the cumulative distribution function of a normal distribution and rewrite it in terms of the error function:

$$\begin{aligned}
 \int_{\frac{1}{2\tau} - \frac{t}{2\sigma^2}}^{\infty} dx \frac{1}{\sqrt{2\pi}\sigma} e^{-\frac{1}{2}\left(\frac{x}{\sigma}\right)^2} &= \frac{1}{\sqrt{\pi}} \int_{\frac{\sigma}{\sqrt{2\tau}} - \frac{t}{\sqrt{2}\sigma}}^{\infty} du e^{-u^2} \\
 &= \frac{1}{2} \cdot \frac{2}{\sqrt{\pi}} \int_{\frac{1}{\sqrt{2}}\left(\frac{\sigma}{\tau} - \frac{t}{\sigma}\right)}^{\infty} du e^{-u^2} \\
 &= \frac{1}{2} \operatorname{erfc} \left(\frac{1}{\sqrt{2}} \left(\frac{\sigma}{\tau} - \frac{t}{\sigma} \right) \right).
 \end{aligned} \tag{F.2}$$

Hence, we have

$$G(t; \sigma) \otimes E(t; \tau) = \frac{1}{2\tau} e^{\frac{\sigma^2}{2\tau^2} - \frac{t}{\tau}} \cdot \operatorname{erfc} \left(\frac{1}{\sqrt{2}} \left(\frac{\sigma}{\tau} - \frac{t}{\sigma} \right) \right).$$

This applies to any convolution of a Gaussian photodetector response with an exponential term in a scintillation time profile.

For electrons, the anticonvolution in Equation 6.16 can be extended to $-\infty$, as the trigger profile is a relatively Gaussian. By the symmetry of the Gaussian distribution, the anticonvolution can be evaluated as a regular convolution, so that the system response is also a Gaussian, with standard deviation $\sigma = \sqrt{\sigma_P^2 + \sigma_T^2}$, where P and T refer to the photodetector and trigger components, respectively.